Anisotropic Thermal and Electrical Properties of CFRP

Vom Promotionsausschuss der
Technischen Universität Hamburg
zur Erlangung des akademischen Grades
Doktor-Ingengieur (Dr.-Ing.)

genehmigte Dissertation (Monografie)

von
Julian M. Karsten

aus Hamburg, Deutschland

2026

Vorsitzender des Prüfungsausschusses:	Prof. Dr.-Ing. Benedikt Kriegesmann (Technische Universität Hamburg)
Gutachter:	Prof. Dr.-Ing. habil. Bodo Fiedler (Technische Universität Hamburg) Prof. Dr.-Ing. Wolfgang Hintze (Technische Universität Hamburg)
Tag der mündlichen Prüfung:	30.07.2026

Technisch-Wissenschaftliche Schriftenreihe

Herausgeber
Prof. Dr.-Ing. habil. Bodo Fiedler

Anschrift
Technische Universität Hamburg (TUHH)
Institut für Kunststoffe und Verbundwerkstoffe
Denickestraße 15
21073 Hamburg

Band 51
Anisotropic Thermal and Electrical Properties of CFRP
DOI: https://doi.org/10.15480/882.17789

Julian M. Karsten
https://orcid.org/0000-0002-8243-4114

1. Auflage
Hamburg 2026

ISSN: 2625-6029



Dieses Werk ist lizenziert unter einer Creative Commons “Namensnennung 4.0 International” Lizenz.

Bibliographische Information der Deutschen Nationalbibliothek
Die deutsche Nationalbibliothek verzeichnet diese Publikation in der Deutschen Nationalbibliothek; detaillierte Informationen sind im Internet über dnb.de abrufbar.

"The fact that the polynomial is an approximation
does not necessarily detract from its usefulness
because all models are approximations.

Essentially, all models are wrong, but some are useful."

George E. P. Box, 1987

Kurzfassung

Kohlenstofffaserverstärkte Kunststoffe (CFK) weisen stark anisotrope thermische und elektrische Eigenschaften in der Laminatebene auf. Die Bestimmung entsprechender Kennwerte ist anspruchsvoll, da die Messgrößen sowohl von der Materialarchitektur als auch von den experimentellen Randbedingungen abhängig sind. Diese Arbeit entwickelt zerstörungsfreie, modellgestützte Verfahren zur Identifikation orthotroper thermischer und elektrischer Transporteigenschaften von CFK-Laminaten an Einzelproben und verknüpft diese mit einer ebenfalls zerstörungsfreien Charakterisierung des Laminataufbaus. Ein Puls-Echo-Ultraschallverfahren wertet C-Scans im Fourierraum aus und rekonstruiert daraus den tiefenabhängigen Verlauf der Lagenorientierung. Eine zuverlässige Orientierungsbestimmung wird für unidirektionale, quasi-isotrope und Bouligand-Laminate unterschiedlicher Dicken und Lagenzahlen nachgewiesen. Oberflächennahe Bereiche, Porosität und ausgeprägte geometrische Merkmale definieren dabei die Grenzen, innerhalb derer die Methode zuverlässig angewendet und interpretiert werden kann. Der anisotrope Wärmetransport wird mittels Wärmepunkt-Infrarot-Thermografie in Kombination mit einem analytischen orthotropen Diffusionsmodell beschrieben. Die richtungsabhängige Messgröße folgt dem inversen Widerstand gegen Wärmediffusion, auf den Hauptachsen ergeben sich die longitudinale und transversale Temperaturleitfähigkeit. Diese Beziehung ermöglicht die Bestimmung der Temperaturleitfähigkeit durch gaußsche Temperaturprofilverbreiterung und Isothermenentwicklungsanalysen. Ergänzend verknüpft ein mischungsregelbasierter Ansatz das Laminatverhalten mit den Diffusivitäten der Konstituenten und dem Faservolumengehalt. Der anisotrope elektrische Transport wird anhand regelmäßiger n-eckiger prismatischer Proben charakterisiert. Umfangsseitige Widerstandsmessungen an Vollflächenelektroden werden über den effektiven Elektrodenabstand und die effektive Messbreite ausgewertet, um die spezifischen elektrischen Hauptwiderstände entlang und quer zur Faserrichtung zu bestimmen. Zusätzliche, von Kontakt- und Kurzschlusseffekten dominierte Konfigurationen definieren die Bedingungen, die für eine verlässliche Bestimmung der Materialwiderstände nötig sind.

Abstract

Carbon fiber-reinforced polymers (CFRPs) exhibit strongly anisotropic in-plane thermal and electrical properties, yet efficient identification of laminate-scale transport parameters remains challenging, since the measured response reflects both material architecture and experimental boundary conditions. This thesis establishes non-destructive, model-based methods for single-specimen identification of orthotropic in-plane thermal and electrical transport properties in CFRP laminates and combines them with a non-destructive characterization of laminate lay-up.

A pulse-echo ultrasonic workflow evaluates C-scan slices in the Fourier domain and reconstructs the depth-dependent ply-orientation profile. Reliable orientation detection is demonstrated for unidirectional, quasi-isotropic, and Bouligand laminates across varying thicknesses and ply counts. Near-surface regions, porosity, and pronounced geometric features define the methodological boundaries within which the method can be applied and interpreted reliably.

Anisotropic thermal transport is quantified by heat-spot infrared thermography combined with an analytical orthotropic diffusion model. Under prescribed heat-flux boundary conditions, the directional response follows the inverse resistivity to diffusion, whose principal-axis values correspond to the longitudinal and transverse thermal diffusivities. This relation enables identification of the directional diffusivities from a single unidirectional specimen through Gaussian-profile broadening and isotherm-evolution analyzes. In addition, a rule-of-mixture approach relates laminate behavior to constituent diffusivities and fiber volume content.

Anisotropic electrical transport is characterized using regular n-gonal prismatic specimens, where perimeter-based resistance measurements under full-face electrodes are evaluated by means of effective electrode distance and effective width to identify the principal longitudinal and transverse resistivities. Additional contact- and shunting-dominated configurations clarify the conditions for reliable resistivity measurement.

Contents

List of Characters and Abbreviations **xiii**

1 Introduction **1**
1.1 Aims and Scope . . . 3
1.2 Thesis Outline . . . 4

2 General Theoretical Background **7**
2.1 Structural Anisotropy . . . 7
2.2 Mechanical Anisotropy . . . 10
2.3 Transport Anisotropy . . . 14

3 Materials and Methods **17**
3.1 Materials . . . 17
3.2 Methods . . . 19
3.2.1 Scientific Methods . . . 19
3.2.2 Sample Preparation . . . 21

4 Fiber Orientation Detection **23**
4.1 Theoretical Background . . . 24
4.1.1 State-of-the-Art Measurement Techniques . . . 24
4.1.2 Selection of Measurement Technique . . . 29
4.1.3 Ultrasonic Testing . . . 30
4.2 Test Setup . . . 41
4.3 Analysis Methodology . . . 44
4.3.1 Pre-Processing . . . 45
4.3.2 Main Processing . . . 52
4.4 Results and Discussion . . . 60
4.4.1 Unidirectional Laminates . . . 61
4.4.2 Quasi-Isotropic Laminates . . . 64
4.4.3 Bouligand Laminates . . . 67
4.4.4 Design Features and Damage . . . 70
4.5 Conclusions . . . 74

5 Anisotropic Thermal Properties **77**
5.1 Theoretical Background 78
5.1.1 Thermal Anisotropy 78
5.1.2 State-of-the-Art Measurement Techniques 86
5.1.3 Selection of Measurement Technique 94
5.1.4 Thermography 95
5.1.5 HST: Governing Equations and General Form 96
5.1.6 HST: Specialized 2D Orthotropic Formulation 99
5.1.7 HST: Specialized 2D Isotropic Formulation 103
5.2 Test Setup 106
5.3 Analysis Methodology 107
5.4 Results and Discussion 116
5.4.1 Thermal Measurements: Matrix and CFRP 116
5.4.2 Analytical Model 117
5.4.3 Temperature Dependency 118
5.4.4 Contextualization of the Measurement Results 119
5.5 Conclusions 121

6 Anisotropic Electrical Properties **123**
6.1 Theoretical Background 124
6.1.1 Electrical Anisotropy 124
6.1.2 Microstructural Mechanisms 130
6.1.3 Electrical Conduction Models 135
6.1.4 Electrical Equivalent Circuit Models 139
6.2 Test Setup 142
6.3 Analysis Methodology 143
6.3.1 Base Model 143
6.3.2 Model Extension: Small Electrode Size 150
6.3.3 Model Extension: Inner Electrodes 152
6.3.4 Resistivity and Microstructural Spacing 154
6.4 Results and Discussion 158
6.4.1 Silver Conductive Laquer 158
6.4.2 Influence of Ply Thickness 160
6.4.3 Polygon Based Resistance Measurements 164
6.5 Conclusions 178

7 Summary **179**

Bibliography **183**

A Appendix: Fiber Orientation Detection **213**
A.1 Software Repository: CompoSE 213
A.2 Methodology Flowchart 215
A.3 2D Discrete Fourier Transform 216
A.4 2D Windowing Functions 220
A.5 Supporting Results 222
A.5.1 Unidirectional Laminates 222
A.5.2 Quasi-Isotropic Laminates 224
A.5.3 Bouligand Laminates 226

B Appendix: Anisotropic Thermal Properties **229**
B.1 Software Repository: TCAM 229
B.2 Methodology Flowchart 233
B.3 Polar Isotherm Evolution 234

C Appendix: Anisotropic Electrical Properties **237**
C.1 Software Repository: PolAR 237
C.2 Methodology Flowchart 238
C.3 Base Model - Parameter Variation 239
C.4 Model Comparison 242

Supervised Student Theses **245**

Research Projects **249**

Scientific Publications **251**

List of Characters and Abbreviations

Latin Characters

Character	Unit	Description
A	m^2	Cross-sectional area
A	–	Anisotropy ratio
a	–	Complex analytic signal of an ultrasonic A-scan
c	–	Isotherm constant
c	m/s	Sound velocity / acoustic wave speed
c_p	$\mathrm{J/(kg\,K)}$	Specific heat capacity
D	m	Contextual length scale
d	m	Diameter
E	Pa	Young's modulus
E	–	Peak energy metric (peak analyzes)
$\mathbf{E}$	V/m	Electric field strength
f	Hz	Frequency
f	–	Isotherm fraction
G	Pa	Shear modulus
$\mathcal{H}$	–	Hilbert transform operator
I	A	Electric current
$\mathbf{J}$	$\mathrm{A/m}^2$	Current density
L	$\mathrm{W\,\Omega/K}^2$	Lorenz number
L	m	Contextual length scale
l	m	Contextual length scale
m	kg	Mass
m	–	Peak score metric (peak analyzes)
N	–	Number of counts (e.g. camera signal, sampling points)

...

Character	Unit	Description
n	–	Shape parameter in generalized rule-of-mixtures models
P_k	–	Prominence of the k-th peak in the angular spectrum
$\dot{Q}$	W	Heat flow
q	W/m^2	Heat flux density
R	Ω	Electrical resistance
R^2	–	Coefficient of determination
r	m	Radius / radial coordinate
r	s/m^2	Thermal resistivity to diffusion
S	–	Angular spectrum
S	–	Peak sharpness metric (peak analyzes)
s	m	Face length of a regular polygon specimen
s	–	Real part of analytic signal of an ultrasonic A-scan
T	K, °C	Temperature
t	s	Time
t	m	Specimen / laminate thickness
U	V	Electrical voltage
V	m^3	Volume
W	°	Full width at half maximum angle (peak analyzes)
w	m	Specimen width
w	–	Weighting factor (peak analyzes)
x, y, z	m	Spatial coordinates (material coordinate system)
Z	Pa s/m	Acoustic impedance

Greek Characters

Character	Unit	Description
α	m^2/s	Thermal diffusivity
α	°	Transition angle (electrode displacement)

...

Character	Unit	Description
β	°	Offset angle between adjacent electrode configurations
χ	–	Thermal generic placeholder metric
δ	m	Gauge length / electrode spacing
Δ	K	General increment indicator
ϵ	–	Small positive constant (numerical stabilization)
ε	–	Emissivity
Γ	–	Dimensionless resistance ratio
η	–	Dimensionless scaling factor (e.g. thickness, polygon scaling, electrode coverage)
λ	W/(m K)	Thermal conductivity
π	–	Circle constant
ρ	$\mathrm{kg/m^3}$	Density
ρ	Ω m	Electrical resistivity
ρ	–	Reflectance
σ	Pa	Stress / tensile strength
σ	S/m	Electrical conductivity
τ	–	Transmittance
θ	°	Relative fiber orientation angle
Θ	°	Global fiber orientation angle
ϕ	°	Phase shift
φ	–	(Fiber) volume fraction

Indices

Index	Description
0	Baseline / empty reference (e.g. empty crucible)
af	Across flats
air	Measured in air
ana	Analytical
arc	Arc length
atm	Atmospheric contribution

...

Index	Description
bb	Blackbody
bw	Back-wall echo
cam	Camera
c	Composite material
c	Contact (electrode/interface)
e	Electronic contribution
eff	Effective (homogenized) property
el	Electrode
env	Environment
f	Fiber material
gau	Distribution function model derived (Gaussian)
fw	Front-wall echo
i	Discrete measurement / angle index
$isoT$	Isotherm (temperature contour)
k	k-th peak / discrete index
m	Matrix material
$meas$	Measured quantity
nom	Nominal
obj	Object
ply	Ply-level
$\perp$	Material direction: transverse, 90°
$\parallel$	Material direction: fiber-parallel, 0°
pts	Sampling points
ref	Reference value
rom	Rule of mixtures
s	Sampling (e.g. sampling frequency f_s)
s	Specimen
sap	Sapphire reference
x	Material axis: fiber direction (local)
y	Material axis: transverse in-plane (local)
z	Material axis: through-thickness (local)

Abbreviations

Abbreviation	Description
AC	Alternating Current
ADC	Analog-to-Digital Converter
ASTM	ASTM International (standards organization)
BL	Bouligand laminate lay-up
CFRP	Carbon Fiber Reinforced Polymer
CNC	Computer Numerical Control
CompoSE	Software: Composite Sonar Evaluation
CT	Computed Tomography
μCT	Micro-Computed Tomography
C-scan	Planar ultrasonic scan image
DC	Direct Current
DSC	Differential Scanning Calorimetry
EEC	Electrical Equivalent Circuit
EPG	Electric Potential Gradient
ESR	Equivalent Series Resistance
FEM	Finite Element Method
FFT	Fast Fourier Transform
FOD	Fiber Orientation Distribution
FRP	Fiber Reinforced Polymer
FWHM	Full Width at Half Maximum
GHP	Guarded Hot Plate
GUI	Graphical User Interface
HDF5	Hierarchical Data Format (v5)
HFM	Heat Flow Meter
HST	Heat-Spot Thermography
IEEE	Institute of Electrical and Electronics Engineers
IR	Infrared
ISO	International Organization for Standardization
LFA	Laser Flash Analysis
LIT	Lock-In Thermography
LWIR	Long-Wave Infrared
MOC	Method of Cells
MOCu	Unaveraged Method of Cells

...

Abbreviation	Description
MT	Mori–Tanaka method
NN	Nearest Neighbor
NDT	Non-Destructive Testing
NTPT	North Thin Ply Technology
NTR	Nano-Thermoreflectance
OFHC	Oxygen-Free High-Conductivity (Copper)
PAN	Polyacrylonitrile
PolAR	Software: Polygon-based Analytical Resistivity
QI	Quasi-isotropic laminate lay-up
ROI	Region of Interest
ROM	Rule of Mixtures
SCL	Silver Conductive Lacquer
SDK	Software Development Kit
SHM	Structural Health Monitoring
TCAM	Software: Thermal Conductivity of Anisotr. Materials
TUHH	Hamburg University of Technology
UD	Unidirectional laminate lay-up
US	Ultrasonic Testing
XRD	X-ray Diffraction
XFA	Xenon Flash Analyzes

1 Introduction

Carbon fiber reinforced polymers (CFRPs) have become a key material class for lightweight structures that must combine high specific stiffness and strength with long-term durability in demanding service conditions. By embedding continuous carbon fibers into a polymer matrix, CFRPs enable tailored performance through deliberate design freedom, including fiber type, fiber volume fraction, ply thickness, and laminate stacking sequence. This design freedom has driven their widespread use in high-performance structures, where components are increasingly expected to provide not only mechanical load-bearing capacity but also additional functional capabilities.

A defining characteristic of CFRPs is their pronounced anisotropy. At the microscale, carbon fibers exhibit intrinsically direction-dependent properties originating from their graphitic microstructure [1, 2], while at the mesoscale and laminate scale, preferential alignment of fibers introduces a strong contrast between the fiber-parallel and transverse directions [3]. As a consequence, the macroscopic behavior of CFRPs is governed by fiber fraction, fiber alignment, and its deviations from the nominal design (e.g., fiber waviness, local misalignment, resin-rich zones, porosity, and inter-laminar interfaces) [4–7]. Although mechanical anisotropy is widely recognized and routinely considered in design [3], transport anisotropy is often treated as secondary despite its direct relevance to multifunctional structures and coupled thermo- and electromechanical phenomena [8–14].

Thermal transport anisotropy is particularly critical because thermal conductivity and diffusivity govern the spatial and temporal evolution of temperature fields in a laminate [15, 16]. In orthotropic CFRPs, the pronounced contrast between fiber-parallel and transverse transport leads to direction-dependent heat spreading, which directly affects temperature gradients, local hot-spot formation, and characteristic timescales of thermal loading [17–19]. In practical terms, this influences the thermal management of enclosed or integrated electronics [20], localized heating concepts (e.g., electrothermal de-icing and resistance-based heating for

processing or repair) [11, 12], and the development of thermally induced stresses that can interact with fatigue and damage evolution [8, 9]. Reliable simulation and design therefore require orientation-specific effective properties and a clear understanding of how fiber architecture and interfacial effects shape the effective in-plane transport tensor under suitable boundary conditions [21–25].

Electrical transport anisotropy is equally important and originates from the heterogeneous conductor–insulator topology of CFRPs: electrically conductive carbon fibers are embedded in an electrically insulating polymer matrix [26, 27]. Along the fiber direction, conduction is governed primarily by the intrinsic conductivity of the fibers and the continuity of the fiber network [28–30]. In contrast, transverse and through-thickness conduction are typically controlled by a sparse network of fiber–fiber transfer events across resin-rich separations and ply interfaces, where junction/contact resistance and near-contact (tunneling) mechanisms become decisive [31–34]. Consequently, the effective electrical response can differ by orders of magnitude between the principal directions, with a strong sensitivity to fiber volume fraction, contact density, and inter-laminar connectivity [27, 29, 35]. This anisotropy underlies multifunctional applications of CFRPs, including electromagnetic interference shielding [36, 37], electrothermal heating concepts [13, 14], and self-sensing approaches based on resistance changes along preferential conduction pathways [38–40].

Despite this relevance, a persistent challenge is that anisotropic transport properties are difficult to quantify in a way that is both orientation-resolved and robust against experimental artifacts [41, 42]. First, fiber orientation is the dominant structural descriptor that governs both mechanical response and effective transport, but the effective orientation state inside a laminate is not always known in advance and can deviate from the nominal stacking sequence due to manufacturing and handling-induced effects [4, 5, 26]. Without reliable and non-destructive access to ply-level orientation information, transport measurements cannot be interpreted unambiguously and model validation remains limited [43–45]. Second, thermal characterization of in-plane anisotropy must address the fact that many established methods require multiple specimens and orientations or depend sensitively on heat losses, emissivity uncertainties, and finite-geometry effects [41, 46–49]; field-based thermography methods offer rich information but demand a rigorous link between the measured transient temperature field and the principal in-plane diffusivities [24, 25, 50–52]. Third, electrical anisotropy measurements are strongly affected by boundary conditions and electrode topology: conventional coupon-based measurements are well suited for longitudinal conduction, whereas

transverse characterization is often dominated by current spreading, contact effects, and the coupling of through-thickness pathways, which can obscure the targeted material parameters unless geometry and modeling are aligned [31, 34, 42, 53–56].

1.1 Aims and Scope

This thesis addresses the need for a coherent and experimentally grounded framework to characterize anisotropic transport in CFRP laminates. The central objective is to link non-destructive characterization of the laminate to orientation-resolved transport characterization, so that experimentally obtained thermal and electrical properties can be interpreted consistently and used for quantitative analysis. To this end, the thesis integrates (i) non-destructive determination of ply-level fiber orientation lay-up at relevant laminate depths, (ii) experimental identification of anisotropic in-plane thermal transport and its interpretation by an analytical model, and (iii) experimental identification of anisotropic in-plane electrical transport and its interpretation by an analytical representation.

The work builds upon three research questions that correspond to the three main chapters:

1. **Fiber Orientation Detection:** *How can the ply-level fiber orientation lay-up in CFRP laminates be determined non-destructively to enable a quantitative interpretation of anisotropic in-plane transport behavior?*
2. **Anisotropic Thermal Properties:** *How can anisotropic in-plane thermal transport in CFRP laminates be determined efficiently by non-destructive testing and interpreted using an appropriate analytical model?*
3. **Anisotropic Electrical Properties:** *How can anisotropic in-plane electrical transport in CFRP laminates be determined efficiently by non-destructive testing and interpreted using an appropriate analytical model?*

The scope of this thesis is limited to continuous-fiber laminates and the characterization of anisotropy at the laminate scale, with the ply-level lay-up serving as the primary architectural descriptor for the observed in-plane transport behavior. The focus is placed on orientation-resolved, experimentally accessible effective transport properties in the principal material directions, i.e., fiber-parallel ($0°$; $\parallel$) and transverse ($90°$; $\perp$), and on evaluation strategies that enable quantitative

interpretation within analytical models and closed-form descriptions. Numerical field simulations (e.g., FEM-based approaches) are not pursued in this work.

Through-thickness transport properties are not treated as the primary target quantities; however, they are an integral part of the overall material response and are therefore discussed where relevant. In addition, selected aspects of the through-thickness contribution are addressed indirectly by investigating laminates with systematically varied ply thickness, spanning approximately 300 gsm (thick-ply) down to 30 gsm (thin-ply) architectures.

Mechanical anisotropy is treated as an essential background, while the principal contributions of this thesis concern the experimental methodology and data-reduction for thermal and electrical transport anisotropy, including measurement concepts, calibration procedures, and uncertainty-relevant boundary-condition considerations. All experimental models, evaluation routines, and control systems are implemented in Python to ensure reproducible workflows and to enable consistent integration of acquisition, processing, and analysis. The thesis provides a fundamental mathematical and physical formulation of the employed models and evaluation procedures. However, a comprehensive software and code review of Python implementations is outside the scope of this work.

1.2 Thesis Outline

Figure 1.1 provides an overview of the thesis workflow and the interdependencies of the three main contributions. Starting from the investigated CFRP material system, the ply-level fiber orientation $\Theta(z_k)$ is determined non-destructively by ultrasonic testing and subsequently serves as the enabling basis for the characterization of anisotropic in-plane transport. Thermal transport is assessed by non-destructive heat-spot thermography and interpreted using an analytical orthotropic heat-diffusion model, whereas electrical transport is assessed by non-destructive resistance measurements and interpreted using a geometry-aware analytical resistance model.

This dissertation is organized into seven chapters. Chapter 1 establishes CFRP laminates as intrinsically anisotropic engineering materials and formulates the central premise of this work: in-plane thermal and electrical transport can only be interpreted and quantified reliably when the underlying ply-resolved fiber orientation state is known. It defines the aims and scope, summarizes

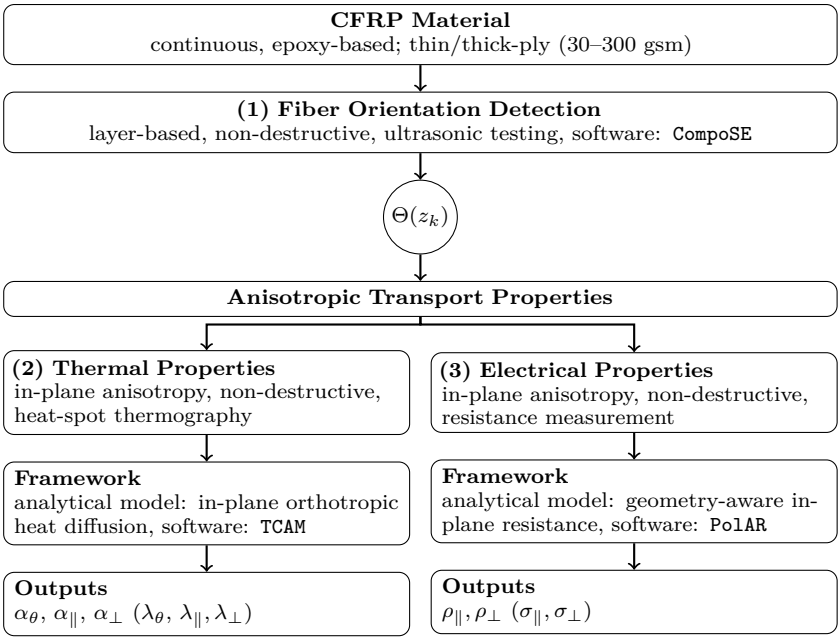


Figure 1.1: Conceptual workflow of the thesis, highlighting the three main contributions and their interdependencies.

the scientific contributions, and positions the three research questions that structure the thesis. Chapter 2 provides the unifying theoretical backbone by linking structural anisotropy, understood as the architectural origin of direction-dependent response, to mechanical anisotropy as a foundational reference, and by formalizing transport anisotropy as the consistent framework for thermal and electrical conduction in CFRP laminates. With the conceptual basis fixed, Chapter 3 specifies the investigated laminate systems and specimen configurations and consolidates the experimental methodology and preparation procedures that are applied consistently across the three main experimental chapters.

Chapter 4 constitutes the first experimental pillar and addresses *Fiber Orientation Detection*. After assessing candidate methods and motivating the selected strategy, it establishes the ultrasonic testing concept, the experimental setup, and the evaluation workflow for non-destructive, ply-level identification of the fiber orientation lay-up. Results are presented and discussed for unidirectional, quasi-isotropic, and Bouligand laminates, complemented by an analysis of characteristic

features and damage signatures; the chapter closes by translating the orientation results into the essential input for subsequent transport analyses. Building on this orientation-resolved basis, Chapter 5 investigates the *Anisotropic Thermal Properties*. It introduces the physical origin of thermal anisotropy, reviews measurement concepts, and motivates thermography in the form of heat-spot thermography. The chapter derives an analytical description for two-dimensional orthotropic heat conduction, details the test setup and evaluation methodology, and reports results spanning matrix and CFRP reference measurements, model behavior, temperature-dependent aspects, and the final contextualization of the extracted in-plane thermal transport properties, including consolidated findings and limitations. In direct analogy, Chapter 6 investigates the *Anisotropic Electrical Properties*. It introduces electrical anisotropy in CFRPs and summarizes relevant conduction mechanisms and equivalent-circuit concepts, then presents the experimental setup and a geometry-based analytical evaluation framework, including model extensions required for practical electrode configurations. The results and discussion quantify and interpret the influence of electrode preparation, ply thickness across thick-ply and thin-ply architectures, and polygon-based resistance measurement concepts, concluding in a consolidated description of the in-plane electrical transport behavior within the analytical framework. Finally, Chapter 7 synthesizes the findings across fiber orientation detection, anisotropic thermal transport, and anisotropic electrical transport, and formulates overarching conclusions and perspectives for further methodological development.

Additional material is provided in Chapters A to C, including supplementary methodological details, extended derivations where appropriate, additional measurement results, and software-related information associated with the experimental and evaluation workflows. The backmatter documents supervised student theses, related research projects, scientific publications, and a curriculum vitae.

2 General Theoretical Background

Carbon fiber reinforced composites represent a unique class of structural materials that combine the low density, chemical resistivity and processability of polymer matrices with the outstanding mechanical performance of carbon fibers. A defining characteristic of CFRPs is their pronounced anisotropy, which arises from the directional nature of the reinforcement. In contrast to isotropic bulk materials, the properties of CFRPs are strongly dependent on fiber orientation, fiber volume fraction, and the intrinsic anisotropy of the carbon fibers themselves. These factors govern the degree to which mechanical, thermal, and electrical properties differ along and transverse to the reinforcement direction, making anisotropy both a challenge and an opportunity for engineering applications. The subsequent subsections present a summary of the primary aspects of anisotropy observed in CFRPs.

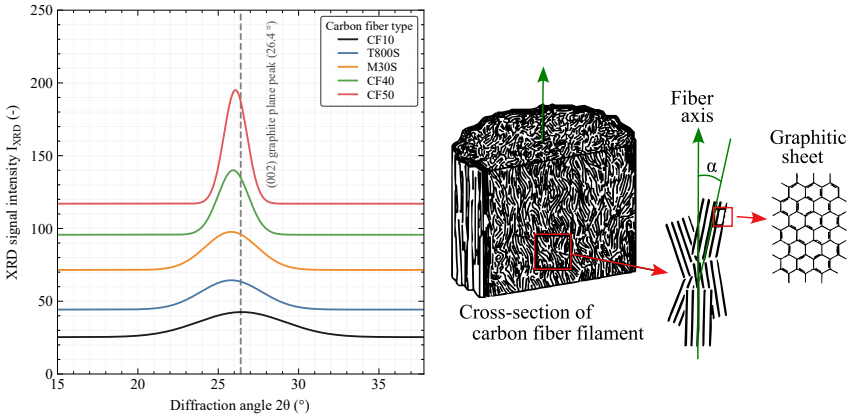
2.1 Structural Anisotropy

The internal architecture of CFRPs is inherently directional. Continuous fibers embedded in a polymer matrix produce long-range alignment that defines a clear material anisotropy between the fiber axis and the transverse directions. Even in woven or randomly oriented configurations. Structural anisotropy therefore persists at the ply, roving, and single-fiber level.

The anisotropic mechanical and transport properties of carbon fibers originate from the orientation distribution of their graphite crystallites and the arrangement of amorphous carbon regions. Depending on the precursor system and processing route, substantial differences in crystallite alignment are observed, which directly affect the degree of anisotropy in the resulting fibers.

Figure 2.1 reproduces the orientation distribution of graphite planes (002) in five representative types of carbon fibers based on PAN (polyacrylonitrile), as reported by Tane et al. [1]. For crystalline graphite, the (002)-plane occurs at

a diffraction angle $2\theta \approx 26.4°$ in X-ray diffraction (XRD) measurements. The results demonstrate that in all fibers, the in-plane directions of the graphitic layers are preferentially aligned along the fiber axis, but the extent of this alignment varies markedly with fiber type. In particular, CF40 and CF50 (HM: high modulus fibers) exhibit highly oriented graphite layers, while fibers such as CF10, T800S, and M30S (HS: standard modulus, high strength fibers) reveal broader distributions, indicating less pronounced alignment. These differences translate into significant variations in the anisotropy of the elastic properties, with the tensile modulus increasing and the transverse modulus decreasing for fibers with a higher orientation of the graphitic planes; see Figure 2.4.



(a) X-ray diffraction patterns for (002) planes of graphite crystallites in PAN-based carbon fibers. Adapted from Tane et al. [1].

(b) Schematic across scales representation of the aligned graphitic microstructure of a carbon fiber. Adapted from Behr et al. [2].

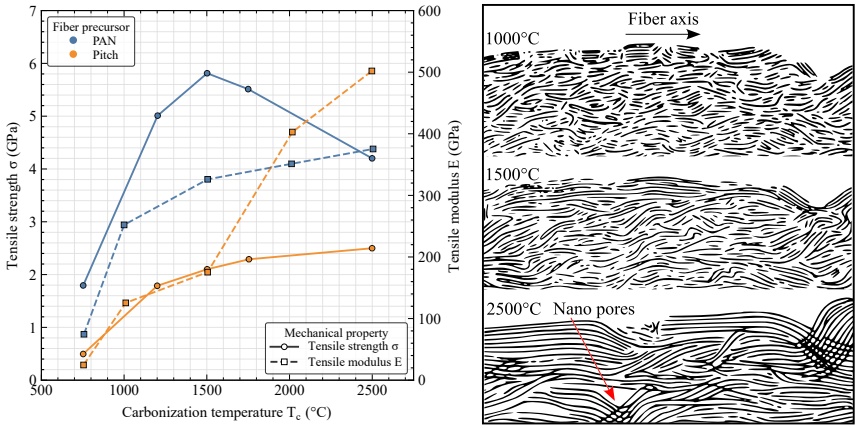
Figure 2.1: Schematic structural anisotropy of carbon fibers. [1, 2]

The systematic structure of carbon fibers has been widely reviewed in the literature [1, 2, 57–59]. PAN-based precursors dominate industrial production and, through stabilization, carbonization, and optional graphitization, yield a turbostratically stacked, graphite-like microstructure with a high degree of preferred axial orientation [1]. Here, turbostratic describes the graphite-like structure in which the graphene layers are parallel but randomly rotated or laterally shifted, so that there is no long-range three-dimensional stacking order. Pitch-derived fibers, particularly those from mesophase pitch (mixture of polycyclic aromatic hydrocarbons), can achieve even higher levels of crystalline orientation, leading

to high moduli, but often reduced tensile strength due to processing-induced flaws [2]. In contrast, polyethylene-derived carbon fibers show a reduced density of interlayer crosslinks, which facilitates easier orientation during heat treatment and thus allows for the formation of highly ordered graphitic domains [57]. Across all precursor systems, the balance between crystalline alignment, crystallite size, and defect density determines the attainable stiffness and strength [58, 59], while simultaneously governing thermal and electrical anisotropy [60, 61].

The effect of carbonization temperature T_c is a critical factor in determining the final anisotropy of carbon fibers. As the carbonization and graphitization temperature increases, both the degree of crystalline alignment and the size of the crystallite improve, leading to a higher elastic modulus [57, 58], see Figure 2.2. PAN-based fibers typically reach their maximum tensile strength around 1500 °C, while their tensile modulus continues to increase with further heat treatment, although at the expense of strength due to crystallite coarsening and defect formation [57]. In contrast, fibers derived from mesophase pitch require higher graphitization temperatures, above 2000 °C, to achieve very high moduli in highly graphitized variants [58]. The structural evolution during heat treatment is associated with the growth and orientation of the graphitic (002)-planes, whereas turbostratic disorder is progressively reduced. As summarized by Park [59], the balance between strength and stiffness is therefore highly sensitive to the final heat treatment schedule. Lower treatment temperatures yield higher strength fibers with moderate anisotropy, whereas higher temperatures produce stiffer, more anisotropic fibers but with reduced tensile strength.

Overall, the comparative analysis of different precursor systems illustrates that the orientation of graphite crystallites is not a fixed characteristic but a tunable microstructural parameter. As emphasized by Newcomb [58] and Park [59], the precursor chemistry and the processing path define the degree of crystalline orientation, crystallite connectivity, and residual amorphous content, thus shaping the anisotropic behavior of the final fiber.



(a) Mechanical properties of carbon fibers as function of the carbonization temperature T_c [58].

(b) Model for the development of carbon layer structures from TEM studies [57].

Figure 2.2: Influence of carbonization temperature T_c on structural and mechanical properties and schematic for the development of carbon layer structures. [57, 58]

2.2 Mechanical Anisotropy

The mechanical properties of carbon fibers represent their relevance in classical engineering and remain the main driver of their widespread industrial adoption. High tensile strength, low density, and high stiffness have established carbon fibers as critical reinforcement materials in aerospace, automotive, and civil engineering applications. [3]

A broad comparison of the mechanical properties of industrially available carbon fibers is given in Figures 2.3 and 2.4. Figure 2.3 summarizes tensile strength σ and the tensile modulus E based on manufacturer data and systematic reviews by Newcomb [58] and Park [59]. The plot illustrates the wide spectrum of commercially available PAN- and pitch-based fibers, ranging from high-strength PAN fibers (HS) with moderate modulus to high-modulus PAN fibers (HM) and ultrahigh-modulus pitch fibers (UHM) with comparatively reduced strength. Such trade-offs directly reflect processing conditions and precursor type, particularly the degree of graphitization.

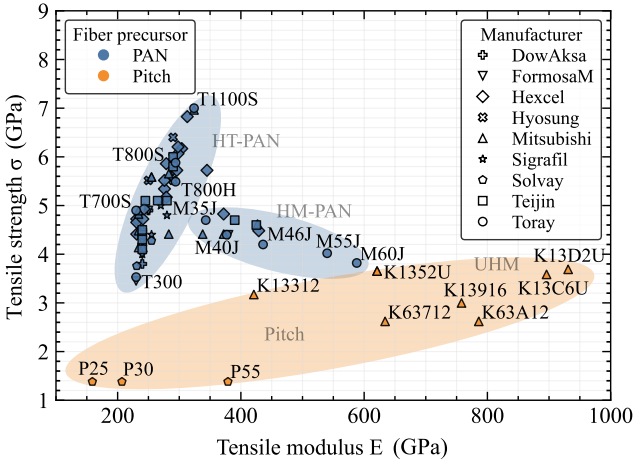


Figure 2.3: Carbon fibers - Overview of mechanical properties: tensile strength σ and tensile modulus E. Data according to manufacturer's data sheets. [58, 59]

Although longitudinal stiffness is often emphasized, the anisotropic nature of carbon fibers becomes evident when considering the transverse elastic modulus G. As shown in Figure 2.4, which reproduces the relationship between E and G from Shirasu et al. [62], fibers with a higher axial orientation exhibit strong anisotropy, characterized by increasing anisotropy ratios $A_E = E_{\parallel}/E_{\perp}$. PAN-based fibers typically display lower anisotropy in comparison to mesophase pitch-derived fibers, consistent with their more turbostratic microstructure.

It is important to note that the evaluation of anisotropy in terms of A_E depends not only on the type of fiber but also on the experimental methodology. As emphasized by Shirasu et al. [62], the transverse modulus values $E_{\perp}$ vary significantly depending on whether they are obtained from direct mechanical testing of a single fiber [63], nanoindentation [62, 64, 65], or micromechanical calculation by resonant ultrasound spectroscopy [1]. This implies that discrepancies in reported A_E ratios often arise from methodological differences rather than intrinsic material variability, as can be seen in Figure 2.4 for T300, T700SC and K13D fibers. This highlights the need for careful consideration of the testing protocol when comparing anisotropy data across different sources.

The anisotropy of carbon fibers alone does not define the mechanical performance of a composite. Once embedded in a polymer matrix, the effective response

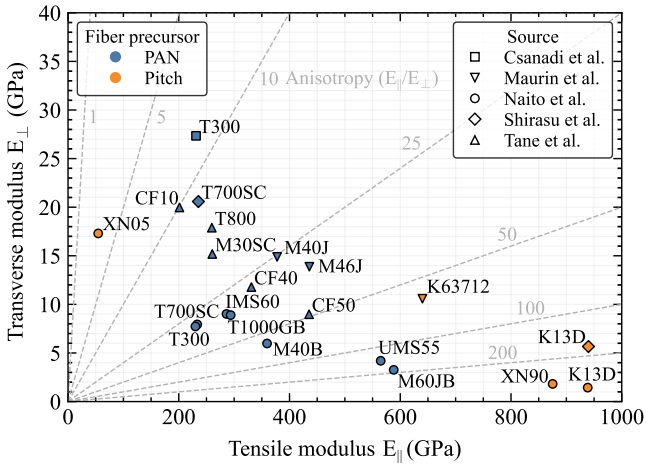


Figure 2.4: Carbon fibers - Overview of anisotropic mechanical properties: transverse modulus $E_\perp$ and tensile modulus $E_\parallel$. [1, 58, 62–65]

results from the interaction between the fibers and the matrix, and the degree of anisotropy in the composite is governed not only by the intrinsic fiber characteristics, but also by their orientation θ, fiber volume content φ_f, and other micromechanical properties. To capture this transition from single-fiber behavior to effective composite properties, simple analytical approaches such as the rule of mixtures are commonly employed [3].

For the longitudinal elastic modulus $E_\parallel$ of a unidirectional lamina, the rule of mixtures (RoM) by Voigt [66] yields a linear dependence on the fiber volume fraction φ_f:

$$E_\parallel = \varphi_f E_{f\parallel} + (1 - \varphi_f) E_m, \tag{2.1}$$

where $E_{f\parallel}$ and E_m denote the elastic moduli of the fiber in longitudinal direction and the matrix, respectively. This relationship illustrates that stiffness along the fiber axis increases almost proportionally with fiber content and is primarily dictated by the high modulus of carbon fibers.

In contrast, the transverse modulus $E_\perp$ follows an inverse rule of mixtures with respect to [67], representing the serial arrangement of compliance contributions of fiber and matrix:

$$\frac{1}{E_\perp} = \frac{1 - \varphi_f}{E_m} + \frac{\varphi_f}{E_{f\perp}}, \tag{2.2}$$

where E_m again is the matrix modulus and $E_{f\perp}$ the corresponding transverse fiber modulus. Consequently, $E_\perp$ remains much lower than $E_\parallel$, even at high fiber volume fractions, and is dominated by the mechanical properties of the polymer matrix.

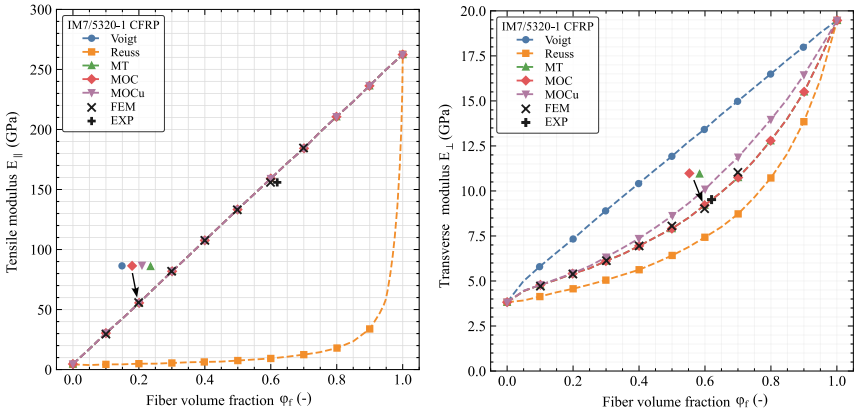
Although the classical rule of mixtures provides a simple first approximation for the longitudinal and transverse elastic moduli of unidirectional composites, it often fails to capture the complex interactions between fibers and matrix. Therefore, more advanced micromechanical models have been developed that improve the predictive accuracy [68–73].

Current available analytical models include the Halpin–Tsai [70, 71] equations and their modifications offer semi-empirical corrections for both longitudinal and transverse stiffness by accounting for fiber geometry and load transfer efficiency.

The Mori–Tanaka (MT) method [72] provides a rigorous mean-field homogenization framework that explicitly accounts for the average stress and elastic energy in a matrix containing misfit inclusions (e.g. voids, resin rich regions).

The Method of Cells (MOC) homogenizes a periodically reinforced composite by analyzing a repeating unit cell and enforcing equilibrium and compatibility across subcell interfaces to obtain effective properties [69]. In unidirectional laminas, MOC commonly applies a rotational averaging to enforce transverse isotropy, whereas the unaveraged variant (MOCu) omits this step and tends to predict higher transverse properties [73].

Kim et al. [73] compare micromechanical model predictions for unidirectional IM7/5320-1 CFRP across fiber volume fraction: $E_\parallel$ varies nearly linearly within the Voigt description, while $E_\perp$ is more model-sensitive; Mori–Tanaka and (averaged) MOC agree closely, while Voigt and MOCu overpredict and Reuss underpredicts $E_\perp$, see Figures 2.5a and 2.5b. Similar comparisons are reported for other properties (e.g., shear moduli and Poisson's ratios) [73].



(a) Longitudinal tensile modulus $E_{\parallel}$.

(b) Transversal tensile modulus $E_{\perp}$.

Figure 2.5: IM7/5320-1 CFRP - Model and experimental data comparison for tensile moduli $E_{\parallel}$ and $E_{\perp}$ against fiber volume fraction φ_f. Data according to Kim et al. [73].

2.3 Transport Anisotropy

Unified Transport Formulation

The structural anisotropy introduced in the mechanical context likewise governs the general transport phenomena in CFRP because these same microstructural descriptors control the directional connectivity and restriction of the heat- and charge-carrying pathways. On the continuum scale, many quasi-static transport problems can be expressed in the common conductivity-type form [74]

$$\mathbf{J}(\mathbf{x}) = \mathbf{L}(\mathbf{x})\,\mathbf{E}(\mathbf{x}), \tag{2.3}$$

$$\nabla\cdot\mathbf{J}(\mathbf{x}) = s(\mathbf{x}), \tag{2.4}$$

$$\nabla\times\mathbf{E}(\mathbf{x}) = \mathbf{0}. \tag{2.5}$$

Here, $\mathbf{J}$ denotes the flux density and $\mathbf{E}$ denotes the driving field that sets the direction and magnitude of the flux. The irrotational condition Equation (2.5) implies that $\mathbf{E}$ derives from a scalar potential u through $\mathbf{E} = -\nabla u$. Spatial differences in u therefore act as the cause of transport and can be interpreted as a potential drop. The tensor $\mathbf{L}$ quantifies how efficient a given driving field is converted into flux. In an anisotropic material, this conversion depends on

direction. Therefore, the same potential gradient can produce different flux levels along the fiber-parallel direction $\parallel$, the transverse in-plane direction $\perp$, and the thickness direction of a CFRP laminate. The divergence Equation (2.4) expresses local conservation. When distributed sources and sinks are absent so that $s = 0$, the flux entering any material volume must leave it. Nonzero $s \neq 0$ represents volumetric generation or extraction [74].

In Chapter 5, Anisotropic Thermal Properties, the general quantities specialize to $\mathbf{J} \equiv \mathbf{q}$ as the heat flux density, $u \equiv T$ as the temperature, and $\mathbf{L} \equiv \boldsymbol{K}$ as the thermal conductivity tensor. Together with energy conservation, this specialization yields the anisotropic transient heat equation (5.11), which is evaluated in Section 5.3.

In Chapter 6, Anisotropic Electrical Properties, they specialize to $\mathbf{J}$ as the current density, $u \equiv V$ as the electric potential, and $\mathbf{L} \equiv \boldsymbol{\sigma}$ as the electrical conductivity tensor. This leads to the anisotropic Laplace equation (6.9). Because the experimental boundary conditions are governed by the electrode topology and current-spreading effects [55], Chapter 6 does not identify $\boldsymbol{\sigma}$ by directly solving Equation (6.9) for the test geometries. Instead, it employs a geometry-specific resistance formulation that explicitly accounts for electrode boundary effects, as detailed in Section 6.3.

Beyond closed-form solutions and approximations, effective transport tensors can be obtained by homogenization on representative microstructure using numerical solvers for Equation (2.3), e.g., FEM schemes [75, 76], resistor-network analogies [77, 78], and related approaches [79], as reviewed in Milton [74]. These methods provide a general computational route from microstructure to effective transport anisotropy and serve here as a broader theoretical context for the approaches adopted in Chapters 5 and 6.

Scalar Anisotropy Values

For compact comparison of transport anisotropy across different mechanisms and material systems, it is useful to reduce the tensorial effective transport behavior into scalar key figures. Let $\mathbf{L}^*$ denote the homogenized transport tensor in Equation (2.3) and let $L_1, L_2, L_3 > 0$ be its principal values (eigenvalues),

associated with the orthonormal principal directions of transport. The maximum anisotropy value is defined as

$$A_{\max} \;=\; \frac{L_{\max}}{L_{\min}} \;=\; \frac{\max\{L_1, L_2, L_3\}}{\min\{L_1, L_2, L_3\}} \;\geq\; 1, \tag{2.6}$$

where $A_{\max} = 1$ corresponds to isotropic transport and larger $A_{\max} > 1$ indicates a stronger direction dependence.

To distinguish in-plane and through-thickness anisotropy in laminate settings, two additional ratios are introduced. Denoting by the principal in-plane values fiber-parallel $L_{\parallel}$ and transverse in-plane $L_{\perp}$ and by L_z the through-thickness value, the planar anisotropy $A_{\parallel\perp}$ and the through-thickness anisotropy $A_{\parallel z}$ are defined as

$$A_{\parallel\perp} \;=\; \frac{L_{\parallel}}{L_{\perp}}, \tag{2.7}$$

$$A_{\parallel z} \;=\; \frac{L_{\parallel}}{L_z}. \tag{2.8}$$

For thermal conduction, $\mathbf{L} \equiv \boldsymbol{\lambda}$, so that anisotropy can be expressed through ratios such as $A_{\parallel\perp} = \lambda_{\parallel}/\lambda_{\perp}$ and $A_{\parallel z} = \lambda_{\parallel}/\lambda_z$. For electrical conduction, $\mathbf{L} \equiv \boldsymbol{\sigma}$. The same anisotropy may also be reported in resistivity form using the corresponding inverse ratios, for example $A_{\perp\parallel} = \rho_{\perp}/\rho_{\parallel}$ and $A_{z\parallel} = \rho_z/\rho_{\parallel}$.

3 Materials and Methods

3.1 Materials

General Materials

For experimental investigations, CFRP specimens with varying fiber areal weights (FAW) and fiber architectures were manufactured. The investigated material systems cover a broad range from conventional aviation-grade laminates with higher FAW down to more specialized thin-ply configurations. In total, FAW ranging from 30–300 $\mathrm{g/m^2}$ were considered. An overview of all investigated materials, including laminate identifier, FAW, stacking sequence (layup), total number of plies n_{ply}, nominal laminate thickness t_{nom}, fiber volume fraction φ_f, and fiber–matrix constituents, is provided in Table 3.1.

Different fiber-orientation configurations were realized, including unidirectional (UD) laminates, quasi-isotropic (QI) layups, and Bouligand (BL) helicoidal layups. This selection enables the investigation of fiber-orientation for both simple and more complex fiber architectures, which are relevant for industrial applications and advanced composite design. UD laminates are utilized for the direction-dependent characterization of anisotropic thermal and electrical properties.

All specimens were manufactured using a hand layup procedure followed by vacuum-bagged prepreg autoclave processing. During layup, intermediate debulking steps were applied to compress the laminate stack and to minimize porosity and trapped air between adjacent plies. The final curing was carried out in an autoclave according to the standard cure cycles specified in the respective manufacturer datasheets [80, 81], including prescribed temperature ramps, dwell times, and consolidation pressures. This manufacturing approach ensured high laminate quality and reproducibility in all different material systems.

Table 3.1: Overview of the CFRP materials investigated, including fiber, matrix, and laminate lay-up.

ID / Abbr.	**Layup**	$n_{\mathbf{ply}}$	**FAW** (g/m^2)	$t_{\mathbf{nom}}$ (mm)	$\varphi_{\mathbf{f}}$ (%)	**Fiber**	**Matrix**
UD-30	$[0°]_{32}$	32	30	0.96	57.4	TO T700SC-12K-60E	NTPT ThinPreg 402
UD-60	$[0°]_{16}$	16	60	0.96	56.8	TO T700SC-12K-60E	NTPT ThinPreg 402
UD-120	$[0°]_{8}$	8	120	0.96	60.3	TO T700SC-12K-60E	NTPT ThinPreg 402
UD-268	$[0]_{4}$	4	268	1.07	60.3	TO T800s	Hexcel Hexply M21
QI-30	$[0°, \pm 45°, 90°]_{4s}$	32	30	0.96	59.0	TO T700SC-12K-60E	NTPT ThinPreg 402
QI-60	$[0°, \pm 45°, 90°]_{2s}$	16	60	0.96	58.7	TO T700SC-12K-60E	NTPT ThinPreg 402
QI-120	$[0°, \pm 45°, 90°]_{s}$	8	120	0.96	59.7	TO T700SC-12K-60E	NTPT ThinPreg 402
QI-300	$[0°, 45°, 90°, -45°]_{2s}$	16	300	4.80	-	TO T700SC-12K-60E	NTPT ThinPreg 402
QI-268-Feature	$[45, -45, 0, 90]_{2s}$	16	268	4.29	-	TO T800s	Hexcel Hexply M21
QI-268-Impact	$[45, 90, -45, 0]_{2s}$	16	268	4.29	-	TO T800s	Hexcel Hexply M21
BL-28.8	$\left[[\theta_i]_{i=0}^{7} \right]_{8\underline{s}}$, $\theta_i = i \cdot 28.8°$	113	40	4.52	-	MI 12k TR50S	MI jER828:jER1001
BL-14.4	$\left[[\theta_i]_{i=0}^{13} \right]_{4\underline{s}}$, $\theta_i = i \cdot 14.4°$	105	40	4.20	-	MI 12k TR50S	MI jER828:jER1001
BL-7.2	$\left[[\theta_i]_{i=0}^{25} \right]_{2\underline{s}}$, $\theta_i = i \cdot 7.2°$	101	40	4.04	-	MI 12k TR50S	MI jER828:jER1001
BL-3.6	$\left[[\theta_i]_{i=0}^{50} \right]_{\underline{s}}$, $\theta_i = i \cdot 3.6°$	102	40	4.08	-	MI 12k TR50S	MI jER828:jER1001

UD = unidirectional laminate; QI = quasi-isotropic laminate; BL = Bouligand helicoidal laminate;
NTPT = North Thin Ply Technology; TO = Toray Industries; MI = Mitsubishi

3.2 Methods

Established preparation and characterization methods were used to ensure consistent specimen manufacturing and to assess material quality and thermophysical properties. These methods and the relevant standards are summarized in the following subsections, whereas the ultrasonic investigations and the dedicated thermal and electrical measurement setups are described in their respective chapters.

3.2.1 Scientific Methods

Light Microscopy and Micro-Section Preparation

A digital light microscope (VHX-6500, Keyence Deutschland GmbH) was used for the qualitative assessment of laminate quality, including ply thickness, fiber distribution, and potential manufacturing defects such as voids or resin-rich regions. For this purpose, representative micro-sections were extracted from selected specimens, embedded in a cold curing epoxy resin (KEM 15 Plus, ATM Qness GmbH), mechanically ground and subsequently polished using an automatic polishing system (Saphir 550, ATM Qness GmbH) with progressively finer abrasive media, including diamond suspension particles up to 1 µm, to obtain a flat and nominally damage-free cross-sectional surface. Optical micrographs were acquired under reflected-light conditions.

Differential Scanning Calorimetry

Differential scanning calimetry (DSC) was employed for quality assurance and thermoanalytical characterization of the composite system, including the determination of the glass transition temperature and the temperature-dependent specific heat capacity. Measurements were carried out using a DSC 204 F1 Phoenix (Netzsch GmbH) according to ISO 11357 [82].

In the DSC setup, a sample crucible and an empty reference crucible were subjected to identical controlled heat flow inside the furnace. The temperature difference between both crucibles, which is derived from endothermic or exothermic processes in the sample, was detected by integrated sensors and converted into the corresponding heat flow signal. Prior to material testing, the system

was calibrated using a sapphire standard with known specific heat capacity. The calibration comprised measurements of the empty crucible and the sapphire reference under identical conditions.

Based on the measured heat flow signals, the specific heat capacity of the specimen was determined according to

$$c_{p,\mathrm{S}}(T) = \frac{\dot{Q}_{\mathrm{S}} - \dot{Q}_0}{\dot{Q}_{\mathrm{Sap}} - \dot{Q}_0} \cdot \frac{m_{\mathrm{Sap}}}{m_{\mathrm{S}}} \cdot c_{p,\mathrm{Sap}}(T), \tag{3.1}$$

where $\dot{Q}_{\mathrm{S}}$, $\dot{Q}_{\mathrm{Sap}}$, and $\dot{Q}_0$ denote the measured heat flow of the specimen, sapphire reference, and empty crucible, respectively, m_{S} and m_{Sap} are the corresponding masses, and $c_{p,\mathrm{Sap}}$ is the tabulated specific heat capacity of the sapphire.

The DSC data obtained were used to verify the adequate curing state of the material and to support the interpretation of temperature-dependent experimental results by enabling the conversion of thermal diffusivity α to thermal conductivity λ.

Fiber Volume Fraction Analysis

The fiber volume fraction was determined by a wet-chemical gravimetric method according to ISO 14127 [83]. In brief, the polymer matrix was selectively dissolved in a nitric-acid-based solution, and the remaining fiber fraction was recovered, rinsed, dried, and quantified by precision weighing. All measurements were performed by the central laboratory of TUHH.

Based on the measured mass fractions and the known constituent densities, the fiber volume fraction was calculated as

$$\varphi_f = \frac{m_f/\rho_f}{(m_f/\rho_f) + (m_m/\rho_m)}, \tag{3.2}$$

where m_f and m_m denote the masses of the fiber and matrix constituents, respectively, and ρ_f and ρ_m are their corresponding densities.

Density Measurement

The bulk density of the specimens was determined using the Archimedes method according to ISO 1183 [84]. Specimens were weighed in air and then reweighed while immersed in a reference fluid of known density. The density was derived from the corresponding immersion-induced reduction in apparent weight (i.e., the buoyant force) as

$$\rho = \rho_{\mathrm{ref}} \frac{m_{\mathrm{air}}}{m_{\mathrm{air}} - m_{\mathrm{ref}}}, \tag{3.3}$$

where m_{air} denotes the mass of the specimen measured in air, m_{ref} the apparent mass measured in the reference fluid, and ρ_{ref} the density of the reference fluid at the measurement temperature. Measurements were conducted at ambient temperature using water as the reference fluid.

3.2.2 Sample Preparation

Cutting and Milling

Specimen cutting and final dimensioning were performed in multiple stages to ensure high dimensional accuracy and reproducibility. The initial trimming of the laminate plates was carried out using a diamond-coated cutting disk mounted on a circular table saw (F45, Altendorf GmbH).

Rectangular specimen geometries were produced using aluminum-oxide cutting blades on water-cooled precision saws (Brilliant 265 and Brilliant 220 CNC, ATM Qness GmbH). This cutting approach minimized thermal and mechanical damage to the edges of the specimen and ensured consistent quality.

Standard specimen dimensions were selected according to the respective experimental requirements. Rectangular specimens of 150 mm × 100 mm were prepared for ultrasonic investigations, while specimens of 40 mm × 40 mm were used for thermal characterization.

Specimens with a regular 24-sided polygonal geometry with $D_{af} = 125\,\mathrm{mm}$, used for the characterization of electrical anisotropy, were manufactured by CNC milling on an isel EuroMod 35 machining center (Isel Germany AG), employing

the same machining setup as described for the preparation of the sample features in Section 3.2.2.

Feature Preparation by Impact

The QI laminate specimen, designated QI-268-Impact, was subjected to a low-velocity impact according to ASTM D7136M [85]. The impact was carried out using a drop-weight impact tower (Instron 9450) with an applied impact energy of 18 J and a hemispherical impactor tip of diameter 16 mm. The sample was used for the detection of ultrasonic fiber-orientation in Section 4.4.4.

Feature Preparation by Milling

The QI laminate specimen, designated QI-268-Feature, was subjected to feature preparation by CNC milling using an isel EuroMod 35 machining center (Isel Germany AG). Machining was performed with a solid carbide high-speed cutting end mill (VHM-HSC shank cutter, diamond-toothed, 1.8 mm diameter; Sorotec GmbH) under air cooling conditions. The manufactured features comprised stepwise milling grooves and bore holes with defined geometries. The specimen serves as a standardized reference sample for ultrasonic testing in lecture courses and was used for the detection of ultrasonic fiber-orientation, as discussed in Section 4.4.4.

4 Fiber Orientation Detection

The direction-dependent transport response of endless fiber reinforced CFRP laminates is governed first and foremost by the internal fiber orientation. Although laminate designs prescribe a nominal stacking sequence, the effective ply-level orientation within a manufactured component can deviate due to global and local deviations, e.g., caused by ply waviness, handling-induced misalignment, impact damage, or machining-related edge effects. Consequently, the first guiding research question of this thesis is addressed here in a qualitative sense: a robust, non-destructive route is required to access the through-thickness fiber orientation lay-up with sufficient depth resolution and interpretability to serve as a reliable structural basis for subsequent directional thermal and electrical transport characterization.

Chapter 4 develops this route using depth-resolved ultrasonic testing. The methodological scope is deliberately positioned between classical defect inspection and microstructural reference methods: rather than imaging individual fibers, the approach infers layer-wise orientation trends from orientation-dependent ultrasonic-wave–material interactions encoded in high-resolution pulse–echo scan data. The theoretical context and motivation are established in Section 4.1, including a structured overview of fiber-orientation-distribution (FOD) measurement techniques and the rationale for selecting ultrasound as the primary non-destructive method. The ultrasonic inspection concept is then experimentally implemented in Section 4.2, defining the acquisition strategy and the boundary conditions required for reproducible volumetric scans.

A dedicated evaluation workflow is introduced in Section 4.3. It combines metadata-driven reconstruction, signal conditioning, robust data cleaning, and Fourier-domain texture analysis with automated peak detection and scoring to obtain a depth-resolved orientation estimate across the laminate thickness. The performance and practical limits of the overall methodology are assessed in Section 4.4, where the results are discussed for unidirectional reference laminates

(Section 4.4.1), quasi-isotropic lay-ups (Section 4.4.2), and Bouligand architectures (Section 4.4.3), complemented by an explicit examination of disturbance cases such as impact damage and machining-related features (Section 4.4.4). The consolidated implications for later transport chapters are summarized in Section 4.5.

4.1 Theoretical Background

4.1.1 State-of-the-Art Measurement Techniques

Destructive Testing Techniques

Destructive methods remain the benchmark for fiber-orientation analysis because of their direct access to the composite microstructure and their ability to resolve individual fibers or fiber bundles with high spatial resolution. Although incompatible with in-service inspection, these techniques are indispensable for fundamental studies and validation of non-destructive approaches.

Microsectioning and Optical Microscopy Microsectioning combined with optical microscopy is the most established destructive technique for fiber-orientation analysis in polymer-matrix composites. Specimens are cut at defined locations, embedded, ground, and polished to obtain a planar cross-section with minimal preparation damage. Depending on the cut plane, fibers appear as circular or elliptical cross-sections or as line segments, enabling the extraction of local orientation angles by image analysis. Classical evaluation uses ellipse fitting with stereological relations [86–90], whereas more advanced approaches rely on structure tensors [91, 92], multi-field image analysis [93], or Fourier-based orientation analysis [94]. Optical microscopy provides sub-micrometer spatial resolution, allowing orientation gradients to be quantified across plies and resin-rich zones and enabling the identification of defects such as waviness or misalignment; with sufficient sections, statistical orientation distributions can be reconstructed. In well-controlled preparation, the achievable accuracy makes the method a common laboratory reference for validation. Its main limitations are high effort and preparation sensitivity, including artifacts such as fiber pull-out, matrix smearing (particularly in thermoplastics), and the inherently two-dimensional sampling

with limited spatial coverage; in addition, the destructive workflow prevents large-area or in-line inspection.

High-Resolution X-ray Micro-Computed Tomography Although X-ray computed tomography is commonly categorized as a non-destructive technique, high-resolution micro-computed tomography (μCT) that resolves individual fibers typically requires extracting small specimens from a component and is therefore destructive at the structural scale. In this regime, voxel sizes on the order of 1 µm or below allow for a direct three-dimensional reconstruction of fiber trajectories and the determination of fiber-orientation distributions or orientation tensors without relying on stereological assumptions [95, 96]. The key advantage of high-resolution μCT is its intrinsically three-dimensional nature, which avoids the geometric bias of planar sectioning and supports orientation analysis either by explicit segmentation and tracking of fibers or bundles, or by tensor-based descriptions derived from local image features. Reported evaluation strategies include fiber tracking and skeletonization [95, 97], mean-intercept-length and fabric-tensor concepts [98], as well as local X-ray transform approaches that can avoid explicit segmentation [92].

However, practical limitations restrict the broader use of high-resolution μCT: the acquisition time and signal-to-noise demands increase strongly with resolution, while the achievable field of view is typically limited to volumes of only a few cubic centimeters, and reconstruction plus orientation analysis can be computationally intensive. In addition, material contrast can be a decisive bottleneck; while glass fibers are often resolvable with conventional laboratory systems, carbon fibers exhibit relatively weak X-ray attenuation compared to polymer matrices, which can require advanced concepts such as synchrotron radiation, phase-contrast imaging, or tracer-based strategies to enable reliable fiber detection [99, 100]. As a result, high-resolution μCT remains primarily a laboratory-scale tool for fundamental investigations and reference measurements rather than a routine method for industrial characterization.

Non-Destructive Testing Techniques

Non-destructive techniques aim to infer fiber orientation without impairing component integrity, enabling inspection of finished parts and, in some cases, in-line process monitoring. While typically offering lower spatial resolution

than destructive methods, non-destructive approaches are essential for industrial application and large-scale statistical assessment.

Ultrasonic Testing Ultrasonic testing (US) constitutes the most established and industrially relevant non-destructive testing technique for fiber-reinforced polymer composites and is routinely employed as the standard inspection method, e.g. in the aerospace sector. Its widespread adoption is driven by a favorable combination of penetration depth, scalability to large and complex components, compatibility with automated scanning systems, and sensitivity to a wide range of types of defects. Beyond conventional defect detection, extensive research has demonstrated that ultrasonic measurements contain detailed information on fiber orientation, ply stacking sequence, and fiber waviness, positioning US as one of the most promising techniques for acquisition of non-destructive fiber orientation distribution at the component scale [43, 101, 102].

The sensitivity of ultrasonic measurements to the orientation of the fiber originates from the pronounced elastic anisotropy of fiber-reinforced composites. Local variations in fiber direction and ply geometry affect ultrasonic wave velocity, attenuation, beam steering, and phase behavior, leading to orientation-dependent texture patterns in ultrasonic images. By performing raster scans in pulse-echo mode, three-dimensional ultrasonic datasets can be acquired that encode the internal laminate architecture over the thickness of the entire component [44, 102]. In contrast to surface-based optical or electromagnetic techniques, US enables access to subsurface plies and internal orientation deviations in thick CFRP laminates, which are characteristic of safety-critical aerospace structures.

A wide spectrum of signal and image-processing approaches has been developed to extract quantitative fiber orientation information from ultrasonic data. Early work demonstrated that in-plane ply orientations and stacking sequences can be inferred from gated C-scans using frequency-domain analysis and directional filtering [101]. Subsequent studies introduced Radon-transform-based techniques and structure-tensor analysis applied to volumetric ultrasonic datasets, enabling spatially resolved mapping of dominant fiber directions within individual layers [43, 44]. These methods were shown to provide stable and repeatable orientation estimates even when individual fiber tows are not directly resolvable.

More advanced tomographic reconstruction approaches have significantly extended the capabilities of ultrasonic FOD analysis. Yang et al. [103] systematically

investigated the influence of ultrasonic frequency, bandwidth, and signal processing on ply-resolved orientation reconstruction, demonstrating that analytic-signal analysis combined with phase-based processing enables robust extraction of ply interfaces and orientation features at industrially relevant frequencies [103, 104]. Building on this framework, Gabor-filter-based information diagram methods were introduced to reconstruct local in-plane fiber orientations in a multi-scale manner, yielding high noise robustness and improved sensitivity to local orientation variations [104]. Planar ultrasound computed tomography further enabled three-dimensional ply-by-ply reconstruction of fiber architecture, including out-of-plane ply distortion and impact-induced changes, for laminate dimensions beyond the practical limits of X-ray computed tomography [105].

Recent research has demonstrated that ultrasonic methods are also capable of detecting and quantifying subtle fiber-orientation-related defects that exhibit weak acoustic impedance contrast. Using phased-array systems, full-matrix capture and advanced beamforming techniques, US has been shown to resolve fiber waviness in-plane and out-of-plane, ply wrinkling, and non-uniform yarn orientations in both cured laminates and preformed CFRP parts [106–109]. These studies highlight the ability of US to characterize orientation deviations that critically influence mechanical performance, but may remain undetected by conventional defect-focused inspections.

In addition to qualitative mapping, ultrasonic FOD data have increasingly been integrated into physics-based modeling and structural assessment workflows. Fiber orientation and waviness fields extracted from ultrasonic measurements have been used to parameterize finite element models, allowing the prediction of residual strain fields, stiffness degradation, and strength reduction factors associated with manufacturing-induced defects [110]. This direct link between non-destructive measurement and structural performance evaluation represents a decisive advantage of ultrasonic methods over purely statistical or surface-sensitive techniques.

Electromagnetic and Eddy-Current Techniques For electrically conductive reinforcements, in particular carbon fibers, electromagnetic methods provide a non-destructive approach for assessing fiber orientation based on the anisotropic electrical and dielectric properties of the material. Eddy-current testing exploits the pronounced directional dependence of electrical conductivity in carbon-fiber reinforced polymers, which arises from preferential current paths along the fiber

direction and depends on the fiber orientation, the fiber volume fraction, and the stacking sequence [111, 112]. By analyzing spatial variations in complex impedance or conductivity maps, dominant fiber or roving orientations can be inferred from the directional response of the induced eddy currents.

Eddy-current techniques are inherently contactless and can be implemented at high scanning speeds, making them attractive for quality assurance and process monitoring applications. Due to the skin effect, the measurement is predominantly sensitive to regions near the surface; however, by employing high excitation frequencies and suitable sensor designs, information from multiple layers can be accessed in dry textiles and thin laminates [112, 113]. Numerous studies have demonstrated the capability of eddy-current methods to detect fiber orientation deviations, misalignment, waviness, gaps, and other manufacturing defects in carbon-fiber textiles and preforms [111, 114, 115].

Diffractometry and Optical Reflection Techniques Optical diffractometry constitutes an early approach for fiber-orientation assessment and is based on the Fourier relationship between a two-dimensional fiber arrangement and its far-field diffraction pattern. In this method, optical micrographs of composite sections are treated as aperture masks and the angular intensity distribution of the resulting Fraunhofer diffraction pattern is used to infer dominant fiber orientations without explicit fiber segmentation [116]. Because of its robustness against local image noise and its ability to provide area-averaged orientation measures, optical diffractometry has mainly been applied as a laboratory technique for rapid orientation characterization from planar sections.

More recent optical approaches exploit the anisotropic reflection behavior of CFRP surfaces. By analyzing orientation-dependent specular reflection under controlled illumination, local fiber directions can be determined directly from surface images using photometric and reflection-based methods [117]. These techniques enable fast, contactless surface inspection and are well suited for quality control of dry fabrics and composite surfaces. However, their applicability is restricted to near-surface regions and is strongly dependent on material-specific optical properties and illumination conditions.

Thermal Imaging Techniques Thermal imaging techniques exploit the strong anisotropy of heat generation and heat transport in carbon-fiber-reinforced polymers to determine fiber orientation in a non-destructive manner. Because of

the high axial thermal diffusivity and electrical conductivity of carbon fibers, both externally induced heat flow and internally generated heat patterns exhibit pronounced orientation dependence, which can be captured using infrared thermography.

Fujita and Nagano [118] proposed a thermal imaging approach based on lock-in infrared thermography combined with periodic laser heating to measure the in-plane angular distribution of thermal diffusivity. The measured anisotropic thermal diffusivity was shown to correlate directly with the fiber orientation distribution, enabling orientation angles to be determined with sub-degree accuracy for unidirectional laminates and to be mapped spatially in discontinuous fiber plates. The method provides area-based orientation information without explicit fiber segmentation and is particularly suitable for sheet-like components.

More recently,Unnikrishnakurup et al. [119] introduced an induction heating-based active thermography technique, in which fiber-orientation-dependent current paths generate characteristic thermal patterns that can be analyzed using image-transform methods such as the Radon transform. This approach enables the identification of dominant ply orientations and, under suitable conditions, their stacking sequence in multi-layer CFRP laminates. In addition, the method has demonstrated sensitivity to fiber waviness and misalignment, highlighting its potential for quality assurance applications.

4.1.2 Selection of Measurement Technique

Ultrasonic testing is the industrial standard [120] for non-destructive inspection of CFRP and therefore offers high practical relevance, broad applicability, and immediate transferability. Crucially, for the present work, it can examine continuous fiber laminates through thickness and provides depth-resolved information without damaging the specimen.

To further structure the choice of a fiber-orientation detection route, three descriptor levels are distinguished. S-FOD denotes a surface fiber-orientation distribution, P-FOD denotes a ply-level distribution, and T-FOD denotes a through-thickness descriptor of the laminate lay-up. Table 4.1 maps established methods to these three levels and serves as a guide to select a technique based on whether surface screening, ply-resolved detail, or a depth-resolved lay-up description is required. For the continuous-fiber laminates considered, the key

requirement is T-FOD, and ultrasonic testing is thus chosen as the primary method.

Table 4.1: Qualitative comparison of destructive and nondestructive methods for fiber-orientation characterization.

Method	NDT	S-FOD	P-FOD	T-FOD
Microscopy	No	Yes	Yes	Yes
Micro-CT	No	Yes	Yes	Yes
Standard X-ray	Yes	Limited	Limited	Limited
Optical reflection	Yes	Yes	Limited	No
Eddy-current	Yes	Limited	Limited	No
Infrared thermography	Yes	Yes	Limited	No
Ultrasonic testing	Yes	Limited	Limited	Yes

S-FOD: Surface fiber-orientation distribution.
P-FOD: Ply-level fiber-orientation distribution.
T-FOD: Through-thickness fiber-orientation distribution.

4.1.3 Ultrasonic Testing

The theoretical background on ultrasonic testing in this chapter is based mainly on the terminology standards of DIN EN ISO 557 [121] and the classic textbooks of Krautkrämer et al. [122], Blitz et al. [123] and Ensminger et al. [124].

Waves describe oscillatory phenomena in space and time. The number of oscillations completed per second is defined as the frequency f, while the magnitude of the oscillation is referred to as the amplitude A. The instantaneous state of an oscillation is characterized by its phase ϕ; consequently, the wavelength λ corresponds to the spatial distance between two successive points that share the same phase. These fundamental descriptors form the basis for understanding wave propagation in general and acoustic waves in particular. For a propagating wave, wavelength, frequency, and phase velocity c are linked by [122],

$$c = f\,\lambda. \tag{4.1}$$

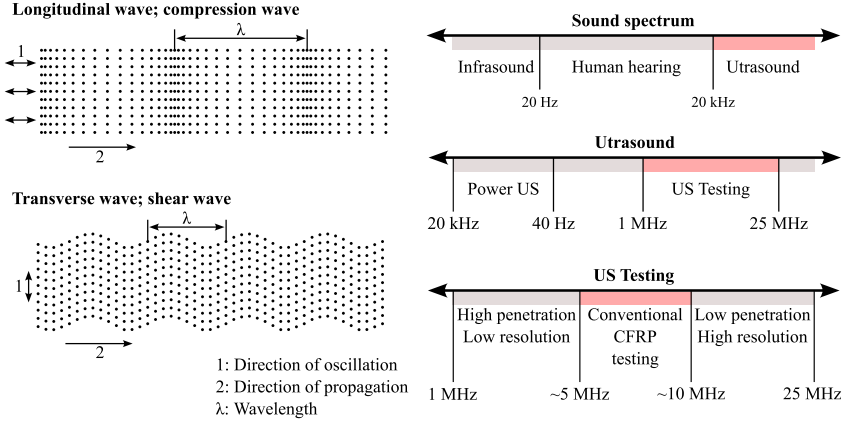
A convenient representation for a harmonic plane wave (e.g., pressure field) is [125, 126]

$$p(\mathbf{x}, t) = p_0 \cos(\omega t - \mathbf{k}\cdot\mathbf{x} + \phi)\,, \qquad \omega = 2\pi f, \qquad |\mathbf{k}| = \frac{2\pi}{\lambda}, \tag{4.2}$$

which highlights how the temporal oscillation ω and the spatial oscillation $\mathbf{k}$ jointly determine propagation.

Acoustic Wave Types

In solid media, acoustic waves can propagate as longitudinal (compressional) or transverse (shear) waves; see Figure 4.1a. For longitudinal waves, the particle displacement occurs parallel to the direction of wave propagation, whereas for transverse waves, the particle motion is perpendicular to the propagation direction. Both types of waves can coexist in solids, and their relative presence depends on the elastic properties of the material as well as the boundary conditions imposed on the wave field. For conventional ultrasonic acquisition, the dominant wave mode intentionally generated is the longitudinal wave. This is mainly because standard piezoelectric transducers, when normally coupled to a surface (e.g. by water or gel), preferentially excite longitudinal waves. In anisotropic solids, such as fiber-reinforced polymer composites, the directional character of bulk waves depends on the propagation direction and can involve coupled longitudinal and shear components (quasi-longitudinal and quasi-transverse modes) [127]. Nevertheless, in typical ultrasonic inspection of CFRP laminates, the measured signals are still dominated by longitudinal or quasi-longitudinal modes, while shear-related modes contribute mainly through reflections, mode conversion, or guided-wave effects. [123, 124]



(a) Acoustic wave types [122]. **(b)** Ultrasonic sound spectrum.

Figure 4.1: General wave types and ultrasonic sound spectrum with focus on CFRP laminate testing [122].

Sound Spectrum

Ultrasound refers to acoustic waves with frequencies that exceed the upper limit of human hearing, approximately 20 kHz; consequently, acoustic frequencies above this threshold are classified as ultrasonic. As summarized in Figure 4.1b, this range is commonly subdivided into the so-called power ultrasound, which typically spans roughly 20–40 kHz and ultrasound for testing applications. Power-ultrasound applications emphasize high acoustic intensities for actuation and energy input (e.g., cleaning, welding, sonochemistry) rather than high spatial resolution. In contrast, ultrasonic nondestructive testing (US) predominantly operates in the megahertz regime, where shorter wavelengths enable the detection of small reflectors and interlaminar features. In industrial US, typical inspection frequencies range from approximately 1 MHz to 25 MHz, where lower frequencies provide higher penetration depth but limited spatial resolution, while higher frequencies improve resolution at the expense of increased attenuation and reduced penetration. For CFRP laminate inspection, this trade-off generally results in the use of mid-range transducers, commonly in the range of about 5–10 MHz, although the optimum frequency depends on laminate thickness, layup, expected defect size, and the required inspection depth. [121, 123, 124]

Unlike electromagnetic waves such as light, acoustic waves rely on direct interactions between adjacent particles and therefore require a material medium for propagation. This fundamental difference explains why the sound velocities vary strongly between gasses, liquids, and solids because they are governed primarily by the density and elastic moduli of the respective medium. [124]

Acoustic Impedance, Reflection, Transmission, and Phase

Many concepts known from optics have direct analogs in acoustics, including reflection and transmission at material interfaces. The governing quantity for interface behavior at normal incidence is the acoustic impedance Z, defined as the ratio of sound pressure p to particle velocity u in a medium and commonly written as [121, 122]

$$Z = \frac{p}{u} = \rho\, c, \tag{4.3}$$

where ρ denotes the density and c the sound velocity. Representative longitudinal acoustic properties of polymer matrices and unidirectional FRP systems, including acoustic impedance Z are summarized in Table 4.2.

For a plane traveling wave at normal incidence, the time-averaged acoustic intensity is [122, 126]

$$\overline{I} = \frac{p_{rms}^2}{Z} = \frac{p_0^2}{2Z}, \tag{4.4}$$

where p_0 is the peak amplitude acoustic pressure of a harmonic wave, and p_{rms} is the corresponding root-mean-square (rms) acoustic pressure. The rms pressure is defined by time averaging the squared pressure over one oscillation period $T = 1/f$, [126]

$$p_{\mathrm{rms}} = \sqrt{\frac{1}{T}\int_0^T p^2(t)\,\mathrm{d}t}, \tag{4.5}$$

and evaluates to $p_{\mathrm{rms}} = p_0/\sqrt{2}$ for a sinusoidal pressure signal $p(t) = p_0\cos(\omega t)$.

At a planar interface between two media with specific acoustic impedances Z_1 (incident side) and Z_2 (transmission side), the pressure-amplitude reflection and transmission coefficients at normal incidence are defined as the ratios of reflected and transmitted pressure amplitudes to the incident pressure amplitude, i.e., $r = p_r/p_i$ and $t = p_t/p_i$. For plane waves, they evaluate to [122]

$$r = \frac{Z_2 - Z_1}{Z_2 + Z_1}, \qquad t = \frac{2Z_2}{Z_2 + Z_1}. \tag{4.6}$$

The corresponding intensity fractions are defined by the ratios of time-averaged intensities, $R = \overline{I}_r/\overline{I}_i$ and $T = \overline{I}_t/\overline{I}_i$. Using the plane-wave relation Equation (4.4), one obtains [125]

$$\begin{aligned} R &= \frac{\overline{I}_r}{\overline{I}_i} = r^2 = \left(\frac{Z_2 - Z_1}{Z_2 + Z_1}\right)^2, \\ T &= \frac{\overline{I}_t}{\overline{I}_i} = \frac{Z_1}{Z_2}\,t^2 = \frac{4Z_1Z_2}{(Z_1 + Z_2)^2}, \\ R + T &= 1 \qquad \text{(lossless interface)}. \end{aligned} \tag{4.7}$$

In contrast to R, which reduces to r^2 because both incident and reflected waves propagate in medium 1, the transmitted fraction T includes the factor Z_1/Z_2 because the transmitted intensity is carried in medium 2. These mechanisms are schematically summarized in Figure 4.2a.

Beyond amplitude changes, impedance contrast also governs phase behavior. If a wave propagates from a lower-impedance medium into a higher-impedance medium ($Z_1 < Z_2$), the reflected wave undergoes a phase inversion ($\Delta\phi_R = \pi$), whereas for $Z_1 > Z_2$ the reflected wave retains its phase; in both cases

the transmitted wave preserves its phase [124]. In CFRP-relevant immersion configurations, this implies the impedance hierarchy

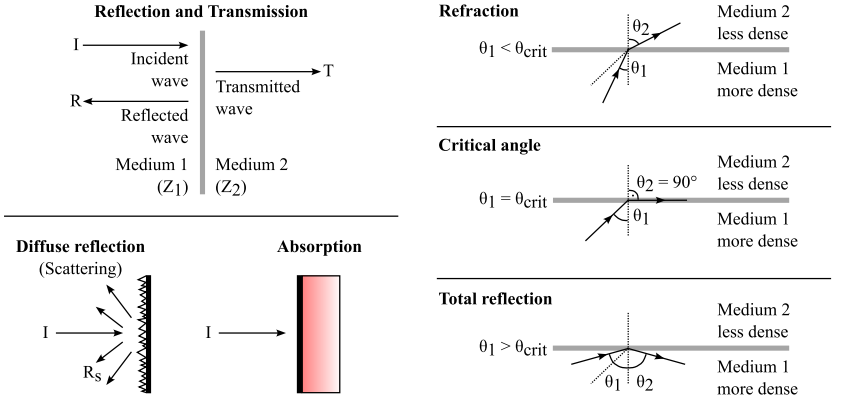
$$Z_{\text{water}} \xrightarrow{\Delta\phi_R=\pi} \ll Z_{\text{matrix}} < Z_{\text{fiber}}, \tag{4.8}$$

so that reflections at the water–matrix interface and at matrix–fiber interfaces are associated with phase inversion.

Table 4.2: Indicative longitudinal ultrasonic properties for selected polymer and FRP materials (room temperature) [128].

Medium	**Sound speed, c** (m/s)	**Attenuation α (1 MHz)** (Np/m)	**Reflection $R^{\star}_{ws}$**	**Transm. $T^{\star}_{ws}$**	**Acoustic impedance Z** (kg/(m^2 s))
Epoxy	2750	31.5	0.195	0.805	$3.82 \cdot 10^6$
UD-GFRP$_{\parallel}$	4950	26.6	0.515	0.485	$9.01 \cdot 10^6$
UD-GFRP$_{\perp,z}$	2990	27.0	0.328	0.672	$5.44 \cdot 10^6$
UD-CFRP$_{\parallel}$	9320	10.5	0.659	0.341	$1.43 \cdot 10^7$
UD-CFRP$^{*}_{\perp,z}$	3150	22.6	0.281	0.719	$4.82 \cdot 10^6$

* Reference materials and characteristic properties used in this thesis.
* Reflection and transmission index ws: water-solid interface.



(a) Acoustic wave interaction phenomena, normal incidence [122].

(b) Acoustic wave interaction phenomena, oblique incidence [124].

Figure 4.2: Acoustic wave interaction phenomena with normal and oblique incidence.

Refraction, Critical Angles, and Mode Conversion

At oblique incidence ($\theta_1 \neq 0$), interface behavior is governed by refraction. For an incident wave traversing an interface between two media with phase velocities c_1 and c_2, Snell's law reads [122]

$$\frac{\sin\theta_1}{c_1} = \frac{\sin\theta_2}{c_2}, \tag{4.9}$$

where θ_1 and θ_2 are measured relative to the surface normal and refer to the propagation directions of the incident and refracted waves, respectively. The resulting phenomena are schematically summarized in Figure 4.2b. In immersion testing (e.g., water–solid), the coupling medium (medium 1) supports only longitudinal waves, whereas the solid (medium 2) supports both longitudinal (L) and shear (S) waves. As a result, an obliquely incident longitudinal wave in the liquid can excite multiple refracted wave modes in the solid (mode conversion), typically a refracted longitudinal and a refracted shear component, each with its own refraction angle determined by Equation (4.9) using the corresponding phase velocity $c_{L,2}$ or $c_{S,2}$. [123]

Critical angles arise when a particular refracted mode in the solid becomes *grazing*, i.e., when its refraction angle reaches $\theta_2 = 90^\circ$ and the associated wave propagates parallel to the interface rather than into the bulk. For a liquid (medium 1) incident on a solid (medium 2), the critical incidence angles for the refracted longitudinal and shear modes in the solid are commonly expressed as [125]

$$\sin(\theta_{\mathrm{crit},L}) = \frac{c_1}{c_{L,2}}, \qquad \sin(\theta_{\mathrm{crit},S}) = \frac{c_1}{c_{S,2}}, \tag{4.10}$$

provided that the right-hand side is ≤ 1. For incidence angles above a given critical angle, the corresponding refracted mode no longer propagates into the solid as a traveling bulk wave; instead, it becomes evanescent and decays away from the interface. Although this work emphasizes normal-incidence pulse-echo inspection, these concepts remain important for CFRP because laminate microstructure, anisotropy, and local curvature can introduce effective obliquity and thereby mode-conversion artifacts. [124, 127]

Attenuation, Scattering, and Absorption

As ultrasonic waves propagate through a material, their amplitude decreases due to absorption, which irreversibly converts acoustic energy into heat, and due to scattering, which redistributes wave energy through interactions with microstructural heterogeneities. These mechanisms are commonly represented by an exponential attenuation law [122].

$$A(x) = A_0 \, \exp(-\alpha x) \,, \tag{4.11}$$

where α is the attenuation coefficient and x is the propagation distance. Since attenuation is frequently reported in decibels, the conversion between nepers and decibels is [122, 125]

$$\alpha_{\mathrm{dB}} = 8.686 \, \alpha_{\mathrm{Np}}. \tag{4.12}$$

In many engineering materials, attenuation increases with frequency and is often empirically approximated by a power law. A convenient unit-invariant form introduces a reference frequency f_{ref} [125],

$$\alpha(f) = \alpha_{\mathrm{ref}} \left(\frac{f}{f_{\mathrm{ref}}} \right)^{n}, \qquad \alpha_{\mathrm{ref}} = \alpha(f_{\mathrm{ref}}) \,, \tag{4.13}$$

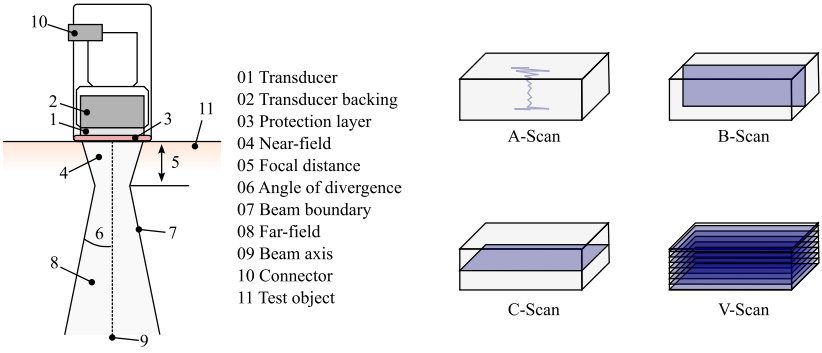
where n is a material-dependent exponent and α_{ref} denotes the attenuation coefficient evaluated at f_{ref}. This representation avoids the ambiguity of the prefactor with respect to the chosen frequency unit. The frequency dependence is of particular relevance in CFRP, where fiber-scale scattering and laminate interfaces can strongly increase the effective attenuation, limiting penetration depth at high inspection frequencies [124].

Ultrasonic Transducers

The generation and detection of ultrasonic waves require suitable transducers that convert electrical energy into mechanical wave motion and vise versa. In modern ultrasonic testing, piezoelectric transducers are predominantly used. They are suitable for high-frequency measurements in the megahertz range, which are required for CFRP laminate inspection. A piezoelectric transducer consists of a piezoelectric element that undergoes mechanical deformation when subjected to an electric field, thus emitting an acoustic wave into the adjacent medium. In contrast, when the element experiences mechanical stress due to an incident

ultrasonic wave, it generates an electrical signal that can be recorded and analyzed. A schematic overview of a typical piezoelectric transducer construction is shown in Figure 4.3a.

In pulsed ultrasonic systems, a practical limitation arises from the intrinsic mechanical after-vibrations of the piezoelectric element following excitation, commonly referred to as ringing. This effect can mask early echo signals and thus reduce temporal resolution, which is particularly critical in high-resolution scanning applications. Various damping strategies and transducer designs are therefore employed to minimize ringing and improve signal fidelity. The excitation waveform also governs the transmitted pulse bandwidth: shorter pulses in time correspond to broader spectra in frequency, which improves the temporal localization of reflectors and thus the axial resolution. [123, 124]



(a) Schematic of a piezoelectric pulse-echo transducer [121].

(b) Schematic of ultrasonic scan types [129].

Figure 4.3: Schematic of a typical piezoelectric pulse-echo transducer and ultrasonic scan types.

Coupling Media

In practical testing scenarios, transducers are mounted in probe housings that ensure mechanical stability and reproducible coupling to the specimen. Efficient transmission of ultrasonic energy requires either direct contact between the probe and the test object or the use of a coupling medium. Common coupling media

include liquids such as water, glycerin, or oils, as well as gasses such as air. Although air coupling offers the advantage of avoiding direct contact with the specimen, it is associated with substantially higher acoustic losses because of the low acoustic impedance of air. As a result, liquid coupling, particularly water coupling, is widely used in ultrasonic inspection systems. Typical implementations include immersion tanks, water-filled wheel probes, and water-jet coupling systems, all of which aim to provide stable and reproducible acoustic transmission conditions while accommodating different specimen geometries and inspection requirements.Representative longitudinal acoustic properties of common coupling media are summarized in Table 4.3. [123, 124, 130]

Table 4.3: Coupling media and indicative longitudinal ultrasonic properties (room temperature) [124, 130].

Medium	**Sound speed, c_l** (m/s)	**Attenuation α (1 MHz)** (Np/m)	**Acoustic impedance Z** (kg/(m^2 s))
Water*	1483	1.65	$1.48 \cdot 10^6$
Gel	–	1.62	$1.47 \cdot 10^6$
Mineral oil	1380–1740	2.15	$1.26 \cdot 10^6$
Petrolatum	–	2.70	$1.17 \cdot 10^6$
Air	343	–	$4.14 \cdot 10^2$

* Reference coupling media and characteristic properties used in this thesis.

Sensitivity, Depth Mapping, and Resolution

The sensitivity of an ultrasonic transducer describes the electrical voltage generated for a given incident acoustic signal, characterizing the efficiency with which the acoustic energy is converted into an electrical signal. The resolution, by contrast, refers to the ability of the ultrasonic system to distinguish between two spatially adjacent features or reflectors. In pulse-echo inspection, the depth z associated with a measured time-of-flight t is commonly approximated by

$$z = \frac{c\,t}{2}, \tag{4.14}$$

where c denotes the relevant wave speed in the medium, and the factor 2 reflects the two-way propagation path in pulse-echo measurements.

The axial resolution (z-direction) is governed primarily by the effective pulse length and is therefore closely related to the usable bandwidth of the transmitted pulse. A common estimate is [125]

$$\delta z \approx \frac{c}{2\,\mathrm{BW}}, \tag{4.15}$$

where BW denotes the effective bandwidth. Increasing frequency and bandwidth improves axial resolution but typically reduces penetration depth because attenuation increases with frequency; see Equation (4.13), which constitutes a central trade-off in CFRP ultrasonic testing. [124, 125]

Lateral resolution (x and y-directions) is primarily governed by the beam footprint at the inspection depth and is influenced by the transducer aperture, wavelength, and focusing. For an unfocused circular aperture of diameter D, a widely used estimate of far-field divergence is [122]

$$\sin\theta_{\mathrm{div}} \approx 1.22\,\frac{\lambda}{D}, \tag{4.16}$$

emphasizing that shorter wavelengths and larger apertures reduce beam spread.

In scanning systems, the lateral discretization is additionally constrained by the positioning and sampling capability of the motion stage. The achievable scan increment is set by the stage mechanics and drive electronics, including the pitch of the lead screw or belt, motor step angle, and the microstepping configuration. Consequently, the effective lateral detail is jointly limited by the footprint of the acoustic beam and the spatial sampling density. If the scan increment is chosen too coarsely, the beam can be undersampled and fine features may be blurred or missed, even when the acoustic field itself would allow finer resolution.

Near- and Far-Field Effects

In addition to frequency-dependent attenuation, near-field effects play an important role in ultrasonic acquisition. In the region close to the transducer surface, commonly referred to as the near field or Fresnel zone, the acoustic pressure distribution is strongly influenced by diffraction and interference effects. As a result, the sound field exhibits pronounced spatial variations with multiple local maxima and minima, which can significantly affect the reflection behavior of

features located within this region. For a circular aperture, the near-field length N is commonly approximated as [122]

$$N \approx \frac{D^2}{4\lambda}. \tag{4.17}$$

In the far field, interference effects diminish and the sound field becomes more uniform; however, the acoustic amplitude decreases with increasing propagation distance due to attenuation in the medium. [121, 122]

Scan Types and Gating

There exist various approaches to constructing and analyzing ultrasonic scans, which differ in complexity and information content. All of these approaches are fundamentally based on the acquisition and combination of individual A-scans. An A-scan represents the time-dependent signal recorded by the receiving transducer after the emission of a single ultrasonic pulse; thus it constitutes a one-dimensional representation of acoustic amplitude as a function of time or, equivalently, propagation depth, at a fixed spatial position [121, 129]. A schematic overview of the common scan types is provided in Figure 4.3b.

A B-scan is obtained by concatenating multiple A-scans acquired along a continuous line on the specimen surface. The resulting representation corresponds to a two-dimensional cross-sectional view of the material along the scanning direction, where one axis represents the scan position and the other the propagation depth. In contrast, a C-scan represents a two-dimensional planar map of ultrasonic information extracted from a selected time-of-flight (ToF) interval (time gate). To generate a C-scan, the transducer scans the entire surface area of interest; the resulting image can be interpreted as a horizontal slice through the specimen and is particularly well suited to identify lateral variations, such as damage, voids, or inhomogeneities, at a given depth. A V-scan extends this concept to volumetric reconstructions obtained from dense three-dimensional grids of A-scans. [121, 129]

4.2 Test Setup

Pulse-Echo Method

The focus of this work is on the pulse-echo method, which represents one of the most widely used ultrasonic inspection techniques. In this approach, a short electrical excitation pulse is applied to a piezoelectric transducer to generate an ultrasonic wave packet. To suppress post-excitation oscillations of the transducer (ringing), a strongly damping backing material is placed behind the piezoelectric element [121, 123]. A schematic representation of the immersion-based pulse-echo arrangement considered in this thesis, comprising a CFRP specimen submerged in a coupling medium (water) and the principal scan directions (scan: x, index: y), is shown in Figure 4.4a.

As the same transducer is used for both transmission and reception, meaningful echo signals can only be recorded after the ringing has sufficiently decayed. Consequently, a minimum stand-off distance between the probe and the specimen surface is required to allow temporal separation of the excitation artifact from the first relevant reflections. This requirement imposes a lower limit on resolvable near-surface features and must be considered when designing the immersion tank setup and the selected water path. [123]

Evaluation of pulse-echo measurements is based on the magnitude and the time-of-flight (ToF) of echoes generated by a single excitation pulse [124]. An individual A-scan may, in principle, be recorded over an arbitrary time window. However, in practice, the ToF range relevant for the analysis is defined a priori. This range can be estimated if the sound velocities in the coupling medium c_m and in the specimen c_s, as well as the corresponding thicknesses of the coupling layer d_m and the specimen d_s, are known. Assuming $c_m < c_s$, the relevant minimum and maximum times can be approximated by

$$t_{\min} \leq \frac{2d_m}{c_m}, \qquad t_{\max} \geq \frac{2d_m}{c_m} + \frac{2d_s}{c_s}. \tag{4.18}$$

A representative A-scan with the principal signal components and their physical origins is depicted in Figure 4.4b. At the beginning of the trace, the electrical excitation pulse and the associated transducer ringing may be present; this interval is typically excluded from further analysis. The first prominent reflection corresponds to the water–CFRP interface and is referred to as the frontwall

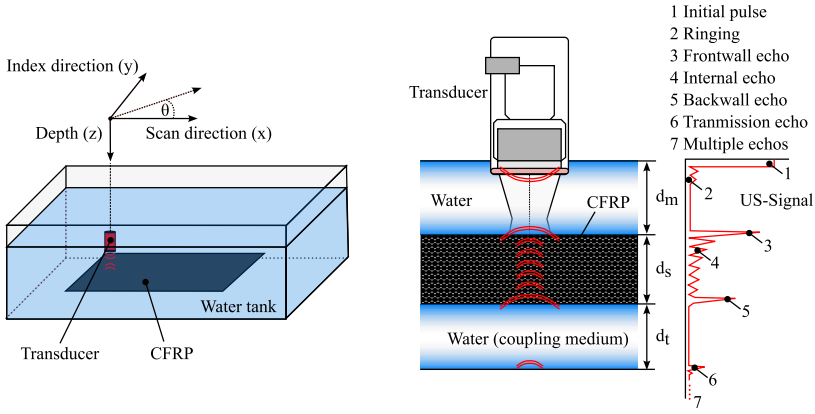
(surface) echo. Subsequent signal components within the interval between the frontwall and the backwall echo are denoted as internal echoes and arise from scattering and reflections at material-internal features, including ply interfaces, fiber-rowing architecture, and defects. In the present work, these internal echoes constitute the primary information carrier for fiber orientation detection, whereas the frontwall and backwall echoes are used mainly for temporal referencing and gating.

The next major reflection originates from the CFRP–water interface on the opposite side and is called the backwall echo [121, 123]. A pronounced intermediate echo between the frontwall and backwall echoes is a strong indicator of a discrete internal reflector, such as a void, crack, or delamination. Conversely, a markedly reduced or absent backwall echo, in combination with enhanced intermediate responses, can indicate strong scattering or a planar defect (e.g., delamination) that attenuates or redirects the energy before it reaches the backwall. In immersion arrangements, an additional late-arriving transmission-type contribution can be observed if the acoustic energy is transmitted through the specimen and reflected at an external reflector located behind the specimen (e.g., the bottom of the water tank, an acoustic mirror), allowing attenuation-based assessments [123, 131].

Following the first sequence of echoes, further sequences of similar temporal extent are often observed. These multiple echoes (multiples) arise from repeated reflections between strong interfaces, leading to higher-order frontwall and backwall returns (not shown in detail). If the pulse repetition rate is sufficiently low, these multiples decay before the next excitation pulse is emitted [123, 124].

Due to the short excitation pulses employed in the pulse-echo method, the transmitted ultrasonic signal exhibits a relatively broad bandwidth. Because higher frequency components are more strongly affected by attenuation, not only the signal amplitude but also the effective center frequency of the reflected echoes may change with propagation distance [124]. Under suitable conditions, this frequency-dependent attenuation can provide additional information for analysis [123].

If the sound velocity within the specimen c_s is not known accurately, it can be determined from the time difference between the frontwall echo and the backwall echo at a location of known thickness. For materials that are not perfectly homogeneous, it is often advantageous to average the sound velocity over multiple measurement positions to obtain a representative effective value. [124]



(a) Schematic of the pulse-echo setup. **(b)** Schematic of the pulse-echo signal.

Figure 4.4: Schematic of the immersion pulse-echo setup and the pulse-echo signal.

Specific Setup

Ultrasonic measurements were performed using an immersion-based pulse–echo testing system supplied by Hillger NDT GmbH [132]. The experimental setup consisted of a computer-controlled ultrasonic scanning system equipped with a focused immersion transducer (type STS 6 PB 6–12 P15, Karl Deutsch GmbH). The transducer features a nominal center frequency of 9 MHz, an active element diameter of 6 mm, and a focal length of 15 mm in water. It was selected to provide broadband frequency content in the 6–12 MHz range, allowing sufficient resolution and sensitivity for through-thickness characterization of carbon fiber reinforced polymer laminates, as demonstrated in multiple studies [102, 103].

The transducer was operated in pulse–echo mode and immersed in a water tank to ensure stable acoustic coupling and reproducible boundary conditions at the fluid–solid interface. The specimen was positioned beneath the probe. The transducer movement was performed using a motorized Cartesian CNC scanning system manufactured by isel Germany GmbH. For all measurements, a constant lateral step size of 0.05 mm was applied in both the x- and y-directions, ensuring uniform spatial sampling across the scan area.

The generation and acquisition of ultrasonic signals were carried out using a USPC 3040 DAC unit. The system is equipped with a 14-bit analog-to-digital

converter (ADC) operating at a maximum sampling rate of 100 MS/s. For all scans, the maximum available sampling rate was used to preserve the optimal resolution of the recorded A-scan signals. The recorded time window was adjusted individually for each scan to account for specimen thickness and probe stand-off distance, ensuring complete capture of the front-wall, internal, and back-wall echos.

During acquisition, no additional hardware-based filtering or signal conditioning was applied beyond the system-internal default settings. All ultrasonic data were recorded in raw form and exported directly from Hillgus acquisition software (version 3.13) without further processing. This ensured that subsequent signal processing and analysis were performed exclusively on unmodified measurement data.

4.3 Analysis Methodology

Building upon the physical principles of pulse-echo ultrasonic testing described in the preceding sections, this subsection summarizes the step-by-step procedure used to extract through-thickness fiber orientation information from high-resolution ultrasonic C-scan measurements. The objective is not the direct imaging of individual fibers, but the inference of local fiber orientation from orientation-dependent wave–material interactions encoded in the recorded ultrasonic signals. To this end, raw A-scan data acquired over a two-dimensional spatial grid are transformed into a depth-resolved fiber-orientation profile of multi-ply composite laminates by combining metadata-driven reconstruction, ultrasonic signal processing, robust data cleaning, and two-dimensional Fourier-domain texture analysis with automated peak detection.

The fiber-orientation measurement and processing workflow proceeds as shown in Figure A.1.

The final output of the workflow is a depth-resolved orientation estimate,

$$\Theta(z_k), \qquad z_k \in [z_{\min}, z_{\max}], \tag{4.19}$$

together with corresponding image-based representations. Here, $\Theta(z_k)$ denotes the dominant fiber-orientation angle associated with the depth coordinate z_k, which is obtained from the time-of-flight index t_k.

4.3.1 Pre-Processing

Data Import

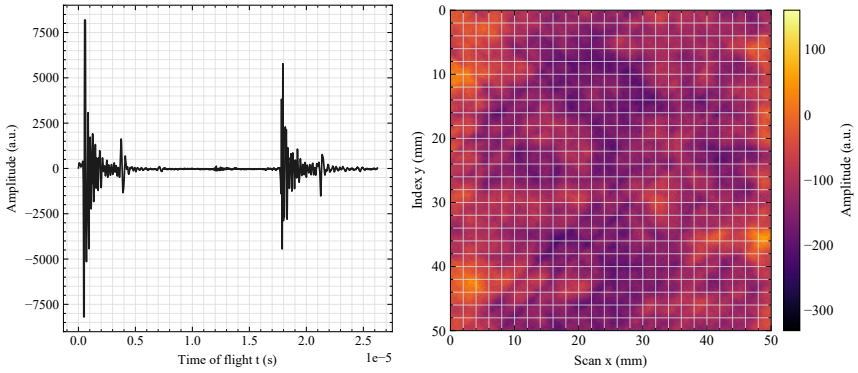
The pre-processing workflow begins with the import of the raw ultrasonic machine data. The measurements are stored in proprietary Hillgus acquisition software ultrasonic evaluation files (.hgv), which contain both the recorded A-scan signals and the associated acquisition metadata. During import, metadata are parsed to extract spatial scan coordinates, sampling rates, time-of-flight information, excitation parameters, and coupling conditions. Based on this information, the measurement data is reconstructed into a three-dimensional data tensor representation, which forms the fundamental data structure for all subsequent processing steps.

The reconstructed ultrasonic dataset is denoted as

$$\mathcal{U}(x_i, y_j, t_k) \in \mathbb{R}^{N_x \times N_y \times N_t}, \tag{4.20}$$

where x_i and y_j denote the discrete in-plane scan coordinates, with indices $i = 1, \ldots, N_x$ and $j = 1, \ldots, N_y$ referring to the spatial scan indices along the two orthogonal scan directions. The index t_k denotes the discrete time-of-flight sampling associated with each A-scan, with $k = 1, \ldots, N_t$. Accordingly, N_x and N_y correspond to the number of scan positions in the two in-plane directions, while N_t denotes the number of temporal sampling points per A-scan. In ultrasonic scanning terminology, the x-direction corresponds to the fast continuous *Scan direction*, while the y-direction represents the slower step-wise *Index direction* between successive scan lines; see Figure 4.4a.

Therefore, each tensor element $\mathcal{U}(x_i, y_j, t_k)$ represents the recorded amplitude of the ultrasound signal at the scan position (x_i, y_j) and the time t_k. Fixing the spatial scan indices (i, j) yields an individual A-scan at a specific scan position, as shown in Figure 4.5a. In contrast, fixing the time index t_k defines a two-dimensional depth-resolved image throughout the scanned area, which is commonly referred to as a C-scan, as shown in Figure 4.5b. This tensor formulation provides a compact and mathematically consistent representation that enables systematic depth-resolved processing, spatial-frequency analysis, and slice-wise fiber orientation estimation.



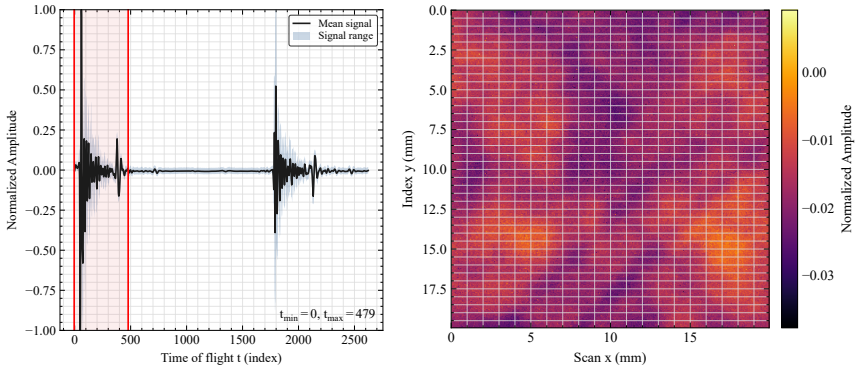
(a) Raw A-scan. **(b)** Raw C-scan.

Figure 4.5: Representative raw A-scan and raw C-scan of a 300 gsm quasi-isotropic CFRP laminate (QI-300).

Regions of Interest Definition

Following the import of raw data, the dataset is manually confined to the physically relevant spatial region and depth interval, also called the region of interest (ROI). This cropping step excludes areas outside the boundaries of the sample, as well as regions affected by defects such as voids or delaminations, which could otherwise bias subsequent analyzes. In addition, enforcing a consistent ratio between the image dimensions and the characteristic fiber diameters across all measurements ensures the comparability of the dataset and improves the robustness and reproducibility. In this study, a default area of $50 \times 50\,\mathrm{mm}^2$ was employed for the detailed analyzes presented in the results section, while a reduced area of $20 \times 20\,\mathrm{mm}^2$ was used for rapid preliminary evaluation of unknown laminae and the optimization of parameters, as illustrated in Figure 4.6b.

In the depth direction, a time-of-flight window is selected that encompasses the specimen between the detected front-wall (surface) and back-wall echoes, as shown in Figure 4.6a. At this stage, the window represents a purely temporal region of interest, while the precise front-wall and back-wall echo positions are identified and refined in subsequent analysis steps. To support a manual pre-selection process, the normalized mean ultrasonic signal and the global signal range are displayed. This visualization facilitates the identification of potential sample misalignments or unexpected signal features and ensures that a sufficiently broad and robust time-of-flight window is selected.



(a) Normalized A-scan signal within the depth ROI.

(b) Normalized C-scan image within the spatial ROI.

Figure 4.6: Normalized ultrasonic A-scan and C-scan data extracted from a representative ROI of a 300 gsm quasi-isotropic CFRP laminate (QI-300).

Envelope Computation

To obtain a robust and physically meaningful amplitude representation of the ultrasonic A-scan signals, the analytic signal is computed using the Hilbert transform. Following the formulation introduced by Gabor [133] and applied to ultrasonic detection by Gammell [134], the measured real-valued ultrasonic signal $s(t)$ is replaced by its complex analytic representation

$$a(t) = s(t) + i\,\mathcal{H}\{s(t)\}, \tag{4.21}$$

where $\mathcal{H}\{\cdot\}$ denotes the Hilbert transform, generating a quadrature component that is phase-shifted by 90° with respect to the original waveform. In the frequency domain, this operation suppresses negative frequency components, yielding a one-sided spectrum that preserves the complete instantaneous amplitude and phase information of the signal.

The analytic signal may be expressed in polar form as

$$a(t) = |a(t)|\,\mathrm{e}^{\,i\,\arg(a(t))}, \tag{4.22}$$

where the real part $\Re\{a(t)\} = s(t)$ corresponds to the recorded ultrasonic signal, $\Im\{a(t)\}$ represents the imaginary quadrature component, $|a(t)|$ denotes the

magnitude of the analytic signal and $\arg(a(t))$ is the instantaneous phase. A visualization of these quantities is provided in Figure 4.7a.

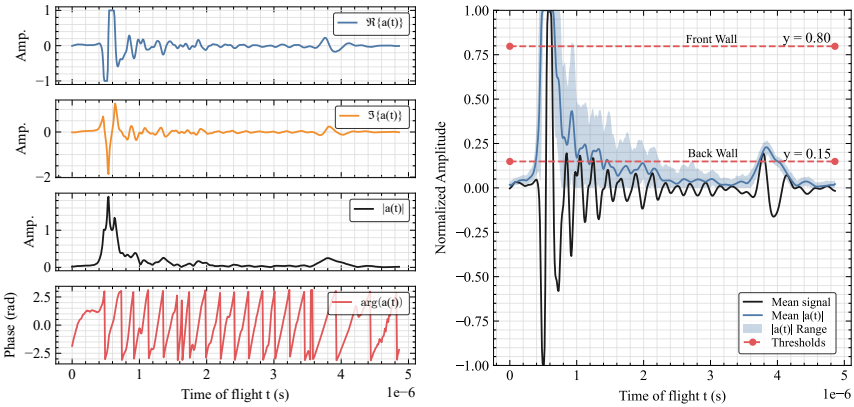
As shown by Gammell [134], the magnitude of the analytic signal provides an amplitude measure that is directly related to the instantaneous rate of arrival of acoustic energy at the transducer. The analytic signal magnitude is insensitive to carrier phase and oscillatory interference effects and therefore yields a more accurate and temporally stable estimate of echo location. In particular, the envelope peak occurs at the true energy maximum of the reflected wave packet.

This property is especially advantageous for ultrasonic inspection of heterogeneous composite materials, where scattering, attenuation, and mode conversion lead to phase instabilities that limit the reliability of rectified or smoothed signals. Although the real part $\Re\{a(t)\}$ retains the oscillatory waveform required for frequency-domain and spectral analyzes, and the instantaneous phase $\arg(a(t))$ may be exploited in phase-sensitive applications (e.g., detection of layer changes).

In this work, the magnitude of the analytic signal $|a(t)|$, is therefore used as the primary amplitude representation in the subsequent processing step. Specifically, it enables the automated and robust identification of front-wall and back-wall echo positions based on amplitude criteria, forming the basis for depth window definition and further signal evaluation.

Depth Boundary Detection

Based on the envelope representation, the front and back-wall echoes are detected automatically for each spatial position. These echoes correspond to the acoustic impedance transitions at the coupling-medium–specimen interface and the specimen–coupling-medium interface, respectively. To enable robust and consistent echo detection throughout the entire dataset, global amplitude thresholds are manually defined on the mean envelope signal $|a(t)|$, as illustrated in Figure 4.7b. The thresholds are selected such that they are sufficiently high to suppress false detections caused by noise and low-amplitude scattering, while remaining low enough to reliably capture the corresponding front-wall and back-wall echo peaks at all spatial locations. The resulting echo positions serve as stable reference points for defining the specimen boundaries in the time-of-flight domain, compensating for local thickness variations, and establishing depth gates for subsequent signal processing and depth-axis alignment.



(a) Analytical signal quantities. **(b)** ROI thresholds.

Figure 4.7: Hilbert-based analytic signal quantities and thresholding used for ultrasonic A-scan processing within a representative ROI of a 300 gsm quasi-isotropic CFRP laminate (QI-300).

Depth Mapping

Once the sample boundaries have been identified, the discrete time-of-flight samples t_k are converted to a physical depth coordinate z_k. This mapping requires an effective sound velocity c_{eff}, which represents a mean propagation velocity within the specimen. In fiber-reinforced polymer composites, the local acoustic velocity generally differs between the fiber and matrix components and may also depend on the orientation and layup of the fiber; for reference values, see Table 4.2. Consequently, a single spatially constant velocity should be understood as an effective mean value rather than a true local material property.

To determine c_{eff}, a reference specimen thickness d_{s} is required. Using the detected echo positions for the front-wall and back-wall at times t_{fw} and t_{bw}, respectively, the effective sound velocity is calculated as

$$c_{\text{eff}} = \frac{2\, d_{\text{s}}}{t_{\text{bw}} - t_{\text{fw}}}, \tag{4.23}$$

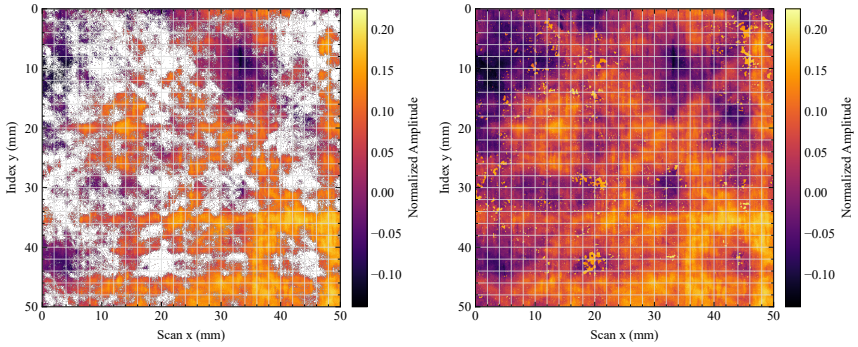
where the factor of two accounts for the two-way pulse–echo propagation path. The depth coordinate corresponding to a given time-of-flight sample t_k is then obtained as

$$z_k = \frac{c_{\text{eff}}}{2}\,(t_k - t_{\text{fw}})\,. \tag{4.24}$$

This depth calibration step maps the ultrasonic data from the temporal domain t_k to a spatial domain z_k, enabling direct comparison of depth-resolved results throughout the scan area. For layered composite materials, accurate depth calibration is essential to ensure that the corresponding layers and interfaces are analyzed consistently at different spatial positions, despite local variations in acoustic properties.

Front-Wall Normalization

The detected front-wall echo amplitudes are normalized to a common reference level for all spatial positions [135, 136]. This operation compensates primarily for coupling-related variability, including minor probe lift-off, local surface unevenness, and small changes in incidence conditions. By enforcing a consistent front-wall amplitude baseline, subsequent depth-resolved analyzes become less sensitive to acquisition-induced gain fluctuations and more comparable in the scan area. This assumption is justified only for plate-like specimens with nearly ideal surface planarity and strictly parallel laminate boundaries. However, pronounced geometric or process-induced deviations, such as post-machining features (e.g., milling steps, chamfers) or asymmetric compaction during manufacturing, can violate this assumption and may therefore bias the front-wall normalization and fiber orientation detection.



(a) C-scan before front-wall normalization and reconstruction.

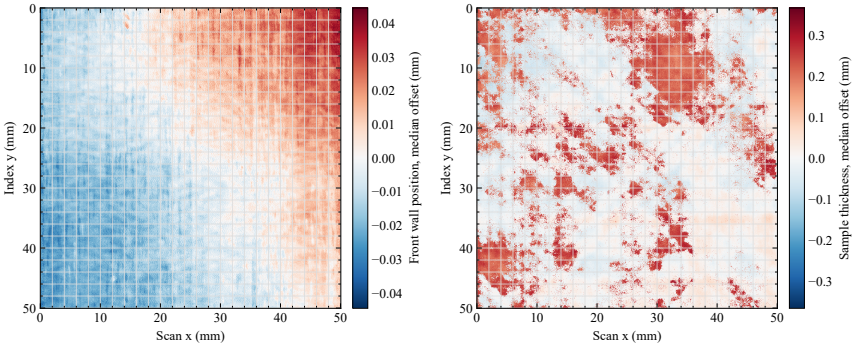
(b) C-scan after front-wall normalization and reconstruction.

Figure 4.8: Comparison of C-scan data before and after front-wall normalization and data cleaning of a 300 gsm quasi-isotropic CFRP laminate (QI-300).

Data Cleaning

Subsequently, invalid or corrupted depth slices are identified based on deviations from the expected spatial and depth-wise signal continuity. Such slices typically originate from acquisition artifacts, locally distorted echo signatures, or at C-Scans near the maximum back-wall echo z_{max}. Where feasible, up to 50 % of missing or unreliable data values are reconstructed using information from neighboring spatial locations or adjacent depth slices. Remaining slices that cannot be reliably corrected are removed to prevent numerical instabilities in subsequent spatial-frequency analysis. The effect of the preprocessing procedure is demonstrated by comparing an unprocessed C-scan with artificially introduced corrupted regions, representing a worst-case scenario, to the corresponding reconstructed and normalized C-scan (Figures 4.8a and 4.8b). [137]

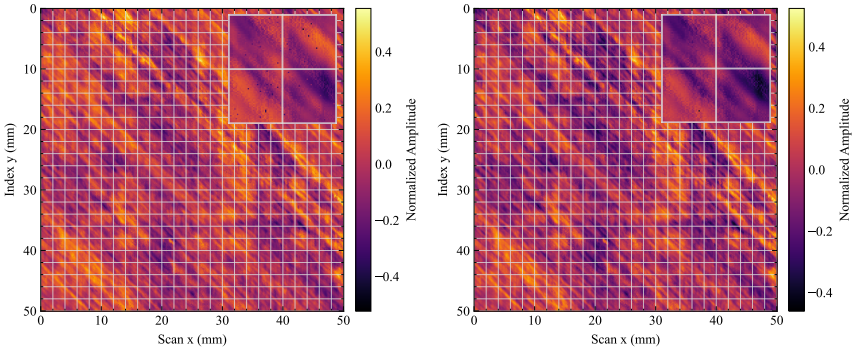
To further assess echo localization quality, the median height differences of the detected front-wall and thickness across the scan area are evaluated and visualized, as shown in Figures 4.9a and 4.9b. The front-wall echo exhibits a high degree of spatial consistency, reflecting the well-defined and sharply localized coupling-medium–specimen interface. In contrast, thickness shows increased spatial variability and localized artifacts, which can be attributed to material inhomogeneity, through-thickness attenuation, scattering at fiber–matrix interfaces, and cumulative damping effects along the propagation path.



(a) Front-wall variability. **(b)** Thickness variability.

Figure 4.9: Comparison of the spatial variability of front-wall and thickness C-scans based on the median height difference of a 300 gsm quasi-isotropic CFRP laminate (QI-300).

As a final pre-processing step, each C-scan depth slice is subjected to isolated outlier suppression [138] followed by planar detrending [139, 140] to reduce artifacts that would otherwise bias the Fourier-domain representation and destabilize subsequent polar re-sampling and angular spectrum peak detection. Isolated outliers are detected by comparison with a local 3×3 pixel median reference and replaced by that median, which effectively removes impulsive spatially sparse corruptions while largely preserving genuine texture [141]. Subsequently, a least-squares best-fit plane is estimated from valid pixels and subtracted, reducing signal strength offsets and global spatial gradients and thus limiting low-frequency dominance and spectral leakage in the 2D-FFT. The combined effect is illustrated in Figure 4.10.



(a) C-scan before outlier removal and detrending.

(b) C-scan after outlier removal and detrending.

Figure 4.10: Effect of isolated outlier removal and planar detrending on C-scans of a 300 gsm quasi-isotropic CFRP laminate (QI-300).

4.3.2 Main Processing

2D Discrete Fourier Transform

Following detrending, a two-dimensional Fourier transform (2D FFT) is applied to each depth-resolved C-scan slice to obtain a spatial-frequency representation of the ultrasonic image. The transformation maps the spatial intensity field onto the Cartesian wavenumber domain defined by the spatial frequencies k_x and k_y, corresponding to the scan directions of the C-scan. Periodic and quasi-periodic

features introduced by the underlying fiber architecture are thus represented as localized concentrations of spectral magnitude in the (k_x, k_y) plane.

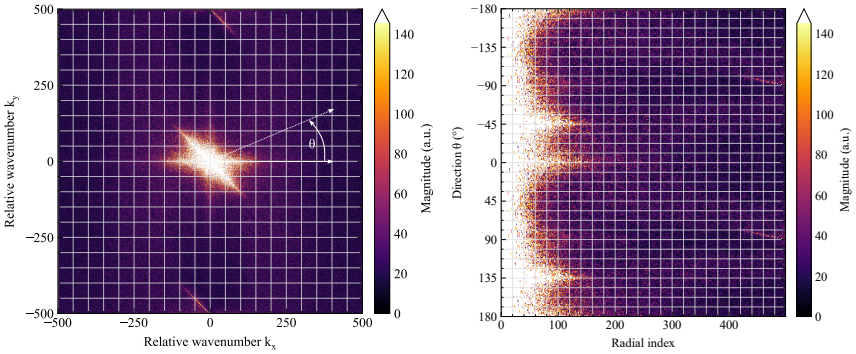
Pronounced fiber alignments manifest as elongated, symmetric lobes in the Fourier magnitude spectrum centered about the origin $(k_x, k_y) = (0, 0)$. These lobes represent dominant spatial frequencies and are oriented perpendicular to the corresponding fiber directions in the spatial domain. In laminates with multiple preferred fiber orientations, several such lobes coexist, forming a star-like spectral pattern whose angular positions encode the principal fiber orientations. The 2D FFT therefore provides a compact and physically interpretable representation in which directional information can be isolated from spatial amplitude variations. A formal definition and illustrative examples of the 2D-FFT are provided in Section A.3, and the resulting spectrum for a representative slice is shown in Figure 4.11a.

Windowing

For high depth C-Scans characterized by very low signal amplitudes and nearly homogeneous spatial intensity distributions, the 2D Fourier magnitude spectrum tends to exhibit an artificial dominance of frequency components aligned with the principal Cartesian axes, in particular at orientations close to $\pm 90°$. This behavior arises from the finite spatial extent of the C-scan window and the implicit rectangular truncation of the signal, which introduces sharp discontinuities at the image boundaries. In the absence of pronounced directional features, these discontinuities can dominate the spectral content and lead to an over-representation of axis-aligned spatial frequencies in the Fourier domain.

The application of spatial windowing functions, such as Hann or Hamming windows, can reduce this effect by smoothly tapering the signal toward the boundaries and thereby suppressing boundary-induced spectral leakage [142]. However, while windowing mitigates the artificial amplification of Cartesian frequency components, it simultaneously redistributes spectral magnitude and introduces secondary lobes at other orientations, which would require additional interpretation and may obscure weak but physically relevant directional features. For the purposes of the present work, no windowing functions are therefore applied. As a consequence, fiber-orientation estimates derived from low-amplitude signals, particularly at higher depths with a reduced signal-to-noise ratio, may exhibit an apparent 90° shift. This limitation is taken into account in the interpretation

of the results and does not affect the analysis of depth regions with sufficiently pronounced directional spatial features. A more detailed graphical illustration of the effects of different windowing functions is provided in Appendix A.4.



(a) 2D-FFT representation. **(b)** Polar representation.

Figure 4.11: 2D-FFT frequency-domain representations used for fiber-orientation analysis of a 300 gsm quasi-isotropic CFRP laminate (QI-300).

Polar Mapping

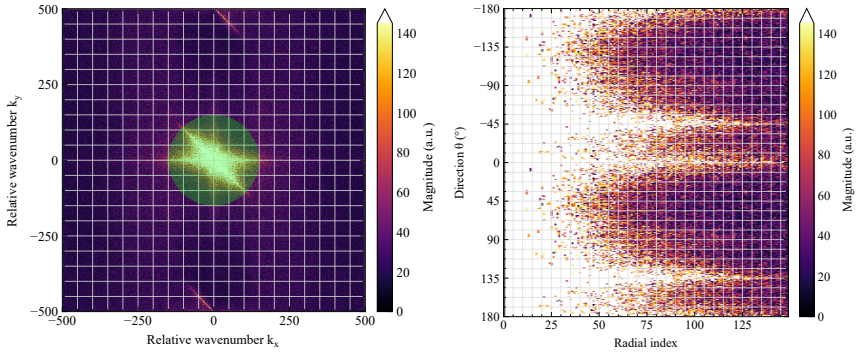
To facilitate direct extraction of directional information, the Cartesian Fourier magnitude spectrum is transformed into polar coordinates with the zero-frequency component placed at the center of the representation. The polar mapping expresses the spectral content as a function of radial spatial frequency and orientation angle, where the radial coordinate corresponds to characteristic spatial scales of the microstructure. The angular coordinate θ is defined with $\theta = 0°$ along the positive horizontal frequency axis ($+k_x$); the direction of increasing θ follows the convention imposed by the image-based polar transform. Importantly, the dominant peaks in the Fourier magnitude indicate the direction of the wave vector and are therefore rotated by 90° with respect to the prevailing direction of the fiber in the spatial domain. Consequently, the fiber-orientation estimate is obtained by applying a ±90° rotation (modulo 180°) between the spectral peak angle and the corresponding spatial fiber direction, the resulting angular dependencies and polar mapping are illustrated in Figure 4.11.

Radial Band Selection

Only a limited band of spatial frequencies contributes meaningfully to fiber-orientation estimation. In the centered spectrum, small radii correspond to large-scale (slowly varying) intensity components, whereas large radii represent fine-scale variations. In high-depth slices with weak texture, the signal contribution at large radii often falls below the noise and sampling-related floor. The polar Fourier spectrum $S_p(r, \theta)$, with radial wavenumber $r = \sqrt{k_x^2 + k_y^2}$, is therefore evaluated only within the bounded interval

$$r_{\min} \leq r \leq r_{\max},$$

chosen to capture spatial frequencies representative of the characteristic texture scale of the fiber architecture. This radial restriction attenuates non-directional background contributions and suppresses high-frequency artifacts, thereby stabilizing the subsequent angular peak analysis. In the present work, a static upper limit $r_{\max}$ is applied uniformly across all depth slices to ensure a consistent and reproducible wavenumber band for orientation extraction, as illustrated in Figure 4.12.



(a) 2D-FFT representation after radial frequency band selection.

(b) Polar representation of the band-limited Fourier spectrum.

Figure 4.12: Band-limited frequency-domain representations used for fiber-orientation analysis of a 300 gsm quasi-isotropic CFRP laminate (QI-300).

Angular Spectrum

After selection of the radial frequency band, the band-limited polar Fourier magnitude spectrum $S_p(r, \theta)$ is reduced to a one-dimensional angular spectrum by integration along the radial direction. In practice, this is achieved by summing the spectral magnitude over the selected radial wavenumber range for each angular position, yielding

$$S(\theta) = \sum_{r=r_{\min}}^{r_{\max}} S_p(r, \theta), \tag{4.25}$$

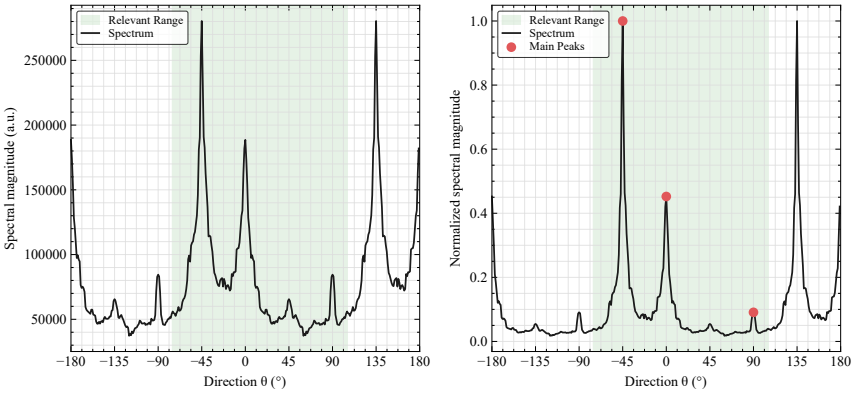
where $r_{\min}$ and $r_{\max}$ denote the lower and upper bounds of the selected radial frequency band. This operation corresponds to a projection of the two-dimensional spectral information onto the angular axis and is implemented numerically as a summation over the radial dimension of the polar spectrum.

The resulting angular spectrum $S(\theta)$, see Figure 4.13a, represents the orientation-dependent distribution of the aggregated spectral magnitude and serves as the primary observable for fiber-orientation estimation. The dominant directions of the fiber manifest themselves as pronounced peaks in $S(\theta)$, while the reduction from a two-dimensional to a one-dimensional representation significantly decreases the complexity of the data without removing relevant directional information. Due to the angular-spectrum symmetry $\theta \equiv \theta \pm 180°$, the analysis can be restricted to a 180° range without loss of information. To facilitate visual identification of standard orientations $[0°, \pm 45°, 90°]$ in subsequent figures, a selected relevant data window $\theta \in [\theta_{\min}, \theta_{\max}] = [75°, 105°]$ is used.

To further emphasize dominant orientations relative to the background, the angular spectrum can optionally be squared, thus increasing the contrast between peak and non-peak regions and producing a quantity that is proportional to a spectral energy density in the sense of Parseval's theorem [143]. Here, Parseval's theorem relates the sum of squared magnitudes of Fourier coefficients to the total signal energy in the spatial domain. Subsequent normalization of the squared spectrum facilitates comparability between depth slices and specimens by removing absolute scaling effects, see Figure 4.13b.

Peak Analysis

In the final main-processing step, dominant peaks in the angular spectrum are detected and characterized automatically. Peak detection is performed using



(a) Angular spectrum before normalization and peak detection.

(b) Angular spectrum after normalization and peak detection.

Figure 4.13: Raw against squared and normalized angular spectrum with peak detection of a 300 gsm quasi-isotropic CFRP laminate (QI-300). The green shaded area highlights the symmetry-reduced angular range.

robust criteria based on peak prominence, peak sharpness, and spectral energy in order to ensure reliable identification of physically meaningful orientation directions. Depending on the material system and analysis objective, one or multiple peaks can be extracted per depth slice. The resulting peak positions define the local fiber-orientation angle(s); see Figure 4.13b, while associated peak metrics provide confidence measures for the orientation estimates. Repeating this procedure for all depth slices yields a depth-resolved fiber-orientation profile across the laminate thickness.

Candidate peak positions are identified using a prominence-based peak detection scheme applied directly to the discrete angular spectrum $S(\theta)$. For each detected peak, a set of quantitative peak metrics is derived from the local spectral characteristics and used to rank and select dominant orientation candidates via a weighted scoring scheme.

The prominence P_k of the k-th peak quantifies how strongly the peak rises above its surrounding baseline. It is defined as the vertical distance between the peak height and the higher of the two local minima (bases) on either side of the peak.

In practice, P_k is obtained from a standard prominence-based peak analysis routine and is expressed in the same normalized units as the angular spectrum:

$$P_k \;=\; S(\theta_k) - \max\Big(S(\theta_{k,\mathrm{base,L}}),\, S(\theta_{k,\mathrm{base,R}})\Big), \tag{4.26}$$

where $S(\theta)$ denotes the angular spectrum and θ_k the peak position.

Peak sharpness is introduced to favor narrow, well-localized orientation responses over broad spectral maxima. It combines information on peak prominence with a measure of peak width and is therefore sensitive to both detectability and angular localization. The peak width is quantified by the full width at half maximum (FWHM), which is determined directly from the angular spectrum using a relative-height criterion. The FWHM W_k represents the angular extent over which the peak amplitude exceeds half of its maximum value. Using the measured FWHM W_k and the angular sampling step $\Delta\theta$, the sharpness S_k of the k-th peak is defined as

$$S_k \;=\; \frac{P_k}{W_k/\Delta\theta + \varepsilon}, \tag{4.27}$$

where P_k denotes the prominence of the peak and a small constant $\varepsilon > 0$ is introduced to avoid division by zero and to stabilize the metric for extremely narrow peaks. This formulation assigns higher sharpness values to peaks that are both prominent and narrowly confined in angle, indicating a well-defined orientation response.

The peak energy E_k characterizes the total spectral contribution associated with a given orientation response. It is defined as the integral of the angular spectrum over the extent of the peak between its left and right bases,

$$E_k \;=\; \int_{\theta_{k,\mathrm{base,L}}}^{\theta_{k,\mathrm{base,R}}} S(\theta)\,\mathrm{d}\theta. \tag{4.28}$$

This quantity represents an aggregated spectral measure rather than a physical energy and accounts for both peak height and peak width. The energy metric is particularly relevant for broad but physically meaningful peaks, for example, in regions with local fiber-orientation dispersion or gradual orientation transitions, where peak height alone would underestimate the relevance of the orientation component.

Weighted Peak Scores

To combine heterogeneous metrics into a single ranking criterion, each metric is normalized by the maximum value across the candidate peaks within the same depth slice. For a generic metric $m_k \in \{P_k, S_k, E_k\}$, the corresponding score $\hat{m}_k$ is defined as

$$\hat{m}_k \;=\; \frac{m_k}{\max_j m_j}, \tag{4.29}$$

where the index j runs over all detected peaks within the same depth slice. Such that $\hat{m}_k \in [0, 1]$ for all peaks in the current slice.

Finally, a weighted score is used to rank peaks and select the dominant direction of fiber orientation. With user-defined weights w_P, w_S, and w_E (with $w_P + w_S + w_E = 1$), the weighted score Q_k is defined as

$$Q_k \;=\; w_P\,\hat{P}_k \;+\; w_S\,\hat{S}_k \;+\; w_E\,\hat{E}_k. \tag{4.30}$$

The peak(s) with the highest Q_k are selected as the most reliable orientation candidates for the corresponding depth slice. This formulation balances peak detectability (prominence), angular localization (sharpness), and total attributed spectral energy, thereby improving robustness against noise, peak splitting, and local spectral artifacts. Unless explicitly specified, the weighting factors w_P, w_S, and w_E are assigned equal values of $1/3$ in the following sections. The exemplary result of the fiber-orientation analysis for the 300 gsm quasi-isotropic CFRP laminate is shown in Figure 4.14.

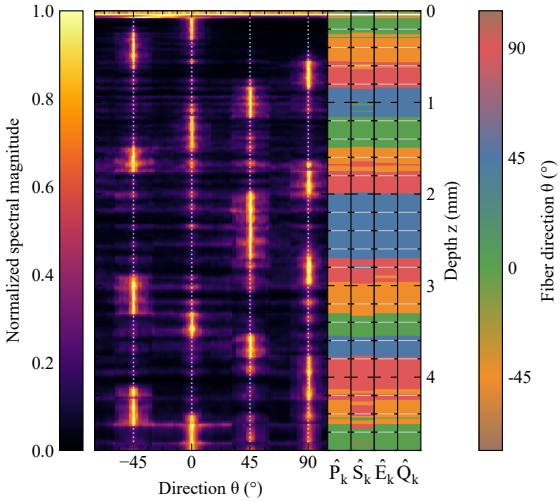


Figure 4.14: Fiber-orientation analysis and peak metrics for a 300 gsm quasi-isotropic CFRP laminate (QI-300).

4.4 Results and Discussion

This chapter presents the experimental results and discussion of ultrasonic fiber-orientation and anisotropy detection in CFRP laminates. The primary objective is to assess the capability of the newly developed and applied ultrasonic methodology, presented in Section 4.3, to qualitatively and quantitatively resolve fiber-orientation information across different laminate architectures, ply thicknesses, and disturbance conditions.

As a first step, the ultrasonic results are qualitatively validated against known laminate layups. This validation approach follows established practice in ultrasonic fiber-orientation detection studies, where reference laminates with well-defined stacking sequences are used to assess detectability, depth resolution, and orientation fidelity. For each investigated specimen, a consistent set of visualizations is provided, comprising the following figures: (a) A through-thickness fiber-orientation analysis based on angular spectral evaluation combined with the weighted orientation score Q_k, as developed in Equation (4.30). (b) A C-scan of the top surface derived from the front-wall echo. (c) A C-scan of the laminate thickness obtained from the time-of-flight difference between the front- and back-wall echoes.

The C-scans for the front-wall and thickness, together with representative optical micrographs, provide an overview of the overall quality of the laminate and enable the identification of potentially disturbing features such as voids, delaminations, impact-induced damage, or machining-related features. These complementary representations establish the structural context required for a reliable interpretation of the ultrasonic fiber-orientation results.

The through-thickness analysis of the angular spectra, in combination with the weighted score Q_k, allows a qualitative evaluation of the accuracy of the fiber-orientation detection with respect to the nominal ply layup, individual ply thicknesses, and achievable depth resolution. This approach facilitates the identification of depth ranges with reliable orientation information, as well as regions where attenuation, scattering, or interface effects limit interpretability.

The discussion of results begins with UD and QI laminates, which serve as standard reference configurations to assess the influence of ply thickness and stacking sequence on ultrasonic orientation detectability. Building upon these reference cases, more complex laminate architectures are subsequently analyzed in the form of Bouligand fiber composites, representing non-standard and highly spatially varying fiber-orientation states. Finally, the influence of structural disturbances, including impact damage and machining-induced features, on ultrasonic fiber-orientation and anisotropy detection is systematically evaluated.

4.4.1 Unidirectional Laminates

The investigation of UD laminates constitutes the fundamental reference case for ultrasonic fiber-orientation detection, as no variation of fiber orientation is expected through the thickness of the laminate. Consequently, potential secondary influences arising from pronounced front- and back-wall echoes, signal attenuation, noise, or manufacturing-related imperfections can be identified particularly well. In addition to the 120 gsm UD laminate shown in Figure 4.15, further results for UD laminates with fiber areal weights of 30 and 60 gsm are provided in Appendix A.5.1.

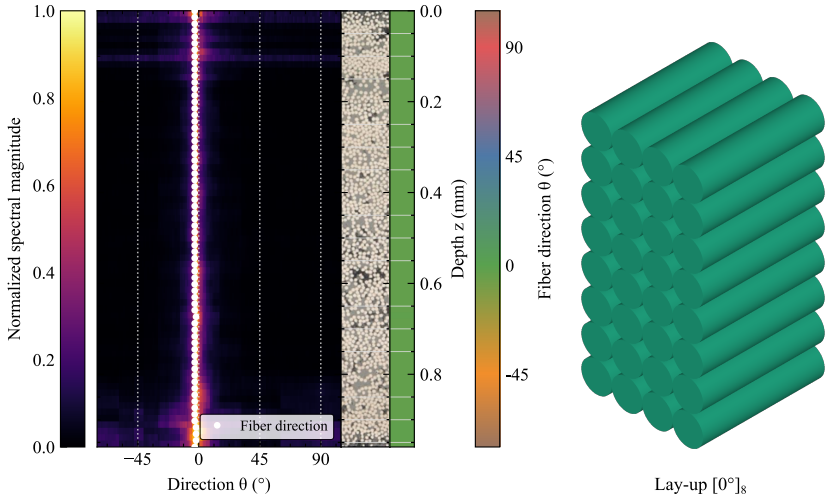
The optical micrographs reveal some small isolated pores, while the fibers aligned in the nominal 0° direction do not show pronounced irregularities. The thickness C-scan likewise provides a clear visualization of the unidirectional laminate structure and indicates a largely homogeneous thickness distribution. Based on the weighted orientation metric Q_k, the nominal 0° fiber orientation is consistently

detected throughout the thickness of the laminate, confirming the expected uniformity of the UD configuration.

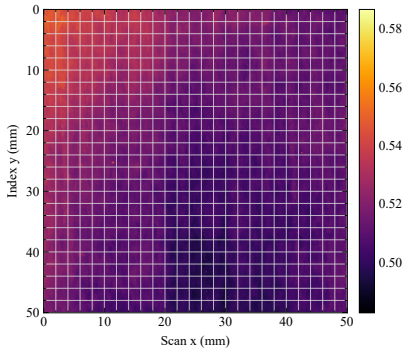
Additional insight is obtained from the angular spectra, which reveal localized deviations from an idealized single-orientation response. In the vicinity of the specimen surfaces, i.e. in the uppermost and lowermost regions of the through-thickness representation, a noticeable broadening of the dominant 0° peak towards neighboring angular directions is observed. This behavior is attributed to the strong front- and back-wall reflections, which locally dominate the ultrasonic response and reduce the effective signal-to-noise ratio of fiber-related backscatter. As a result, spectral leakage effects occur, leading to a smearing of the angular distribution despite an unchanged underlying fiber orientation.

A largely thickness-independent angular broadening is observed for the 30 gsm UD specimen in Figure A.8. The optical micrographs and the thickness C-scan show pronounced porosity, indicating reduced manufacturing quality. These pores add distributed scattering that blurs the fiber-driven response and weakens the directional selectivity of the angular spectrum.

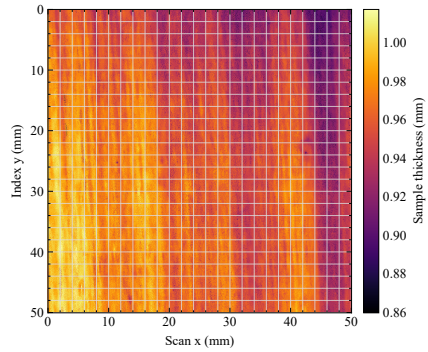
The same effect can also be promoted by other reflective surfaces, as they increase scattering and broaden the angular peaks without changing the underlying fiber direction. Peak broadening therefore makes orientation detection less predictive, even if the nominal direction is still recovered by Q_k. At the same time, peak broadening is informative. It can indicate porosity, fiber misalignment, or insufficient consolidation. As shown later, it can also reveal designed laminate features, and strong fiber angle variation through thickness.



(a) Trough thickness fiber-orientation analysis, micrograph and weighted score Q_k (left); schematic of the lay-up, with the 0° plies highlighted in green (right).



(b) Top surface (front-wall).



(c) Thickness (front-to-back-wall).

Figure 4.15: Trough-thickness fiber-orientation analysis of a 120 gsm unidirectional CFRP laminate (UD-120).

4.4.2 Quasi-Isotropic Laminates

The investigation of QI laminates represents the next step in the ultrasonic fiber-orientation analysis, as it enables the detection of multiple, distinct fiber-orientation angles through the laminate thickness. In contrast to UD laminates, QI configurations provide a suitable benchmark for assessing depth resolution and the capability to resolve individual plies with different orientations.

In addition to the 120 gsm QI laminate shown in Fig. 4.16, further results for QI laminates with fiber areal weights between 30 and 60 gsm are provided in Appendix A.5.2. The optical micrographs reveal again isolated pores, while the characteristic stacking sequence $[0^\circ, \pm 45^\circ, 90^\circ]_{ns}$ can be clearly identified. The thickness C-scan further supports this observation and allows a qualitative visualization of individual layers, most notably the $\pm 45^\circ$ layers, due to their pronounced contrast.

Taking into account the fiber-orientation results obtained from the weighted metric Q_k, the nominal ply orientations are consistently detected throughout the laminate thickness for the 120 gsm specimen. Isolated misclassifications of individual measurement points can be observed; however, these can be interpreted in the context of achievable depth resolution.

Based on a sampling rate of $f_s = 100$ MS/s and an assumed longitudinal wave velocity of $c_{cfrp} \approx 3050$ m/s in CFRP, the depth increment per sampling point in pulse–echo operation is given by

$$\Delta z_{res} = \frac{c_{cfrp}}{2 f_s}, \tag{4.31}$$

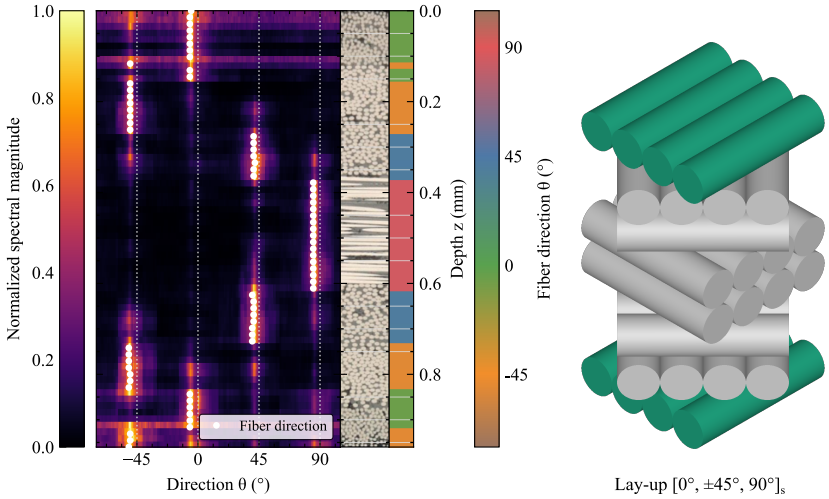
which results in a depth resolution z_{res} of 15.25 μm for the current ultrasonic test setup. The number of sampling points resolving a single ply in the thickness direction can therefore be estimated as

$$N_{\text{pts}} = \frac{t_{\text{ply}}}{\Delta z_{res}} = \frac{2 f_s \, t_{\text{ply}}}{c_{cfrp}}. \tag{4.32}$$

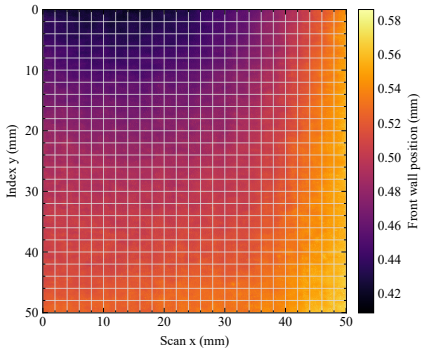
For the 120 gsm laminate, an individual ply thickness of approximately 0.12 mm is resolved by 7.9 pts/ply in the thickness direction, potentially allowing a trained operator or algorithm to distinguish isolated misclassifications from systematic orientation changes.

For thinner plies, such as those present in the 60 gsm (depth resolution: 3.9 pts/ply) and especially the 30 gsm laminates (depth resolution: 2.0 pts/ply), this distinction becomes increasingly ambiguous. The reduced number of measurement points per ply limits the ability to reliably separate true orientation transitions from local misclassifications, thereby constraining the unambiguous detection of individual layers. Measurement systems with higher sampling rate could mitigate this limitation, albeit at the expense of increased data volumes and longer computational processing times.

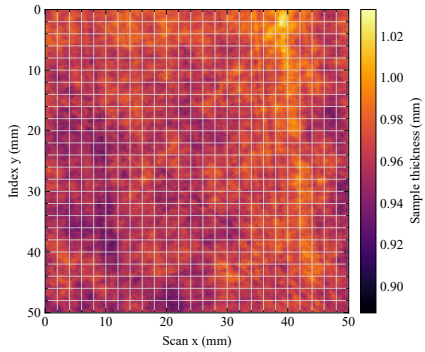
In addition, the same effects previously observed for UD laminates, namely peak broadening and increased scattering in the angular spectrum, are also present in the QI configurations. They result from the superposition of fiber-related scattering with strong signal transitions at material interfaces, such as the front and back surfaces, and from additional scattering at pores. This effect is clearly visible in the 30 gsm laminate. Here, the higher void content makes these contributions sufficiently strong that reliable ply-level orientation detection is no longer possible beyond a depth of approximately 0.4 mm.



(a) Trough thickness fiber-orientation analysis, micrograph and weighted score Q_k (left); schematic of the lay-up, with the 0° plies highlighted in green (right).



(b) Top surface (front-wall).



(c) Thickness (front-to-back-wall).

Figure 4.16: Trough-thickness fiber-orientation analysis of a 120 gsm quasi-isotropic CFRP laminate (QI-120).

4.4.3 Bouligand Laminates

Bouligand helicoidal layups (BL) [144] represent a distinct laminate architecture, as they do not exhibit discrete jumps in fiber orientation as observed in quasi-isotropic laminates. Instead, the fiber angle varies continuously through the laminate thickness, resulting in a quasi-spiral rotation of the fiber direction. This characteristic makes BL laminates particularly well suited for assessing the ability of ultrasonic methods to resolve smoothly varying orientation states and to capture gradual anisotropy transitions.

In addition to the 40 gsm BL laminate with a continuous angular increment of $\theta_i = 3.6^\circ$ per ply (depth resolution: 2.6 pts/ply), shown in Fig. 4.17, further results for laminates with angular increments of 7.2° and 14.4° are provided in Appendix A.5.3. Optical micrographs reveal no detectable porosity, indicating a very high quality laminate. For the $\theta_i = 3.6^\circ$ configuration, the laminate layup

$$\left[[\theta_i]_{i=0}^{50}\right]_{\mathrm{s}}, \qquad \theta_i = i \cdot 3.6^\circ, \qquad n_{\mathrm{ply}} = 102, \tag{4.33}$$

can be clearly identified in the micrographs. The thickness C-scan, on the contrary, does not allow a direct visual distinction of individual plies; apart from a slight global tilt of the laminate, the specimen appears optically homogeneous.

Taking into account the fiber orientation results derived from the weighted metric Q_k, the continuously varying fiber orientation of the $\theta_i = 3.6^\circ$ laminate is adequately detected throughout the laminate thickness, up to the nominal maximum thickness of approximately 4 mm. A moderate broadening of the angular spectrum leads to a small angular scatter around the expected local fiber orientation of individual plies, but still yields a reliable qualitative fiber-orientation detection.

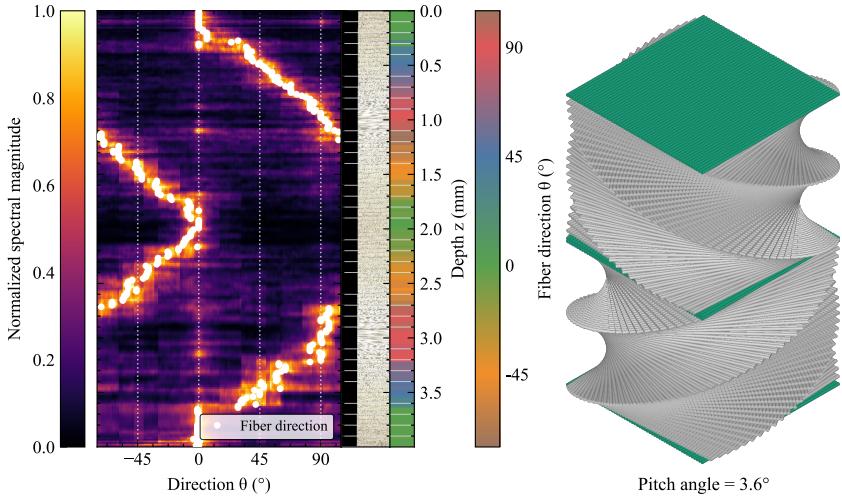
For laminates with a larger angular increment of $\theta_i = 7.2^\circ$, the general trend of the rotating fiber orientation remains clearly identifiable.

However, isolated artifacts begin to appear in the form of an overrepresentation of 0° and, more prominently, 90° orientations, which are not present in the nominal BL architecture. These artifacts are not related to physical fiber alignments, but could arise from method- and instrument-inherent effects that become dominant when the directional contrast of the ultrasonic data diminishes due to the continuously rotating fiber orientation.

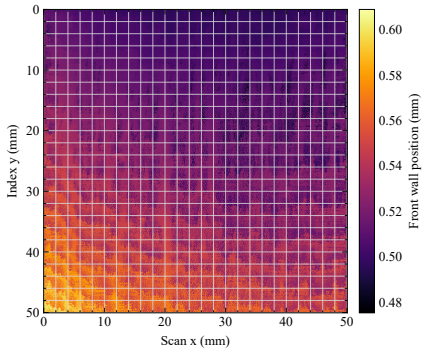
The pronounced exaggeration of the 90° response is a systematic consequence of the 2D FFT applied to quasi-homogeneous spatial input data. As demonstrated in Fig. A.4, a purely homogeneous signal, devoid of any directional texture, produces a dominant 90° peak as a result of the FFT implementation and its associated axis ordering.

In contrast, the occurrence of an additional 0° peak may be related to instrument- or scanning-induced effects rather than to the intrinsic fiber architecture of the laminate. Experimental observations indicate that this response remains aligned with the machine scan axis and does not rotate with the specimen, suggesting a non-material origin. One plausible explanation is that weak, scan-related structures cause one of the principal axes of the raw measurement grid to become overrepresented. Such effects may arise from motion-dependent or synchronization-related influences during data acquisition and can be interpreted by the 2D FFT-based angular analysis as an apparent fiber orientation aligned with the scan direction.

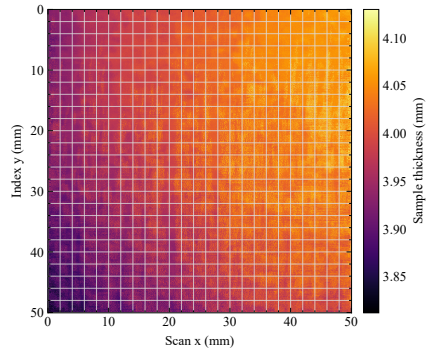
This behavior becomes more pronounced for the $\theta_i = 14.4^\circ$ laminate. The stronger rotation of the fiber-orientation spiral results in increased ultrasonic attenuation and incoherent scattering, which progressively reduces the directional contrast of the fiber-related signal. Although local fiber orientation can still be qualitatively inferred in near-surface regions, spectral peak-based orientation analysis becomes increasingly ambiguous and ultimately fails at greater laminate depths. This observation highlights a fundamental limitation of the applied ultrasonic approach when addressing laminates with rapidly varying in-plane fiber orientations, particularly in combination with increased inspection depth.



(a) Trough thickness fiber-orientation analysis, micrograph and weighted score Q_k (left); schematic of the lay-up, with the 0° plies highlighted in green (right).



(b) Top surface (front-wall).



(c) Thickness (front-to-back-wall).

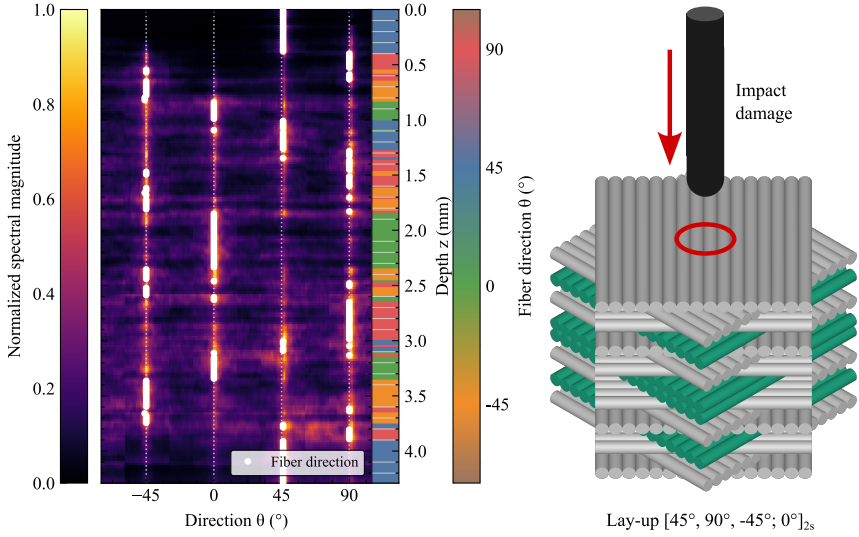
Figure 4.17: Trough-thickness fiber-orientation analysis of a 40 gsm, 3.6° Bouligand CFRP laminate (BL-3.6°).

4.4.4 Design Features and Damage

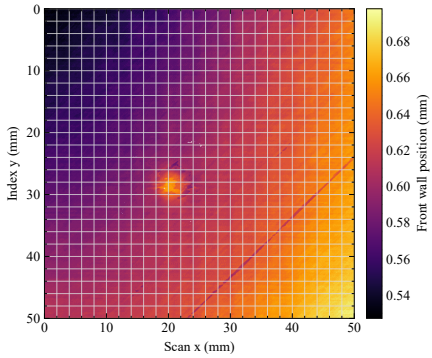
Typical influence factors such as damage and deliberately introduced features are examined with respect to their impact on the fiber-orientation detection capability. The negative influence of porosity on orientation detection has already been demonstrated and discussed for the QI-30 gsm laminates (Section 4.4.2).

An example of FOD analysis applied to a representative impact damage in a 268 gsm quasi-isotropic laminate is shown in Fig. 4.18. The impact damage is visible as a localized indentation in the surface C-scan and as pronounced delamination features in the C-scan of the nominal specimen thickness. The maximum delaminated area extends over approximately 15×15 mm^2, corresponding to about 10 % of the total scan area. Evaluation of the fiber orientation using the weighted metric Q_k shows that the nominal stacking sequence $[45°, 90°, -45°, 0°]_{2s}$ is still reliably detected across the specimen thickness. The implemented FOD approach therefore appears to be largely insensitive to localized impact-induced delaminations of the investigated extent. This behavior can be attributed, on the one hand, to the fact that a simple low-velocity impact primarily affects interlaminar integrity while only marginally altering the global fiber orientation. On the other hand, the applied data-cleaning procedure (Section 4.3.1) enables the reconstruction of locally missing depth information without introducing a distorting influence on the angular orientation analysis.

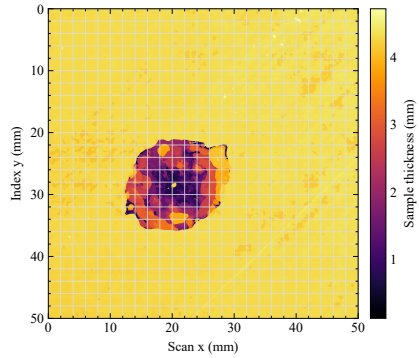
Figure 4.19 shows a representative composite design feature configuration in the form of deep milling grooves and through-holes, which together affect up to approximately one third of the total specimen area. At the surface, the specimen is initially disturbed only by the through-holes, whereas the milling features begin at a depth of about 1 mm and progressively increase in extent, as clearly visible in the thickness C-scan. These results illustrate the practical limits of the fiber-orientation detection approach. While the initially undisturbed surface region of the specimen is still reliably identified using the weighted metric Q_k, the directional resolution gradually degrades with increasing influence of the milling features. In this case, the data-cleaning algorithms are unable to reconstruct the missing information in a physically meaningful manner. Furthermore, the milling operations introduce additional early-occurring internal interfaces, which act as strong acoustic reflectors. These interfaces lead to a pronounced broadening of the angular spectrum, analogous to the effects previously discussed for the front-wall and back-wall reflections. As a consequence, the angular spectral



(a) Trough thickness fiber-orientation analysis, micrograph and weighted score Q_k (left); schematic of the lay-up, with the 0° plies highlighted in green (right).



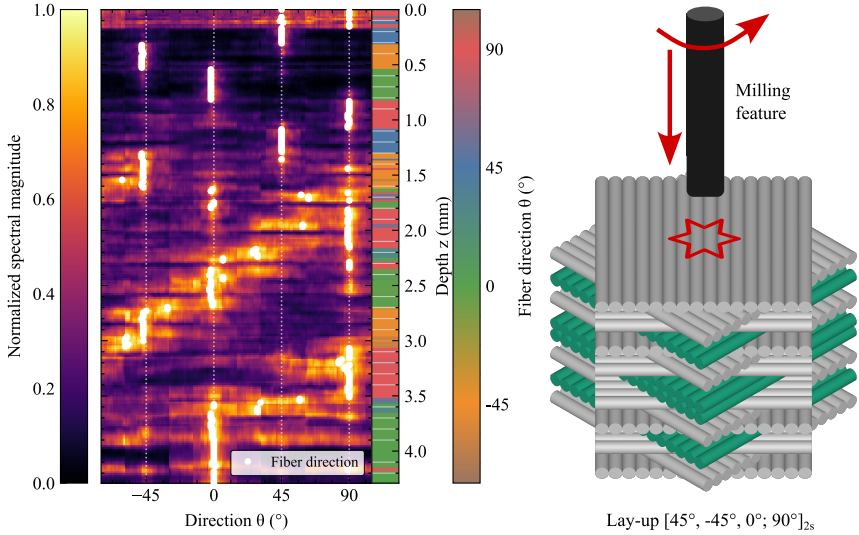
(b) Top surface (front-wall).



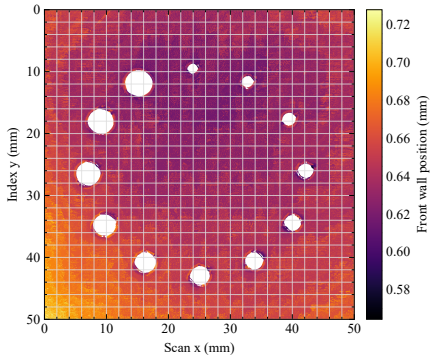
(c) Thickness (front-to-back-wall).

Figure 4.18: Trough-thickness fiber-orientation analysis of a 268 gsm, quasi-isotropic CFRP laminate with impact damage (QI-268-Impact).

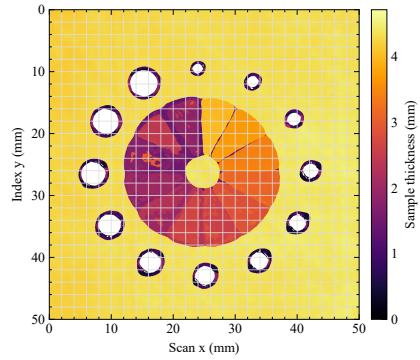
analysis loses its ability to resolve fiber orientations unambiguously in regions dominated by such geometric features.



(a) Trough thickness fiber-orientation analysis, micrograph and weighted score Q_k (left); mirrored schematic of the lay-up, with the 0° plies highlighted in green (right).



(b) Top surface (front-wall).



(c) Thickness (front-to-back-wall).

Figure 4.19: Trough-thickness fiber-orientation analysis of a 268 gsm, quasi-isotropic CFRP laminate with milling features (QI-268-Feature).

4.5 Conclusions

This chapter presents a non-destructive ultrasonic methodology to quantify through-thickness, ply-level fiber-orientation in CFRP laminates, providing a key input for orientation-aware interpretation of anisotropic transport.

The complete workflow is implemented within the open-source Python framework *CompoSE*, providing a pipeline from ultrasonic raw-data import to depth-resolved processing and analysis, including fiber-orientation detection, 2D/3D damage visualization, and standardized evaluation.

The proposed analysis is positioned between conventional defect inspection and microstructural methods. It does not resolve individual fibers; instead, depth-resolved C-scan slices are analyzed in the Fourier domain to extract layer-wise orientation patterns from laminate-scale texture signatures. The dominant fiber directions emerge as angular peaks and are quantified by the peak-based metric Q_k to reconstruct the laminate stacking sequence. By combining complementary descriptors, including geometric peak characteristics and energy-based measures, Q_k exhibits increased robustness against peak broadening and reduced signal-to-noise ratios.

Reliable orientation detection was demonstrated across a range of industrially relevant lay-up configurations, covering unidirectional, quasi-isotropic, and Bouligand architectures with varying ply thicknesses, fiber areal weights, and up to > 100 plies. The approach further proved largely insensitive to certain localized distortions, such as impact damage and delamination, and enabled orientation evaluation in laminates with total thicknesses in the multi-millimeter range.

The remaining limitations are based on physics and define the operational boundaries of the ultrasonic method. Surface-near regions exhibit reduced directional selectivity due to dominant front- and back-wall reflections, which diminish the relative contribution of fiber-related backscatter. Increased porosity, internal defects, and pronounced geometric features (e.g., milling) introduce additional scattering and strong local reflectors, thus broadening spectral peaks and degrading directional resolvability and effective depth resolution. Further optimization potential lies in tuning the ultrasonic transducer frequency and the signal sampling rate to trade depth resolution against penetration depth depending on the application. Future work can focus on extending the methodology to geometri-

cally complex curved structures and on resolving locally varying fiber orientations, as encountered, for example, in tailored fiber placement processes.

5 Anisotropic Thermal Properties

Directional heat transport in CFRP laminates is intrinsically anisotropic, as the reinforcing fibers provide very high axial heat conduction, while the polymer matrix exhibits much lower, isotropic transport. This chapter therefore develops a non-destructive methodology to quantify in-plane thermal transport and to interpret the identified transport parameters in direct correspondence with the fiber-orientation information established in the preceding chapters.

Chapter 5 develops this route by combining localized thermal excitation with infrared thermography and an orientation-sensitive evaluation strategy. Methodologically, the approach is positioned between classical steady-state or contact-based thermal analysis, which often enforces a fixed heat-flow direction and provides averaged responses, and microstructural reference techniques that are not applicable at the structural scale. Instead of prescribing a one-dimensional heat flux, the method exploits the anisotropic spreading of a transient temperature field after spot-like heating and links the identified principal transport directions explicitly to the fiber-parallel reference defined by Θ from Chapter 4. The theoretical context is established in Section 5.1, complemented by a structured overview of established thermal measurement techniques and the rationale for selecting a thermography-based concept for directional characterization (Sections 5.1.2 and 5.1.3).

The experimental implementation is introduced in Section 5.2, defining the heat-spot thermography test setup, calibration steps, and acquisition boundary conditions required for reproducible measurements. Then a dedicated evaluation framework is presented in Section 5.3 and implemented in the `tcam` processing environment. The performance and limitations of the methodology are assessed in Section 5.4, and the consolidated implications for the thermal characterization strategy of this thesis are summarized in Section 5.5.

5.1 Theoretical Background

Thermal conductivity and thermal diffusivity are fundamental material properties governing heat transport in solids. Thermal diffusivity α is the parameter that controls the rate at which heat perturbations spread through a medium, while thermal conductivity λ represents the capacity of the material to conduct heat once a gradient is established [145]. Together, these properties determine both the spatial distribution and the temporal evolution of temperature fields and therefore form the physical basis for all thermographic measurement techniques.

Figure 5.1 provides a comparative overview of thermal conductivity and diffusivity for major classes of engineering materials. Metals generally exhibit high thermal conductivity and diffusivity, enabling rapid heat spreading, whereas polymers and polymer matrices are characterized by comparatively low values of both properties. Fiber-reinforced polymer composites span a particularly wide range, as their effective thermal transport behavior depends strongly on fiber type, fiber volume fraction, and orientation, resulting in pronounced anisotropy between in-plane and through-thickness directions.

This wide variability and directional dependence of thermal properties in carbon fiber–reinforced polymers presents a significant challenge for experimental characterization. In particular, conventional thermal measurement techniques are often limited to isotropic assumptions, predefined heat-flow directions, or averaged material responses. As a result, careful selection of a suitable measurement approach is essential to enable a non-destructive, directionally resolved evaluation of in-plane thermal transport behavior.

The following section therefore introduces established thermal measurement techniques and discusses their respective capabilities and limitations with respect to anisotropic materials. Based on this comparison, an appropriate experimental method is selected for the investigation of in-plane thermal anisotropy in CFRP within the framework of this thesis.

5.1.1 Thermal Anisotropy

The thermal transport behavior of carbon fiber-reinforced composites is governed by the intrinsic anisotropy of the highly conductive reinforcing fiber and its orientation, while the polymer matrix itself is isotropic with lower thermal

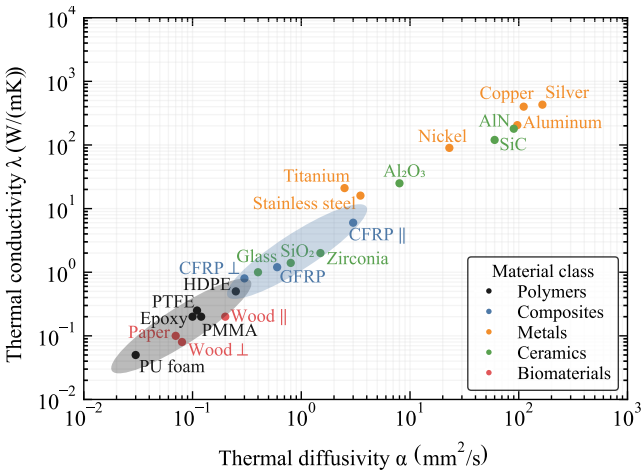


Figure 5.1: Representative thermal conductivity and diffusivity ranges for different material types.

conductivity. In general, the effective thermal conductivity and the thermal diffusivity are tensorial properties that differ substantially between the fiber axis and the transverse directions.

Carbon Fibers

The intrinsic thermal conductivity of carbon fibers has been investigated in detail by Hatta et al. [60] and Zhang et al. [146]. These studies highlight how the processing (Pitch- / PAN-based carbon fibers), microstructure, and temperature govern the wide variation in thermal transport properties observed among commercial carbon fibers.

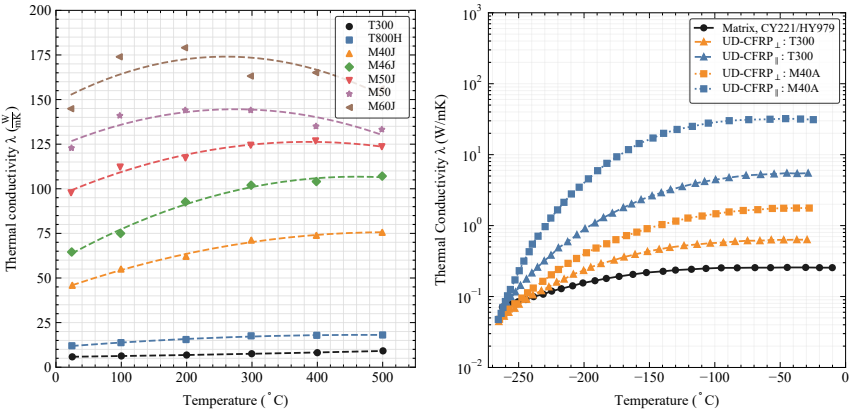
Hatta et al. [60] measured the thermal diffusivity α of single filaments with diameters of approximately 7 µm using a light-irradiation type alternating current (AC) calorimetry system, performed in vacuum to suppress convective losses. Specific heat c_p was obtained by differential scanning calorimetry (DSC), and density ρ from bulk characterization, allowing conductivity to be determined via 5.38. The results were validated against unidirectional CFRPs measured by laser flash analysis, showing good agreement with the values estimated from additive mixture rules. In contrast, Zhang et al. [146] applied a steady-state short-hot-wire technique, where a single carbon fiber is attached as a pin fin

to a thin platinum hot wire operated under direct current (DC) heating. From the measured temperature rise of the hot wire and analytical solutions of one-dimensional heat conduction, λ of the single fiber could be deduced directly with respect to a standard resistance reference. In the same setup, electrical conductivity was obtained via a four-point method, enabling direct correlation of thermal and electrical transport.

Hatta et al. [60] studied a broad range of PAN-based fibers from Toray Industries, including high-strength T-series (T300, T800H), high-modulus MJ-series (M35J–M60J), and standard modulus M-series. Conductivities at room temperature ranged from $\approx 6\,\mathrm{W/(m\,K)}$ (T300) up to $> 120\,\mathrm{W/(m\,K)}$ (M50), with higher values consistently linked to an increased degree of preferred crystalline orientation and higher electrical conductivity. Zhang et al. [146] examined fibers produced under different manufacturing conditions (e.g. methylnaphthalene pitch fibers, PAN-based fibers of varying modulus), reporting conductivities in the range $\approx$ 120–600 $\mathrm{W/(m\,K)}$, again strongly correlated with microstructural properties.

Hatta et al. [60] found that for most PAN-based fibers (T300, T800H, M40J), thermal conductivity increased approximately linearly with temperature between 25–500 °C. In contrast, very high-modulus fibers (M50, M60J) showed a turnover, as can be seen in Figure 5.2a. Conductivity values increased up to about 250–350 °C but decreased at higher temperatures, attributed to phonon-phonon scattering dominating the crystallite alignment effects. Hatta et al. [60] confirmed that the temperature effects depend on the fiber type, well-graphitized fibers with high electrical conductivity exhibited a relatively weak temperature dependence, while lower quality fibers were more sensitive to defect scattering.

Both experimental and modeling studies consistently confirm that heat conduction in carbon fibers is dominated by phonons, with electrons contributing only marginally compared to metals [60, 146]. The large variability of λ across different grades of fiber arises from microstructural factors such as crystallite size, preferred orientation, and defect density, which are determined by precursor type and processing history. Fibers derived from mesophase pitch exhibit the highest conductivities due to their large, well-aligned graphitic domains [147], while PAN-fibers generally contain turbostratic disorder and smaller crystallites, resulting in much lower values [148]. The processing temperature is particularly critical. PAN fibers carbonized at higher temperatures develop larger crystallites and improved alignment of the (002) graphite planes, leading to higher conductivity



(a) Temperature dependence of the thermal conductivity of C-fibers [60].

(b) Temperature dependence of the thermal conductivity of UD-CFRP [3].

Figure 5.2: Temperature dependence of the thermal conductivity for carbon fibers and UD-CFRP [3, 60].

[149]. At elevated temperatures, well-graphitized high-modulus fibers enter the regime where intrinsic phonon–phonon Umklapp scattering dominates, causing conductivity to decrease beyond 250–350 °C, as observed by Hatta et al. [60].

Polymer Matrix

Although carbon fibers typically dominate the highly anisotropic heat conduction in a CFRP, the polymeric matrix still plays a non-trivial role in overall thermal behavior, both in setting a baseline thermal conductivity and in mediating heat flow through the fiber–matrix interface and through the transversal direction. Unlike carbon fibers, most polymer matrices, thermosets or thermoplastics, are intrinsically low in thermal conductivity, and in their unmodified bulk form they tend to be approximately isotropic because their molecular structure is disordered and lacks long-range orientation.

In typical amorphous polymers, the measured thermal conductivities lie in a narrow window of about 0.1–0.5 W/(m K) [150, 151]. A useful conceptual model is a thermal resistance network, where entanglement and random orientation of chains dominate phonon scattering and limit propagation paths, producing

quasi-isotropic heat conduction at the macroscopic scale [150]. However, this quasi-isotropy is not absolute; under certain conditions, polymers can also show thermal anisotropy, particularly if they develop chain alignment, partial crystallinity, or if they contain anisotropic fillers. For example, in stretched or mechanically oriented amorphous polymers, thermal conductivity along the stretch or chain orientation direction can increase relative to the transverse direction [152, 153].

In semi-crystalline polymers, the crystalline domains or ordered chain segments tend to conduct heat better than the amorphous regions. Thus, the degree of crystallinity, crystal orientation, and the connectivity of crystalline domains influence the effective thermal conductivity. Studies on polyethylene have shown that increasing crystallinity increases thermal conductivity [154]. At the same time, the interface between the crystalline and amorphous phases introduces thermal boundary resistance, which limits the benefit of perfect crystallinity. Some empirical models suggest that stretched molecular chains under tensile load, even within the amorphous region, can sometimes outperform crystalline clusters in phonon conduction [155].

Overall improvement of matrix conductivity, for example through thermally conductive fillers, is common practice for more thermally balanced composites [151]. If the fillers are isotropically dispersed and randomly oriented, they may enhance the bulk thermal conductivity of the matrix without introducing a strong anisotropy. However, if the fillers are anisotropic (e.g. graphene sheets, carbon nanotubes) and align preferentially because of processing, flow, electric/magnetic fields, or shear, then the matrix-filler-subsystem can itself become anisotropic. In such cases, heat conduction along the direction of filler alignment may be significantly enhanced compared to the perpendicular directions [151, 156].

In terms of composites, although the matrix is a relatively poor conductor, its isotropic or weakly anisotropic nature is important. It provides a bridge to transfer heat between fibers in the transverse directions and helps fill gaps and mitigate interfacial thermal resistance.

Carbon Fiber Reinforced Composites

The fiber volume fraction φ_f plays an essential role in determining the effective thermal conductivity of CFRPs, since it essentially weights the contributions of the high-conductivity fibers and the low-conductivity matrix in parallel or series heat conduction routes. As fiber content increases, more conductive fiber

pathways are available in the composite, enhancing longitudinal conductivity and changing the proportion in transverse transport where the matrix and interfaces dominate.

Bard et al. [18] measured the thermal conductivities of unidirectional HTS40, Epikote 496 CFRP laminates over a range of fiber volume fractions and compared them with classical mixture models. The experimental data for $\lambda_{\parallel}$ in the fiber direction closely match the Voigt [66] rule of mixtures:

$$\lambda_{\parallel} = \varphi_f \lambda_{f\parallel} + (1 - \varphi_f)\lambda_m \tag{5.1}$$

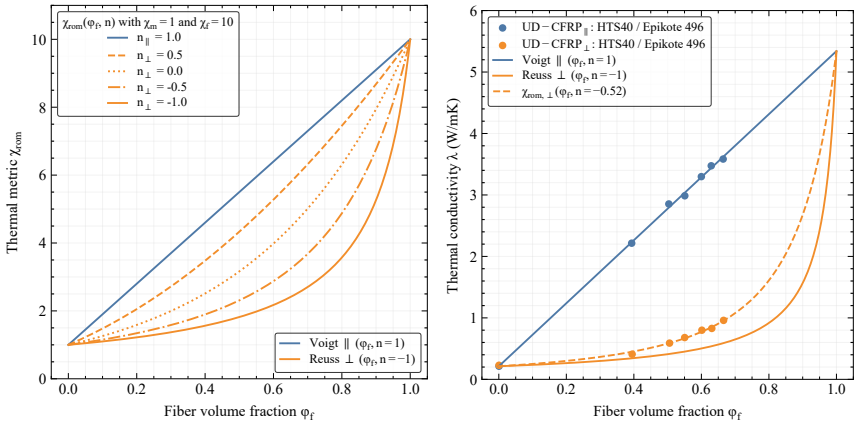
In this formulation, $\lambda_{\parallel}$ denotes the effective thermal conductivity of the composite in the fiber direction, φ_f is the volume fraction of the fiber, $\lambda_{f\parallel}$ represents the intrinsic longitudinal thermal conductivity of the carbon fibers and λ_m corresponds to the thermal conductivity of the polymer matrix. This suggests that thermal conductivity can be effectively considered as an additive in the fiber direction, enabling the extraction of the inherent longitudinal conductivity of the fiber.

In contrast, the $\lambda_{\perp}$ data are systematically higher than the Reuss [67] prediction, even when optimistic fiber transverse conductivity values are assumed, indicating that the simple series bound is too pessimistic.

$$\frac{1}{\lambda_{\perp}} = \frac{1 - \varphi_f}{\lambda_m} + \frac{\varphi_f}{\lambda_{f\perp}}, \tag{5.2}$$

To improve the fit, Bard et al. [18] evaluated more advanced micromechanical models (self-consistent model [18], Rayleigh model [22, 157], and Lewis–Nielsen model [21, 158]). Among these, the Lewis-Nielsen model, with parameters accounting for fiber packing and morphology, provided the most accurate fit, at higher fiber volume fractions, although deviations remained at low fiber content.

Within Section 5.3, a modified rule of mixtures model has been introduced with Equation (5.58), replacing Reuss model for the calculation of $\lambda_{\perp}$. The adjustment factor r is introduced in this model. It is also applicable to Bard's findings; comprehensive results are displayed in Figure 5.3b.



(a) Schematic fiber volume fraction dependence of the thermal metric χ_{rom} of UD-CFRP.

(b) Experimental fiber volume fraction dependence of the thermal conductivity λ of UD-CFRP [18].

Figure 5.3: Schematic and experimental fiber volume fraction dependence of the general thermal metric χ_{rom} and conductivity λ of UD-CFRP.

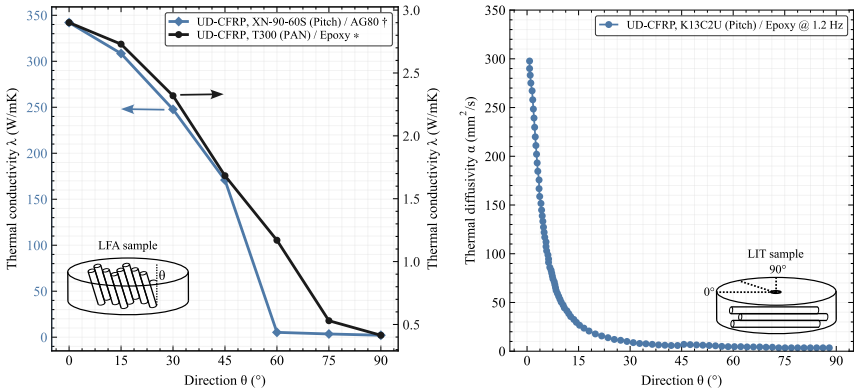
The thermal conductivity of CFRPs is strongly temperature dependent, with particularly pronounced effects in the cryogenic regime. Chen et al. [159] measured unidirectional T300 and T700 epoxy composites between approximately −230 °C and ambient temperature and reported a steep increase of λ from about 0.15 W/(m K) at −230 °C up to nearly 5 W/(m K) at 25 °C, with the strongest variation occurring below −125 °C. This behavior was attributed to phonon-dominated transport in the carbon fibers, where increased phonon mean free paths at low temperatures lead to strong changes in effective composite conductivity. Shim et al. [160] confirmed that the temperature effect is not only significant in magnitude but also in its influence on anisotropy: composites reinforced with pitch-based fibers of varying cross-section (round, C-, hollow type) exhibited a clear rise of longitudinal conductivity with temperature, while transverse conductivity showed a smaller increase, leading to a decreasing anisotropy factor with rising temperature. Complementary results summarized by Schürmann [3] underline the steep rise of conductivity at extremely low temperatures for unidirectional T300 and M40A composites with epoxy (CY221/HY979), where the parallel conductivity exceeds the perpendicular by more than an order of magnitude at cryogenic temperatures, while the slope flattens close to ambient

conditions, see Figure 5.2b. Collectively, these findings highlight that CFRPs are particularly sensitive to temperature in the cryogenic domain, where conductivity may change by orders of magnitude, whereas at ambient temperature variations become less critical.

The direction-dependent thermal transport in unidirectional carbon-fiber-reinforced polymers has been analyzed using a variety of experimental methods. Fang et al. [17] investigated the in-plane anisotropy of pitch-based UD-CFRP (XN-90-60S fibers / AG80 epoxy) by laser flash analysis. Their study revealed a strong dependence of apparent thermal conductivity on the fiber orientation angle, with λ continuously decreasing from the fiber direction (0°) to the transverse direction (90°). Finite element simulations reproduced this trend and demonstrated that geometric constraints, especially the radius-to-thickness ratio, significantly affect the accuracy of measured in-plane conductivities. For near-transverse directions, a drop in thermal conductivity was observed. This phenomenon was assumed to correlate with a change in the heat transfer process from a continuous to a zigzag path. Similar measurements by Touni [161] for UD-CFRP (T300 fibers / generic epoxy) with a lower overall conductivity did show a much narrower drop for near transverse thermal conductivities; see Figure 5.4a. The results underscore that both the anisotropic nature of the heat flow and the geometry of the sample must be considered.

In contrast, Ishizaki and Nagano [19] employed a lock-in thermography approach to map the in-plane thermal diffusivity of a pitch-based UD-CFRP (K13C2U fibers / generic epoxy). Their non-contact periodic heating setup enabled spatially resolved measurement of thermal diffusivities $\alpha_\parallel$, $\alpha_\perp$, and intermediate angular components at high directional resolution without machining oriented specimens.

Compared to the laser flash measurements by Fang et al. [17] and Touni [161], the directional dependence of thermal diffusivity obtained by Ishizaki and Nagano [19] using lock-in thermography exhibits a much steeper decrease, with α already dropping significantly at fiber orientation angles of about 10°. This discrepancy arises from fundamental differences in both the measurement technique and the microstructural configuration of the investigated specimens. Lock-in thermography probes near-surface, frequency-dependent heat diffusion with high spatial resolution, making it particularly sensitive to local variations in fiber orientation and interfacial resistance. In contrast, laser flash and steady-state techniques yield volumetric averages of the bulk material response. Such methodological and



(a) Directional thermal conductivity of UD-CFRP measured by laser flash analysis †[17],*[161].

(b) Directional thermal diffusivity of UD-CFRP measured by lock-in thermography [19].

Figure 5.4: Directional dependence of the thermal conductivity or diffusivity of UD-CFRP obtained by laser flash analysis and lock-in thermography. [17, 19, 161]

structural differences must be carefully considered when interpreting experimental data or developing simulation and homogenization models, as they directly influence the apparent degree of anisotropy extracted from measurement.

5.1.2 State-of-the-Art Measurement Techniques

The reliable determination of thermal transport parameters, namely thermal conductivity λ and thermal diffusivity α, is fundamental in both research and industrial practice. With reference to Equation (5.38), not all techniques provide direct access to both quantities. Some measure α and require auxiliary measurements of ρ and c_p [46, 47], while others directly determine λ under steady-state conditions [162, 163].

Measurement techniques can be classified according to various criteria:

- *Steady-state / transient methods:* Steady-state techniques establish a stable temperature gradient under constant heat flux and are normally used for the measurement of thermal conductivity, while transient methods monitor the time-dependent thermal response to a pulse or modulated excitation, often used for the measurement of thermal diffusivity [15, 164].

- *Contact / non-contact methods:* Contact techniques (e.g. guarded hot plate (GHP), heat flow meter (HFM)) require direct thermal contact with sensors, whereas optical methods (e.g. laser flash analysis (LFA), lock-in thermography (LIT), Heat-Spot Thermography (HST)) employ remote heating and infrared detection [165, 166].
- *Material suitability:* If the method is suitable for a variety of measurement ranges, encompassing thermal insulators and conductors, as well as diverse types of material, including dense solids, porous materials, thin films, liquids, and gases. [23, 167].
- *Temperature range:* Some industrial methods (e.g. LFA, GHP) can operate from cryogenic to above 2000 °C [46, 47], while others are restricted to near-ambient temperature conditions.
- *Atmosphere:* Measurements may require vacuum, inert gases, or controlled humidity to minimize convection and oxidation, particularly in LFA or hot wire setups [49, 167].
- *Sample geometry:* Certain techniques require specific sample shapes. Thin discs or plates for LFA [47] or GHP [162], thin films for Nano-Thermoreflectance (NTR) [168], while others are more flexible (HST [50, 52], LIT [24, 25]).
- *Non-destructive vs. destructive:* Optical methods such as LIT and HST can be designed to allow completely non-destructive testing [166, 169], while LFA and other methods may require machining samples to standard geometries [162].
- *Speed and throughput:* Transient methods (LFA, NTR, LIT, HST) allow rapid measurements in nanoseconds to minutes [24, 46, 168], while steady-state methods often require minutes to hours to reach equilibrium [162, 163].

In the following sections, the most widely established thermal measurement techniques applied in the field of fiber-reinforced composites are briefly introduced. The methods are categorized into steady-state and transient approaches. Based on this overview, an appropriate technique is subsequently selected and improved to enable an precise determination of the anisotropic in-plane thermal properties of CFRP materials.

Steady-State Methods

Guarded Hot Plate (GHP) The guarded hot plate method is regarded as the primary steady-state technique for determining the thermal conductivity of insulating materials. It is standardized in ASTM C177 [163] and ISO 8302 [162]. The apparatus consists of a central electrically heated metering section surrounded by a guard heater to minimize lateral heat flow. The specimen is placed between the hot plate and the cold plate, establishing a unidirectional temperature gradient. The heat flux through the sample is determined from the electrical power supplied to the metering section, while the temperature difference across the sample is measured with embedded sensors. From Fourier's law, the thermal conductivity is obtained as:

$$\lambda = \frac{Q\,L}{A\,\Delta T} \tag{5.3}$$

where Q is the measured heat flow, L is the thickness of the specimen, A is the measuring area and ΔT is the mean temperature difference. Due to the guarded design and power-based flux determination, the GHP method achieves high accuracy, typically within 1–3% under carefully controlled conditions. However, measurements require large, machined specimens and long equilibration times, often extending to several hours. The GHP is therefore best suited for reference measurements, certification, and laboratory studies demanding high precision. [163, 170]

Heat Flow Meter (HFM) The heat flow meter method is a derivative of the guarded hot plate, employing calibrated heat flux transducers to measure heat flow directly. It is standardized in ASTM C518 [171]. In this setup, a sample is placed between two parallel plates maintained at different temperatures, similar to the GHP configuration. However, instead of determining the heat flux from electrical power input, thin-film heat flux sensors at the specimen interfaces provide a direct measurement of the transmitted heat. The apparatus is calibrated against reference materials of known thermal conductivity in the same conductivity range as the sample. The HFM method provides a faster and simpler operation than the GHP, with typical test durations of minutes rather than hours. Its accuracy is lower (around 3–5%), limited by the precision of the flux sensor calibration and long-term drift. Consequently, HFM is widely employed in quality control and routine testing of materials such as polymer

foams, insulation boards, and building panels, where high throughput is favored over ultimate accuracy. [171, 172]

Transient Methods

Transient thermal measurement techniques are governed by the finite time required for a thermal disturbance to propagate over a characteristic length scale of the specimen. For a representative length l, such as the sample thickness or the radius of a localized heat input, the diffusion time can be estimated as

$$t_c \sim \frac{l^2}{\alpha}. \tag{5.4}$$

This relation shows that the temporal response observed in a transient experiment is jointly determined by the material diffusivity and the imposed heat-flow geometry. Consequently, the applicability of a given transient method is constrained by whether the resulting diffusion time falls within the measurable time window of the infrared detector and data acquisition system. Materials with high thermal diffusivity or small characteristic length scales produce very short transients that may exceed the temporal resolution of the detector, whereas low-diffusivity materials or large length scales lead to long transients with reduced signal amplitude and increased sensitivity to noise and heat losses.

Laser Flash Analysis (LFA) The laser flash method, introduced by Parker et al. [46] in 1961, remains the most established transient technique for bulk solids. A thin specimen is irradiated on one side by a short laser or xenon flash pulse, and the rear-face temperature rise is recorded by an infrared detector. The thermal diffusivity α is calculated from the half-rise time of the transient response according to the following equation:

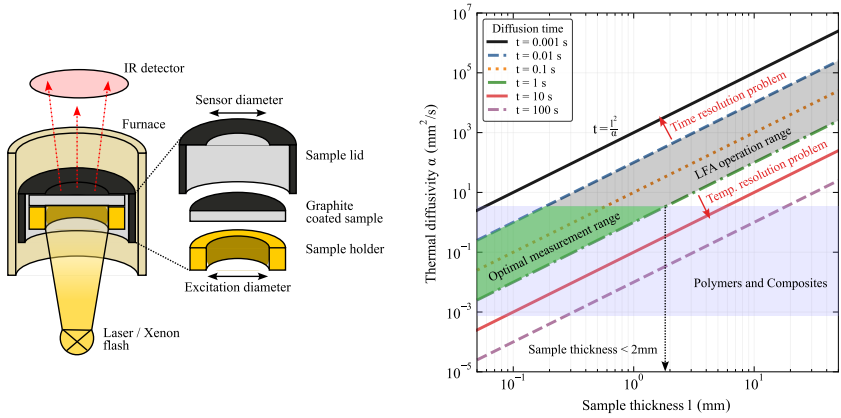
$$\alpha = 0.1388 \, \frac{L^2}{t_{1/2}}, \tag{5.5}$$

where L is the thickness of the specimen and $t_{1/2}$ is the time required to reach half of the maximum increase in the temperature of the rear face.

Subsequent refinements by Cowan [173], Cape and Lehman [48], and Clark and Taylor [49] addressed finite pulse duration, radiative and convective heat losses, and multilayer corrections. These improvements are codified in the

international standard ASTM E1461 [47], which prescribes evaluation procedures and experimental requirements to ensure reproducibility. Modern commercial instruments also employ numerical fitting of the full transient curve to extend accuracy across a wider range of materials and conditions. [174]

The operational range of the LFA method is inherently constrained by the thickness of the sample, as defined by the transient diffusion time according to Equation (5.4). For a given thermal diffusivity α, the characteristic diffusion time must be within the dynamic range of the detector system. At short diffusion times (i.e., for thin or highly conductive samples), the measurable signal is limited by the temporal resolution of the infrared detector and data acquisition system, which typically lies in the millisecond regime. Conversely, at long diffusion times (i.e., for thick or poorly conducting samples), the signal amplitude decreases, and the measurement accuracy becomes restricted by the temperature resolution and baseline stability of the detection optics. As a result, for materials with low diffusivity such as polymers and fiber reinforced composites, the thickness of the specimen must generally remain below approximately 2 mm to ensure a suitable signal-to-noise ratio and a reliable determination of the half-rise time in accordance with ASTM E1461 [47].



(a) Schematic LFA setup. **(b)** LFA nominal thickness range.

Figure 5.5: Laser flash analysis of composites: measurement setup and thickness range.

Nano thermoreflectance techniques (NTR) extend the half-rise time approach of the LFA to thin films by exploiting the temperature dependence of the optical

reflectivity. In a typical setup, a fast pump laser delivers a short heat pulse to the specimen surface, while a probe laser monitors the resulting reflectivity change at the same surface. The transient reflectivity signal is directly proportional to the surface temperature evolution, enabling evaluation of the thermal diffusivity using the same characteristic half-rise time concept as in LFA. Because the probed signal originates from the heated surface rather than the rear face of the specimen, thermoreflectance is particularly well suited for polymer films with thicknesses ranging from a few nanometers to several micrometers and low thermal diffusivity, where conventional LFA is inapplicable. [168]

Lock-in Thermography (LIT) Lock-in thermography is a non-destructive, phase-sensitive technique that derives thermal transport properties from the amplitude and phase of periodic temperature oscillations induced by modulated heating. A specimen is excited by a laser, halogen lamp, or electrical source with sinusoidal modulation, and the surface temperature response is captured by an infrared camera. Through Fourier analysis of the lock-in signal, the thermal diffusivity α and, when combined with specific heat and density, the thermal conductivity λ can be extracted. The key advantage of LIT lies in its ability to suppress noise and increase sensitivity while offering spatially resolved measurements. The theoretical basis and instrumentation are extensively covered in Breitenstein et al. [166], while Fabbri and Fenici [175] and Salazar et al. [176] introduced the early concepts of three-dimensional photothermal radiometry.

Applications to polymers and insulating solids have confirmed the utility of the method for low-conductivity materials. Bedoya et al. [177] demonstrated front-detection laser-spot thermography for thermal characterization of insulating solids, achieving a reliable determination of both α and derived λ. In follow-up work, Bedoya et al. [178] showed that LIT can be implemented with non-research-grade infrared cameras without significant loss of accuracy if acquisition and modulation are optimized, opening the method to wider industrial use. Wolf et al. [179] highlighted the applicability to thin films and coatings, where conventional transient methods such as LFA fail due to constraints of the sample geometry.

A major strength of LIT is its ability to characterize anisotropic transport in fiber-reinforced composites. Salazar et al. [176] were among the first to demonstrate that photothermal and lock-in techniques can resolve directional diffusivities in anisotropic solids, using angular-dependent heating and detection. Fujita and Nagano [118] further extended the approach by using in-plane diffusivity maps

to estimate fiber orientation distributions in CFRP laminates, allowing non-destructive microstructural characterization. Building on this concept, Ishizaki and Nagano [19] developed a validated three-dimensional anisotropic model on CFRPs, showing that in-plane and through-thickness components can be determined from a single experiment. Miyachi et al. [180] applied line-heating LIT to discontinuous CFRPs, revealing a direct correlation between the density distributions of the thickness, the void content, and the quality of the resin impregnation. More recently, Bedoya et al. [25] compared laser-spot and laser-line lock-in thermography, providing a systematic framework for measuring in-plane anisotropy and quantifying uncertainty.

Several methodological advances have improved the scope and robustness of LIT. Gaverina et al. [169] introduced the constant-velocity flying-spot method, in which the moving heat source creates an anisotropic footprint that encodes $\alpha_{\parallel}$ and $\alpha_{\perp}$ with high precision. Salazar et al. [181] presented a step-heating laser-spot thermography variant, simplifying the setup, by combining a low-end laser and an entry-level IR camera, while maintaining sensitivity to anisotropic transport. Bedoya et al. [182] explored laser-spot thermography to visualize heat convection phenomena in fluids, emphasizing the interplay between conduction and convective fields in open systems. These developments demonstrate the flexibility of LIT-based approaches beyond classical modulated heating.

In conclusion, lock-in thermography has evolved from a defect-detection technique into a quantitative tool for determining thermal diffusivity and, in combination with density and heat capacity, thermal conductivity [166]. Its main strengths lie in the non-contact and non-destructive nature of the method, the noise suppression achieved through phase-sensitive detection, and the possibility of investigating anisotropic heat transport by varying the excitation geometry [19, 25, 118, 169, 176]. These capabilities make LIT highly attractive for polymers, thin films, and fiber-reinforced composites [177, 179, 180]. However, LIT requires calibration and a complex model-based evaluation, and the achievable accuracy is generally lower than that of absolute techniques such as laser flash analysis [46, 183]. In addition, the influence of convection, radiation, and boundary conditions can complicate data models [178, 181, 182]. Alternative approaches, such as heat-spot thermography, have therefore been developed to achieve anisotropy sensitivity similar to that obtained with even simpler setups and analytical models [25, 181].

Heat-Spot Thermography (HST) Heat-spot thermography refers to a family of transient, non-contact techniques in which a localized, typically Gaussian-shaped heat pulse is applied to a specimen surface and the subsequent thermal spreading is recorded by an infrared camera. The radial evolution of the temperature distribution follows the diffusion law. By fitting the temporal broadening of the thermal profile, α can be extracted directly [24, 51, 184]. With this method, unlike laser flash analysis, both heating and detection can take place on the identical surface or opposite surfaces, allowing for more flexible sample geometry requirements, especially regarding sample thickness.

A variety of methodological developments have expanded the scope of HST. Welch et al. [50] demonstrated as early as 1987 that the angular spreading of a localized heat spot allows the determination of in-plane anisotropic diffusivity components in plates. Dong et al. [185] presented an infrared sequence transformation technique for robust in situ evaluation under tilted optical conditions. Gfroerer et al. [186] and Basheer et al. [187] adapted HST for the use of a low-cost hot rod heating element. Genna and Ucciardello [188] applied the HST approach to electroplated coatings, quantifying in-plane diffusivity.

The method has also been applied to polymers and composites. Pech-May et al. [52] proposed determination of in-plane diffusivities of using focused laser-spot illumination, giving insight into appropriate heating times, and proposing that the measurement technique is not influenced by heat losses by convection or radiation. Kalyanavalli et al. [189] demonstrated the determination of diffusivity in basalt fiber-reinforced epoxy composites, highlighting sensitivity to fiber reinforcement and interfacial coupling. Applications to insulating materials include the work of Cernuschi et al. [51] and Bison et al. [190], who adapted thermographic spot methods to thermal barrier coatings, allowing the simultaneous estimation of in-plane and depthwise diffusivities. Bedoya and colleagues [177, 178, 182] further refined laser-spot thermography to visualize convection effects in front-detection configurations and to demonstrate that low-cost infrared cameras can deliver reliable diffusivity values when combined with robust data processing. In addition to static standard HST methods, Gaverina et al. [169] presented the constant velocity flying-spot approach, in which a moving heat source creates an anisotropic thermal footprint allowing calculation of in-plane tensorial properties with high precision [169].

HST is a flexible non-contact technique for assessing thermal diffusivity in a wide range of materials. Its strengths include simple experimental setups,

flexible sample geometry requirements, and a unique sensitivity to in-plane anisotropy, which makes it particularly attractive for polymers, coatings, and fiber-reinforced composites. Compared with lock-in thermography, HST offers faster implementation and lower hardware demands.

5.1.3 Selection of Measurement Technique

The selection of an appropriate thermal property characterization technique is a prerequisite for the investigation of anisotropic heat transport in fiber-reinforced polymer composites. The objective of this thesis is the non-destructive and directionally resolved evaluation of in-plane thermal transport behavior over a continuous angular domain. Conventional single point-based, mean value-based, or directionally constrained methods are therefore insufficient, as they provide only limited directional information and are typically restricted to predefined heat-flow geometries.

Table 5.1: Overview of thermal conductivity and diffusivity measurement techniques. [19, 24, 25, 50–52, 118, 166, 168–170, 172, 174–194]

Method*	**Type**	**Property**	**Range** α (mm^2/s) λ ($W/(m\,K)$)	**Material**
LFA (NTR)	Transient	α_t	0.01–2000	Solids
LIT	Transient	$\alpha_\parallel, \alpha_\perp, \alpha_t$	$\approx$ 0.1–100	Solids
HST	Transient	$\alpha_\parallel, \alpha_\perp, \alpha_t$	$\approx$ 0.1–100	Solids
GHP	Steady-state	λ_t	0.003–2	Solids
HFM	Steady-state	λ_t	0.002–2	Solids

*Methods: LFA: Laser/Xenon Flash Analysis; NTR: Nano-Thermoreflectance; LIT: Lock-in Thermography; HST: Heat-Spot Thermography; GHP: Guarded Hot Plate; HFM: Heat Flow Meter.

HST was selected as the primary experimental technique because it enables spatially resolved analysis of in-plane thermal diffusion following localized optical excitation. By applying a Gaussian-shaped laser heat source and recording the resulting spatiotemporal surface temperature field, the method allows the indirect evaluation of thermal diffusion behavior along arbitrary in-plane directions without requiring prior knowledge of material symmetry or fiber orientation.

The technique is inherently non-destructive and contact-free, relying solely on optical excitation and infrared thermographic detection. Sample preparation is minimal, and the measurable lateral dimensions are not constrained by the method itself but by the optical field of view and excitation positioning, enabling

application to specimens ranging from laboratory-scale coupons to large structural components.

A overview of the presented techniques is provided in Table 5.1, covering the properties measured, the measurement range, the appropriate material classes, and the potential ability to resolve anisotropy.

5.1.4 Thermography

Infrared thermography is based on the measurement of thermal radiation emitted by matter as a consequence of its temperature. As emphasized by Maldague [41], an infrared camera is fundamentally not a thermometer but a radiometer, it measures radiance within a given spectral band, from which a temperature can only be inferred under additional assumptions.

Any body at a temperature above absolute zero emits electromagnetic radiation with a spectral distribution governed by Planck's law. For an ideal blackbody, the spectral radiance is given by [41]

$$N_{\mathrm{bb}}(\lambda, T) = \frac{2hc^2}{\lambda^5} \frac{1}{\exp\left(\frac{hc}{\lambda k_{\mathrm{B}} T}\right) - 1}, \tag{5.6}$$

where h is Planck's constant, c the speed of light, k_{B} the Boltzmann constant, λ the wavelength and T the absolute temperature.

Real materials deviate from blackbody behavior and are therefore characterized by an emissivity ε, defined as the ratio of the emitted radiance to that of a blackbody at the same temperature. More generally, emissivity is not a constant but depends on wavelength, temperature, surface condition, and viewing direction. This leads to a specific object radiance [41]

$$N_{\mathrm{obj}}(\lambda, T, \theta) = \varepsilon N_{\mathrm{bb}} \quad \textit{with} \quad \varepsilon = \varepsilon(\lambda, T, \theta), \tag{5.7}$$

where θ denotes the observation angle.

Infrared thermography exploits the temperature dependence of thermal radiation by measuring radiance within a finite spectral band and converting it into an apparent surface temperature. In the present work, long-wave infrared (LWIR) thermography is used, with a spectral sensitivity of approximately 7.5–14 µm, which is well suited for near-ambient temperatures.

For real surfaces, the camera detected radiance results from a superposition of emitted, reflected, and transmitted contributions, governed by the surface emissivity ε, the reflectance $\rho = (1-\varepsilon)$, and the transmittance τ of the intervening medium.

Consequently, the radiance received by the camera can be schematically expressed as [41]

$$N_{\mathrm{cam}} = \tau_{\mathrm{atm}} \left[\varepsilon N_{\mathrm{bb}} + (1-\varepsilon) N_{\mathrm{env}}\right] + (1-\tau_{\mathrm{atm}}) N_{\mathrm{atm}}, \tag{5.8}$$

where N_{obj} denotes the radiance of the object, N_{env} represents the radiance originating from the surrounding environment and reflected by the surface of the object, and N_{atm} accounts for atmospheric self-emission along the optical path. The factor τ_{atm} describes the atmospheric transmittance between the object and the camera.

As a consequence, the temperature reported by an infrared camera represents an apparent temperature that coincides with the true surface temperature only if the emissivity, environmental reflections, and atmospheric effects are accurately known and controlled. These dependencies impose a fundamental limitation on absolute temperature measurements by infrared thermography. In experimental practice, uncertainties due to spatially varying emissivity are commonly reduced by applying thin, high-emissivity surface coatings (e.g. graphite), which establish a uniform radiative boundary condition with low influence on in-plane heat diffusion [99, 195].

For transient thermographic experiments, additional uncertainty arises from detector noise and temporal drift. In Heat-Spot Thermography, this limitation is addressed by focusing on relative temperature fields and their spatiotemporal evolution rather than on absolute temperature values. This approach substantially relaxes calibration requirements while retaining full sensitivity to thermal diffusivity and anisotropy.

5.1.5 HST: Governing Equations and General Form

Although HST, as described in Section 5.1.2, has long been used to characterize thermal diffusivity [51, 52, 118], ambiguities have persisted, especially for anisotropic media, regarding what directional quantity is actually measured and how it should be reconstructed from transient temperature fields [176, 196]. The following chapters therefore aim to provide a clear and systematic interpretation

of the underlying physical quantities and their extraction from experimental data.

HST can be formulated as a transient, anisotropic heat-conduction problem in which a localized optical excitation deposits energy in the specimen and the ensuing spatiotemporal temperature field is recorded at the surface. In its most general theoretical form, the method rests on a constitutive relation for anisotropic conduction, local energy conservation, and the resulting transient heat equation. For pulsed or short-time excitation, the temperature field can be expressed compactly using the Green's function of the anisotropic diffusion operator, which provides a direct link between the excitation and the observed temperature evolution.

Fourier's law

In anisotropic media, the conductive heat flux $\mathbf{q}$ is related to the temperature gradient by Fourier's law [197] with a second-order thermal conductivity tensor $\boldsymbol{K}$ [15, 198]:

$$\mathbf{q}(\mathbf{x}, t) = -\boldsymbol{K}\,\nabla T(\mathbf{x}, t). \tag{5.9}$$

The tensor $\boldsymbol{K}$ is symmetric and positive definite for physically admissible materials, ensuring non-negative dissipation and well-posed diffusion.

First Law of Thermodynamics

Local conservation of energy yields the balance between the rate of change of internal energy, the divergence of the heat flux, and volumetric heat sources. Introducing the volumetric heat capacity $C = \rho c_p$ and a volumetric source term $s(\mathbf{x}, t)$ gives [15]

$$C\,\frac{\partial T(\mathbf{x}, t)}{\partial t} = -\nabla\cdot\,\mathbf{q}(\mathbf{x}, t) + s(\mathbf{x}, t). \tag{5.10}$$

In HST, $s(\mathbf{x}, t)$ represents the effective energy deposition associated with laser absorption (often modeled as a temporally short input for pulsed excitation or as a prescribed temporal profile for continuous excitation).

Transient Heat Equation

Combining Equations (5.9) and (5.10) yields the anisotropic transient heat equation [15]

$$C\,\frac{\partial T(\mathbf{x},t)}{\partial t} = \nabla\cdot\big(\boldsymbol{K}\,\nabla T(\mathbf{x},t)\big) + s(\mathbf{x},t). \tag{5.11}$$

It is convenient to introduce the thermal diffusivity tensor

$$\mathbf{D} = \frac{\boldsymbol{K}}{C}, \tag{5.12}$$

so that the governing operator is expressed in terms of $\mathbf{D}$ when C is spatially uniform. In the idealized infinite-medium limit and in the absence of boundaries, the evolution of T is then determined by the anisotropic diffusion operator associated with $\mathbf{D}$.

Green's Function – Solution of the Heat Equation

For an instantaneous point-like energy input Q deposited at $\mathbf{x} = \mathbf{0}$ and $t = 0$ (i.e., $s(\mathbf{x},t) = Q\,\delta(\mathbf{x})\,\delta(t)$), the temperature field in an unbounded n-dimensional anisotropic medium admits a closed-form Green's-function representation. The resulting fundamental solution is [199]

$$T(\mathbf{x},t) = \frac{Q}{C}\,\frac{1}{(4\pi t)^{n/2}\sqrt{\det\mathbf{D}}}\,\exp\!\left[-\frac{\mathbf{x}^{\top}\mathbf{D}^{-1}\mathbf{x}}{4t}\right], \qquad t>0. \tag{5.13}$$

Equation (5.13) shows explicitly that material anisotropy affects both the spatial decay and the amplitude of the temperature field: the directional spreading of heat is governed by the quadratic form $\mathbf{x}^{\top}\mathbf{D}^{-1}\mathbf{x}$ in the exponential term, while the normalization factor $\sqrt{\det\mathbf{D}}$ controls the overall amplitude of the response.

Principal directions and isotropic limit

Let $\mathbf{D}$ be diagonalizable with orthonormal eigenvectors and eigenvalues $\alpha_i > 0$, such that $\mathbf{D} = \mathbf{R}\,\mathrm{diag}(\alpha_1,\dots,\alpha_n)\,\mathbf{R}^{\top}$. In the principal coordinate system $\mathbf{x}' = \mathbf{R}^{\top}\mathbf{x}$, the exponent in Equation (5.13) separates into a sum of directional contributions,

$$\mathbf{x}^{\top}\mathbf{D}^{-1}\mathbf{x} = \sum_{i=1}^{n}\frac{x_i'^{\,2}}{\alpha_i},$$

so that diffusion proceeds with direction-dependent characteristic lengths $\sim \sqrt{\alpha_i t}$ along the principal axes. In the isotropic limit, $\mathbf{D} = \alpha\,\mathbf{I}$, Equation (5.13) reduces to the standard isotropic Green's function [15, 199],

$$T(\mathbf{x}, t) = \frac{Q}{C}\,\frac{1}{(4\pi\alpha t)^{n/2}}\,\exp\!\left(-\frac{|\mathbf{x}|^2}{4\alpha t}\right), \qquad t > 0. \tag{5.14}$$

5.1.6 HST: Specialized 2D Orthotropic Formulation

This subsection specializes the general HST formulation in Section 5.1.5 to the most relevant case of in-plane heat diffusion in a two-dimensional orthotropic medium, representative for unidirectional fiber-reinforced composites. The principal material axes are assumed to be aligned with the Cartesian coordinates (x, y). The in-plane thermal diffusivity and conductivity tensors are therefore diagonal and given by

$$\mathbf{D} = \mathrm{diag}(\alpha_x, \alpha_y), \qquad \boldsymbol{K} = \mathrm{diag}(\lambda_x, \lambda_y), \qquad \boldsymbol{K} = C\,\mathbf{D}, \tag{5.15}$$

with volumetric heat capacity $C = \rho c_p$.

Transient Heat Equation and Green's-Function Solution

Starting from Fourier's law (5.9) and the local energy balance (5.10), the general transient heat equation (5.11) reduces, for spatially uniform $\mathbf{D}$ and an unbounded in-plane domain, to the orthotropic diffusion equation [199]

$$\frac{\partial T(x,y,t)}{\partial t} = \nabla\cdot\big(\mathbf{D}\,\nabla T(x,y,t)\big) = \alpha_x\,\frac{\partial^2 T}{\partial x^2} + \alpha_y\,\frac{\partial^2 T}{\partial y^2}, \qquad (x,y)\in\mathbb{R}^2,\ t>0. \tag{5.16}$$

This form highlights that the spreading rates along x and y are governed by the principal in-plane diffusivities α_x and α_y.

For an instantaneous point-like energy input Q at $(x, y) = (0, 0)$ and $t = 0$, the fundamental solution of Equation (5.16) follows directly as the $n = 2$ specialization of the general anisotropic Green's function (5.13) [199]:

$$T(x,y,t) = \frac{Q}{C}\,\frac{1}{4\pi t\,\sqrt{\alpha_x\alpha_y}}\,\exp\!\left[-\frac{x^2}{4\alpha_x t} - \frac{y^2}{4\alpha_y t}\right], \qquad t > 0. \tag{5.17}$$

The temperature field remains Gaussian in space, while its widths evolve anisotropically according to the principal diffusivities.

Isotherms

Isotherms of Equation (5.17) are obtained by fixing a temperature fraction $f \in (0, 1)$ relative to the peak value, i.e. $T = f\,T(0, 0, t)$. This yields

$$\frac{x^2}{4\alpha_x t} + \frac{y^2}{4\alpha_y t} = c, \qquad c = -\ln f. \tag{5.18}$$

Contours are therefore ellipses with time-dependent semi-axes

$$a(t) = \sqrt{4c\,\alpha_x t}, \qquad b(t) = \sqrt{4c\,\alpha_y t}. \tag{5.19}$$

A schematic illustration for an orthotropic material with anisotropy factor $\alpha_x/\alpha_y = 10$ is provided in Figure 5.6a.

Heat Flux and Temperature Gradients

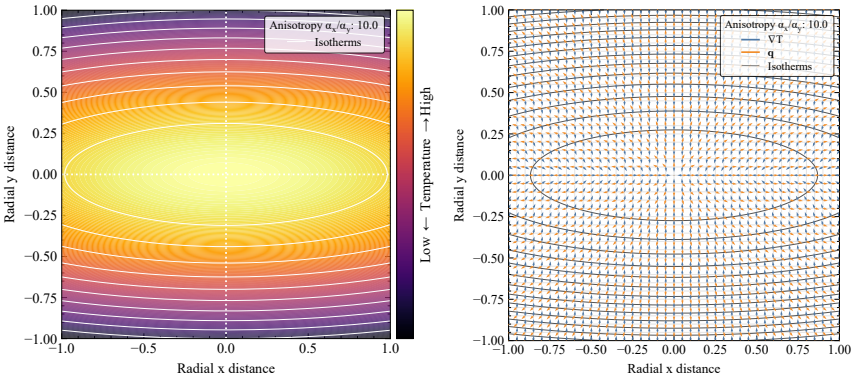
Fourier's law (5.9) implies that $\mathbf{q} = -\boldsymbol{K}\nabla T$. For orthotropic media, $\mathbf{q}$ and ∇T are generally not collinear, except when the gradient is aligned with a principal axis. Consequently, off-axis diffusion exhibits direction-dependent skew between heat-flux and temperature-gradient vectors. A schematic visualization of $\mathbf{q}$ and ∇T for $\alpha_x/\alpha_y = 10$ is shown in Figure 5.6b. [176]

Principal Thermal Diffusivities

Two evaluation routes are considered to estimate the principal in-plane diffusivities.

(i) From Gaussian profile widening (Variant 1) Along the principal axes, Equation (5.17) reduces to one-dimensional Gaussian profiles [16],

$$T(x, 0, t) \propto \exp\left(-\frac{x^2}{4\alpha_x t}\right), \qquad T(0, y, t) \propto \exp\left(-\frac{y^2}{4\alpha_y t}\right). \tag{5.20}$$



(a) Isotherms after laser-spot heating of an orthotropic material.

(b) Heat flux gradients and temperature gradients.

Figure 5.6: Schematic in-plane representation of isotherms, heat flux, and temperature gradients after laser-spot heating of an orthotropic material.

Defining the corresponding squared width parameters yields

$$b_x^2(t) = 4\alpha_x t, \qquad b_y^2(t) = 4\alpha_y t, \tag{5.21}$$

and therefore

$$\alpha_x = \frac{1}{4}\frac{db_x^2}{dt}, \qquad \alpha_y = \frac{1}{4}\frac{db_y^2}{dt}. \tag{5.22}$$

(ii) From isotherm growth over time (Variant 2) Selecting a fixed fraction $f \in (0,1)$, and thus a fixed $c = -\ln f$ in Equation (5.18), the squared semi-axes follow linear growth laws,

$$a^2(t) = 4c\,\alpha_x\,t + a_0^2, \qquad b^2(t) = 4c\,\alpha_y\,t + b_0^2, \tag{5.23}$$

where a_0^2 and b_0^2 are offset parameters, capturing the combined influence of non-ideal excitation and measurement effects (e.g., finite source size and duration). The principal diffusivities are then obtained from the slopes,

$$\alpha_x = \frac{1}{4c}\frac{da^2}{dt}, \qquad \alpha_y = \frac{1}{4c}\frac{db^2}{dt}. \tag{5.24}$$

Directional Properties

Let $\mathbf{n}(\theta) = (\cos\theta, \sin\theta)^\top$ denote a unit direction at angle θ with respect to the x-axis.

(i) Directional resistivity to diffusion In practical photothermal measurements with prescribed surface heat flux, the experimentally accessible directional metric is naturally associated with the inverse diffusivity tensor $\mathbf{D}^{-1}$, motivating the definition of the directional resistivity to diffusion r_θ [176, 200]:

$$r_\theta = \mathbf{n}^\top \mathbf{D}^{-1} \mathbf{n} = \frac{\cos^2\theta}{\alpha_x} + \frac{\sin^2\theta}{\alpha_y} \neq \frac{1}{\alpha_\theta}. \tag{5.25}$$

Equivalently, one may write the inverse representation

$$\frac{1}{r_\theta} = \frac{\alpha_x \alpha_y}{\alpha_x \sin^2\theta + \alpha_y \cos^2\theta}. \tag{5.26}$$

Here $r_x = 1/\alpha_x$ and $r_y = 1/\alpha_y$ are the principal resistivities. The inequality in Equation (5.25) emphasizes that equal-resistivity and equal-diffusivity contours coincide only along the principal axes.

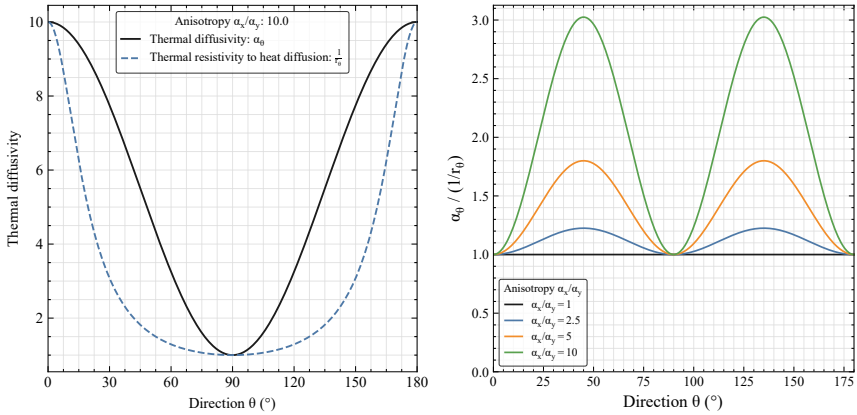
(ii) Directional thermal diffusivity The directional thermal diffusivity is given by [176, 200]

$$\alpha_\theta = \mathbf{n}^\top \mathbf{D} \mathbf{n} = \alpha_x \cos^2\theta + \alpha_y \sin^2\theta \neq \frac{1}{r_\theta}. \tag{5.27}$$

(iii) Directional thermal conductivity With $\lambda_i = C\,\alpha_i$ $(i = x, y)$, the directional conductivity follows as

$$\lambda_\theta = \lambda_x \cos^2\theta + \lambda_y \sin^2\theta = C\,\alpha_\theta = C\,(\alpha_x \cos^2\theta + \alpha_y \sin^2\theta). \tag{5.28}$$

Equations (5.25)–(5.28) extend the principal values to arbitrary in-plane directions.



(a) Fixed anisotropy ratio $\alpha_x/\alpha_y = 10$. **(b)** Varying anisotropy ratios.

Figure 5.7: Schematic directional dependence of α_θ and $1/r_\theta$.

5.1.7 HST: Specialized 2D Isotropic Formulation

This subsection considers the isotropic limit of the general HST formulation presented in Section 5.1.5. For isotropic materials, such as polymer matrices, the thermal diffusivity is identical in all spatial directions,

$$\alpha_x = \alpha_y = \alpha, \tag{5.29}$$

and the diffusivity tensor reduces to

$$\mathbf{D} = \alpha\,\mathbf{I}, \tag{5.30}$$

where $\mathbf{I}$ denotes the identity matrix.

Transient Heat Equation and Green's-Function Solution

With $\mathbf{D} = \alpha\mathbf{I}$, the general transient heat equation (5.11) simplifies to the isotropic diffusion equation in two dimensions,

$$\frac{\partial T(\mathbf{x},t)}{\partial t} = \alpha\,\nabla^2 T(\mathbf{x},t), \qquad \mathbf{x}\in\mathbb{R}^2,\ t>0. \tag{5.31}$$

For an instantaneous point-like energy input Q applied at the origin, the corresponding Green's-function solution follows directly as the $n = 2$ isotropic specialization of Equation (5.13) [199]:

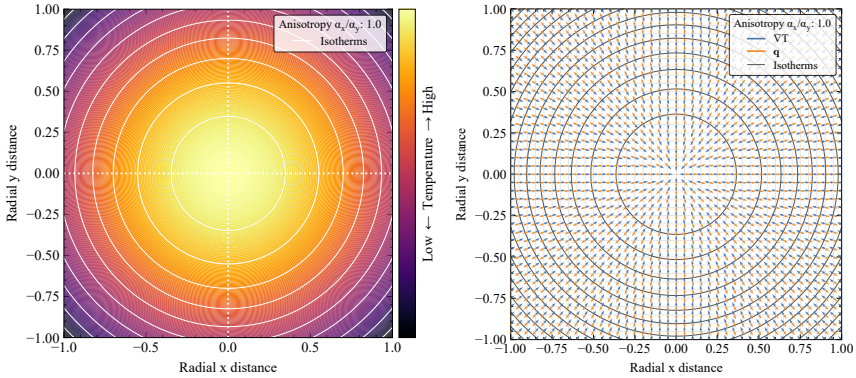
$$T(r,t) = \frac{Q}{C}\,\frac{1}{4\pi\alpha t}\exp\left(-\frac{r^2}{4\alpha t}\right), \qquad r = \sqrt{x^2+y^2},\ t > 0. \tag{5.32}$$

Isotherms

The temperature field is radially symmetric, and all isotherms are circular. Fixing a relative temperature level $T/T(0,0,t) = f \in (0,1)$ yields

$$r_f^2(t) = 4\alpha t\, c, \qquad c = -\ln f, \tag{5.33}$$

demonstrating that isotherm radii grow diffusively with time. A schematic representation of the resulting isotherms is shown in Figure 5.8a.



(a) Isotherms after laser-spot heating of an isotropic material

(b) Heat flux gradients and temperature gradients.

Figure 5.8: Schematic in-plane representation of isotherms, heat flux, and temperature gradients after laser-spot heating of an isotropic material.

Heat Flux and Temperature Gradients

For an isotropic material, the thermal conductivity tensor reduces to a scalar multiple of the identity, $\boldsymbol{K} = \lambda\,\mathbf{I}$, such that Fourier's law $\mathbf{q} = -\boldsymbol{K}\nabla T$ implies

strict collinearity between the heat-flux vector $\mathbf{q}$ and the temperature gradient ∇T for all directions. Consequently, heat propagation and temperature decay are directionally invariant, and no angular dependence or skew between $\mathbf{q}$ and ∇T arises. This behavior contrasts fundamentally with the orthotropic case, where anisotropy leads to a directional misalignment between heat flux and temperature gradient except along principal material axes, as discussed in Section 5.1.6. A schematic visualization of $\mathbf{q}$ and ∇T for $\alpha_x/\alpha_y = 1$ is shown in Figure 5.8b.

Determination of Thermal Diffusivity

The scalar thermal diffusivity can be extracted from the spatiotemporal temperature field using two equivalent evaluation strategies.

(i) From Gaussian profile widening (Variant 1) Along any radial direction, for example the x-axis, Equation (5.32) reduces to a one-dimensional Gaussian profile [16],

$$T(x, 0, t) \propto \exp\left(-\frac{x^2}{4\alpha t}\right). \tag{5.34}$$

Defining the squared width parameter $b^2(t) = 4\alpha t$ yields the equivalent relation

$$\alpha = \frac{1}{4}\,\frac{db^2}{dt}. \tag{5.35}$$

(ii) From isotherm growth over time (Variant 2) Selecting a fixed isothermal fraction $f \in (0, 1)$, and thus a fixed $c = -\ln f$ in Equation (5.33), the squared radius of the corresponding isotherm follows a linear growth law,

$$r_f^2(t) = 4c\,\alpha\,t + r_0^2, \tag{5.36}$$

where r_0^2 is an offset parameter accounting for deviations from the ideal point-source and imaging assumptions, such as finite excitation size and duration. The thermal diffusivity is then obtained from the slope of the linear relation,

$$\alpha = \frac{1}{4c}\,\frac{dr_f^2}{dt}. \tag{5.37}$$

Directional Properties

For an isotropic material with $\mathbf{D} = \alpha\mathbf{I}$, all directional thermal properties are invariant with respect to the orientation angle θ:

$$\alpha_\theta = \alpha, \qquad r_\theta = \frac{1}{\alpha}, \qquad \lambda_\theta = C\,\alpha. \tag{5.38}$$

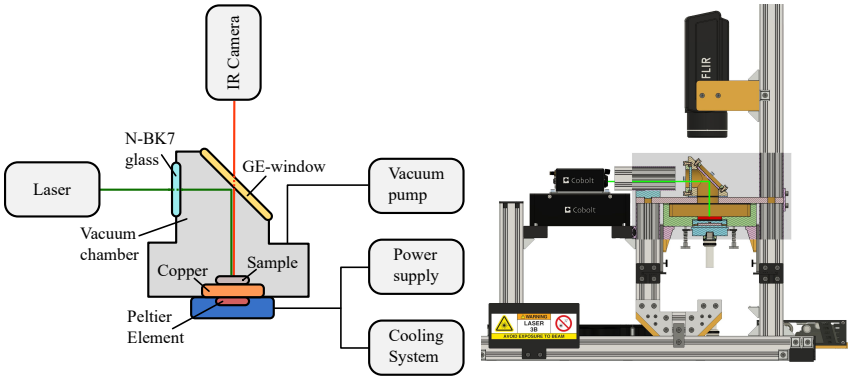
5.2 Test Setup

A schematic and CAD-based overview of the experimental setup is shown in Figure 5.9a. The complete measurement system, including the optical layout, thermal excitation concept, temperature control, data acquisition, and evaluation software, was designed and implemented in-house to specifically meet the requirements of spatially resolved thermal anisotropy measurements. Thermal excitation was provided by a diode-pumped solid-state laser operating in continuous-wave mode (Cobolt 06-DPL, HÜBNER Photonics) with a maximum output power of 400 mW, a wavelength of 532 nm, and a beam diameter of 700 µm. The laser exhibits a near-Gaussian intensity distribution with a fundamental transverse mode (TEM_{00}) and a beam quality factor of $M^2 \leq 1.1$. All measurements were conducted with an effective heating power of 200 mW with a heating duration of 3 s. Because of the near-ideal Gaussian beam profile, no additional optical components were required to focus the laser onto the sample surface. The beam redirection was achieved using a transmissive NBK-7 glass element in combination with a reflective GE window.

The specimens were placed directly onto a highly conductive copper plate without the use of an additional thermal coupling medium. Homogeneous heating conditions at the sample surface were verified prior to laser excitation by acquiring infrared images. The temperature control of the copper plate was performed using a Peltier element (TEC1-12706), allowing regulation within a temperature range of 10 °C to 80 °C. The resulting transient surface temperature field was recorded using a Teledyne FLIR A645 infrared camera, maximum resolution 640 × 480 pixels (50 Hz), maximum frame rate 200 Hz) (160 × 480 pixels). All measurements were performed with a reduced spatial resolution of 101 × 101 pixels at an approximate frame rate of 100 Hz.

To minimize heat losses due to conduction and convection, all experiments were conducted under vacuum conditions at pressures below 10 Pa. Under these con-

ditions, radiative heat transfer remains unaffected and constitutes the dominant heat loss mechanism. Image acquisition and data analysis were performed using a custom Python 3.10 [201] application that incorporates Matplotlib [202] and SciPy [203], with a graphical user interface implemented using NiceGUI [204]. All temperature fields are presented as relative temperature changes ΔT, obtained by subtracting a reference image acquired under ambient conditions prior to laser heating from each subsequent thermogram. Since the analysis relies exclusively on relative temperature variations, this procedure does not affect the interpretation of the results. For statistical robustness, five independent measurements were performed for each experimental configuration, defined by the combination of sample and reference temperature.



(a) Schematic overview of the heat-spot-thermography setup.

(b) CAD-based overview of the heat-spot-thermography setup.

Figure 5.9: Schematic and CAD illustrations of the experimental setup for anisotropic thermal measurements.

5.3 Analysis Methodology

In the present evaluation framework, the theoretical foundation of HST for orthotropic materials, as developed in Section 5.1.6, is adopted as the basis for the interpretation of the data. Building on this formulation, the evaluation routine is optimized by directly determining the directional resistance to diffusion, r_θ, from the measured temperature fields. This is achieved through two complementary and robust approaches: (i) Gaussian fitting and (ii) isothermal fitting of the temperature profiles. The resulting principal values of r_θ provide a stable quantity

from which the directional thermal diffusivity α_θ of the composite is subsequently calculated. Finally, an analytical model based on an adapted rule of mixtures is introduced to relate the measured composite diffusivities to the effective thermal diffusivities of the individual constituents, namely fiber α_f and matrix α_m.

The thermal measurement and processing workflow proceeds as shown in Figure B.4.

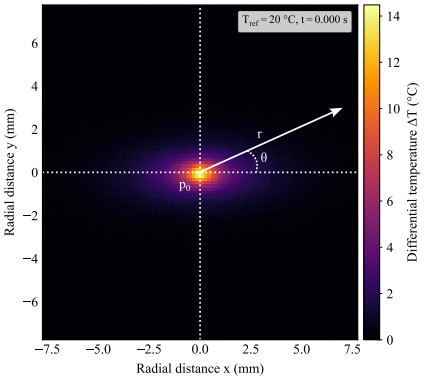
For illustrative purposes, the figures presented in this section are based on experimental data obtained from a representative 120 gsm UD-CFRP specimen (UD-120). Figures 5.10a and 5.10c show the infrared images at the start and the end of the cooling process after laser spot excitation in Cartesian coordinate representation, defining the relevant time frame for evaluation. For a more convenient representation of the direction-dependent evaluation, the infrared data are first transformed into a dedicated polar-coordinate representation.

Polar Thermogram Representation

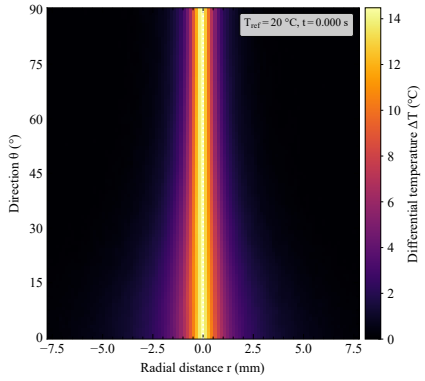
The full-length symmetric polar coordinate representation, as seen in Figures 5.10b and 5.10d, is a coordinate transformation that maps the temperature distribution of the two-dimensional IR image $I(x, y)$ from Cartesian to polar coordinates. This transformation is centered on a reference point $p_0 = (x_0, y_0)$ and evaluates the temperature values as a function of the radial distance r and the polar angle θ which corresponds to the direction of the sample relative to the direction of the fiber ($0^\circ : fiber_\parallel$, $90^\circ : fiber_\perp$). First, a standard polar warp $W(\theta, r)$ is calculated with θ uniformly sampled between $0^\circ - 360^\circ$ and $r \in [0, r_1]$, with r_1 as the outer radius of the sample. The warp evaluates the Cartesian image at polar locations by interpolation.

$$W(\theta, r) = I(x_0 + r\cos\theta,\ y_0 + r\sin\theta), \qquad \theta \in [0, 2\pi),\ r \in [0, r_1]. \tag{5.39}$$

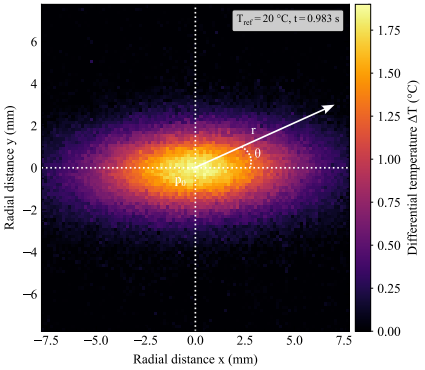
Then a full-length radial extension is constructed by pairing opposite directions and assigning them to negative radii. Concretely, the directions $\theta \in [\pi, 2\pi)$ are mapped to $\theta - \pi \in [0, \pi)$ with the radius sign flipped; this yields a representation on $r \in [-r_1, r_1]$ while keeping only $\theta \in [0, \pi]$:



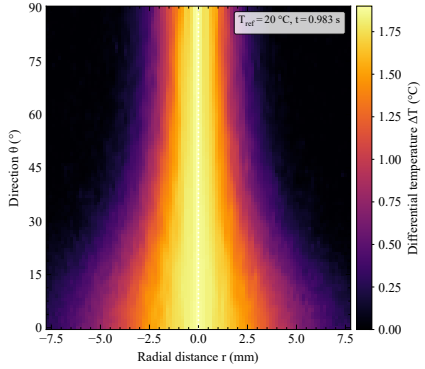
(a) Cooling start: conventional Cartesian coordinate representation.



(b) Cooling start: full-length symmetric polar coordinate representation.



(c) Cooling end: conventional Cartesian coordinate representation.



(d) Cooling end: full-length symmetric polar coordinate representation.

Figure 5.10: IR images at the start (top row) and end (bottom row) of the cooling process after laser spot heating of a 120 gsm unidirectional CFRP laminate (UD-120).

$$P(\theta, r) = \begin{cases} W(\theta, r), & r \geq 0,\ \theta \in [0, \pi] \\ W(\theta + \pi, -r), & r < 0,\ \theta \in [0, \pi] \end{cases} \tag{5.40}$$

Axial symmetry, which implies an orthothrope material, is imposed with respect to the $\theta = \frac{\pi}{2}$ axis by averaging each ray with its mirror $\pi - \theta$. Because this makes the two halves redundant, we retain only the first quadrant.

$$S(\theta, r) = \tfrac{1}{2}\big[P(\theta, r) + P(\pi - \theta, r)\big], \qquad \theta \in [0, \tfrac{\pi}{2}],\ r \in [-r_1, r_1]. \tag{5.41}$$

This procedure yields a compact, symmetry-aware polar representation that is well suited for analyzing direction-dependent temperature profiles line-by-line, while avoiding redundant data at opposite directions and substantially reducing computational effort.

Directional Diffusivity and Resistivity

A central point for HST of anisotropic material is that the boundary condition is heat-flux prescribed, as shown in Figure 5.6b. As a consequence, the angular dependence probed by a circular spot follows the inverse-diffusivity form $r_\theta = \mathbf{n}^\top \mathbf{D}^{-1} \mathbf{n}$, and the measured directional quantity is its reciprocal $1/r_\theta$ rather than the arithmetic projection $\alpha_\theta = \mathbf{n}^\top \mathbf{D}\, \mathbf{n}$, except on the principal axes where both coincide. Previous works [200, 205] precisely highlight this distinction and its practical impact on data interpretation in anisotropic materials.

In this section, the formulation relevant for determining in-plane directional thermal transport properties from laser-spot heating experiments on orthotropic materials is summarized. The description is expressed in terms of the thermal resistivity tensor $\mathbf{R}$, which provides a natural framework to represent anisotropic heat diffusion and to link experimental observables with the parameters of the underlying material.

(i) Anisotropic heat equation in principal axes For an orthotropic material with in-plane principal axes $\mathbf{x} = (x, y)^T$ and principal diffusivities $\alpha_x = \alpha_\parallel$ and $\alpha_y = \alpha_\perp$, the tensors

$$\mathbf{D} = \begin{pmatrix} \alpha_x & 0 \\ 0 & \alpha_y \end{pmatrix}, \qquad \mathbf{R} = \mathbf{D}^{-1} = \begin{pmatrix} \alpha_x^{-1} & 0 \\ 0 & \alpha_y^{-1} \end{pmatrix}, \tag{5.42}$$

govern transient heat conduction as described by the anisotropic heat diffusion equation (5.16). The corresponding Green's function for an instantaneous point energy input in an unbounded medium with respect to $\mathbf{R}$ can be derived from Equation (5.13) as

$$T(\mathbf{x}, t) = \frac{Q}{C} \frac{\sqrt{\det \mathbf{R}}}{4\pi t} \exp\left[-\frac{1}{4t} \mathbf{x}^\top \mathbf{R} \mathbf{x} \right], \qquad t > 0, \tag{5.43}$$

(ii) Directional resistivity in polar form Introducing polar coordinates $\mathbf{x} = (x, y)^\top = r(\cos\theta, \sin\theta)^\top$ and the corresponding unit direction vector

$$\mathbf{n}(\theta) = \begin{pmatrix} \cos\theta \\ \sin\theta \end{pmatrix}, \tag{5.44}$$

the quadratic form appearing in the Green's function (5.43) can be written as

$$\mathbf{x}^\top \mathbf{R} \mathbf{x} = r^2 \, \mathbf{n}^\top \mathbf{R} \mathbf{n} = r^2 \, r_\theta, \tag{5.45}$$

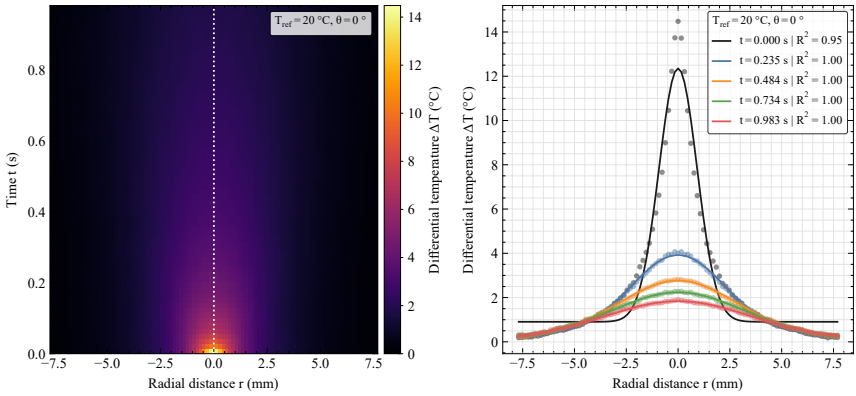
with the directional resistivity to diffusion r_θ as defined in Equation (5.25). The final temperature field in polar coordinates with respect to $\mathbf{R}$ thus becomes

$$T(r, \theta, t) = \frac{Q}{C} \frac{1}{4\pi t \sqrt{\alpha_x \alpha_y}} \exp\left[-\frac{r^2 r_\theta}{4t} \right]. \tag{5.46}$$

(iii-1) Radial Gaussian broadening (Variant 1) For any fixed direction θ, the polar Green's function in Equation (5.46) represents a one-dimensional Gaussian in the radial coordinate r. Up to an amplitude factor depending on t, its radial dependence can be written as

$$T(r, \theta, t) \propto \exp\left[-\frac{r^2}{b^2(t, \theta)} \right], \qquad b^2(t, \theta) = \frac{4t}{r_\theta}. \tag{5.47}$$

Experimentally, the radial temperature distribution $T(r, \theta, t)$ is evaluated as a function of time and fitted to the Gaussian form in Equation (5.47), yielding the temporal evolution of the squared Gaussian width $b^2(t, \theta)$. The progressive broadening of the temperature profile during the cooling phase is illustrated in Figure 5.11. Panel (a) shows the full-length symmetric polar representation of the infrared data at the representative direction $\theta = 0°$, while panel (b) depicts the corresponding Gaussian representation in accordance with Equation (5.47).



(a) Full-length symmetric polar coordinate representation.

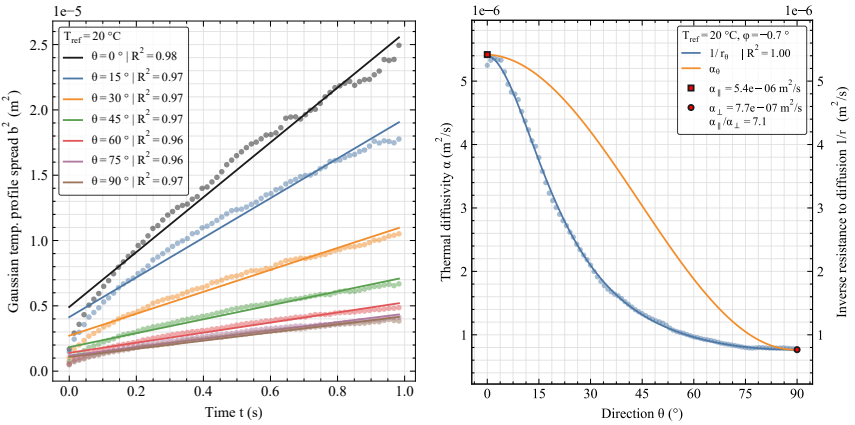
(b) Symmetric time dependent Gaussian fit representation.

Figure 5.11: Evolution of the temperature profile over time in fiber-direction ($0° : fiber_{\parallel}$) during cooling process of a 120 gsm unidirectional CFRP laminate (UD-120).

Equation (5.47) predicts a strictly linear evolution. Thus, the experimentally measured diffusive broadening slope provides direct access to the inverse directional resistivity to diffusion

$$\frac{1}{r_\theta} = \frac{1}{4}\frac{db^2}{dt}(\theta). \tag{5.48}$$

For anisotropic materials, the evaluation is performed independently for each in-plane direction θ, so that the inverse directional resistivity to diffusion is obtained as a directional quantity. This directional dependence is illustrated in Figure 5.12a. Owing to the in-plane orthotropic symmetry of UD-CFRP, the resulting directional properties are fully represented within a single quadrant and are therefore reported as quarter-plane plots, as shown in Figure 5.12b.



(a) Diffusive broadening. **(b)** Thermal diffusivity.

Figure 5.12: Directional diffusive broadening, inverse thermal resistivity and diffusivity of the Gaussian analytical model of a 120 gsm unidirectional CFRP laminate (UD-120).

(iii-2) Polar isotherm evolution (Variant 2) As an alternative to the Gaussian-profile analysis, the directional inverse resistivity $1/r_\theta$ may alternatively be obtained from the temporal growth of fixed-fraction isotherms, as detailed in Section B.3. Both approaches exploit the same underlying Green's function solution and yield similar angular dependences. In practice, Gaussian fitting is preferred due to its improved robustness against noise and its use of the full radial temperature profile, whereas isotherm-based methods rely on a single contour level.

(iv) Principal diffusivities and α_θ reconstruction Following the definition of the directional resistivity to diffusion in Equation (5.25), its inverse is given analytically by Equation (5.26). The experimentally accessible quantity $1/r_\theta$, obtained from the Gaussian broadening slope via Equation (5.48) (Variant 1), or Polar isotherm evolution via Equation (B.6) (Variant 2), is therefore fitted to Equation (5.26) to determine the principal in-plane thermal diffusivities α_x and α_y.

In the special cases where the evaluation direction coincides with a principal material axis, the principal diffusivities follow directly from Equation (5.25) as

$$\frac{1}{r_x} = \alpha_x, \qquad \frac{1}{r_y} = \alpha_y. \tag{5.49}$$

Once the principal values are known, the conventional directional thermal diffusivity is uniquely reconstructed using the tensorial definition Equation (5.27), as shown in Figure 5.12b. From these results, derived quantities such as the directional thermal conductivity can subsequently be calculated, as already shown in Equation (5.28).

Analytical Models

Analytical modeling of the anisotropic thermal diffusivity of unidirectional fiber-reinforced composites is based on established approaches that were originally developed for thermal conductivity in heterogeneous materials. Pietrak and Wisniewski [22] provide a comprehensive overview of these models, including their applicability and limitations for composite materials. In long fiber reinforced composites, effective thermal conductivity is primarily determined by intrinsic conductivities of the fibers and the matrix, the volume fraction of the fiber, and the degree of anisotropy introduced by the fiber orientation, while interfacial thermal resistance at the fiber-matrix boundary and microstructural characteristics (e.g. spatial heterogeneity, fiber waviness, misalignment, porosity, voids) remain critical factors controlling heat transfer.

To model the anisotropic in-plane thermal metric

$$\chi = \begin{cases} \alpha, & \text{(diffusivity domain)} \\ 1/r, & \text{(inverse resistivity domain)} \end{cases} \tag{5.50}$$

for unidirectional fiber reinforced composites, the following approach is proposed: The rule of mixtures (RoM) allows an estimation of material properties by weighting the contributions of matrix (m) and fibers (f) according to the fiber volume fraction φ_f. RoM-approaches have been used successfully to model the stiffness, heat capacity, mass density, and thermal conductivity of composite materials [206]. To capture directional and microstructural effects, a generalized power mean approach with a single shape parameter $-1 \leq n \leq 1$ is used [207].

$$\chi_{rom} = \left((1-\varphi_f)\cdot\chi_m^n + \varphi_f\cdot\chi_f^n\right)^{\frac{1}{n}} \tag{5.51}$$

This leads to the longitudinal thermal metric being represented by the arithmetic RoM, which corresponds to the fiber-parallel model by Voigt [66]. The transversal thermal metric is represented by the inverse RoM, which corresponds to the fiber-perpendicular model by Reuss [67]. The irregularity at $n \to 0$ is represented by a logarithmic mixture model by Simpkin and Lichtenecker [208, 209].

$$\chi_{rom} = \begin{cases} (1-\varphi_f)\cdot\chi_m + \varphi_f\cdot\chi_f, & n=+1 \quad \text{(Voigt [66])} \qquad (5.52) \\ \chi_m^{1-\varphi_f}\cdot\chi_f^{\varphi_f}, & n\to 0 \quad \text{(Simpkin [208])} \qquad (5.53) \\ \left(\dfrac{(1-\varphi_f)}{\chi_m} + \dfrac{\varphi_f}{\chi_f}\right)^{-1}, & n=-1 \quad \text{(Reuss [67])} \qquad (5.54) \end{cases}$$

Building on the RoM introduced above, we express the orientation dependence of the effective thermal metric $\chi_{\theta,rom}$ by the general directional laws according to Equations (5.26) and (5.27) with respect to the principal material directions of the unidirectional laminate. The Voigt model [66] is generally accurate for fiber-parallel properties, whereas the Reuss model [67] tends to underestimate transverse properties [210]. To consistently combine both principal values, the following formulation is proposed:

$$\frac{1}{r_{\theta,rom}} = \frac{\chi_{\parallel,rom}\chi_{\perp,rom}}{\chi_{\perp,rom}\cos^2\theta + \chi_{\parallel,rom}\sin^2\theta} \qquad (\chi = \frac{1}{r}) \tag{5.55}$$

$$\alpha_{\theta,rom} = \chi_{\parallel,rom}\cos^2\theta + \chi_{\perp,rom}\sin^2\theta \qquad (\chi = \alpha) \tag{5.56}$$

and

$$\chi_{\parallel,rom} = \chi_{rom}(n=1) \qquad = (1-\varphi_f)\,\chi_m \;+\; \varphi_f\,\chi_f, \tag{5.57}$$

$$\chi_{\perp,rom} = \chi_{rom}(n=n_\perp) \qquad = \left((1-\varphi_f)\,\chi_m^{n_\perp} \;+\; \varphi_f\,\chi_f^{n_\perp}\right)^{\frac{1}{n_\perp}} \tag{5.58}$$

Here, χ_m and χ_f denote the thermal metrics of the matrix and fiber, φ_f is the volume fraction of the fiber and $n_\perp$ defines the shape parameter for the

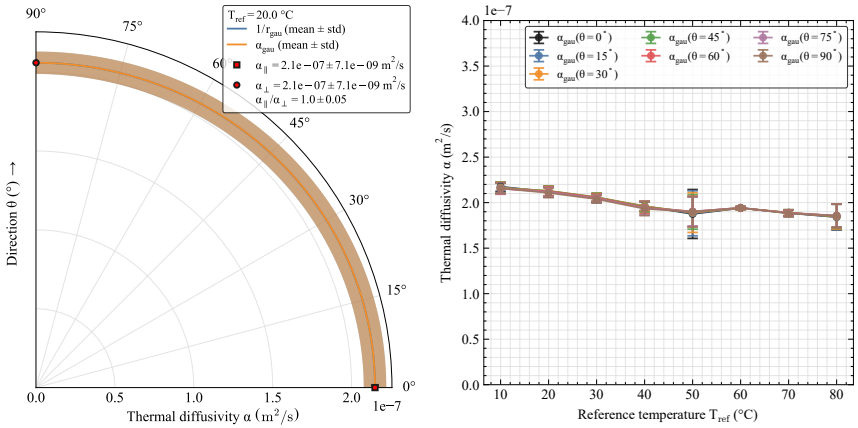
transverse direction. This compact formulation links the rules of mixture with general directional laws and allows a direct fit with the experimental data.

5.4 Results and Discussion

5.4.1 Thermal Measurements: Matrix and CFRP

The following section provides a detailed analysis and discussion of the results obtained from Gaussian distribution widening for the 120 gsm UD-CFRP (UD-120) and ThinPreg 402 neat matrix samples.

Figure 5.13a shows the thermal diffusivity of the ThinPreg 402 matrix at $T_{\mathrm{ref}} = 20 \pm 1\,^{\circ}\mathrm{C}$. As expected for an isotropic polymer, the diffusivity remains effectively constant regardless of the measurement direction. The nearly circular elliptical fit reproduces the experimental data with good accuracy, demonstrating the effectively homogeneous thermal transport behavior of the neat matrix in the absence of fiber reinforcement. The resulting anisotropy ratio $\alpha_{\parallel}/\alpha_{\perp} = 1.00 \pm 0.04$, confirms the isotropic in-plane diffusivity within experimental uncertainty.

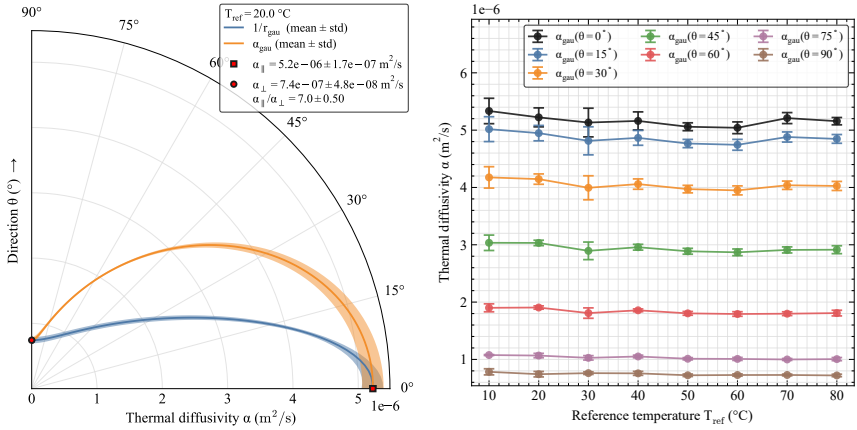


(a) Direction dependency. **(b)** Temperature dependency.

Figure 5.13: Direction and temperature-dependent thermal diffusivity of neat matrix ThinPreg 402.

Figure 5.14a shows the mean thermal diffusivity and corresponding standard deviation of the 120 gsm UD-CFRP at $T_{\mathrm{ref}} = 20 \pm 1,^{\circ}$ C. The material exhibits

the expected strong in-plane anisotropy, with maximal diffusivity along the fiber direction ($\theta = 0°$) and minimal values transversely ($\theta = 90°$). This directional contrast reflects the dominant heat-transport contribution of the carbon fibers. The resulting composite in-plane anisotropy ratio $\alpha_{\parallel}/\alpha_{\perp} = 7.00 \pm 0.50$ confirms pronounced anisotropic thermal behavior.



(a) Direction dependency. **(b)** Temperature dependency.

Figure 5.14: Direction and temperature-dependent thermal diffusivity of a 120 gsm unidirectional CFRP laminate (UD-120).

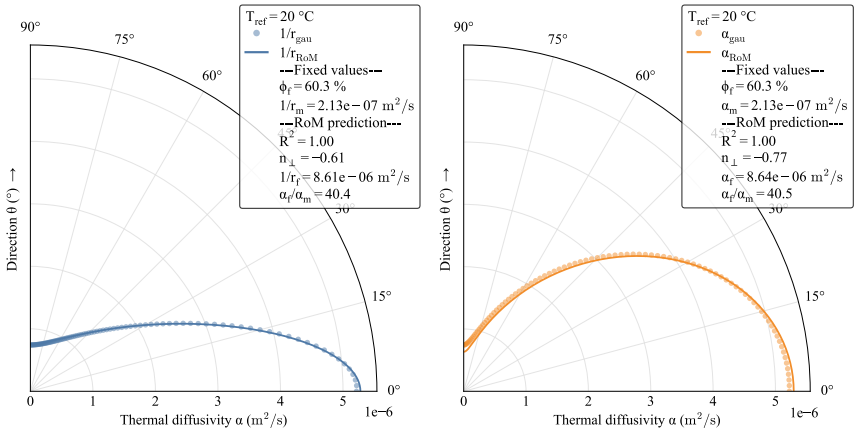
5.4.2 Analytical Model

By applying the rule-of-mixtures formulation in Equation (5.56), the directional thermal diffusivity profile of the UD-CFRP can be reproduced under the given material assumptions, as shown in Figure 5.15a. To avoid parameter degeneracy, the diffusivity of the matrix $\alpha_m = 0.21$ mm^2/s and the fiber volume fraction $\varphi_f = 60.3$ vol.% were fixed using independent measurements, as described in Section 3.2. The additional RoM parameter $n_{\perp}$ compensates for the underestimation of transverse transport inherent to the classical formulation of Reuss [67].

The analytical predictions show good agreement with the experimental data, yielding an ideal coefficient of determination. In the fiber-parallel direction, the analytical approximation matches the measurements within their statistical uncertainty and results in a fiber diffusivity of $\alpha_f = 8.64$ mm^2/s, reflecting the dominant role of carbon fibers in longitudinal heat transport. In contrast,

transverse heat transfer remains significantly lower due to interfacial and microstructural constraints. The resulting anisotropy ratio of the constituents $\alpha_f/\alpha_m = 40.5$ quantifies the strong intrinsic anisotropy.

A direct comparison of the two RoM formulations, one in thermal diffusivity space Figure 5.15a and one in inverse resistivity space Figure 5.15b, shows that both yield practically identical fiber properties. This confirms that the parameter $n_\perp$ provides the flexibility necessary to achieve consistent model performance in both thermal domains.



(a) RoM-model inverse thermal resistivity to diffusion $1/r_\theta$.

(b) RoM-model of the thermal diffusivity α_θ.

Figure 5.15: Analytical RoM-models to predict fiber metric χ_f for $1/r_\theta$ and α_θ of a 120 gsm unidirectional CFRP laminate (UD-120).

5.4.3 Temperature Dependency

Figures 5.13b and 5.14b depict the temperature dependence of the thermal diffusivity between 10 °C and 80 °C for the neat ThinPreg 402 matrix and the corresponding 120 gsm T700SC UD–CFRP composite (UD-120) at various orientations. Across this range, a slight decrease in thermal diffusivity is observed. Given that the glass transition temperature of the ThinPreg 402 matrix is 170 °C, no structural or phase-related changes in the matrix are expected in this temperature interval. Instead, the moderate decline in $\alpha(T)$ is consistent with the intrinsic thermophysical behavior of polymer-based systems: the specific

heat capacity c_p of the epoxy matrix increases markedly with temperature, while the thermal conductivity λ remains approximately constant or decreases slightly due to enhanced phonon–phonon scattering, and the density ρ changes only marginally. Because $\alpha = \lambda/(\rho c_p)$, these combined trends naturally result in a gradual reduction of the effective thermal diffusivity.

Table 5.2: Overview of the material properties and investigated thermal conductivities at $T_{\mathrm{ref}} = 20 \pm 1\,^{\circ}\mathrm{C}$.

Sample	$\boldsymbol{c_p}$ (J/gK)	$\boldsymbol{\rho}$ (g/cm^3)	$\boldsymbol{\alpha_{gau,\parallel}}$ (mm^2/s)	$\boldsymbol{\alpha_{gau,\perp}}$ (mm^2/s)	$\boldsymbol{\lambda_{gau,\parallel}}$ (W/mK)	$\boldsymbol{\lambda_{gau,\perp}}$ (W/mK)
HexPly M21	1.42	1.28	0.22	0.22	0.40	0.40
Thinpreg 402	1.54	1.21	0.21	0.21	0.39	0.39
UD-268	0.79	1.58	3.24	0.44	4.04	0.55
UD-120	0.90	1.55	5.20	0.74	7.25	1.03

5.4.4 Contextualization of the Measurement Results

To ensure comparability with data from the literature, the measured thermal diffusivities were converted to thermal conductivities using the density of the material ρ and the specific heat capacity c_p. These properties were determined independently, with the density measured via Archimedes' principle and the specific heat capacity obtained from differential scanning calorimetry (DSC). The corresponding thermal conductivity at the reference temperature T_{ref} was then calculated using Equation (5.38).

An overview of the material parameters and the resulting thermal conductivities is provided in Table 5.2. The material properties were experimentally determined or extracted from the manufacturer's datasheets [211, 212]. The literature values for the thermal diffusivity of CFRPs typically range from 2.4–3.4 mm^2/s in the fiber direction and 0.38–0.6 mm^2/s in the transverse direction [52, 178], while the thermal conductivity of neat epoxy matrices generally lies between 0.17 and 0.24 W/mK [213, 214].

The thermal transport values obtained are slightly higher than the values typically reported in the literature for neat epoxy resins and unidirectional CFRPs. This deviation is not unexpected, as the investigated matrix systems (ThinPreg 402 and HexPly M21) are high-quality aerospace-grade materials whose purity, low void content and optimized cure state can inherently lead to slightly increased

thermal transport. Moreover, the experimental configuration may contribute to elevated apparent diffusivities: early-time in-plane heat spreading is measured under minimal loss conditions, whereas residual through-thickness heat flow and thermal coupling to the copper base plate can further increase the effective in-plane response. Although the results remain physically consistent, additional comparative studies using complementary measurement techniques are required to establish a definitive quantitative alignment with the broader literature.

Table 5.3: Overview of RoM model results at $T_{\mathrm{ref}} = 20 \pm 1\,^{\circ}\mathrm{C}$ and literature values $\lambda_{f,ref}$ [215, 216].

Sample	$\boldsymbol{\varphi_f}$ (%)	$\boldsymbol{n_\perp}$ (–)	$\boldsymbol{\alpha_f/\alpha_m}$ (–)	$\boldsymbol{\alpha_{\mathrm{m},rom}}$ (mm^2/s)	$\boldsymbol{\alpha_{\mathrm{f,rom}}}$ (mm^2/s)	$\boldsymbol{\lambda_{\mathrm{f,rom}}}$ (W/mK)	$\boldsymbol{\lambda_{\mathrm{f,ref}}}$ (W/mK)
UD-268	56.6	−1.00	26.3	0.22	5.54	7.83	11.3
UD-120	60.3	−0.77	40.5	0.21	8.64	11.71	9.37–12.70

The fitted RoM parameters derived from the directional thermal diffusivity measurements are summarized in Table 5.3. The predicted fiber diffusivities show a clear material dependence, with $\alpha_{\mathrm{f,rom}} = 5.54\,\mathrm{mm}^2/\mathrm{s}$ for the T800S system (UD-268) and $\alpha_{\mathrm{f,rom}} = 8.64\,\mathrm{mm}^2/\mathrm{s}$ for the T700SC system (UD-120), reflecting the differences in intrinsic thermal transport associated with fiber grade and processing. When converted to thermal conductivity, the resulting values $\lambda_{\mathrm{f,rom}} = 7.83\,\mathrm{W/mK}$ and $\lambda_{\mathrm{f,rom}} = 11.71\,\mathrm{W/mK}$ fall within or close to the ranges reported by the manufacturer [215] and the recent work by Jang et al. [216], indicating general consistency between the predictions of the model and the established reference data.

The fitted transverse-shape parameter $n_\perp$ assumes values of -1 and -0.77, indicating that the transverse transport in the two laminates spans from the Reuss lower bound to a moderately enhanced conduction regime. The case $n_\perp = -1$ (ThickPly, UD-268) corresponds to the classical series-limit, yielding the lowest effective transverse conductivity and reflecting strong interfacial control along with a predominantly serial heat-flow pathway through fiber–matrix interfaces. In contrast, $n_\perp = -0.77$ (ThinPly, UD-120) increases the effective transverse conductivity above the Reuss limit, suggesting a reduced interfacial dominance, potentially arising from differences in fiber packing density, local alignment quality or resin-rich regions. Minor deviations from reference fiber conductivities are expected, as the model does not explicitly capture intra-fiber anisotropy or mesoscale heterogeneities. Nevertheless, the overall agreement demonstrates

that the extended RoM formulation reliably captures the essential features of directional heat transport in UD-CFRPs.

5.5 Conclusions

This chapter established a labor- and material-efficient Heat-Spot Thermography (HST) approach for direction-resolved in-plane thermal transport in CFRP laminates. In contrast to conventional one-directional techniques, HST infers anisotropy from a single localized excitation in a non-destructive, contact-free manner with minimal sample preparation.

To achieve reproducible analysis under controlled conditions, a dedicated measurement setup was developed and integrated into the software framework `TCAM`. The resulting workflow couples laser excitation, temperature control, synchronized infrared acquisition, automated evaluation, and standardized reporting. Controlled boundary conditions over $T_{\mathrm{ref}} \in [10, 80]\,^{\circ}\mathrm{C}$ and vacuum operation at $p < 10\,\mathrm{Pa}$ suppress convective and gas-conduction losses, leaving radiative exchange as the dominant heat loss mechanism. These controlled conditions improve comparability, while automated replicate measurements increase statistical robustness.

A key outcome is the physically consistent interpretation of HST under a prescribed heat-flux boundary condition: the circular heat spot probes the inverse-diffusivity projection so that the direction-resolved observable is $1/r_\theta$ rather than α_θ except on the principal material axes. Two consistent extraction routes for $1/r_\theta$ were established, based on Gaussian-profile broadening and isotherm evolution, allowing a choice between robustness and computational efficiency without changing the inferred angular dependence.

Measurements on neat polymers and unidirectional CFRP confirmed full reconstruction of the orthotropic in-plane diffusivity tensor $\left(\alpha_{\parallel}, \alpha_{\perp}\right)$ from a single specimen, with principal values and anisotropy ratios consistent with data from the literature. Furthermore, the generalized rule-of-mixtures formulation allows constituent properties to be derived from the measured thermal diffusivity.

Future work can reduce the laser heating duration toward an impulsive excitation to even better match analytical assumptions. In addition, the methodology could be extended to identify through-thickness diffusivity by implementing excitation and observation on opposite sides of the specimen.

6 Anisotropic Electrical Properties

Electrical charge transport in CFRP laminates is inherently direction dependent: electrically conductive carbon fibers provide preferential pathways along their axial direction, whereas the polymer matrix is insulating. At the laminate scale, the resulting macroscopic response is therefore governed not only by constituent conductivities and fiber volume fraction, but also by the realized fiber orientation state and the continuity of the conductive network, including fiber–fiber and ply–ply contacts. These features produce strong electrical anisotropy, i.e., a pronounced directional dependence of conductivity that can span several orders of magnitude between the fiber direction and transverse/through-thickness directions [29, 30, 35, 217, 218]. A sound theoretical description of this anisotropy is essential for applications including lightning strike current paths [219, 220], electromagnetic shielding [27, 36, 37], induction processes [221–223], and electrical self-sensing/structural health monitoring [224, 225].

For the electrical characterization strategy pursued in this thesis, resistance-based measurements provide a complementary, non-destructive route to quantify direction-dependent charge transport at the structural scale and to extract physically interpretable in-plane transport parameters that are suitable for comparison across specimens and processing states.

Chapter 6 develops a geometry-aware route to identify orthotropic in-plane electrical properties from angle-resolved resistance measurements on regular n-gonal prismatic specimens. The central idea is that the measured resistance between opposite faces, $R(\theta_i)$, varies systematically with the angle θ_i between the imposed current path and the fiber-parallel reference direction. By defining this reference using the fiber orientation information Θ established in Chapter 4, the angular resistance dataset can be interpreted in a physically meaningful coordinate system and reduced to principal in-plane resistivities that are directly comparable across lay-ups and manufacturing conditions. The chapter further accounts for measurement-specific contributions, most importantly contact- and electrode-related effects, within the analytical identification framework.

The theoretical foundations required for this evaluation, including anisotropic conduction concepts and the measurement formulations used in this work, are summarized in Section 6.1. The experimental implementation is then introduced in Section 6.2, followed by the analytical evaluation methodology in Section 6.3. The resulting parameter identification and model performance are assessed in Section 6.4, and the consolidated implications for electrical transport characterization within the broader thesis context are summarized in Section 6.5.

6.1 Theoretical Background

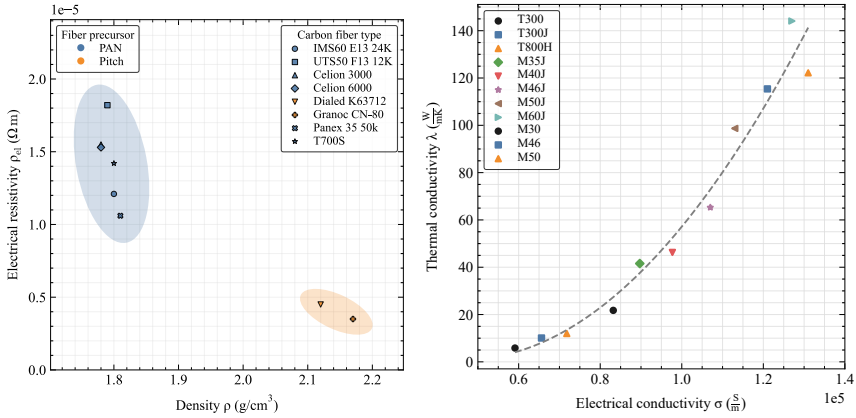
6.1.1 Electrical Anisotropy

Carbon Fibers

The axial electrical transport of carbon fibers is commonly quantified by the filament resistivity ρ and its inverse, the electrical conductivity σ, and it is strongly influenced by precursor and processing state. In practical measurements on fibers and tows, the electrical response is typically assessed along the fiber axis, because this direction governs charge transport in most composite-relevant applications and enables comparatively robust measurement when the gauge length, filament count (for tows), and contact conditions are controlled. In the study by Safarova and Gregr [61], several commercial PAN-based and pitch-based fiber tows were characterized, and the resulting data provide a clear separation between the two fiber families: PAN-based tows exhibit substantially higher resistivities than pitch-based tows, corresponding to lower conductivities in the fiber direction.

Beyond precursor type, the reported data highlights that resistivity correlates with material density and, by implication, with the degree of graphitization and structural perfection attained during high-temperature treatment. Specifically, the pitch-based fibers in Safarova and Gregr [61] show higher densities (on the order of $\sim$ 2.12–2.17 g/cm^3) and markedly lower axial resistivities (about $\rho_{f,\mathrm{pitch}} \approx (3.5\text{–}4.5) \times 10^{-6}\,\Omega\,\mathrm{m}$) than the PAN-based fibers (densities around $\sim$ 1.78–1.81 g/cm^3 and resistivities roughly $\rho_{f,\mathrm{PAN}} \approx (1.0\text{–}1.8) \times 10^{-5}\,\Omega\,\mathrm{m}$). This systematic offset is consistent with the well-established observation that pitch-derived fibers can be processed to a more highly graphitized state than typical PAN-derived fibers, yielding higher axial conductivities. Importantly, for

engineering use, this means that literature conductivity values are not transferable across carbon fibers as a generic class; rather, they must be interpreted at the level of fiber family and, ideally, specific fiber type. The density–resistivity relationship and the distinct clustering of PAN- and pitch-based fibers are illustrated in Figure 6.1a.



(a) Electrical resistivity of PAN based and pitch based carbon fibers [61].

(b) Relationship between electrical and thermal conductivity [60].

Figure 6.1: Electrical resistivity of PAN based and pitch based carbon fibers and the relationship between electrical and thermal conductivity of carbon fibers [60, 61].

Thermal conductivity λ and electrical conductivity σ are not independent in carbon fibers and, by extension, in CFRP, because both are governed by the underlying fiber microstructure (e.g., degree of graphitic alignment, crystallite size, and defect density) and therefore tend to vary between fiber types and processing conditions. As a conceptual reference, the ratio of thermal to electrical conductivity in conductors, where heat and charge transport is dominated by electrons (e.g. metals), is linked by the Wiedemann–Franz relationship [226]

$$L = \frac{\lambda}{\sigma} = \frac{\pi^2}{3}\left(\frac{k}{e}\right)^2 T, \tag{6.1}$$

where k is the Boltzmann constant, e is the electron charge and T is the temperature. The ratio on the right hand side is called the Lorenz number L [227]. However, carbon fibers exhibit pronounced anisotropy and a substantial contribution of phonon transport to λ, so universal Wiedemann–Franz scaling is generally

not expected. Nevertheless, direct single-fiber measurements show a clear correlation between λ and σ across different carbon fiber types and manufacturing conditions [60], as illustrated in Figure 6.1b.

At the composite scale, the coupling becomes indirect and depends on the fiber-network topology and interfacial contact state: both effective λ and σ increase with fiber volume fraction and fiber alignment along the transport direction, yet they respond differently to interfacial phenomena because electrical transfer is highly sensitive to fiber–fiber and electrode contact resistances, whereas thermal transport is additionally governed by thermal boundary resistances and the matrix contribution [224]. Finally, λ and σ are coupled in the governing equations through resistive heating, since the electrical current generates a volumetric heat source that can elevate the local temperature and thereby alter the apparent σ, which must be considered whenever electrical characterization is performed at non-negligible power levels [217].

Fiber Composites: Principal Electrical Properties

As we have seen, carbon fibers are electrical conductors, while polymer matrices are considered excellent electrical insulators. For an UD CFRP with a nearly insulating polymer matrix, longitudinal conductivity is well approximated by a rule-of-mixtures (Voigt or upper Wiener bound [30, 66]) relation [217]:

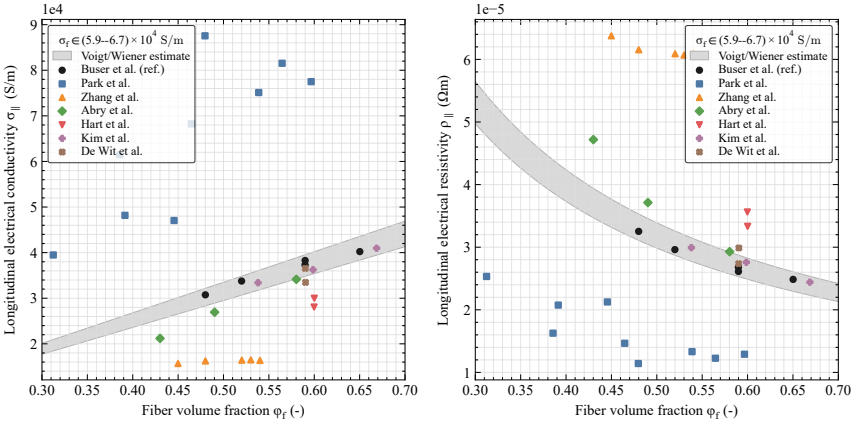
$$\sigma_{\parallel} \leq \varphi_f \sigma_f + (1-\varphi_f)\sigma_m \approx \varphi_f \sigma_f, \qquad \textit{with} \qquad \sigma_m \approx 0 \tag{6.2}$$

$$\rho_{\parallel} \geq \left(\frac{\varphi_f}{\rho_f} + \frac{1-\varphi_f}{\rho_m} \right)^{-1} \approx \frac{\rho_f}{\varphi_f}, \qquad \textit{with} \qquad \rho_m \to \infty \tag{6.3}$$

where φ_f is the fiber volume fraction, and σ_f and σ_m are the fiber and matrix conductivities, respectively. Deviations below the upper Wiener bound can arise from electrically ineffective (e.g., broken) fibers introduced during processing. Ponomarenko et al. [30] report such reductions in pultruded CFRP, while at higher $\varphi_f \gtrsim 0.6$ interfiber contacts allow current to bypass broken fibers so that $\sigma_{\parallel}$ again approaches the upper bound.

Recent work has also emphasized that confirming Equation (6.2) experimentally is highly sensitive to enforcing appropriate boundary conditions (e.g. uniform current injection) and to excluding contact contributions [217]. A visual representation of literature-reported measurement data for the longitudinal electrical

conductivity and the corresponding resistivity of PAN-based UD CFRP laminates is provided in Figure 6.2. A representative range of longitudinal fiber conductivity of $\sigma_f = (5.9\text{–}6.7) \times 10^4$ S/m, used here for the Voigt and Wiener estimate band, is based on Toray TC1200 data reported by Buser et al. [217], who employed a state-of-the-art six-probe measurement methodology as discussed in Section 6.1.1.



(a) Longitudinal electrical conductivity. **(b)** Longitudinal electrical resistivity.

Figure 6.2: Longitudinal electrical conductivity and resistivity of PAN based UD CFRP as found in the literature [29, 34, 38, 146, 217].

In contrast to Equation (6.2), no comparably predictive and generally applicable rule-of-mixtures exists for the transverse conductivities $\sigma_\perp$ (in-plane) and σ_z (through-thickness) of UD CFRP. In an idealized two-phase model with a perfectly insulating matrix, the transverse Reuss or lower Wiener bound [67] is dominated by the matrix and therefore approaches $\sigma_\perp \to 0$ and $\sigma_z \to 0$, which is not representative of real laminates. Finite transverse transport arises because current can traverse the matrix primarily through a stochastic network of fiber–fiber contacts and near-contacts: adjacent fibers may touch directly (giving rise to constriction/contact resistance) or be separated by thin resin layers across which charge transport can occur via tunneling or field-assisted conduction, so that the effective transverse response is governed by contact topology rather than phase averaging [29, 31, 32]. Consequently, $\sigma_\perp$ and σ_z depend sensitively on microstructural details such as fiber packing and misalignment, local waviness, fiber volume fraction, porosity, and processing pressure/surface condition that

modifies the inter-fiber contact resistance [29, 77]. From a measurement perspective, this topology-controlled transverse transport also amplifies the influence of boundary conditions (current spreading, electrode size, and effective conducting thickness), such that inverse identification of $\sigma_\perp$ and σ_z typically requires multi-terminal measurements and/or field modeling rather than direct coupon resistance conversion [34, 54].

In this work, electrical anisotropy is treated using a resistivity-based formulation; accordingly, representative literature values of principal resistivities were collected to provide physically plausible reference ranges, as can be seen in Table 6.1. The listed anisotropy ratio is defined as stated in Equation (6.10). Across the dataset, longitudinal resistivities are consistently on the order of $10^{-5}\,\Omega\,\mathrm{m}$, while transverse in-plane resistivities range from 10^{-1} to $10^{0}\,\Omega\,\mathrm{m}$ when explicitly reported, implying a typical in-plane anisotropy of $A_{xy} \sim 10^{4}$–10^{5}. When through-thickness values are available, the contrast could be even stronger, with $A_{xz} \sim 10^{5}$ [34], reflecting the fact that thickness-direction current relies predominantly on inter-ply and contact-limited pathways.

Because the numerical values are already given in the table, the following summary focuses exclusively on the respective measurement approach. (a) Acosta et al. [55] determine the orthotropic in-plane resistivities of a UD-CFRP ply using a two-probe resistance measurement, i.e., the voltage drop is recorded between the current-injection electrodes, so that the extracted resistivities inherently include contact and lead contributions. (b) Hart and Zhupanska [34] identify the laminate's principal-direction resistivities by combining four-probe measurements for in-plane characterization with a six-probe configuration to resolve the remaining principal component, thereby separating current injection from voltage sensing and improving robustness against contact resistances while enabling directional decoupling. (c) Scholle and Sinapius [40, 54] do not perform a dedicated resistivity identification campaign; instead, they assume representative orthotropic UD-CFRP resistivity ranges (longitudinal estimated via a rule-of-mixtures-type parallel-path argument, transverse taken from literature ranges) and use these as fixed inputs to interpret measured potential fields. (d) Park et al. [29] report fiber-level resistivity and infer composite-level longitudinal behavior by invoking a parallel-path / rule-of-mixtures argument at an assumed fiber volume fraction; the work emphasizes the resulting in-plane anisotropy level rather than providing a consistently reusable transverse identification based on a specific composite-scale probe configuration. (e) Buser et al. [217] compile longitudinal transport data for multiple UD-CFRP systems and obtain the re-

ported longitudinal conductivities using a six-probe measurement scheme, while transverse principal components are not targeted and therefore not extracted.

Table 6.1: UD CFRP principal resistivities and derived in-plane anisotropy ratios.

Ref.	Appr. (–)	φ_f (–)	$\rho_{\parallel}$ ($\Omega\,m$)	$\rho_{\perp}$ ($\Omega\,m$)	A_{xy} (–)
Acosta [55]	a	0.40	4.25×10^{-5}	3.56×10^{-1}	8.37×10^{3}
Hart [34]	b	0.60	3.40×10^{-5}	6.23×10^{-1}	1.83×10^{4}
Scholle [40, 54]	c	0.60	$(2.0–2.8) \times 10^{-5}$	0.55–2.2	$(0.9–5.9) \times 10^{5}$
Park [29]	d	0.60	$(1.25–1.67) \times 10^{-5}$	–	10^{3}–10^{4}
Buser [217]	e	0.48–0.65	$(2.5–3.5) \times 10^{-5}$	–	–

1D Resistance Measurement: 2-, 4-, and 6-Probe Methods

A large fraction of electrical characterization strategies for CFRP coupons aims to approximate a predominantly 1D axial current state in the gauge section, such that the measured resistance can be related to an effective axial resistivity by a geometry factor plus a contact/lead contribution. Under this idealization, the measured resistance is commonly expressed as [29, 56, 217]

$$R \;=\; \rho\,\frac{L}{A} \;+\; R_{\mathrm{c}}, \tag{6.4}$$

where L is the electrode spacing, A the cross-sectional area, and R_{c} summarizes the contributions of the electrode, lead, and electrode–specimen interface. The simplest implementation is the two-probe method, in which the same electrodes inject current and sense voltage; consequently, the measurement inherently includes R_{c}, and the conversion in Equation (6.4) becomes reliable only if the electrode coupling is stable and sufficiently low relative to the bulk contribution, or if additional procedures are used to separate bulk and contact terms [56, 217]. For this reason, four-probe methods are generally preferred for the determination of DC properties in CFRP. By separating current electrodes from voltage probes, the measured potential drop is taken within the gauge section, strongly reducing the influence of electrode/contact voltage drops on the inferred bulk response [56, 217]. However, even in four-probe form, the validity of a 1D back-calculation rests on the assumption that the current density in the gauge section is sufficiently uniform and that the voltage probes sample an essentially 1D potential gradient; in highly anisotropic CFRP this assumption can fail because anisotropy promotes

preferential current channeling and nonuniform current spreading, so that the apparent resistance may represent a boundary-condition-dependent mixture of longitudinal and transverse contributions rather than a single axial material parameter [29]. To explicitly assess whether the sought 1D condition is achieved, Van Den Berg et al. [56] extend the classical four-probe concept to a six-probe configuration by measuring the voltage drop on both specimen surfaces over the same gauge length (e.g., V_t top-surface and V_b bottom-surface), which provides an experimental diagnostic for through-thickness nonuniformity that is particularly relevant in UD laminates with large $\sigma_{\parallel}/\sigma_{\perp}$ ratios [56, 217]. In the uniform-gauge limit, where $V_t \approx V_b$ within measurement uncertainty, the longitudinal conductivity can be reduced using the conventional relation Van Den Berg et al. [56]

$$\sigma_{\parallel} = \frac{\delta}{w\,t}\,\frac{I}{V}, \qquad V \approx V_t \approx V_b, \tag{6.5}$$

with injected current I, specimen width w, thickness t, and gauge length δ. Conversely, a systematic deviation $V_t \neq V_b$ indicates that the gauge section does not satisfy the intended 1D condition and that reliable property extraction requires either improved electrode design/specimen aspect ratios or an explicit field-based evaluation of the measurement configuration rather than direct use of Equation (6.4). [29, 56, 217]

6.1.2 Microstructural Mechanisms

Along the fibers, carbon filaments provide quasi-continuous conducting channels. Consequently, $\sigma_{\parallel}$ is predominantly governed by the intrinsic fiber conductivity, the fiber volume fraction, fiber length and fiber breakage with comparatively limited sensitivity to the details of transverse contacts. In contrast, conduction in transverse in-plane $\sigma_{\perp}$ or thickness direction σ_z requires current transfer between adjacent fibers and/or across ply interfaces. These transfers occur through a combination of direct fiber–fiber contacts, contact resistance at touching sites, and tunneling or near-contact transport across thin resin layers. Because these transverse pathways form convoluted, stochastic networks, $\sigma_{\perp}$ and σ_z are strongly topology-dominated and can change significantly with processing (e.g. compaction pressure, curing, surface treatments, and additives) and defects (e.g. cross-ply cracks and delamination) that alter contact incidence and interphase properties. A schematic of the conductive network within a UD CFRP is shown in Figure 6.3. [30, 35, 39, 224]

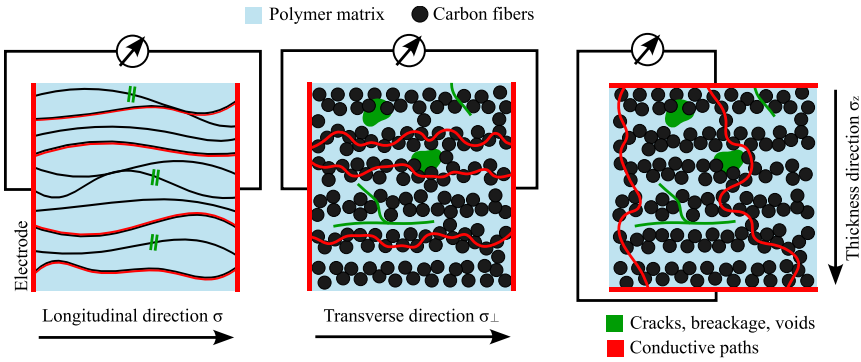


Figure 6.3: Schematic of the conductive network within a UD CFRP based on Wen et al. [39] and Wang et al. [224].

Surface Treatment and Contact Resistance

Electrical resistance measurements on CFRP are strongly influenced by the electrical contact between the electrode and the composite surface. In addition to the intrinsic bulk resistance of the laminate, the measured resistance includes a contact contribution that originates from a limited number of microscopic current transfer spots and from interfacial layers such as resin rich surface regions. For resistance based sensing and for parameter identification, the contact contribution must be treated as a systematic component since it can dominate the measurement at short gauge lengths and can introduce apparent nonlinearities if it changes during loading. Scholle [79] emphasizes three practical requirements for usable contacts. The contact resistance should be as small as possible, spatially homogeneous over the electrode area, and as strain invariant as possible.

Scholle [79] investigates three surface conditions prior to electrode application, as can be seen in Figure 6.4. The untreated condition keeps the surface as manufactured. Surface grinding is implemented by sanding with a medium 600 grit paper to locally remove the polymer rich surface layer and to expose fibers for improved electrical coupling. Chemical surface activation is implemented by sulfuric acid etching. It is noted that aggressive polishing can damage the fibers and, therefore, can alter the electrical behavior, which motivates the comparison of chemical etching versus mechanical removal methods.

Table 6.2 summarizes contact resistances reported by Scholle [79] for different electrode technologies and surface preparations. The reported R^2 values indicate

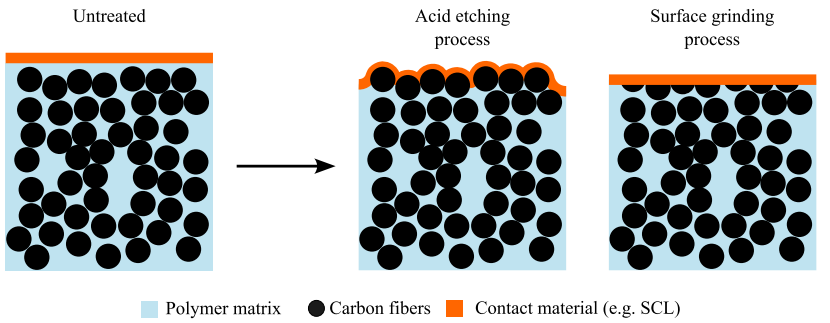


Figure 6.4: Schematic of the contact surface depending on sample preparation within a UD CFRP based on Scholle [79].

the repeatability of the resistance versus spacing regression for each contact preparation. Two robust observations follow from these data. First, electrodeposition based contacts in combination with soldering yield the lowest and most repeatable contact resistances, typically below 1 Ω and in several cases close to 0.2 Ω with values R^2 close to unity, indicating good repeatability. Second, paint based or epoxy based contacts depend strongly on the surface condition. Silver paint on a sanded surface can reach approximately 1 Ω with high repeatability, while the same paint on an etched surface shows a substantially higher resistance and poor repeatability. Carbon paint and silver filled epoxy lead to markedly larger resistances and inferior repeatability, up to kilohms for carbon paint on a sanded surface.

Scholle [79] supports these findings with qualitative microstructural evidence. Silver paint is reported to wet the complex CFRP surface topography and to penetrate scratches from sanding, which plausibly increases the number of parallel current transfer sites and reduces the constriction dominated contact resistance. Silver filled epoxy is described as too viscous to achieve comparable wetting and infiltration, which is consistent with the systematically larger contact resistances. For electroplated electrodes, it is highlighted that surface cleaning and the removal of boundary layers is essential for uniform deposition and durable bonding. Etched surfaces improve the electroplating conditions, but handling induced delamination can still occur if the deposited layer is mechanically weakened.

Table 6.2: Contact resistances reported by Scholle [79]

Electrode material	Surface condition	R_c (Ω)	R^2 (–)
Silver-filled epoxy[a]	Untreated	13.9	0.52
Silver-filled epoxy[a]	Etched	11.4	0.50
Silver-filled epoxy[a]	Sanded	7.4	0.54
Silver paint[b]	Etched	4.2	0.04
Silver paint[b]	Sanded	1.2	0.95
Silver paint RS Pro[b]	Sanded	1.0	0.995
Ni electroplating + solder[c]	Untreated	0.9	0.94
Ni electroplating + solder[c]	Etched	0.8	0.99
Ni electroplating + solder[c]	Sanded	0.2	0.997
Ni electroplating + solder[c]	Sanded and etched	0.7	0.95
Ag electroplating + solder[c]	Etched	0.9	0.92
Ag electroplating + solder[c]	Sanded	0.2	0.998
Ni electroplating + silver epoxy[d]	Etched	0.6	0.98

[a] Adhesive contact using a silver-filled epoxy.
[b] Paint contact applied directly on the prepared CFRP surface.
[c] Electrodeposition contact with subsequent soldering.
[d] Hybrid contact consisting of Ni electrodeposition with a silver-epoxy bonding layer.

Interfiber Spacing and Electron Tunneling

Along the fiber direction, electron transport is dominated by continuous filaments; at the nano-scale, the near-graphitic bonding structure of carbon fibers provides electronic states that enable comparatively free electron motion along the fiber axis [228]. In contrast, transverse transport within a single carbon fiber is substantially poorer and has been associated with cross-sectional defects and an apparent skin-core structure [228]. At the composite scale, any non-fiber direction conduction therefore cannot be explained by intrinsic fiber transport alone; rather, it emerges from fiber–fiber transfer events that become possible through real contacts and near-contacts between adjacent filaments, as well as through imperfect interlaminar consolidation [27, 195].

In this contact-controlled regime, the decisive microstructural quantity is not a macroscopic ply spacing, but the distribution of local inter-fiber separations and contact states. A useful abstraction is to parameterize the packing by the fiber diameter d_f and an effective (matrix) inter-fiber spacing d_s, which can be used to represent an effective layer thickness via $h = d_f + d_s$ and thereby relate packing to the number of conductive layers and the density of potential transfer sites across the laminate thickness [195]. Increasing fiber volume fraction generally reduces characteristic separations and increases the probability of contacts/near-contacts,

which can raise transverse conductivity in a strongly nonlinear manner, consistent with a rapidly densifying conductive network [27, 195, 228]. Conversely, resin-rich interlaminar regions and limited interlayer connectivity increase effective separation and suppress through-thickness transport [27, 195]. These considerations motivate the interpretation of measured transverse and through-thickness resistivities as microstructure-sensitive quantities that encode both spacing statistics and the quality of fiber transfer events.

Electron tunneling provides a physically grounded mechanism for charge transfer at fiber–fiber near-contacts when the carbon surfaces are separated by an extremely thin polymer film. Liu et al. [195] define the insulating film thickness s in angstroms (Å) and, using a Holm–Kirschstein tunneling model, compute a critical thickness of $s_0 = 7.6\,\text{Å}$ (i.e., 0.76 nm). Tunneling is a quantum-mechanical process in which electrons traverse an insulating barrier despite having insufficient classical energy to overcome it; the transmission probability depends strongly on barrier thickness and therefore yields a highly nonlinear, typically exponential, distance dependence [33, 195]. This mechanism is fundamentally different from approximately Ohmic transport along a continuous carbon filament [195, 228]. As a consequence, tunneling may materially affect transverse or through-thickness conductivity while leaving the longitudinal conductivity largely unchanged, because fiber–fiber transfer plays a negligible role for the primary axial current path [195].

Consequently, because tunneling-assisted transfer is only viable at sub-nanometer gaps, appreciable transverse and through-thickness conduction at the laminate scale can only arise where the microstructure provides a sufficiently dense population of effective fiber contacts, i.e., regions that appear visually in contact at the micrograph scale and, in reality, are separated at most by an ultrathin residual matrix film.

Percolation Effect

Luo et al. [229] show that, in a CFRP reinforced with short fibers, conductivity can display percolation-like behavior in the sense of Kirkpatrick [32], because the formation of a connected conductive pathway is controlled by the density of effective inter-fiber contacts, the local arrangement of fibers, microstructural features, and tunneling gaps. By fitting principal-directional conductivity data, they obtained percolation thresholds that were approximately direction-independent,

reported to fluctuate in a narrow band of about $\varphi_{f,\mathrm{perc}} = 0.10$–$0.15$. A common geometric reference for short-fiber networks is the continuum-percolation scaling for randomly oriented conducting cylinders, which relates the percolation threshold to the fiber aspect ratio A_R via [230]

$$\varphi_{f,\mathrm{perc}} \approx \frac{C}{A_R}, \qquad A_R = \frac{L}{d}. \tag{6.6}$$

The factor C is a dimensionless proportionality factor that depends on the idealized percolation model and on the adopted connectivity criterion, so it is not universal even for cylinder networks. Using the processed short-fiber geometry reported by Luo et al. [229], $L_f \approx 64$ μm and $d_f \approx 7$ μm, gives $A_R \approx 9.1$. Combining this with the fitted threshold band $\varphi_{f,\mathrm{perc}} = 0.10$–$0.15$ of Luo et al. [229] yields an effective proportionality factor $C_{\mathrm{eff}} = \varphi_{f,\mathrm{perc}} A_R \approx 0.91$–$1.37$, which is higher than the values often quoted for ideal, isotropically random cylinder systems ($C \approx 0.7$ [230]). This deviation is consistent with the fact that real short-fiber composites depart from the ideal assumptions. The preferred orientation lowers the probability of three-dimensional inter-fiber connectivity and thus increases $\varphi_{f,\mathrm{perc}}$. Agglomeration, or incomplete dispersion reduce the density of effective conductive contacts and can shift the apparent threshold upward, as emphasized by Luo et al. [229] and reviewed by Bauhofer and Kovacs [230]. For endless fiber reinforced laminates, the aspect-ratio percolation picture is not the appropriate framework for the fiber direction, because longitudinal connectivity is already present through quasi-continuous fibers over structural length scales. In this case, longitudinal transport is governed by fiber-dominated pathways and contact injection effects rather than by the emergence of a spanning cylinder network, while percolation-type arguments remain primarily relevant for transverse and through-thickness transport where connectivity depends on inter-fiber contacts. Also, in the context of structural UD CFRP, where engineering-relevant fiber volume fractions are typically on the order of $\varphi_f \approx 0.50$–0.65, such values lie well above the thresholds identified by Luo et al. [229].

6.1.3 Electrical Conduction Models

For an UD CFRP lamina, the macroscopic electrical behavior is described in a local material coordinate system (x, y, z), where x denotes the fiber direction ($\parallel$), y the transverse in-plane direction ($\perp$), and z the through-thickness direction. The proportionality between electric field $\mathbf{E}$ and current density $\mathbf{J}$ is characterized

by the electrical conductivity $\boldsymbol{\sigma}$ via Ohm's law, while the electrical resistivity $\boldsymbol{\rho}$ is defined as its inverse, $\boldsymbol{\rho} = \boldsymbol{\sigma}^{-1}$. Assuming orthotropic symmetry of the UD lamina, $\boldsymbol{\sigma}$ and $\boldsymbol{\rho}$ are commonly taken as diagonal in the local basis [217]:

$$\mathbf{J} = \boldsymbol{\sigma}\,\mathbf{E}, \qquad \mathbf{E} = -\nabla V, \tag{6.7}$$

$$\boldsymbol{\sigma} = \begin{bmatrix} \sigma_x & 0 & 0 \\ 0 & \sigma_y & 0 \\ 0 & 0 & \sigma_z \end{bmatrix}, \qquad \boldsymbol{\rho} = \boldsymbol{\sigma}^{-1}. \tag{6.8}$$

Under steady-state conditions without internal sources, charge conservation $\nabla \cdot \mathbf{J} = 0$ yields the anisotropic Laplace equation for the electric potential V,

$$\nabla \cdot J = \nabla \cdot (\boldsymbol{\sigma} \nabla V) = 0 \;\; \Rightarrow \;\; \sigma_x \frac{\partial^2 V}{\partial x^2} + \sigma_y \frac{\partial^2 V}{\partial y^2} + \sigma_z \frac{\partial^2 V}{\partial z^2} = 0, \tag{6.9}$$

for homogeneous $\boldsymbol{\sigma}$ within the domain.

Electrical anisotropy is conveniently quantified by conductivity (or resistivity) ratios, e.g.,

$$A_{xy} = \frac{\sigma_x}{\sigma_y} = \frac{\rho_y}{\rho_x}, \qquad A_{xz} = \frac{\sigma_x}{\sigma_z} = \frac{\rho_z}{\rho_x}. \tag{6.10}$$

Directional Properties and Limitations

A common simplification in anisotropic transport is to treat a measurement at an in-plane angle as probing a single directional material property, i.e., an effective axial resistivity/conductivity that depends only on orientation. Such reductions are mathematically meaningful only if the experiment enforces a quasi-one-dimensional transport state with nearly parallel current streamlines and a well-defined, spatially uniform relationship between the electric field and the current density along the chosen axis. Achieving this requires boundary conditions that actively prevent lateral current spreading, for example, by using full-face electrodes, and injection/collection configurations that minimize contact constriction. If these conditions are not met, the measured response reflects a coupled, multi-dimensional field solution, and it cannot be treated as a simple projection of the constitutive tensor. [42, 53]

For UD CFRP, these prerequisites are frequently violated by the electrode arrangements that are most relevant for structural health monitoring and laboratory

characterization, including finite surface pads, partial-width electrodes, and arbitrarily placed electrode arrays. As emphasized by Acosta et al. [55], once the uniform current assumption is not met, such as for surface injection with non-uniform current diffusion, the measured resistance is influenced by current-spreading effects and specimen/electrode geometry, even in otherwise simple conductive plates. This geometric sensitivity is amplified in UD CFRP because the polymer matrix is essentially insulating, and the conduction mechanisms differ fundamentally by direction. Consequently, a single geometry-independent "directional conductivity" is generally not identifiable from surface-electrode measurements, because the experiment does not constrain the current to remain collinear with the nominal measurement direction [26, 55, 77].

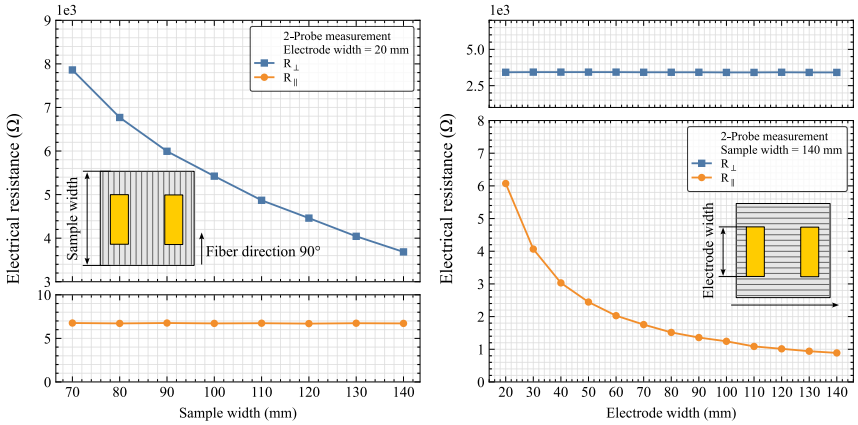
The practical implication is that the surface-electrode resistance in UD CFRP should be interpreted as an apparent configuration-specific response that reflects a coupled dependence on (i) electrode footprint and placement, (ii) specimen dimensions (including width and thickness), and (iii) local quality and statistics of inter-fiber contacts and electrode–composite coupling [40, 54, 55].

Geometry-Aware Models

A central conclusion of Acosta et al. [55] is that electrical resistance measurements with surface electrodes on UD CFRP are inherently geometry dependent: the measured resistance is not solely a material property, but is systematically shaped by specimen dimensions, electrode footprint, and electrode placement through direction-dependent current spreading and bridging effects. Because their framework provides an explicit and physically interpretable mapping from electrode/specimen geometry to an effective conducting cross-section and path length, it is adopted in this thesis as the methodological baseline for developing and extending geometry-aware resistance models. [55]

From the configurations summarized in Figures 6.5a and 6.5b, Acosta et al. [55] conclude that the governing conducting cross-section (i.e., an "effective width") is direction-dependent because the dominant current path aligns with the fiber direction in UD CFRP. When electrodes probe the longitudinal (0°) direction, the measured resistance is essentially insensitive to the sample width but decreases strongly with increasing electrode width, indicating that the current remains confined to the electrode footprint and that the electrode width defines the effective width. Conversely, for the transverse (90°) direction, the resistance

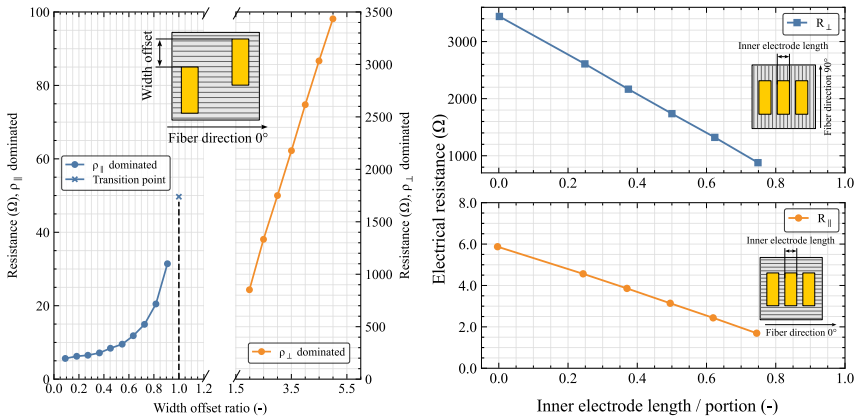
decreases with increasing sample width but is nearly insensitive to electrode width, consistent with current spreading across the full specimen width via inter-fiber contacts, so that the sample width governs the effective width. The electrode misalignment study on longitudinal (0°) direction in Figure 6.6a further supports a regime change controlled by the electrode overlap: for width-offset ratios below unity, fibers directly bridge the electrodes and the response remains fiber-dominated with an effective width given by the remaining overlap; as the offset approaches unity, the overlap vanishes and the resistance rises sharply, reflecting the transition to an inter-fiber-contact-controlled path. For offsets beyond unity (no direct fiber bridging), the resistance follows an approximately linear increase with offset because the effective width saturates at the sample width while the effective distance between electrodes increases. Finally, the inner-electrode results in Figure 6.6b show a systematic "bridge effect": introducing a highly conductive intermediate copper electrode provides a partial shunt that reduces the effective electrode separation, producing an approximately linear reduction in resistance with increasing inner-electrode length fraction in both longitudinal and transverse cases; therefore, electrode arrays can influence (and potentially bias) the intended two-electrode measurement unless such bridging is explicitly accounted for in the model. [55]



(a) Sample width influence on longitudinal and transverse resistance [55].

(b) Electrode width influence on longitudinal and transverse resistance [55].

Figure 6.5: Influence of sample width and electrode width on electrical resistance measured in 2-probe configuration [55].



(a) Influence of electrode width offset ratio on electrical resistance [55].

(b) Influence of inner electrodes on electrical resistance [55].

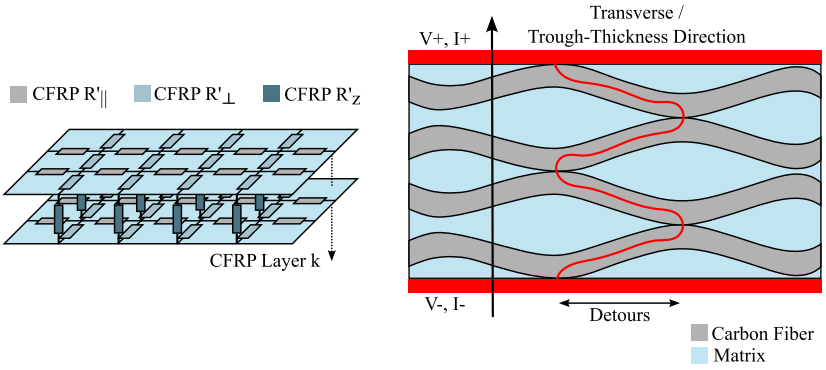
Figure 6.6: Influence of electrode width offset ratio and inner electrodes on electrical resistance [55].

6.1.4 Electrical Equivalent Circuit Models

Electrical equivalent circuit (EEC) models represent CFRP as an interconnected assembly of resistive elements that approximate the dominant current paths in the composite. The central motivation is practical: real CFRP coupons exhibit strong microstructural heterogeneity (fiber waviness, bundle architecture, stochastic fiber–fiber contacts, and ply interfaces), such that macroscopic resistance changes under load or damage are more naturally interpreted as changes in an evolving conductive network than as changes in a single bulk resistivity. In this sense, EEC models form a bridge between (i) continuum descriptions and (ii) the discrete, contact-mediated nature of conduction in fiber composites. [224]

At the basic level, the EEC representations decompose the composite into (a) intrinsic fiber-segment resistances along the filament direction $R'_{\parallel}$, (b) inter-fiber contact resistances $R'_{\perp}$, and (c) optional interlaminar (through-thickness) resistances R'_{z} if the laminate architecture requires current transfer across plies. This decomposition is consistent with the microstructure-based resistor-network formulation of Yu et al. [77], where each fiber end and each fiber–fiber contact is treated as a network node, fiber segments are modeled as resistors, and contact resistances are explicitly introduced at contact nodes. Because contact quality and contact area can vary widely (e.g. due to sizing, compaction state, or local

normal pressure), the contact resistance R_c' may dominate conduction and cannot, in general, be eliminated. A schematic of such an EEC is given in Figure 6.7a. [77, 224]



(a) 3D-multi-layer schematic EEC of CFRP in principal directions [77].

(b) Detour of conductive path in transverse or thickness direction [77].

Figure 6.7: Schematic detour of conductive path along carbon fiber and 3D-multi-layer schematic EEC of CFRP in principal directions [77].

A particularly influential EEC abstraction for unidirectional CFRP under tensile loading and material failure is the serial array of discrete parallel cells introduced by Park et al. [231]. In that framework, the laminate is represented as a chain of cells whose characteristic length scale corresponds to an electrical ineffective length δ_{ec}, interpreted as an average spacing of electrically relevant contact points along the fibers. Fiber fragmentation under load progressively removes the conducting segments; however, conduction can be sustained locally until all segments between adjacent contact points become ineffective. This concept rationalizes why resistance evolution may show an initially modest change followed by a nonlinear increase at higher strain, and it also provides a compact parameterization of the internal conductive network state via δ_{ec}. Importantly, Park et al. emphasized that measured resistance evolution can depend on the measurement configuration (e.g., DC two-probe versus four-probe) because electrode/contact effects and current injection geometry alter the effective participation of near-surface conductive paths, motivating an explicit modeling of the measurement circuit rather than assuming that a unique material resistivity is directly observed. [231]

While serial–parallel cell models are attractive for their analytic tractability, they embed strong assumptions about how contacts are distributed. Xia et al. [232] addressed this limitation by formulating a random resistor-network model for UD CFRP in which fiber–fiber contacts are sparsely and randomly distributed, and network voltages are solved using Kirchhoff's laws. Their analysis shows that the resistance increment caused by the failure/removal of a single conducting element depends not only on an assumed resistor length but also on the actual local contact density. A key outcome is that an electrically ineffective length δ_{ec} can systematically deviate from the true mean contact spacing at higher contact densities. Therefore, fitting-based parameters can reproduce network-level behavior for a specific set of boundary conditions, yet they should not be treated as direct microstructural descriptors unless the assumed contact-distribution statistics have been independently verified. [232]

To reduce reliance on phenomenological fitting, Yu et al. [77] proposed a 3D microstructure-based resistor-network model that generates a representative UD microstructure while introducing a waviness parameter that creates multiple contact opportunities, as can be seen schematically in Figure 6.7b. In their formulation, contact point locations are randomized to reflect the stochastic nature of contacts, and contact resistances are incorporated at nodes. In particular, they discussed that contact resistance can vary by orders of magnitude depending on surface treatments and therefore developed a simplified analytical estimate for unsized fibers based on Hertzian contact mechanics and Holm constriction resistance [31]. Their sensitivity study identifies fiber waviness as a controlling factor for transverse resistivity in UD CFRP, underscoring that transverse conduction is governed by rare geometry-mediated contact pathways rather than by intrinsic fiber resistivity alone. [77, 224]

For structural health monitoring (SHM) and non-destructive evaluation (NDE), EEC models are often constructed at the coupon or laminate scale to connect measured resistance changes to damage size and location. Roh et al. [233] developed an electrically equivalent resistor-grid model for UD laminates in which orthotropic conduction is embedded by assigning substantially different resistor values along and transverse to the fiber direction. They fitted grid dimensions and effective network width by matching the measured baseline resistance, then represented impact damage by modifying/removing elements in the grid; the resulting model reproduced measured impact-induced resistance changes with small discrepancy for the investigated configuration. For cross-ply laminates, Roh et al. further proposed a route model that distinguishes in-plane and

through-thickness routes and expresses the measured resistance change as a combination of in-plane and thickness-direction contributions along the preferred low-resistance paths. These laminate-scale models are particularly useful when the experimental observable is a multi-electrode resistance map, because they provide a computationally light inverse relationship between resistance perturbations and damage geometry. [224, 233]

6.2 Test Setup

All electrical measurements were performed with an LCR-/ESR meter P 2170 from PeakTech GmbH [234]. The instrument was operated in AC mode at a fixed frequency of $f = 100\,\mathrm{Hz}$, and the resistance was taken as the real part of the measured impedance using the serial equivalent-circuit evaluation R_{ser}, as this is automatically selected for low AC resistivity measurements with $|Z| < 10\,\mathrm{k\Omega}$ [234].

The excitation frequency was selected to ensure quasi-static measurement conditions. This choice is adequate in light of the wide-band results of Kim and See [28], who report that the apparent longitudinal conductivity decreases with increasing frequency due to progressively stronger reactive/inductive contributions (e.g., magnetic flux coupling between neighboring fibers); thus, operating far below their impedance-spectroscopy range (10 kHz–100 MHz) minimizes frequency-induced dispersion and yields a close approximation of the DC-relevant resistance. In addition, AC excitation is preferable to purely DC measurements because it enables phase-sensitive evaluation of the resistive component while suppressing DC offsets (e.g., thermoelectric and contact-potential drifts [235, 236]) and reducing time-dependent polarization effects [237] at the electrode–CFRP interface, thereby improving measurement stability and signal-to-noise ratio.

The specimens were contacted with two physical electrodes, so that current injection and voltage pickup occurred at the same electrode pair. The measurement was nevertheless implemented as a four-wire Kelvin connection [238] to these two electrodes. In a Kelvin connection, the excitation current is forced through a pair of force leads, while the voltage is measured with a separate pair of high-impedance sense leads connected at the device under test. Because the sense inputs draw negligible current, the voltage drop along the leads is negligible and the contribution of lead and cable resistance is largely removed from the measured resistance. The measured value still includes the electrode–specimen

interfacial contribution of the two contacts because no separate internal voltage electrodes were used and the sensing points remain on the electrodes rather than within the specimen.

Electrical contacts were realized with silver conductive lacquer Acheson Silver DAG 1415 supplied by Plano GmbH. The lacquer was applied on the specimen side surfaces using masking tape templates to control electrode dimensions and to obtain well-defined edges. After application, the lacquer was allowed to dry and stabilize before measurement. The electrical leads were attached to the lacquered areas in a mechanically stable manner to minimize motion-induced fluctuations.

6.3 Analysis Methodology

This section establishes the analytical framework used to evaluate angle-dependent electrode-to-electrode resistance measurements on regular n-sided polygon specimens of UD CFRP. Building on the effective cross-section formulation of Acosta et al. [55], the method links the measured resistance $R(\theta_i)$ to the orthotropic in-plane resistivities $\rho_{\parallel}$ and $\rho_{\perp}$ through geometry-derived path lengths and effective electrode widths. Subsequent subsections introduce (i) the baseline "full-face" model, (ii) extensions for finite electrode size and for perimeter-bridging inner electrodes, and (iii) concise dimensionless relations for comparing model variants.

The electrical measurement and processing workflow proceeds as shown in Figure C.1.

6.3.1 Base Model

The base model approach builds on the analytical framework proposed by Acosta et al. [55], who predicted electrode-to-electrode resistance in UD CFRP rectangular coupon specimens using two geometry-dependent descriptors: the effective electrode distance D_e and the effective width W_e. To retain a computationally efficient one-dimensional formulation while still accounting for electrode placement and overlap effects, these descriptors are generalized here to a regular n-sided polygon specimen and evaluated as explicit functions of the discrete measurement

orientation θ_i. The general electrode-to-electrode resistance formulation of Acosta [55] can be expressed as

$$R \;=\; \rho_{\text{eff}}\,\frac{D_e}{W_e\,t}, \tag{6.11}$$

where $\rho_{\text{eff}} \in \{\rho_{\parallel},\, \rho_{\perp}\}$ is the effective resistivity associated with the dominating conduction direction and t the laminate thickness.

The regular n-sided polygon specimen is characterized by the distance across flats D_{af}. The apothem, defined as the perpendicular distance from the polygon center to the midpoint of any face, is $a = D_{\text{af}}/2$. The face length then follows as

$$s \;=\; 2a\tan\!\left(\frac{\pi}{n}\right) \;=\; D_{\text{af}}\tan\!\left(\frac{\pi}{n}\right). \tag{6.12}$$

An angular resistance dataset is acquired by measuring between two electrodes on opposite polygon faces while varying the in-plane orientation θ between the electrode-pair axis and the UD fiber direction. For a regular n-sided polygon, the admissible orientations are discrete and determined by the constant face offset angle

$$\beta \;:=\; \frac{2\pi}{n}. \tag{6.13}$$

Accordingly, the measurement angles can be indexed as

$$\theta_i \;:=\; i\,\beta, \qquad i \in \mathbb{Z}. \tag{6.14}$$

Because the resistance is evaluated between electrodes placed on opposite faces, the geometry must admit pairs of opposite faces, which requires an even number of faces,

$$n \;=\; 2m, \qquad m \in \mathbb{N}. \tag{6.15}$$

For an orthotropic lamina it is sufficient to cover the symmetry-relevant interval $0^\circ \le \theta \le 90^\circ$. To include both bounding directions 0° and 90° exactly within the discrete set $\{\theta_i\}$ under ideal conditions, the step angle must divide $\pi/2$, i.e.,

$$\frac{\pi}{2} \;=\; q\,\beta \quad\Longleftrightarrow\quad n \;=\; 4q, \qquad q \in \mathbb{N}. \tag{6.16}$$

Accordingly, the distinct orientations spanning 0° to 90° (inclusive) are

$$i \;=\; 0, 1, \ldots, \frac{n}{4}, \qquad N_\theta \;=\; \frac{n}{4} + 1. \tag{6.17}$$

Following Acosta et al. [55] and Equation (6.11), the surface-electrode resistance R with respect to θ_i is written as

$$R(\theta_i) \;=\; \rho_{\text{eff}}\,\frac{D_e(\theta_i)}{W_e(\theta_i)\,t}, \tag{6.18}$$

The key modeling decision is that different conduction mechanisms dominate at small and large θ, motivating a two-regime formulation governed by a threshold angle α. The full analytical prediction becomes the piecewise function

$$R_{\text{ana}}^{(\text{base})}(\theta_i) \;=\; \begin{cases} R_1^{(\text{base})}(\theta_i), & \theta_i < \alpha, \quad \rho_{\text{eff}} = \rho_{\parallel}, \\ R_2^{(\text{base})}(\theta_i), & \theta_i \geq \alpha, \quad \rho_{\text{eff}} = \rho_{\perp}. \end{cases} \tag{6.19}$$

This construction will preserve the interpretability of $\rho_{\parallel}$ and $\rho_{\perp}$ as direction-specific resistivities while allowing the regular polygon angular response to be modeled with minimal additional parameters.

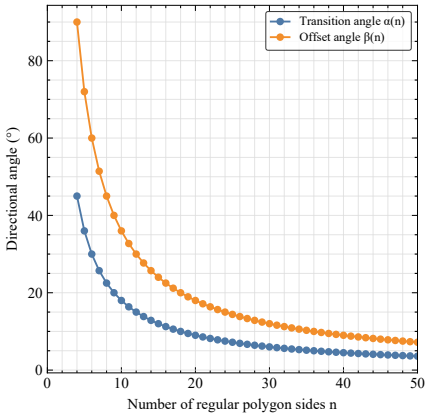
The transition angle α, which defines the threshold between the longitudinal and transverse resistance regime, is defined using a geometric overlap criterion for the electrodes. For sufficiently small θ, a finite overlap exists between the electrode footprint and the fiber-aligned conduction path in 0° direction. The angular threshold for a round specimen would be computed as

$$\alpha \;=\; \arctan\!\left(\frac{l_{\text{el}}}{D}\right), \tag{6.20}$$

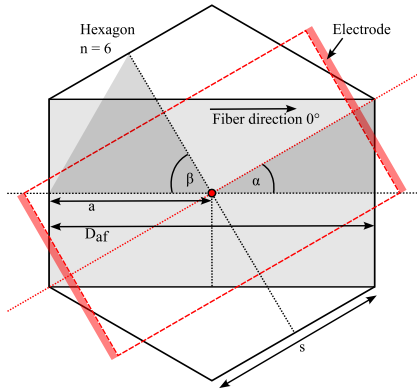
where l_{el} is an electrode-length along the outer surface and D is the diameter. As straight stripe electrodes are enforced, Equation (6.20) for a regular n-sided polygon uses $D = D_{af}$ as the specimen length scale and $l_{\text{el}} = s$ as the characteristic electrode length for one face. The transition angle therefore becomes a function of n:

$$\alpha(n) \;=\; \arctan\!\left(\frac{s}{D_{\text{af}}}\right) \;=\; \frac{\beta}{2} = \frac{\pi}{n}. \tag{6.21}$$

A comparison of the schematic evolution of the transition angle α and the offset angle β for a regular n-sided polygon in Figure 6.8 shows that β exceeds α for all $n \geq 3$. Consequently, only the measurement aligned with the fiber direction (0°) is assigned to Case 1, the longitudinal-dominant regime. All remaining measurement orientations are assigned to Case 2, the transverse-dominant regime. In the following, both cases are described in detail.



(a) Transition angle α.



(b) Schematic of a hexagon ($n = 6$).

Figure 6.8: Transition angle α which defines the threshold between the longitudinal and transverse resistance regime in an n-sided specimen in UD CFRP.

Case 1: Longitudinal-Dominant Regime

For $\theta < \alpha$, conduction is dominated by the high conductivity along fibers, and the effective width is governed by the geometric overlap between the electrode footprint and the fiber-bridging corridor. The resistance is modeled as

$$R_1^{(\text{base})}(\theta_i) \;=\; \rho_{\parallel}\,\frac{D_{e,1}(\theta_i)}{W_{\text{e},1}(\theta_i)\,t}, \qquad \theta_i \le \alpha, \tag{6.22}$$

where

$$D_{e,1}(\theta_i) \equiv D_{e,1} = D_{af} \tag{6.23}$$

denotes the inner distance between the electrodes. The electrode overlap width $W_{\text{e},1}(\theta_i)$ equals the complete length of the electrodes $l_{\text{el}} = s$, therefore

$$W_{e,1}(\theta_i) \equiv W_{e,1} = s \tag{6.24}$$

For a n-sided regular polygon, the longitudinal-dominant regime is only physically accessible and meaningful for the $\theta_{i=0} = 0°$ configuration, as $\theta_{i=1} = \beta > \alpha$. Consequently, Equation (6.22) reduces to the polygon-specific Case 1 expression

$$R_1^{(\text{base})}(\theta_i = 0°) = \rho_{\parallel}\,\frac{D_{\text{af}}}{s\,t} \;=\; \frac{\rho_{\parallel}}{t}\,\cot\!\left(\frac{\pi}{n}\right). \tag{6.25}$$

This relation provides direct access to $\rho_{\parallel}$ from a resistance R_{0° measured at $\theta_i = 0^\circ$. Rearranging of Equation (6.25) yields the longitudinal electrical resistivity as

$$\rho_{\parallel} \;=\; R_{0^\circ}\,\frac{s\,t}{D_{\mathrm{af}}} \;=\; R_{0^\circ}\,t\,\tan\!\left(\frac{\pi}{n}\right). \tag{6.26}$$

Case 2: Transverse-Dominant Regime

For $\theta_i \geq \alpha$, the dominant conduction path relies mainly on inter-fiber contacts and transverse transport. The corresponding Case 2 resistance is written as

$$R_2^{(\mathrm{base})}(\theta_i) \;=\; R_{\perp,2}(\theta_i) + R_{\parallel,2}(\theta_i) \;=\; \rho_{\perp}\,\frac{D_{e,2}(\theta_i)}{W_{e,2}(\theta_i)\,t} + R_{\parallel,2}(\theta_i), \qquad \theta_i \geq \alpha, \tag{6.27}$$

with transversal contribution to resistance $R_{\perp,2}(\theta_i)$, longitudinal contribution to resistance $R_{\parallel,2}(\theta_i)$, effective electrode distance $D_{e,2}(\theta_i)$, effective electrode width $W_{e,2}$, and laminate thickness t. It is assumed that

$$R_{\parallel,2}(\theta_i) < R_{\perp,2}(\theta_i). \tag{6.28}$$

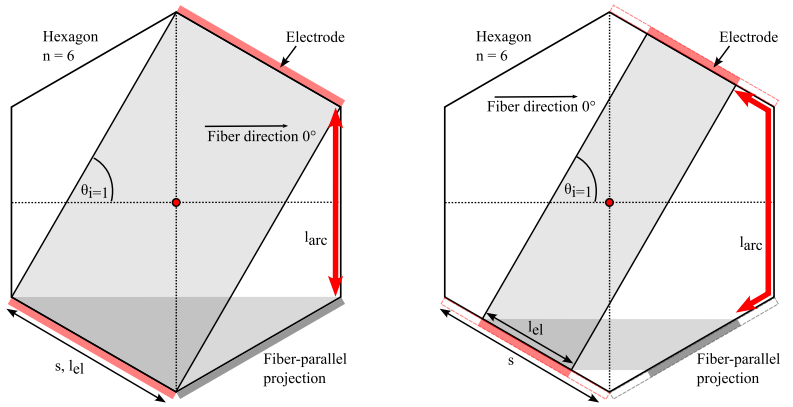
Following the reasoning of Acosta et al. [55], the high longitudinal conductivity causes a rapid redistribution of charge along the fibers. As a result, the transverse electric field is not confined to the local electrode footprint but broadens across the entire specimen width. In the transverse dominant regime, this motivates the approximation

$$W_{e,2}(\theta_i) \equiv W_{e,2} = D_{\mathrm{af}}. \tag{6.29}$$

The longitudinal conductivity is sufficiently higher compared with the transverse conductivity such that the potential is approximately constant along the fiber direction. Under this assumption, any translation of an electrode parallel to the 0° fiber axis is treated as equipotential, and resistance is governed by an effective transverse distance between the electrodes. Therefore, to obtain $D_{e,2}(\theta_i)$ geometrically, an electrode is translated parallel to the 0° fiber direction until it lies on the same specimen half as the opposing electrode. After this equipotential translation, the remaining separation is represented by an equivalent arc length l_{arc} along the polygon perimeter between the translated electrode location and

the fixed electrode, see Figure 6.9a. For discrete orientations; Equation (6.14), the perimeter segment spans $2i-1$, which yields

$$D_{e,2}(\theta_i) \;=\; l_{\mathrm{arc}}(\theta_i) \;=\; s\,(2i-1) \;=\; s\left(\frac{n}{\pi}\theta_i - 1\right), \qquad \theta_i \geq \alpha. \tag{6.30}$$



(a) Schematic of the full electrode length basic model (base).

(b) Schematic of the small electrode size model (el).

Figure 6.9: Schematic of the full-length electrode configuration (base) and reduced electrode length configuration (el).

Even in the transverse-dominant regime, a small longitudinal contribution can persist. This is expected for two complementary reasons. First, the electrodes remain separated by a finite geometric projection onto the 0° fiber axis, so a direct fiber-parallel segment is always available in principle. Second, transverse transport in UD CFRP is strongly constrained by inter-fiber contacts and near-neighbor junctions; consequently, the energetically favorable conduction network tends to follow shortest-path segments that repeatedly re-enter the high-conductivity fiber direction to bypass locally resistive transverse connections. In other words, even when the macroscopic electrode pairing is mainly transverse, the microscopic current topology generally includes fiber-parallel detours enforced by limited transverse connectivity.

For a regular n-sided polygon with opposite faces contacted at their midpoints, the electrode center-to-center distance is D_{af} (across flats) and the longitudinal projection is

$$L_{\parallel}(\theta_i) \;=\; D_{\mathrm{af}}\cos(\theta_i), \qquad \theta_i \geq \alpha, \tag{6.31}$$

which yields the conservative projected lower bound

$$R_{\parallel}^{*}(\theta_i) \;\geq\; \rho_{\parallel}\,\frac{L_{\parallel}(\theta_i)}{s\,t} \;=\; \rho_{\parallel}\,\frac{D_{\mathrm{af}}}{s\,t}\cos(\theta_i) \;=\; R_{0^\circ}\cos(\theta_i) \qquad \theta_i \geq \alpha. \tag{6.32}$$

However, the magnitude of the longitudinal contribution in Case 2 cannot be attributed to the geometric projection alone, because the aforementioned fiber-parallel detours add an additional, effectively angle-independent component that is superimposed on the projected term. In an ideal setting, one could attempt to anchor this additional contribution by evaluating the longitudinal branch at the transition angle α using the formulation of Acosta et al. [55]; yet for a regular polygon the region $0^\circ \leq \theta < \alpha$ is not experimentally accessible, and the limiting electrode overlap at $\theta \to \alpha$ drives the overlap-based estimate toward a singular, formally infinite resistance [55]. Therefore, $R_{\parallel,\mathrm{offset}}$ at α cannot be identified directly from the current measurement geometry, and importing it from a theory based on electrode overlap [55] would be ill-conditioned.

We therefore represent the longitudinal contribution in Case 2 by a minimal decomposition into (i) the projected geometric term $R_{\parallel}^{*}(\theta_i)$ and (ii) an additive correction $R_{\parallel,\mathrm{offset}}$ that captures any residual longitudinal influence not explained by projection:

$$R_{2\parallel}^{(\mathrm{base})}(\theta_i) \;=\; R_{\parallel,\mathrm{offset}} \;+\; R_{\parallel}^{*}(\theta_i), \qquad R_{\parallel}^{*}(\theta_i) \geq R_{0^\circ}\cos(\theta_i), \qquad \theta_i \geq \alpha. \tag{6.33}$$

Substituting Equations (6.29) and (6.30) into Equation (6.27) gives the polygon specific Case 2 expression

$$\begin{aligned} R_{2}^{(\mathrm{base})}(\theta_i) &= \frac{\rho_{\perp}}{t}\,\frac{l_{\mathrm{arc}}(\theta_i)}{D_{\mathrm{af}}} + R_{2\parallel}^{(\mathrm{base})}(\theta_i) \\ &= \frac{\rho_{\perp}}{t}\,\tan\!\left(\frac{\pi}{n}\right)\left(\frac{n}{\pi}\theta_i - 1\right) + R_{2\parallel}^{(\mathrm{base})}(\theta_i), \qquad \theta_i \geq \alpha. \end{aligned} \tag{6.34}$$

Rearranging Equation (6.34) and solving for $\rho_{\perp}$ yields

$$\rho_{\perp} \;=\; \frac{t\left[R_{\theta_i} - R_{2\parallel}^{(\mathrm{base})}(\theta_i)\right]}{\tan\!\left(\frac{\pi}{n}\right)\left(\frac{n}{\pi}\theta_i - 1\right)}, \qquad \theta_i \geq \alpha. \tag{6.35}$$

To assess the sensitivity of the base model with respect to geometric and specimen parameters, a parametric variation is considered in C.3.

6.3.2 Model Extension: Small Electrode Size

The baseline formulation implicitly assumes that each electrode fully covers the corresponding polygon face, such that the available injection/collection width is face-length limited. In practical implementations, however, the electrode footprint along a face may be smaller than the face length, while remaining centered on that face. We denote the electrode length by l_{el} and consider the special case

$$l_{\mathrm{el}} \leq s. \tag{6.36}$$

For convenience, we introduce the electrode coverage factor

$$\eta_{\mathrm{el}} \;:=\; \frac{l_{\mathrm{el}}}{s}, \qquad 0 < \eta_{\mathrm{el}} \leq 1, \tag{6.37}$$

which quantifies the fractional face coverage.

Case 1: Longitudinal-Dominant Regime

In Case 1, the center-to-center electrode separation remains unchanged by reducing l_{el}, because the electrodes remain centered on their faces. The dominant modification is therefore the effective width in the conducting cross section. Accordingly, the Case 1 resistance expression (6.22) is generalized by replacing the effective width term by an electrode-length–limited width,

$$W_{\mathrm{e},1}^{(\mathrm{el})}(\theta) \;=\; \min\Big\{\, l_{\mathrm{el}},\, W_{\mathrm{e},1}(\theta) \Big\}, \qquad \theta_i < \tilde{\alpha}. \tag{6.38}$$

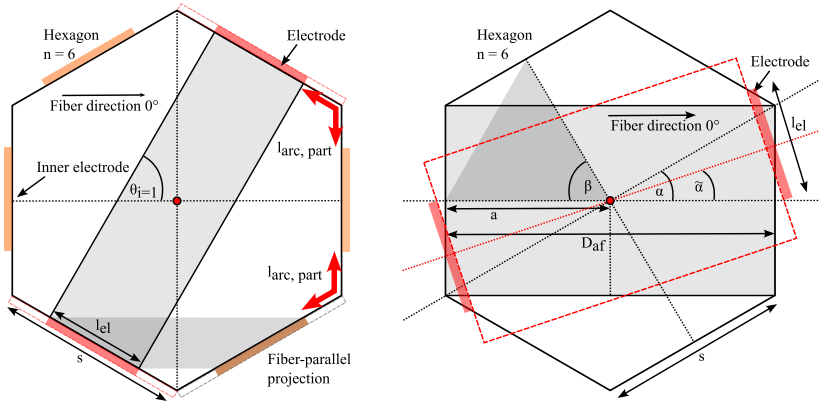
Because the available overlap collapses sooner for smaller footprints, the transition angle becomes electrode-size dependent. The corresponding boundary $\tilde{\alpha}$ is defined implicitly by the vanishing-overlap condition

$$W_{\mathrm{e},1}^{(\mathrm{el})}(\tilde{\alpha}) = 0, \tag{6.39}$$

and satisfies $\tilde{\alpha} \leq \alpha$ for $l_{\mathrm{el}} < s$, as can be seen in Figure 6.10b.

$$\tan\tilde{\alpha} = \frac{l_{\mathrm{el}}}{D_{\mathrm{af}}} = \eta_{\mathrm{el}} \tan\alpha \tag{6.40}$$

At $\theta_i = 0^\circ$, the overlap does not limit the effective width and the Case 1 expression reduces to a one-dimensional form with an electrode-footprint–limited



(a) Schematic of the inner electrode model (in).

(b) Electrode length reduced transition angle $\tilde{\alpha}$.

Figure 6.10: Schematic of the inner electrode configuration (in) and electrode length reduced transition angle $\tilde{\alpha}$.

cross section. Under the conservative assumption that the current-carrying width cannot exceed the electrode footprint, the 0° resistance becomes

$$R_1^{(\mathrm{el})}(\theta_i = 0^\circ) \;=\; \rho_\parallel \frac{D_{\mathrm{af}}}{l_{\mathrm{el}}\, t} \;=\; \frac{\rho_\parallel}{t}\,\frac{s}{l_{\mathrm{el}}}\,\cot\!\left(\frac{\pi}{n}\right) \;=\; \frac{\rho_\parallel}{\eta_{\mathrm{el}}\, t}\,\cot\!\left(\frac{\pi}{n}\right). \tag{6.41}$$

Consequently, the identification of $\rho_\parallel$ from the measured 0° resistance R_{0° is modified to

$$\rho_\parallel \;=\; R_{0^\circ}\,\frac{l_{\mathrm{el}}\, t}{D_{\mathrm{af}}} \;=\; R_{0^\circ}\,\eta_{\mathrm{el}}\,\frac{s\, t}{D_{\mathrm{af}}} \;=\; R_{0^\circ}\,\eta_{\mathrm{el}}\, t\,\tan\!\left(\frac{\pi}{n}\right), \tag{6.42}$$

which recovers the full-face result in the limiting case $\eta_{\mathrm{el}} \to 1$.

Case 2: Transverse-Dominant Regime

For Case 2, the finite electrode footprint primarily affects the effective arc-length separation that enters $D_{e,2}(\theta_i)$. If, each electrode is centered on its face but has a smaller length $l_{\mathrm{el}} < s$, then an additional uncovered segment of length $(s - l_{\mathrm{el}})/2$ remains on each side of the contacted face before the nearest vertex is reached. Consequently, the arc-length contribution increases by the uncovered lengths on

the two contacted faces, i.e. by $(s - l_{\mathrm{el}})$ in total. The adapted Case 2 separation becomes

$$\begin{aligned} D_{e,2}^{(\mathrm{el})}(\theta_i) &= l_{\mathrm{arc}}^{(\mathrm{el})}(\theta_i) = s\,(2i-1) + (s - l_{\mathrm{el}}) = s\,(2i - \eta_{\mathrm{el}}) \\ &= s\left(\frac{n}{\pi}\theta_i - \eta_{\mathrm{el}}\right), \qquad \theta_i \geq \tilde{\alpha}, \end{aligned} \tag{6.43}$$

where θ_i is understood in radians in the last representation. The full-face result Equation (6.30) is recovered for $\eta_{\mathrm{el}} \to 1$.

This modification propagates into Case 2 by replacing $D_{e,2}(\theta_i)$ with $D_{e,2}^{(\mathrm{el})}(\theta_i)$

$$\begin{aligned} R_2^{(\mathrm{el})}(\theta_i) &= \frac{\rho_\perp}{t}\,\frac{l_{\mathrm{arc}}^{(\mathrm{el})}(\theta_i)}{D_{\mathrm{af}}} + R_{2\parallel}^{(\mathrm{el})}(\theta_i) \\ &= \frac{\rho_\perp}{t}\,\tan\!\left(\frac{\pi}{n}\right)\left(\frac{n}{\pi}\theta_i - \eta_{\mathrm{el}}\right) + R_{2\parallel}^{(\mathrm{el})}(\theta_i), \qquad \theta_i \geq \tilde{\alpha}. \end{aligned} \tag{6.44}$$

Rearranging Equation (6.44) and solving for $\rho_\perp$ yields

$$\rho_\perp = \frac{t\left[R_{\theta_i} - R_{2\parallel}^{(\mathrm{el})}(\theta_i)\right]}{\tan\!\left(\frac{\pi}{n}\right)\left(\frac{n}{\pi}\theta_i - \eta_{\mathrm{el}}\right)}, \qquad \theta_i \geq \tilde{\alpha}. \tag{6.45}$$

A direct comparison of the model parameters between the extended model with a small electrode size and the base model is provided in Section C.4.

6.3.3 Model Extension: Inner Electrodes

To capture the bridge effect reported by Acosta et al. [55], we consider a configuration in which, in addition to the two active electrodes used for a given resistance measurement, inner electrodes are placed on every face of the regular n-sided polygon. All electrodes (active and passive/inner) share the same footprint l_{el}, centered on their respective faces, with

$$l_{\mathrm{el}} = \eta_{\mathrm{el}}\, s, \tag{6.46}$$

where η_{el} denotes the electrode coverage factor introduced in Equation (6.37). Following Acosta [55], each additional electrode acts as a local low-resistance bridge along the otherwise resistive perimeter route. In the present analytical framework, this is captured by reducing the effective electrode separation D_e by the cumulative bridged length along the active conduction path.

Case 1: Longitudinal-Dominant Regime

In the longitudinal-dominant regime, the dominant conduction path is the direct fiber-parallel connection between the two active electrodes, not a perimeter route. Therefore, for $\theta_i = 0^\circ$ the inner electrodes do not lie on the conduction path and do not contribute to bridging. Consequently, the Case 1 separation remains unchanged,

$$D_{e,1}^{(\mathrm{in})}(\theta_i) \;=\; D_{e,1}(\theta_i), \qquad \theta_i \le \tilde{\alpha}. \tag{6.47}$$

Case 2: Transverse-Dominant Regime

In the transverse-dominant regime, the shortest-path interpretation is governed by the perimeter arc-length between the two active faces. With inner electrodes placed on every face, each traversed face segment provides a low-resistance bridge of length $l_{\mathrm{el}} = \eta_{\mathrm{el}}\, s$. Since the selected arc comprises $(2i-1)$ face segments, the total bridged length along the Case 2 conduction route is defined as

$$L_i(\theta_i) \;=\; (2i-1)\, l_{\mathrm{el}} \;=\; (2i-1)\, \eta_{\mathrm{el}}\, s, \tag{6.48}$$

and the effective Case 2 separation is reduced accordingly,

$$D_{e,2}^{(\mathrm{in})}(\theta_i) \;=\; D_{e,2}^{(\mathrm{el})}(\theta_i) \;-\; L_i(\theta_i), \qquad \theta_i \ge \tilde{\alpha}. \tag{6.49}$$

Using the finite-electrode arc-length representation, one obtains

$$\begin{aligned} D_{e,2}^{(\mathrm{in})}(\theta_i) \;&=\; s\left(\frac{n}{\pi}\theta_i - \eta_{\mathrm{el}}\right) \;-\; \eta_{\mathrm{el}}\, s\,(2i-1) \\ &=\; s\left(\frac{n}{\pi}\theta_i - \eta_{\mathrm{el}}\right) \;-\; \eta_{\mathrm{el}}\, s\left(\frac{n}{\pi}\theta_i - 1\right) \\ &=\; s\,\frac{n}{\pi}\theta_i\,(1-\eta_{\mathrm{el}}), \qquad \theta_i \ge \tilde{\alpha}. \end{aligned} \tag{6.50}$$

Accordingly, the Case 2 expression is adapted to

$$\begin{aligned} R_2^{(\mathrm{in})}(\theta_i) &= \frac{\rho_\perp}{t}\,\frac{D_{e,2}^{(\mathrm{in})}(\theta_i)}{D_{\mathrm{af}}} + R_{2\parallel}^{(\mathrm{in})}(\theta_i) \\ &= \frac{\rho_\perp}{t}\,\tan\!\left(\frac{\pi}{n}\right)\left(\frac{n}{\pi}\theta_i\,(1-\eta_{\mathrm{el}})\right) + R_{2\parallel}^{(\mathrm{in})}(\theta_i), \qquad \theta_i \ge \tilde{\alpha}. \end{aligned} \tag{6.51}$$

Rearranging Equation (6.51) and solving for $\rho_\perp$ yields

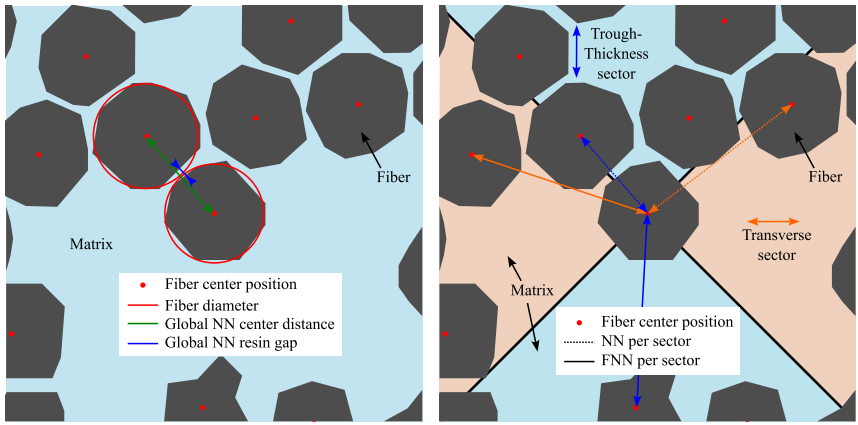
$$\rho_\perp = \frac{t\left[R_{\theta_i} - R_{2\parallel}^{(\mathrm{in})}(\theta_i)\right]}{\tan\left(\frac{\pi}{n}\right)\left(\frac{n}{\pi}\theta_i\left(1-\eta_{\mathrm{el}}\right)\right)}, \qquad \theta_i \geq \tilde{\alpha}. \tag{6.52}$$

A direct comparison of the model parameters between the extended model with inner electrodes and the model with small electrodes is provided in Section C.4.

6.3.4 Resistivity and Microstructural Spacing

The polygon-based electrical resistance model used in this work is formulated at the specimen scale and relies on homogenized principal resistivities as effective parameters. While this enables a tractable interpretation of macroscopic measurements, the model does not explicitly represent microscopic transport mechanisms such as fiber–fiber contacts, tunneling across resin gaps, or local current constriction effects, nor can it unambiguously separate contributions from in-plane transverse pathways and through-thickness connectivity within the fitted transverse response. Micrograph-derived nearest-neighbor (NN) metrics of the fibers, therefore, serve as a complementary microstructure-resolving descriptor that supports the interpretation of resistivity trends and helps assess whether observed differences are consistent with changes in inter-fiber spacing, resin-rich regions, and directional packing heterogeneity. Since ply thickness or fiber areal weight (FAW), and the associated manufacturing process, can systematically influence fiber packing density, alignment stability, and the probability of contacts or near-contacts, these NN metrics provide a direct geometric proxy for tunneling potential and shortest-path limitations. In particular, thin-ply laminates are commonly associated with improved manufacturing quality because reduced ply thickness promotes more uniform consolidation and suppresses ply-scale microstructural heterogeneity [239, 240]. Typical consequences include fewer resin-rich regions, reduced thickness variations, a more homogeneous fiber distribution, and a lower likelihood of locally under-compacted areas that interrupt efficient electrical transfer paths. Accordingly, differences in NN spacing distributions and directional NN measures are expected to be most pronounced when the thin-ply material is compared to the standard- or thick-ply material, providing mechanistic context for the macroscopic resistivity differences in terms of inter-fiber transfer probability and pathway tortuosity.

However, a simple global NN distance does not distinguish between geometrically favorable paths for current flow in different directions. In UD laminates, the relevant inter-fiber transfer events occur predominantly in the laminate plane, yet their directional character can still be separated into contributions aligned with the local thickness axis versus the in-plane transverse direction. To capture this anisotropic potential, the neighborhood of each fiber is divided into directional sectors, and the nearest-neighbor distances are evaluated within each sector. The resulting directional statistics provide proxies for (i) tunneling potential, via short matrix gaps, and (ii) the presence of matrix rich regions that may force current to detour, via the largest among directionally constrained nearest-neighbor distances, the so called farthest of the nearest directional neighbors.



(a) Global NN and resin gap. **(b)** Directional NN and FNN.

Figure 6.11: Schematic of global and directional nearest neighbors metrics.

Micrograph Segmentation

Polished cross-section micrographs are processed in Fiji (ImageJ) [241] to obtain a robust fiber segmentation suitable for geometric analysis. First, each grayscale micrograph is binarized by applying Otsu's method [242], which selects a global threshold by maximizing the between-class variance of foreground (fiber) and background (matrix). The binary mask is then refined using a Watershed [243] transformation to separate touching fibers and to mitigate merged regions caused by insufficient contrast or polishing artifacts.

Subsequently, Fiji's particle analysis is applied to each segmented fiber region. For each region, the area-weighted centroid is extracted and used as the fiber center position

$$\mathbf{x}_i = (x_i, y_i), \tag{6.53}$$

and the corresponding fiber diameter is estimated from the equivalent circular diameter associated with the measured area A_i,

$$d_{f,i} = 2\sqrt{\frac{A_i}{\pi}}. \tag{6.54}$$

The exported fiber table contains, at minimum, (x_i, y_i), A_i, and derived $d_{f,i}$ for all fibers $i = 1, \ldots, N$ within the field of view.

The Fiji fiber analysis output is imported into Python for nearest-neighbor analysis. Let $\mathbf{x}_i$ denote the center of fiber i and $d_{f,i}$ its equivalent diameter. For each fiber, Euclidean center-to-center distances to all other fibers are computed as

$$\Delta_{ij} = \|\mathbf{x}_j - \mathbf{x}_i\|_2, \qquad i \neq j. \tag{6.55}$$

From these pairwise distances, four metrics are derived, as can be seen in Figure 6.11.

Global Nearest-Neighbor Center Distance

For each fiber i, the global NN center distance is defined as

$$\Delta_i^{\mathrm{NN}} = \min_{j \neq i} \Delta_{ij}. \tag{6.56}$$

Global Nearest-Neighbor Resin Gap

To approximate the minimum matrix separation between two neighboring fibers, the nearest-neighbor resin gap is computed by subtracting the average of the two diameters from the NN center distance,

$$g_i^{\mathrm{NN}} = \max\left(0,\ \Delta_i^{\mathrm{NN}} - \frac{d_{f,i} + d_{f,j^*(i)}}{2}\right), \tag{6.57}$$

where $j^*(i) = \arg\min_{j \neq i} \Delta_{ij}$ denotes the index of the nearest neighbor. The truncation at zero avoids negative gaps that may arise from segmentation uncertainty.

Directional Nearest Neighbors

To distinguish preferential spacing in thickness and transverse directions, the neighborhood around each fiber is divided into four 90° angular sectors, defined with respect to a fixed coordinate system (x, y). For a candidate neighbor j, the relative displacement vector and its angle are

$$\mathbf{r}_{ij} = \mathbf{x}_j - \mathbf{x}_i, \qquad \varphi_{ij} = \operatorname{atan2}(r_{ij,y}, r_{ij,x}). \tag{6.58}$$

Two opposite sectors are associated with the thickness direction, and two opposite sectors with the transverse direction. For each fiber i and each sector s, the sector-constrained nearest-neighbor distance is

$$\Delta_{i,s}^{\mathrm{NN}} = \min_{j \in \mathcal{S}_s(i)} \Delta_{ij}, \tag{6.59}$$

where $\mathcal{S}_s(i)$ denotes the set of neighbors whose angle φ_{ij} lies within sector s.

The farthest of the nearest neighbors (FNN) is then defined as the maximum of these sector-wise nearest distances within a given sector. In the thickness direction this yields

$$\mathrm{FNN}_{z,i} = \max\left(\Delta_{i,\mathrm{up}}^{\mathrm{NN}},\ \Delta_{i,\mathrm{down}}^{\mathrm{NN}}\right), \tag{6.60}$$

and for the transverse in-plane direction

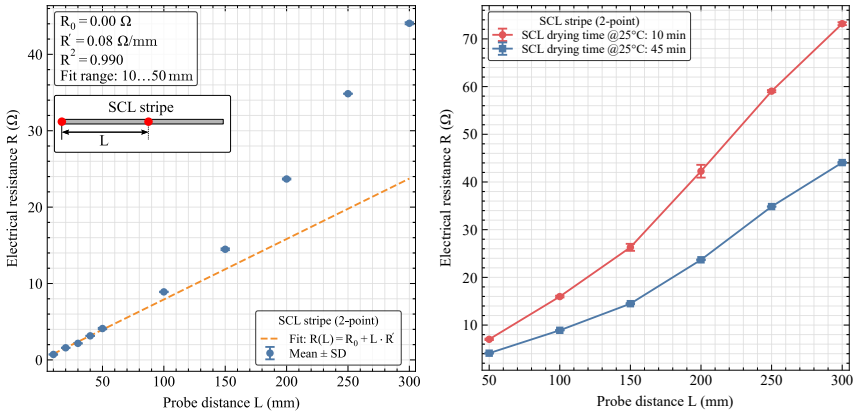
$$\mathrm{FNN}_{\perp,i} = \max\left(\Delta_{i,\mathrm{left}}^{\mathrm{NN}},\ \Delta_{i,\mathrm{right}}^{\mathrm{NN}}\right). \tag{6.61}$$

Intuitively, $\mathrm{FNN}_{z,i}$ and $\mathrm{FNN}_{\perp,i}$ quantify the largest local matrix rich region among the nearest available neighbors in the respective opposing directions. Large FNN values indicate that, in at least one of the two opposing sectors, the closest potential transfer partner is comparatively far away, implying a reduced probability of fiber contacts and short tunneling gaps and an increased likelihood that the shortest conductive path must detour around these matrix regions.

6.4 Results and Discussion

6.4.1 Silver Conductive Laquer

To quantify the characteristic resistance level of the applied silver conductive lacquer (SCL), reference measurements were performed on a lacquer stripe deposited on an electrically insulating polymer substrate. The stripe had a nominal width of $w = 1\,\mathrm{mm}$ and was measured over probe distances of $L = 10\,\mathrm{mm}$–$300\,\mathrm{mm}$. The dry-film thickness was estimated as $t \approx 10\,\mu\mathrm{m}$–$60\,\mu\mathrm{m}$. Resistance was measured by direct two-point probing with multimeter contacts, using replicate measurements at each spacing to assess repeatability. Figure 6.12a summarizes the resulting mean resistance values as a function of the probe distance L.



(a) Electrical line resistance R'.

(b) Influence of drying time.

Figure 6.12: Electrical resistance measurements on a conductive SCL stripe with different measurement distances and drying times.

For a first-order parameterization, the data were interpreted using the line-resistance model

$$R(L) = R_0 + R'L, \tag{6.62}$$

where R_0 aggregates contact and local constriction contributions and R' represents the apparent line resistance of the SCL stripe. The linear regression was restricted to the short-distance regime $L = 10\,\mathrm{mm}$–$50\,\mathrm{mm}$, yielding $R' \approx 0.08\,\Omega/\mathrm{mm}$. This restriction is motivated by the manual application procedure. Because the

SCL was applied by hand using a brush, only short distances can be deposited within a single brush stroke. Larger stripe lengths are therefore formed by multiple strokes with partial overlaps, such that locally increased thickness and altered microstructure (e.g., local binder accumulation with reduced silver volume fraction, agglomeration-induced packing heterogeneity, and drying-related microcracks) occur at overlap zones. Therefore, the thickness of the SCL is not uniform along the stripe, which implies spatial variations of the cross-sectional area A and consequently, of the local line resistance. Under these conditions, a global linear approximation is generally not well suited because both the effective cross-section and the local application quality can dominate the measured resistance response, particularly at longer distances where overlap-related inhomogeneities accumulate. In the constrained linear regression, the intercept was driven to $R_0 = 0\,\Omega$, indicating that any contact and constriction contributions were negligible within the repeatability of the measurement or could not be resolved separately from the line term in the current two-point measurement configuration.

The effective resistivity was estimated under a one-dimensional current-flow approximation with cross-sectional area $A = t\,w$ as

$$\rho_{\mathrm{eff}} = R\,\frac{A}{L} = R\,\frac{t\,w}{L}, \tag{6.63}$$

and the corresponding effective conductivity as

$$\sigma_{\mathrm{eff}} = \frac{1}{\rho_{\mathrm{eff}}} = \frac{L}{R\,A} = \frac{L}{R\,t\,w}. \tag{6.64}$$

The geometric parameters and the resulting reference quantities are reported in Table 6.3.

Table 6.3: Effective electrical estimates for SCL reference measurements.

Sample	$\boldsymbol{R'}$ (Ω/mm)	$\boldsymbol{\rho_{\mathrm{eff}}}$ ($\Omega\,$m)	$\boldsymbol{\sigma_{\mathrm{eff}}}$ (S/m)
SCL	≈ 0.08	8.0×10^{-7}–4.8×10^{-6}	2.08×10^{5}–1.25×10^{6}

SCL = silver conductive lacquer.

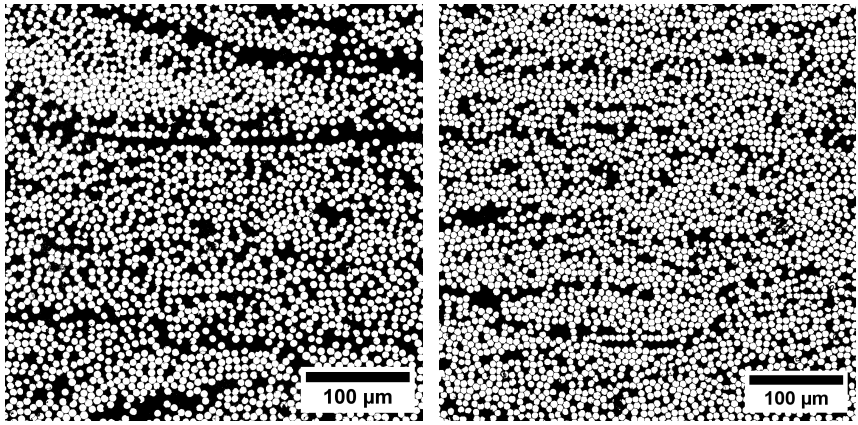
To assess the influence of curing on the electrical performance of the SCL, two resistance series were recorded at different drying times. Following the manufacturer's technical guidance, the coating is typically touch-dry after approximately 10 min, whereas the final coating properties continue to develop with ongoing solvent evaporation and film consolidation during further air drying and/or

accelerated drying. Consequently, resistance was measured after 10 min and after 45 min of ambient drying, as summarized in Figure 6.12b. While both datasets exhibit the same principal behavior of increasing resistance with increasing probe spacing, the absolute resistance level is systematically lower for the more completely dried SCL. Compared to 10 min, the 45 min values are reduced to approximately 55–60 %. A supplementary reference measurement after 24 h yielded resistance values comparable to the 45 min condition, indicating that the SCL electrical performance had largely stabilized within this drying time.

6.4.2 Influence of Ply Thickness

Segmented binary micrographs in Figure 6.13 were evaluated according to Section 6.3.4 to quantify microstructural spacing metrics that may govern contact-controlled electrical transport. Since all FAW configurations in this study have the same laminate thickness, a comparable fiber volume fraction φ_f, and were processed under identical manufacturing conditions, systematic differences in the results can be attributed primarily to FAW-related differences in local fiber packing and resin distribution rather than to global specimen geometry. Qualitatively, the micrographs indicate a subtle but consistent trend: the higher-FAW configuration (UD-120) exhibits more pronounced matrix-rich, river-like resin features with a preferential orientation in transverse fiber direction, while the lower-FAW configuration (UD-30) appears more homogeneously distributed with comparatively smaller, lake-like or cofferdam-like [239] resin-rich regions. This observation is in line with reports in the literature that local resin channeling and matrix-rich regions can be more pronounced for higher areal-weight plies and thus increase mesoscale heterogeneity [239, 240]. From an electrical perspective, such resin-rich features are relevant because they locally suppress the probability of fiber–fiber transfer events and, therefore, may increase the effective resistivity of the components in contact-controlled directions.

Quantitatively, the global nearest-neighbor (NN) center-to-center distances Δ^{NN} are essentially identical for both materials (6.75 µm for UD-120 and 6.74 µm for UD-30, Table 6.4), which is remarkably close to the nominal fiber diameter of 7 µm. The normalized histograms in Figure 6.14a also do not show a significant shift. This indicates that, on average, the microstructure provides frequent opportunities for fiber–fiber transfer via contacts and near-contacts in both configurations; hence, a global difference in mean fiber spacing alone is not expected to dominate differences in off-axis electrical behavior. The gap metric



(a) CFRP UD-120 edited binary micrograph.

(b) CFRP UD-30 edited binary micrograph.

Figure 6.13: UD-120 and UD-30 binary micrographs after application of Otsu's method and Watershed transformation, nominal fiber diameter 7 µm.

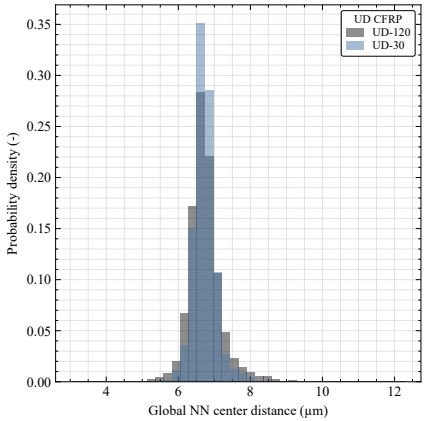
g^{NN}, interpreted as the resin separation between neighboring fibers, yields mean values of 0.24 µm for UD-120 and 0.16 µm for UD-30 (Table 6.4), with the corresponding distributions shown in Figure 6.14b. These absolute values must be treated with care, because the estimated gaps are affected by pixel discretization and segmentation artifacts: at 500 × magnification, one pixel corresponds to 0.385 µm, and the Watershed transformation introduces an artificial one-pixel separation between adjacent fibers even when they visually touch. Consequently, g^{NN} is not a direct proxy for the sub-nanometer separations relevant to electron tunneling, but rather a comparative indicator of how frequently resin-separated near-neighbor pairs occur in the segmented microstructure. In this comparative sense, the larger mean g^{NN} and the shifted distribution for UD-120 suggest a higher prevalence of resin separations between nearest neighbors, and implying a reduced probability of low-resistance transfers and potentially higher effective resistivity in contact-controlled directions.

The farthest-nearest-neighbor (FNN) directional metrics further support this interpretation. Normalized histograms in Figure 6.15b show that UD-120 tends to slightly larger $FNN_{\perp}$ and FNN_z values than UD-30, which is consistent with more frequent local interruptions of the fiber neighborhood by matrix-rich regions. Moreover, FNN_z is systematically larger than $FNN_{\perp}$ by approximately

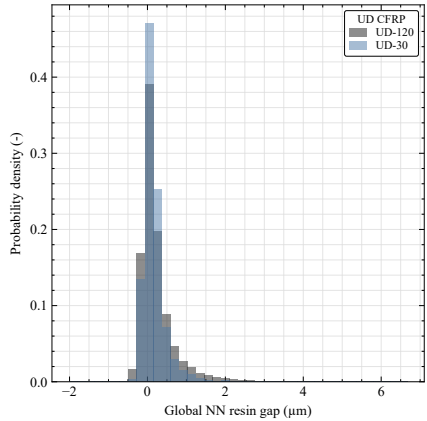
Table 6.4: Mean nearest-neighbor spacing metrics from micrograph evaluation for UD CFRP.

Sample	$\boldsymbol{\Delta^{NN}}$ (μm)	$\boldsymbol{g^{NN}}$ (μm)	$\boldsymbol{FNN_{\perp}}$ (μm)	$\boldsymbol{FNN_z}$ (μm)
UD-120	6.75	0.24	9.35	9.41
UD-30	6.74	0.16	8.80	8.91

$\sim$1 % for both materials (UD-120: 9.41 µm vs. 9.35 µm; UD-30: 8.91 µm vs. 8.80 µm, Table 6.4). While small, this asymmetry is physically consistent with a slightly reduced probability of forming short fiber–fiber transfer paths in thickness direction and, therefore, with similar or marginally better conductivity in the transverse direction compared to the through-thickness direction. Overall, the micrograph metrics indicate that both materials are densely packed (as reflected by $\Delta^{NN} \approx d$), but that UD-120 exhibits a higher statistical presence of resin separations and slightly increased directional neighborhood distances. Since tunneling-assisted transfer requires sub-nanometer film thicknesses, these results are best interpreted as changes in the probability and spatial distribution of effective contacts and near-contacts rather than as direct measures of tunneling distances; accordingly, the observed FAW-dependent resin-rich morphology and the gap-related statistics support the hypothesis of a potentially increased contact-controlled transverse and through-thickness resistivity for UD-120 relative to UD-30.

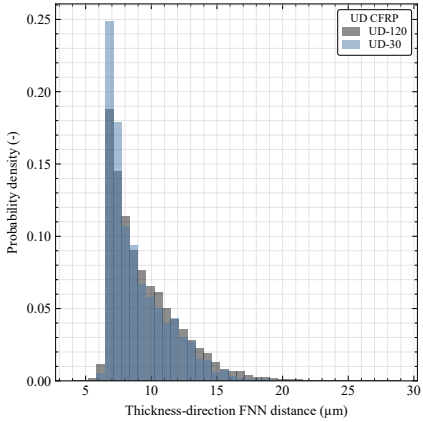


(a) Global nearest neighbor fiber center distance Δ^{NN}.

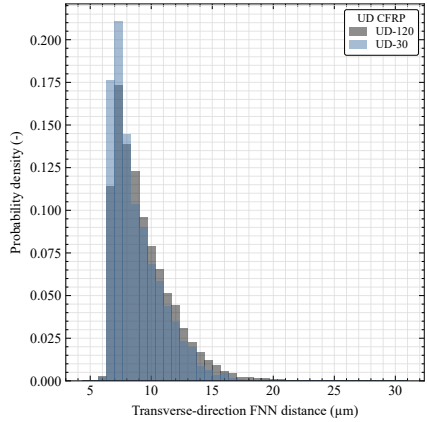


(b) Global nearest neighbor resin gap distance g^{NN}.

Figure 6.14: Global normalized histograms from micrograph-based fiber segmentation for UD-120 and UD-30 CFRP.



(a) Farthest of the nearest neighbors in thickness direction FNN_z.



(b) Farthest of the nearest neighbors in transverse direction $FNN_\perp$.

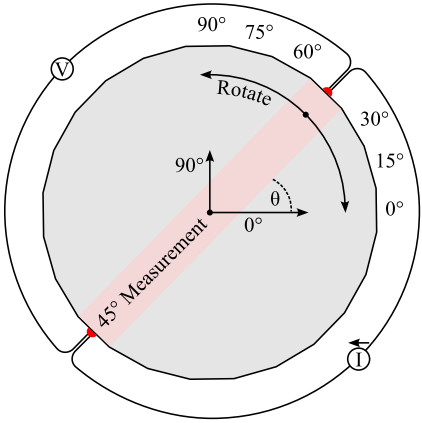
Figure 6.15: Directional normalized histograms from micrograph-based fiber segmentation for UD-120 and UD-30 CFRP.

6.4.3 Polygon Based Resistance Measurements

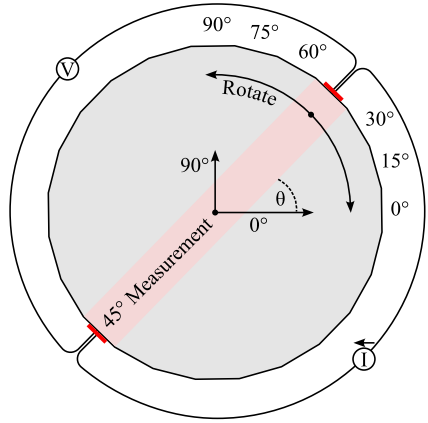
To evaluate the validity of the n-sided polygon model and to assess whether the modeled principal resistivities $\rho_{\parallel}$ and $\rho_{\perp}$ can be predicted accurately and remain consistent with literature data, the present work employs a 24-sided (lat. icositetragon) prismatic specimen and acquires a circumferential resistance dataset in discrete increments of $\beta = 15°$. For each angular position θ_i, the resistance is measured between two opposite facets whose across-flats separation is $D_{af} = 125\,\mathrm{mm}$. Within the polygon-model framework, the electrode configuration primarily defines the electrical boundary conditions at the perimeter (effective electrode footprint, presence of passive inner electrode segments, and the associated degree of shunting) and thus determines which analytical model variant applies. The four configurations shown in Figure 6.16 are therefore treated as systematic boundary-condition variants rather than practical alternatives, enabling a controlled comparison between the measured $R(\theta_i)$ and the corresponding model predictions for different probe and electrode representations (see the corresponding model derivations in Section 6.3.1 ff.).

Configuration (a), SCL-0 (Figure 6.16a), represents the lowest preparation effort because no silver conductive lacquer is applied and the specimen is directly contacted by the multimeter measurement probes. In model interpretation, this case can be assigned to the extended model for small electrode size (*el*) (see Section 6.3.2) if the probe width ($\sim 1\,\mathrm{mm}$) is interpreted as the effective electrode footprint and if contact resistances are neglected. Operationally, SCL-0 carries the highest risk of variable contact quality and probe misplacement, because the probes must be positioned repeatably near the facet center; small offsets can change the local current injection pattern along the polygon boundary and thereby increase scatter in $R(\theta_i)$. Additionally, resistance values will increase exponentially with electrode misplacement [55]. Consequently, SCL-0 is preparation-efficient but metrologically sensitive, and deviations from the prediction (*el*) should be interpreted primarily as contact- and placement-related effects rather than as intrinsic material response.

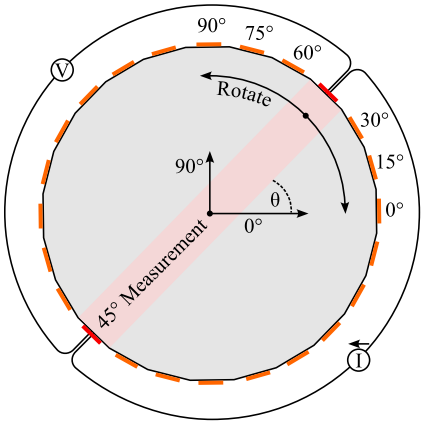
Configuration (b), SCL-2F (Figure 6.16b), applies full-face SCL electrodes only to the two facets addressed for a given θ_i, while all remaining facets remain uncoated. This setup comes closest to a two-probe coupon-like boundary condition with well-defined electrodes, because current is injected over the full facet area and no passive metallization is present that could shunt current along the perimeter. Consequently, SCL-2F is described by the (*base*) model (see Section 6.3.1) and



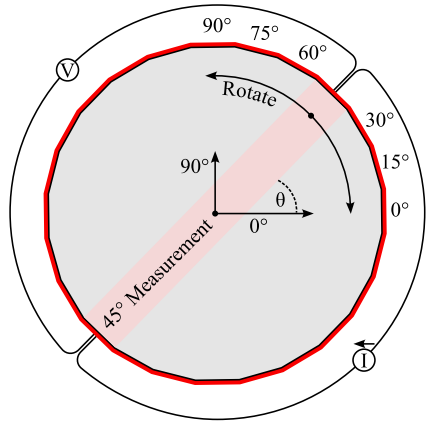
(a) SCL-0: Direct probe point contact, no SCL.



(b) SCL-2F: Face-striped SCL electrodes, measurement faces only.



(c) SCL-24F: Face-striped SCL electrodes, all faces.



(d) SCL-CC: Continuous SCL coating of outer surface.

Figure 6.16: Schematics of electrode configurations for the 24-sided specimen for resistance measurements.

is used as the reference configuration for comparisons across FAW, orientations, and model variants. Although the resulting current field is not strictly one-dimensional due to anisotropy and the prismatic boundary, SCL-2F minimizes avoidable boundary short-circuiting and provides the most direct link between the measured $R(\theta_i)$ dataset and the intended (*base*) interpretation.

Configuration (c), SCL-24F (Figure 6.16c), is designed for efficiency during a full circumferential sweep: all facets are partially metallized ($l_{el} \approx 10\,mm < s \approx 16.46\,mm$) in a single application step, and the measurement can be performed for all θ_i without intermediate cleaning, recoating, or drying. The trade-off is that passive inner electrodes on unaddressed facets modify the boundary conditions and introduce additional shunting paths that alter current spreading and the effective resistance. This configuration is captured by the (*in*) model (see Section 6.3.3), which explicitly accounts for the presence of passive metallized segments or inner electrodes and the resulting topology-dependent current redistribution. SCL-24F thus represents a practical compromise: it improves repeatability of electrode placement and reduces preparation time substantially, at the cost of requiring the (*in*) interpretation rather than the (*base*) reference model.

Configuration (d), SCL-CC (Figure 6.16d), represents the apparent topological limit of the (*in*) model concept: as the metallized electrode length approaches the the total face length s, the perimeter becomes a nearly closed SCL ring. In the ideal limiting case $\rho_{\mathrm{SCL}} \ll \rho_{\mathrm{CFRP}}$, the measured resistance would be expected to be dominated by the SCL coating, so that the CFRP contribution becomes progressively masked by perimeter short-circuiting. However, literature and previous measurements indicate $\rho_{\mathrm{SCL}} \approx 8.0 \times 10^{-7}$–$4.8 \times 10^{-6}\,\Omega\,\mathrm{m}$, while typical longitudinal CFRP resistivities are $\rho_{\parallel} \approx (1.14\text{–}5.29) \times 10^{-5}\,\Omega\,\mathrm{m}$ [217], i.e., the contrast is on the order of one magnitude rather than multiple decades. Under these conditions, SCL-CC cannot be treated as an ideal short-circuit boundary; instead, the measured response remains a coupled SCL/CFRP system. As such, SCL-CC provides an informative upper-bound modification of the boundary conditions and a benchmark for the robustness range of the (*in*) topology interpretation when approaching the closed-ring limit.

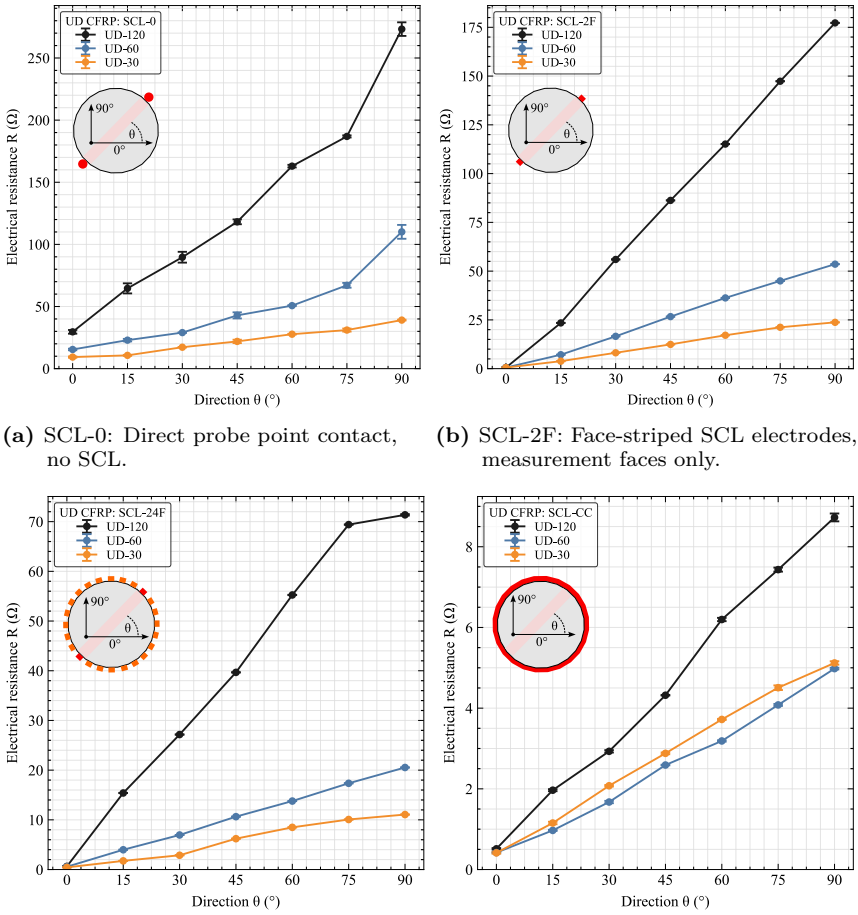
To investigate whether the extracted principal resistivities are robust with respect to microstructure-driven changes in electrical path formation, all electrode configurations in Figure 6.16 were applied consistently to UD CFRP laminates manufactured from plies with different areal weights (FAW = 30, 60, and 120 gsm). Although the global laminate thickness and φ_f are comparable, varying FAW

changes the effective ply thickness and the number of ply interfaces for a fixed laminate build, and it can promote subtle differences in local fiber packing, resin-rich features, and interlayer connectivity. These effects directly influence the density and quality of fiber–fiber transfer sites (contacts and near-contacts) that govern transverse and through-thickness current transport as already seen and discussed in Section 6.4.2. In addition, QI CFRP was characterized with the same measurement configurations as an external benchmark for the experimental procedure and for qualitative comparison; however, because no dedicated analytical polygon model is formulated for QI layups in the present work, the QI results are interpreted descriptively rather than through parameter identification of $\rho_{\parallel}$ and $\rho_{\perp}$.

24 Sided Specimen: UD CFRP

Reference SCL-2F, Config (b). The reference configuration SCL-2F, shown in Figure 6.17b, provides the most direct experimental realization of the base-model boundary conditions, since only the two addressed faces are metallized while all other facets remain electrically inactive. Across all UD configurations, the measured directional response exhibits a near-linear increase in $R_{\mathrm{meas}}(\theta_i)$ over the sampled transverse regime from 15° to 90°. This behavior is consistent with the base-model interpretation that, once θ_i exceeds the transition regime, the effective resistance is governed predominantly by contact-controlled transverse transport and its geometric projection. Notably, the transition itself cannot be resolved experimentally: for the 24-sided geometry the predicted transition angle α lies below the first measurable increment at 15°, such that any non-monotonic or unsteady behavior between 0° and 15° would remain undetected. While the 0° measurement appears broadly consistent with the overall modulation, it must be interpreted separately because different conduction mechanisms dominate at $\theta = 0°$ (fiber-dominated longitudinal transport) compared to $\theta \geq 15°$ (mixed transverse and through-thickness transfer governed by fiber–fiber contacts and near-contacts), and no model-based evidence exists that the response must remain strictly monotonic in the unmeasured range.

A comparison of the 0° measurements across FAW (Figure 6.18a) shows essentially identical resistances for UD-30, UD-60, and UD-120. This is expected within the polygon model framework: for 0° the response is dominated by longitudinal fiber conduction, and since laminate thickness and φ_f are comparable, the effective conducting cross section and thus $R_{\mathrm{meas}}(0°)$ should not change appreciably with



(a) SCL-0: Direct probe point contact, no SCL.

(b) SCL-2F: Face-striped SCL electrodes, measurement faces only.

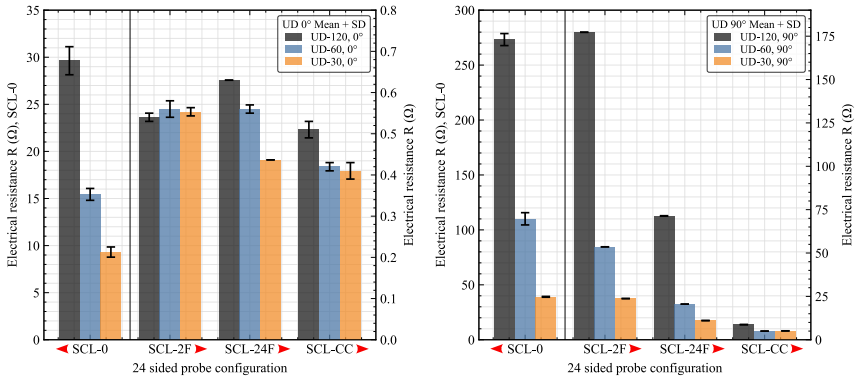
(c) SCL-24F: Face-striped SCL electrodes, all faces.

(d) SCL-CC: Continuous SCL coating of outer surface.

Figure 6.17: Electrical resistance measurements for the 24-sided probe of UD CFRP with different fiber areal weights. **Note:** The y-axis limits differ between panels.

FAW. In contrast, for larger angles the resistance increases systematically with FAW, following $R_{\text{meas}}^{\text{UD-120}}(\theta_i) > R_{\text{meas}}^{\text{UD-60}}(\theta_i) > R_{\text{meas}}^{\text{UD-30}}(\theta_i)$ (see also the 90° comparison in Figure 6.18b). This trend is physically plausible because the transverse response is controlled by electrical path formation through a sparse network of fiber transfer sites. For otherwise comparable laminates, varying FAW changes the effective ply thickness and the number of inter-ply interfaces, which can modify interlayer connectivity, resin-rich features, and the probability of short transfer paths; the associated microstructure trends and their implications for path formation are discussed in Section 6.4.2. In this context, the notably lower transverse-direction resistances observed for the thin-ply configurations are consistent with an increased likelihood of conductive pathways, including contributions in thickness direction that are intrinsically coupled into the measured $\rho_{\perp}$ because the electrodes span the full laminate thickness.

The base-model parameter identification for SCL-2F (Table 6.5) reflects these observations: $\rho_{\parallel}$ remains nearly constant across FAW, whereas $\rho_{\perp}$ decreases markedly for thinner plies. The UD-120 values fall within typical literature ranges for standard/medium-ply UD CFRP [55, 217], while the thin ply configurations yield substantially reduced effective $\rho_{\perp}$, supporting the interpretation that FAW-driven microstructural changes predominantly affect contact-controlled transport rather than longitudinal fiber-dominated conduction.



(a) UD CFRP 0° measurement. **(b)** UD CFRP 90° measurement.

Figure 6.18: 0° and 90° comparison of the electrical resistance measurements for the 24-sided probe of UD CFRP.

SCL-24F, Config (c). The SCL-24F configuration (Figure 6.17c) exhibits an overall directional resistance modulation that is qualitatively similar to the SCL-2F reference, i.e., a largely monotonic and approximately linear increase of $R_{\mathrm{meas}}(\theta_i)$ over the transverse regime $15^\circ \leq \theta_i \leq 90^\circ$. Although, UD-120 shows an uncertain 90° measurement point at $71.37\,\Omega$ that deviates from the otherwise smooth angular progression observed across the remaining angles. Compared to SCL-2F, the absolute resistance level is reduced across the transverse angles, consistent with additional perimeter shunting introduced by the passive metallization or inner electrodes on non-addressed faces.

At 0°, SCL-24F yields sub-ohmic resistances that remain in the same order of magnitude as SCL-2F, as expected for a predominantly fiber-dominated longitudinal response. However, in contrast to SCL-2F, where $R_{\mathrm{meas}}(0^\circ)$ is essentially FAW-independent, SCL-24F exhibits a systematic FAW-dependent drift already at 0°, with $R_{\mathrm{meas}}^{\text{UD-120}}(0^\circ) \approx 0.63\,\Omega$, $R_{\mathrm{meas}}^{\text{UD-60}}(0^\circ) \approx 0.56\,\Omega$, and $R_{\mathrm{meas}}^{\text{UD-30}}(0^\circ) \approx 0.44\,\Omega$, i.e., $R_{\mathrm{meas}}^{\text{UD-120}}(\theta_i) > R_{\mathrm{meas}}^{\text{UD-60}}(\theta_i) > R_{\mathrm{meas}}^{\text{UD-30}}(\theta_i)$ even in the nominally longitudinal case. A plausible electrotechnical interpretation is that the passive inner electrodes adjacent to the active measurement faces modify the local current injection boundary condition: the nearby metallized facets act as low-resistance equipotential regions, which promotes circumferential current redistribution near the electrode edges and increases the degree of local transverse current transfer required to satisfy the altered boundary constraints. As a result, a small mixed-mode contribution is superimposed onto the otherwise longitudinal response, and this contribution can inherit microstructure sensitivity that would otherwise manifest primarily at larger θ_i. This coupling mechanism is not explicitly represented in the current (*in*) formulation and could, in principle, be parameterized by an additional near-field coupling term that depends on the distance between the active electrodes and the nearest passive metallized surfaces.

In the transverse regime $15^\circ \leq \theta_i \leq 90^\circ$, the FAW ranking remains consistent with the SCL-2F trends, and the identified transverse resistivity $\rho_\perp$ obtained from SCL-24F remains close to the SCL-2F reference, with deviations within approximately -7% to $+14\%$ across the investigated UD variants while maintaining high fit qualities ($R^2 \approx 0.96$–1.00; Table 6.5). The sign of the deviation changes between samples and therefore does not indicate a systematic bias; rather, the observed scatter is consistent with secondary experimental influences such as small variations in manual SCL application (electrode footprint and edge definition), local coating thickness variations, and specimen-to-specimen contact condition variability. In contrast, $\rho_\parallel$ shows a systematic reduction relative to

SCL-2F (approximately −28% to −53% across FAW), consistent with the interpretation that passive metallization primarily perturbs the near-electrode current density distribution and thus the effective longitudinal contribution captured by the parameter identification; such near-field coupling effects are not explicitly represented in the current (*in*) model formulation and therefore constitute a clear avenue for future model refinement.

Table 6.5: Fit quality and principal resistivities for SCL-2F and SCL-24F. Values in parentheses denote the relative deviation with respect to SCL-2F within the same sample.

Sample	Config	Model	$\rho_{\parallel}$ ($\Omega\,m$)	$\rho_{\perp}$ ($\Omega\,m$)	R^2 (–)
UD-120	SCL-2F	base	6.87×10^{-5} (0.0%)	1.15×10^{-1} (0.0%)	1.00
UD-120	SCL-24F	in	4.92×10^{-5} (−28.3%)	1.17×10^{-1} (+1.8%)	0.98
UD-60	SCL-2F	base	7.09×10^{-5} (0.0%)	3.50×10^{-2} (0.0%)	1.00
UD-60	SCL-24F	in	4.39×10^{-5} (−38.1%)	3.25×10^{-2} (−7.1%)	1.00
UD-30	SCL-2F	base	6.99×10^{-5} (0.0%)	1.58×10^{-2} (0.0%)	0.99
UD-30	SCL-24F	in	3.28×10^{-5} (−53.0%)	1.80×10^{-2} (+13.9%)	0.96

SCL-CC, Config (d). The SCL-CC configuration (Figure 6.17d) yields the lowest absolute resistance levels among all investigated setups, consistent with the intended boundary condition: a continuous circumferential SCL coating acts as a low-resistance shunt along the specimen perimeter and thereby bypasses a substantial fraction of the otherwise contact-controlled CFRP transport, particularly as the measurement direction approaches the transverse regime. In contrast to interpretations based on an increasingly long perimeter path of SCL, the measured angular response remains nearly linear even at elevated angles. This indicates that the finite line resistance of the SCL circumference does not become the only contribution over the explored range; instead, the SCL primarily enforces a quasi-equipotential boundary and reduces sensitivity to angle-dependent current spreading. Any residual increase toward 90° is therefore more consistently attributed to the growing contribution of transverse-dominated CFRP transport and current-transfer effects at the electrode–laminate interface, rather than to a pure "long-path" conductive path along the SCL, as discussed in Section 6.4.1.

The FAW dependence is still visible but markedly reduced compared to SCL-2F and SCL-24F, with a trend of $R_{\mathrm{meas}}^{\mathrm{UD\text{-}120}}(\theta_i) > R_{\mathrm{meas}}^{\mathrm{UD\text{-}60}}(\theta_i) \approx R_{\mathrm{meas}}^{\mathrm{UD\text{-}30}}(\theta_i)$, which is consistent with the expectation that, once the perimeter shunt dominates,

microstructure-driven variations in CFRP transfer-site connectivity only weakly influence the overall response.

At 0°, the resistance is in the same order of magnitude as for SCL-2F and appears slightly lower. A plausible interpretation is that, for $\theta = 0°$, the longitudinal CFRP path between opposite faces represents an exceptionally low-resistance route due to fiber-dominated conduction and the shortest effective through-material connection, such that the total response is governed by the parallel competition between (i) the direct CFRP path and (ii) the longer circumferential SCL path; in this regime, the longitudinal CFRP contribution can remain comparable to or even dominate the coupled system response. For increasing θ_i, the CFRP contribution becomes progressively more resistive, and the current preferentially redistributes into the SCL circumference, leading to the overall suppressed resistance magnitude and the reduced FAW sensitivity.

Because SCL-CC represents the topological limit of the perimeter-metallization concept and the measured response is strongly governed by the coupled SCL/CFRP boundary condition, the inverse identification of intrinsic CFRP $\rho_{\parallel}$ and $\rho_{\perp}$ is not meaningful within the scope of the current analytical formulations. Accordingly, SCL-CC is used here primarily as a qualitative boundary-condition benchmark rather than as a configuration for quantitative resistivity extraction.

SCL-0, Config (a). The SCL-0 configuration (Figure 6.17a) differs fundamentally from the SCL-based electrode setups because current injection is realized by direct multimeter probe contact without a defined metallized electrode footprint. As a result, the measured angular response between 15° and 90° is no longer strictly linear in the same manner as observed for SCL-2F. In particular, the high-angle measurements exhibit an apparent upward shift relative to a linear continuation from intermediate angles, most pronounced at 90°, indicating that the effective boundary condition at the contact is not stable across θ_i. In absolute terms, R_{meas} is substantially higher than for SCL-2F over the full angular range, which is consistent with (i) the strongly reduced effective electrode area (probe tip instead of full-facet electrodes), leading to increased current constriction and a more localized current density field, and (ii) additional contact resistances at the probe–surface interface that are not controlled by a reproducible SCL coating and can vary with contact force, surface roughness, and local fiber exposure.

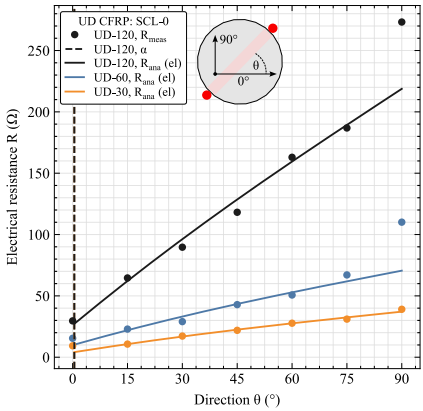
Despite these limitations, the FAW ordering remains preserved across angles and is visible even at 0°, i.e., $R_{\mathrm{meas}}^{\mathrm{UD\text{-}120}}(\theta_i) > R_{\mathrm{meas}}^{\mathrm{UD\text{-}60}}(\theta_i) > R_{\mathrm{meas}}^{\mathrm{UD\text{-}30}}(\theta_i)$. The presence

of this ordering in the nominally longitudinal case is physically plausible under probe contact because the injected current couples into only a limited number of surface fibers and local fiber bundles; since it is unlikely that the probes repeatedly contact the same set of fibers and micro-contacts, the measurement becomes sensitive to local connectivity and mixed-mode transfer near the contact, thereby allowing FAW-driven differences in transverse/through-thickness path formation to bias $R_{\mathrm{meas}}(0^\circ)$. In other words, SCL-0 does not isolate a purely fiber-dominated longitudinal response but rather superimposes local transfer and contact effects onto the nominal 0° measurement.

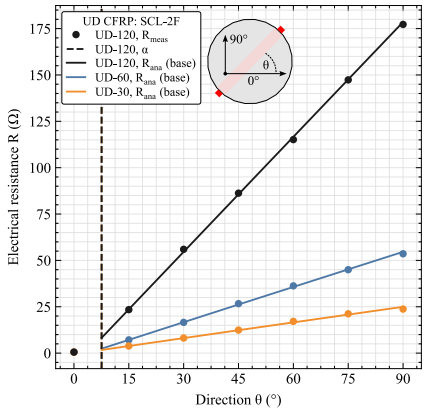
Consistent with this interpretation, the (*el*) model fit quality is poor compared to the SCL-2F reference, and the identified principal resistivities become physically implausible for quantitative material characterization (Table 6.6). In particular, $\rho_{\parallel}$ is strongly overestimated for UD-120 (+235.5% relative to SCL-2F) and still elevated for UD-60 (+67.5%), while UD-30 happens to agree closely (+2.3%). Simultaneously, $\rho_{\perp}$ increases for all FAW levels (+19.2% to +63.6%). These trends can be rationalized by the fact that SCL-0 violates key assumptions of the analytical boundary condition: the current injection is not uniform over a facet, the effective electrode footprint is not well defined, and contact resistances introduce an additional (largely angle-independent) resistance contribution that is not represented in the present (*el*) model. Together with the strong sensitivity to probe placement (and the established exponential resistance increase with electrode misplacement [55]), the configuration is therefore ill-conditioned for extracting reliable $\rho_{\parallel}$ and $\rho_{\perp}$ values. Consequently, SCL-0 is suitable primarily for qualitative trend checks, whereas quantitative resistivity identification between two probes should rely on configurations with defined and repeatable boundary electrodes (SCL-2F).

Table 6.6: Fit quality and principal resistivities for SCL-0 Values in parentheses denote the relative deviation with respect to SCL-2F within the same sample.

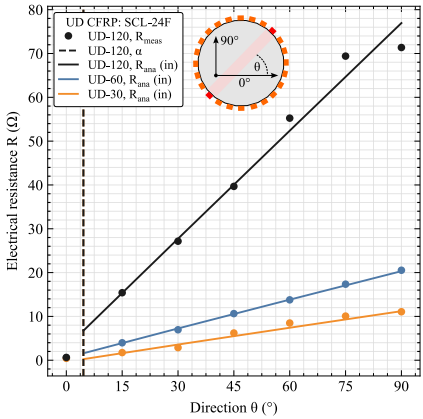
Sample	**Config**	**Model**	$\boldsymbol{\rho_{\parallel}}$ ($\Omega\,m$)	$\boldsymbol{\rho_{\perp}}$ ($\Omega\,m$)	$\boldsymbol{R^2}$ (–)
UD-120	SCL-0	el	2.30×10^{-4} (+235.5%)	1.37×10^{-1} (+19.2%)	0.89
UD-60	SCL-0	el	1.19×10^{-4} (+67.5%)	4.63×10^{-2} (+32.1%)	0.68
UD-30	SCL-0	el	7.15×10^{-5} (+2.3%)	2.58×10^{-2} (+63.6%)	0.99



(a) SCL-0: Direct probe point contact, no SCL.



(b) SCL-2F: Face-striped SCL electrodes, measurement faces only.



(c) SCL-24F: Face-striped SCL electrodes, all faces.

(d) SCL-CC: Continuous SCL coating of outer surface - model not applicable.

Figure 6.19: Analytical electrical resistance modulation for the 24-sided probe of UD CFRP with different fiber areal weights. **Note:** The y-axis limits differ between panels.

24 Sided Specimen: QI CFRP

Quasi-isotropic CFRP measurements are used to evaluate the measurement method and the associated contact configurations. Accordingly, the results are interpreted in terms of measurement robustness and contact-induced effects. The directional datasets in Figure 6.21 and the mean resistance per configuration in Figure 6.20 indicate that the SCL configurations (SCL-2F, SCL-24F, and SCL-CC) yield sub-ohm resistance levels, comparable in magnitude to those typically measured for UD CFRP at 0°.

This outcome may appear surprising at first glance, but it follows naturally from the QI stacking sequence. Because 0°, ±45°, and 90° plies are present, at least one ply orientation is usually close to the measurement axis, i.e., the line connecting the electrodes. Therefore, multiple low-resistance in-plane pathways contribute in parallel. As a consequence, resistivity becomes very low and there is no significant directional difference.

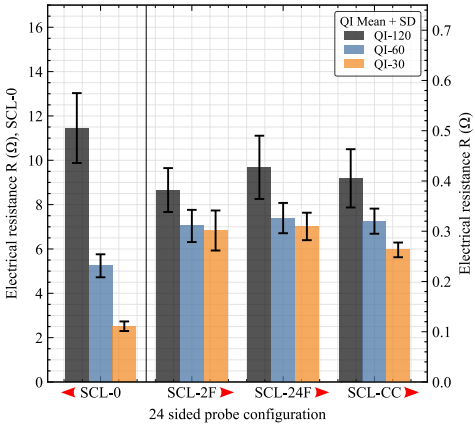
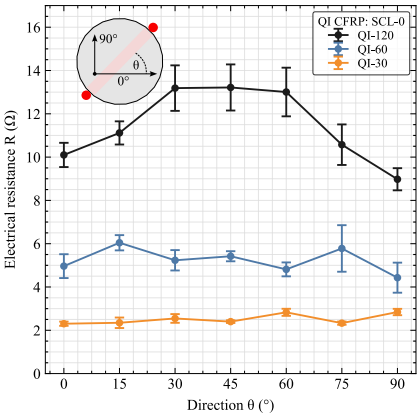


Figure 6.20: Mean values of electrical resistance measurements for the 24-sided probe of QI CFRP.

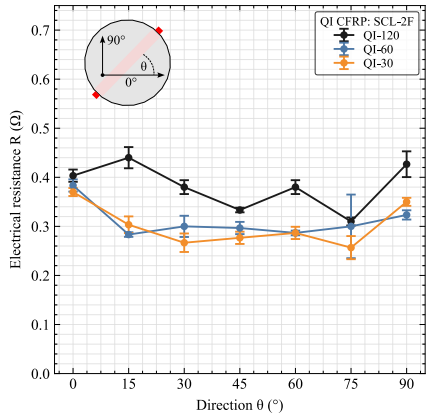
From a purely geometric expectation, intermediate directions such as 15°, 30°, 60°, and 75° could be expected to yield marginally higher resistances. However, the measured QI datasets do not exhibit a distinct and quantifiable minimum at these angles (Figure 6.21), suggesting that the effective contact probability and current redistribution in the QI architecture are sufficiently high that differences between these intermediate angles and the principal directions cannot be reliably resolved

within the resolution of the present measurement. A plausible interpretation is that inter-ply fiber crossings and the associated density of contact points provide additional transfer opportunities compared to UD laminates, thereby reducing the contrast between directly fiber aligned and misaligned measurement angles and masking any small-angle benefit.

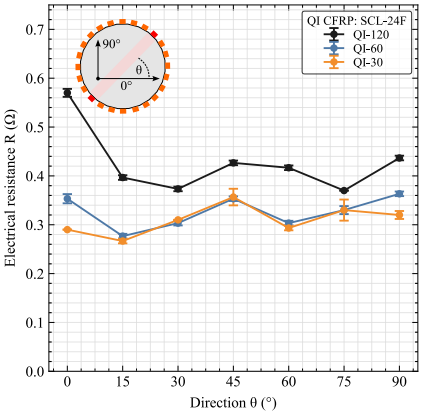
The following QI results align with the expected behavior based on the preceding interpretations. The configuration without SCL (SCL-0) exhibits qualitatively different behavior. As shown in Figure 6.20, the QI mean resistances in SCL-0 are substantially higher than the SCL-based configurations (multi-ohm instead of sub-ohm), reflecting the reduced and ill-defined probe contact area and the presence of contact resistances; nevertheless, the QI SCL-0 means are lower than the corresponding UD 0° SCL-0 values discussed previously, which is consistent with the notion that fiber crossings and a higher density of transfer sites can reduce the sensitivity to probe placement and local contact variability. Across all QI configurations, the FAW trend 120 > 60 > 30 gsm is retained in the mean values, most clearly for SCL-0 and still discernible for SCL-2F/24F/CC (Figure 6.20). This indicates that, in addition to interlaminar cross-fiber contacts, intralaminar packing and the FAW-dependent microstructure effects discussed for UD CFRP continue to influence the effective resistance of QI laminates, even though the QI architecture provides multiple fiber orientations and therefore reduces the directional contrast. Overall, the QI results support the experimental consistency of the electrode configurations and reinforce the interpretation that FAW-driven changes in connectivity can persist as a secondary influence even in layups with an inherently higher contact density.



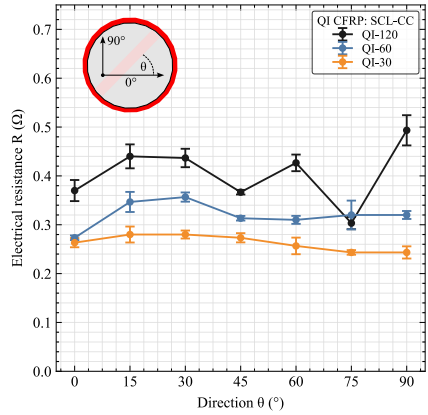
(a) SCL-0: Direct probe point contact, no SCL.



(b) SCL-2F: Face-striped SCL electrodes, measurement faces only.



(c) SCL-24F: Face-striped SCL electrodes, all faces.



(d) SCL-CC: Continuous SCL coating of outer surface.

Figure 6.21: Electrical resistance measurements for the 24-sided probe of QI CFRP with different fiber areal weights. **Note:** The y-axis limits differ between panels.

6.5 Conclusions

This chapter established a methodology to identify in-plane electrical anisotropy in CFRP from angle-dependent two-terminal resistance measurements on n-gonal prismatic specimens. The key outcome is a geometry-consistent transfer of coupon-based *effective path length* and *effective cross section* concepts [55] to regular polygons. This approach enables the acquisition of a complete set of angle-dependent resistance measurements on a single specimen, which is then mapped to the orthotropic principal resistivities $\rho_{\parallel}$ and $\rho_{\perp}$.

The identification strategy was formalized as an analytical model in which the electrode topology is treated as a first-order boundary condition. The base formulation assumes full-face electrodes on the addressed facets. Under this reference configuration, UD CFRP measurements yielded resistivities in literature-consistent magnitudes. The identified longitudinal resistivity $\rho_{\parallel}$ remained essentially invariant across FAW for comparable laminate thickness. In contrast, the transverse-effective resistivity $\rho_{\perp}$ showed a strong FAW dependence, with thinner plies exhibiting lower resistance and reduced effective anisotropy. Micrograph-derived nearest-neighbor spacing metrics confirmed a higher density of fiber–fiber transfer opportunities at lower FAW, indicating that $\rho_{\perp}$ represents an effective mixed-mode quantity governed by coupled transverse and through-thickness transfer.

Two practically relevant setup variations were evaluated within the same modeling framework: finite probe-like contacts and passive metallization on non-addressed faces. Both configurations introduce strong contact, constriction, or shunting effects that can dominate the measured response. Therefore, they are not suitable for quantitative identification of the resistivities of the material. However, they can be described and interpreted qualitatively within the model.

The methodology was also applied to QI laminates, which—as expected—exhibited nearly angle-invariant resistivity. The measured level was on the same order and slightly below the UD longitudinal response, indicating that the increased density of fiber intersections promotes electrical transport.

Future work could establish a measurement standard for anisotropic laminates that enables reproducible identification of fiber-orientation-dependent resistivities.

7 Summary

This thesis targets non-destructive, experimentally efficient quantification of anisotropic in-plane transport in continuous-fiber CFRP laminates at the laminate scale. Many existing approaches are labor-intensive, require multiple specimens and fiber orientations, or do not consistently relate measured fields to the underlying laminate architecture. To address this gap, the following research questions are answered by three complementary model-based methodologies.

Research Question 1 (Fiber Orientation Detection): How can the ply-level fiber orientation layup in CFRP laminates be determined non-destructively to enable a quantitative interpretation of anisotropic in-plane transport behavior? This question is answered by establishing a depth-resolved ultrasonic methodology that delivers a structurally meaningful ply-level orientation description through the laminate thickness. The approach bridges conventional defect inspection and microstructural reference methods. It does not resolve individual fibers; instead, it extracts layer-wise orientation trends from volumetric pulse–echo data via Fourier-domain texture analysis of C-scan slices. Dominant fiber directions appear as angular peaks and are reliably selected using the peak-scoring metric Q_k. This yields a depth-resolved fiber orientation descriptor $\Theta(z_k)$ that serves as the architectural reference for transport characterization. Reliability is demonstrated for unidirectional, quasi-isotropic, and Bouligand architectures across industrially relevant thicknesses and ply counts. Disturbance analyzes define practical limits: near-surface regions are affected by strong front-/back-wall reflections, and porosity or geometric features broaden spectral peaks and reduce directional resolvability.

Research Question 2 (Anisotropic Thermal Properties): How can anisotropic in-plane thermal transport in CFRP laminates be determined efficiently by non-destructive testing and interpreted using an appropriate analytical model? This question is answered by a Heat-Spot Thermography (HST) measurement-and-evaluation route that reconstructs the in-plane orthotropic thermal diffusivity

response of unidirectional CFRP from a single specimen under controlled boundary conditions. Localized excitation and infrared field acquisition are combined with a closed-form orthotropic diffusion model that enforces symmetry and principal directions. A key outcome is the interpretation of what HST measures under a prescribed heat-flux boundary condition. The direction-dependent observable corresponds to an inverse-diffusivity projection ($1/r_\theta$) rather than α_θ, except on the principal axes. Two consistent extraction routes are provided, based on Gaussian-profile broadening and isotherm evolution. They offer a robustness–efficiency trade-off without changing the inferred angular dependence. Measurements on neat polymers and unidirectional CFRP demonstrate single-specimen identification of $\alpha_\parallel$ and $\alpha_\perp$ with anisotropy ratios in the expected range. A generalized rule-of-mixtures formulation further enables constituent-level reconstruction from the measured diffusivity response.

Research Question 3 (Anisotropic Electrical Properties): How can anisotropic in-plane electrical transport in CFRP laminates be determined efficiently by non-destructive testing and interpreted using an appropriate analytical model? This question is answered by a geometry-aware resistance-characterization concept using regular prismatic n-gonal specimens. The geometry enables symmetry-complete acquisition of angle-dependent two-terminal resistances on a single sample and their mapping to the orthotropic principal resistivities $\rho_\parallel$ and $\rho_\perp$. The identification strategy is formulated as an analytical model in which electrode topology is treated as a first-order boundary condition. Under well-defined full-face electrode configurations, the method yields literature-consistent resistivity magnitudes for unidirectional CFRP. The results show that $\rho_\parallel$ remains essentially invariant with fiber areal weight for comparable laminate thickness. In contrast, the transverse-effective resistivity $\rho_\perp$ is strongly dependent on the ply architecture, consistent with the microstructure-governed inter-fiber contact network controlling off-axis conduction. Electrode variations clarify applicability: probe-like finite contacts and passive metallization on non-addressed faces introduce constriction or shunting effects that can dominate the response, and are therefore unsuitable for quantitative identification without additional modeling. Quasi-isotropic laminates exhibit an almost angle-invariant response in the same order of magnitude as the unidirectional longitudinal values.

In synthesis, the thesis provides a unified characterization framework that connects laminate architecture and transport in a model-consistent way. The ultrasonic descriptor $\Theta(z_k)$ supplies the ply-resolved structural reference, enables thermal and electrical measurements to be interpreted against the actual fiber orientation

state. The transport chapters further show that principal in-plane properties can be identified from single-specimen data when boundary conditions and electrode or heat-input geometries are explicitly prescribed and incorporated into an analytical evaluation that preserves orthotropic symmetry. A coherent central result is that transverse-dominated conductivities are the most microstructure-sensitive metrics. They reflect how effectively charge or heat transfers between fiber bundles through the matrix and interfaces, which is governed by the connectivity of conductive pathways. Accordingly, the thesis defines quantitative validity criteria for each method and provides a basis for standardized, anisotropy-aware reporting of laminate-scale transport properties.

Usage of AI-Based Tools

AI-based tools were used selectively during the preparation of this thesis as supportive aids in the research and writing process. In particular, tools such as ChatGPT by OpenAI Ireland Ltd, Overleaf AI writing tools by Digital Science UK Limited and Writeful by ThinqLab Ltd were employed for language refinement, text restructuring, and improvement of clarity and readability. The use of these tools was limited to auxiliary tasks and did not replace the author's own scientific reasoning, interpretation of the results, or critical evaluation of sources. All scientific content, methodological developments, data analysis, and conclusions presented in this thesis are the sole responsibility of the author and were independently derived in accordance with the principles of good scientific practice.

Bibliography

[1] M. Tane, H. Okuda, and F. Tanaka. "Nanocomposite Microstructures Dominating Anisotropic Elastic Modulus in Carbon Fibers." In: *Acta Materialia* 166 (Mar. 2019), pp. 75–84. ISSN: 13596454. DOI: 10.1016/j.actamat.2018.12.029.

[2] M. J. Behr, B. G. Landes, B. E. Barton, M. T. Bernius, G. F. Billovits, E. J. Hukkanen, J. T. Patton, W. Wang, C. Wood, D. T. Keane, J. E. Rix, and S. J. Weigand. "Structure-Property Model for Polyethylene-Derived Carbon Fiber." In: *Carbon* 107 (Oct. 2016), pp. 525–535. ISSN: 00086223. DOI: 10.1016/j.carbon.2016.06.032.

[3] H. Schürmann. *Konstruieren mit Faser-Kunststoff-Verbunden: mit 39 Tabellen*. 2., bearb. und erw. Aufl. VDI-[Buch]. Berlin Heidelberg: Springer, 2007. 672 pp. ISBN: 978-3-540-72189-5.

[4] M. Thor, M. G. R. Sause, and R. M. Hinterhölzl. "Mechanisms of Origin and Classification of Out-of-Plane Fiber Waviness in Composite Materials—A Review." In: *Journal of Composites Science* 4.3 (Sept. 4, 2020), p. 130. ISSN: 2504-477X. DOI: 10.3390/jcs4030130.

[5] M. Mehdikhani, L. Gorbatikh, I. Verpoest, and S. V. Lomov. "Voids in Fiber-Reinforced Polymer Composites: A Review on Their Formation, Characteristics, and Effects on Mechanical Performance." In: *Journal of Composite Materials* 53.12 (May 2019), pp. 1579–1669. ISSN: 0021-9983, 1530-793X. DOI: 10.1177/0021998318772152.

[6] A. S. Mahmood, J. Summerscales, and M. N. James. "Resin-Rich Volumes (RRV) and the Performance of Fibre-Reinforced Composites: A Review." In: *Journal of Composites Science* 6.2 (Feb. 10, 2022), p. 53. ISSN: 2504-477X. DOI: 10.3390/jcs6020053.

[7] D. A. Jesson and J. F. Watts. "The Interface and Interphase in Polymer Matrix Composites: Effect on Mechanical Properties and Methods for Identification." In: *Polymer Reviews* 52.3 (July 2012), pp. 321–354. ISSN: 1558-3724, 1558-3716. DOI: 10.1080/15583724.2012.710288.

[8] Y. Weitsman. "Residual Thermal Stresses Due to Cool-Down of Epoxy-Resin Composites." In: *Journal of Applied Mechanics* 46.3 (Sept. 1, 1979), pp. 563–567. ISSN: 0021-8936, 1528-9036. DOI: 10.1115/1.3424606.

[9] A. Mirzaei and M. Shokrieh. "Evolution of the Temperature Rise and Damage in Laminated Composites with Stress Concentration under Fatigue Loading." In: *Composites Part B: Engineering* 254 (Apr. 2023), p. 110607. ISSN: 13598368. DOI: 10.1016/j.compositesb.2023.110607.

[10] N. Forintos and T. Czigany. "Multifunctional Application of Carbon Fiber Reinforced Polymer Composites: Electrical Properties of the Reinforcing Carbon Fibers – A Short Review." In: *Composites Part B: Engineering* 162 (Apr. 2019), pp. 331–343. ISSN: 13598368. DOI: 10.1016/j.compositesb.2018.10.098.

[11] A. V. Shiverskii, M. Owais, B. Mahato, and S. G. Abaimov. "Electrical Heaters for Anti/De-Icing of Polymer Structures." In: *Polymers* 15.6 (Mar. 22, 2023), p. 1573. ISSN: 2073-4360. DOI: 10.3390/polym15061573.

[12] L. C. Kontaxis, I. E. Chontzoglou, and G. C. Papanicolaou. "Efficient Use of Carbon Fibers as Heating Elements for Curing of Epoxy Matrix Composites." In: *Molecules* 26.16 (Aug. 23, 2021), p. 5095. ISSN: 1420-3049. DOI: 10.3390/molecules26165095.

[13] R. Li, W. Xu, and D. Zhang. "Impacts of Thermal and Mechanical Cycles on Electro-Thermal Anti-Icing System of CFRP Laminates Embedding Sprayable Metal Film." In: *Materials* 14.7 (Mar. 24, 2021), p. 1589. ISSN: 1996-1944. DOI: 10.3390/ma14071589.

[14] Y. Ma, Z. Zheng, X. Liu, Y. Bao, and Y. Gong. "Joule Heating of Carbon Fiber Composites: Mechanisms, Quantification Methods, and Structural Design." In: *Composites Part A: Applied Science and Manufacturing* 200 (Jan. 2026), p. 109378. ISSN: 1359835X. DOI: 10.1016/j.compositesa.2025.109378.

[15] D. W. Hahn and M. N. Özişik. *Heat Conduction*. 1st ed. Wiley, 2012. ISBN: 978-0-470-90293-6. DOI: 10.1002/9781118411285.

[16] J. Crank. *The Mathematics of Diffusion*. 2. ed., repr. Oxford: Univ. Pr, 2011. 414 pp. ISBN: 978-0-19-853411-2.

[17] Z. Fang, M. Li, S. Wang, Y. Li, X. Wang, Y. Gu, Q. Liu, J. Tian, and Z. Zhang. "Geometrical Effect on Thermal Conductivity of Unidirectional Fiber-Reinforced Polymer Composite along Different In-plane Orientations." In: *Applied Composite Materials* 25.6 (Dec. 2018), pp. 1255–1268. ISSN: 0929-189X, 1573-4897. DOI: 10.1007/s10443-017-9664-y.

[18] S. Bard, F. Schönl, M. Demleitner, and V. Altstädt. "Influence of Fiber Volume Content on Thermal Conductivity in Transverse and Fiber Direction of Carbon Fiber-Reinforced Epoxy Laminates." In: *Materials* 12.7 (Apr. 2, 2019), p. 1084. ISSN: 1996-1944. DOI: 10.3390/ma12071084.

[19] T. Ishizaki and H. Nagano. "Measurement of 3D Thermal Diffusivity Distribution with Lock-in Thermography and Application for High Thermal Conductivity CFRPs." In: *Infrared Physics & Technology* 99 (June 2019), pp. 248–256. ISSN: 13504495. DOI: 10.1016/j.infrared.2019.04.023.

[20] T. Seong Jang, D. Soo Oh, J. Kyu Kim, K. In Kang, W. Ho Cha, and S. Woo Rhee. "Development of Multi-Functional Composite Structures with Embedded Electronics for Space Application." In: *Acta Astronautica* 68.1–2 (Jan. 2011), pp. 240–252. ISSN: 00945765. DOI: 10.1016/j.actaastro.2010.08.009.

[21] R. C. Progelhof, J. L. Throne, and R. R. Ruetsch. "Methods for Predicting the Thermal Conductivity of Composite Systems: A Review." In: *Polymer Engineering & Science* 16.9 (Sept. 1976), pp. 615–625. ISSN: 0032-3888, 1548-2634. DOI: 10.1002/pen.760160905.

[22] K. Pietrak and T. S. Wisniewski. "A Review of Models for Effective Thermal Conductivity of Composite Materials." In: *Journal of Power Technologies* 95 (2015), pp. 14–24.

[23] Y. Guo, K. Ruan, X. Shi, X. Yang, and J. Gu. "Factors Affecting Thermal Conductivities of the Polymers and Polymer Composites: A Review." In: *Composites Science and Technology* 193 (June 2020), p. 108134. ISSN: 02663538. DOI: 10.1016/j.compscitech.2020.108134.

[24] A. Salazar, M. Colom, and A. Mendioroz. "Determining the Thermal Diffusivity and the Principal Directions on Anisotropic Moving Samples with Laser-Spot Thermography." In: *International Journal of Heat and Mass Transfer* 176 (Sept. 2021), p. 121447. ISSN: 00179310. DOI: 10.1016/j.ijheatmasstransfer.2021.121447.

[25] A. Bedoya, A. Salazar, A. Mendioroz, and E. Marín. "Measuring the In-Plane Thermal Diffusivity of Anisotropic Solids by Lock-in Infrared Thermography: Laser-spot vs Laser-Line Heating." In: *Journal of Applied Physics* 135.13 (Apr. 7, 2024), p. 135102. ISSN: 0021-8979, 1089-7550. DOI: 10.1063/5.0198882.

[26] D. Chung. "Processing-Structure-Property Relationships of Continuous Carbon Fiber Polymer-Matrix Composites." In: *Materials Science and Engineering: R: Reports* 113 (Mar. 2017), pp. 1–29. ISSN: 0927796X. DOI: 10.1016/j.mser.2017.01.002.

[27] Q. Zhao, K. Zhang, S. Zhu, H. Xu, D. Cao, L. Zhao, R. Zhang, and W. Yin. "Review on the Electrical Resistance/Conductivity of Carbon Fiber Reinforced Polymer." In: *Applied Sciences* 9.11 (June 11, 2019), p. 2390. ISSN: 2076-3417. DOI: 10.3390/app9112390.

[28] H. C. Kim and S. K. See. "Electrical Properties of Unidirectional Carbon-Epoxy Composites in Wide Frequency Band." In: *Journal of Physics D: Applied Physics* 23.7 (July 14, 1990), pp. 916–921. ISSN: 0022-3727, 1361-6463. DOI: 10.1088/0022-3727/23/7/026.

[29] J. B. Park, T. K. Hwang, H. G. Kim, and Y. D. Doh. "Experimental and Numerical Study of the Electrical Anisotropy in Unidirectional Carbon-Fiber-Reinforced Polymer Composites." In: *Smart Materials and Structures* 16.1 (Feb. 1, 2007), pp. 57–66. ISSN: 0964-1726, 1361-665X. DOI: 10.1088/0964-1726/16/1/006.

[30] A. T. Ponomarenko, V. G. Shevchenko, S. V. Letyagin, and C. Klason. "Anisotropy of Conductivity in Carbon Fiber-Reinforced Plastics with Continuous Fibers." In: Smart Structures & Materials '95. Ed. by I. Chopra. San Diego, CA, May 8, 1995, pp. 831–840. DOI: 10.1117/12.208323.

[31] R. Holm. *Electric Contacts*. Berlin, Heidelberg: Springer Berlin Heidelberg, 1967. ISBN: 978-3-642-05708-3. DOI: 10.1007/978-3-662-06688-1.

[32] S. Kirkpatrick. "Percolation and Conduction." In: *Reviews of Modern Physics* 45.4 (Oct. 1, 1973), pp. 574–588. ISSN: 0034-6861. DOI: 10.1103/RevModPhys.45.574.

[33] R. Zhang, Y. Bin, R. Chen, and M. Matsuo. "Evaluation by Tunneling Effect for the Temperature-Dependent Electric Conductivity of Polymer-Carbon Fiber Composites with Visco-Elastic Properties." In: *Polymer Journal* 45.11 (Nov. 2013), pp. 1120–1134. ISSN: 0032-3896, 1349-0540. DOI: 10.1038/pj.2013.40.

[34] R. J. Hart and O. Zhupanska. "The Role of Electrical Anisotropy and Effective Conducting Thickness in Understanding and Interpreting Static Resistance Measurements in CFRP Composite Laminates." In: *Journal of Composite Materials* 54.7 (Mar. 2020), pp. 867–882. ISSN: 0021-9983, 1530-793X. DOI: 10.1177/0021998319870860.

[35] J. F. Nascimento, T. A. Ezquerra, F. J. Baltà-Calleja, and J. C. Seferis. "Anisotropy of Electrical Conductivity and Structure in Polymer-carbon Fiber Composite Materials." In: *Polymer Composites* 16.2 (Apr. 1995), pp. 109–113. ISSN: 0272-8397, 1548-0569. DOI: 10.1002/pc.750160202.

[36] J. Hong, P. Xu, H. Xia, Z. Xu, and Q.-Q. Ni. "Electromagnetic Interference Shielding Anisotropy Enhanced by CFRP Laminated Structures." In: *Composites Science and Technology* 203 (Feb. 2021), p. 108616. ISSN: 02663538. DOI: 10.1016/j.compscitech.2020.108616.

[37] E. Mikinka, T. Whittaker, P. Synaszko, W. Whittow, G. Zhou, and K. Dragan. "The Influence of Impact-Induced Damage on Electromagnetic Shielding Behaviour of Carbon Fibre Reinforced Polymer Composites." In: *Composites Part A: Applied Science and Manufacturing* 187 (Dec. 2024), p. 108464. ISSN: 1359835X. DOI: 10.1016/j.compositesa.2024.108464.

[38] J. Abry. "In Situ Detection of Damage in CFRP Laminates by Electrical Resistance Measurements." In: *Composites Science and Technology* 59.6 (May 1999), pp. 925–935. ISSN: 02663538. DOI: 10.1016/S0266-3538(98)00132-8.

[39] J. Wen, Z. Xia, and F. Choy. "Damage Detection of Carbon Fiber Reinforced Polymer Composites via Electrical Resistance Measurement." In: *Composites Part B: Engineering* 42.1 (Jan. 2011), pp. 77–86. ISSN: 13598368. DOI: 10.1016/j.compositesb.2010.08.005.

[40] P. Scholle and M. Sinapius. "Influence of the Electrical Anisotropy of Unidirectional Carbon Fiber Reinforced Plastics on Their Self Strain Sensing Properties." In: *Composites Part C: Open Access* 8 (July 2022), p. 100256. ISSN: 26666820. DOI: 10.1016/j.jcomc.2022.100256.

[41] X. P. V. Maldague. *Nondestructive Evaluation of Materials by Infrared Thermography*. London: Springer London, 1993. ISBN: 978-1-4471-1997-5. DOI: 10.1007/978-1-4471-1995-1.

[42] A. Chelly, S. Glass, J. Belhassen, and A. Karsenty. "Broad Review of Four-Point Probe Correction Factors: Enhanced Analytical Model Using Advanced Numerical and Experimental Cross-Examination." In: *Results in Physics* 48 (May 2023), p. 106445. ISSN: 22113797. DOI: 10.1016/j.rinp.2023.106445.

[43] L. Nelson, R. Smith, and M. Mienczakowski. "Ply-Orientation Measurements in Composites Using Structure-Tensor Analysis of Volumetric Ultrasonic Data." In: *Composites Part A: Applied Science and Manufacturing* 104 (Jan. 2018), pp. 108–119. ISSN: 1359835X. DOI: 10.1016/j.compositesa.2017.10.027.

[44] L. J. Nelson and R. A. Smith. "Fibre Direction and Stacking Sequence Measurement in Carbon Fibre Composites Using Radon Transforms of Ultrasonic Data." In: *Composites Part A: Applied Science and Manufacturing* 118 (Mar. 1, 2019), pp. 1–8. ISSN: 1359-835X. DOI: 10.1016/j.compositesa.2018.12.009.

[45] X. Yang and M. Kersemans. "On the Ultrasonic Characterization of the Stacking Sequence of CFRP Laminates." In: *NDT & E International* 138 (Sept. 2023), p. 102897. ISSN: 09638695. DOI: 10.1016/j.ndteint.2023.102897.

[46] W. J. Parker, R. J. Jenkins, C. P. Butler, and G. L. Abbott. "Flash Method of Determining Thermal Diffusivity, Heat Capacity, and Thermal Conductivity." In: *Journal of Applied Physics* 32.9 (Sept. 1961), pp. 1679–1684. ISSN: 0021-8979, 1089-7550. DOI: 10.1063/1.1728417.

[47] ASTM International. *ASTM E1461-13, Test Method for Thermal Diffusivity by the Flash Method*. 2013. DOI: 10.1520/E1461-13R22.

[48] J. A. Cape and G. W. Lehman. "Temperature and Finite Pulse-Time Effects in the Flash Method for Measuring Thermal Diffusivity." In: *Journal of Applied Physics* 34.7 (July 1, 1963), pp. 1909–1913. ISSN: 0021-8979, 1089-7550. DOI: 10.1063/1.1729711.

[49] L. M. Clark and R. E. Taylor. "Radiation Loss in the Flash Method for Thermal Diffusivity." In: *Journal of Applied Physics* 46.2 (Feb. 1, 1975), pp. 714–719. ISSN: 0021-8979, 1089-7550. DOI: 10.1063/1.321635.

[50] C. S. Welch, D. M. Heath, and W. P. Winfree. "Remote Measurement of In-Plane Diffusivity Components in Plates." In: *Journal of Applied Physics* 61.3 (Feb. 1987), pp. 895–898. ISSN: 0021-8979, 1089-7550. DOI: 10.1063/1.338140.

[51] F. Cernuschi, A. Russo, L. Lorenzoni, and A. Figari. "In-Plane Thermal Diffusivity Evaluation by Infrared Thermography." In: *Review of Scientific Instruments* 72.10 (Oct. 2001), pp. 3988–3995. ISSN: 0034-6748, 1089-7623. DOI: 10.1063/1.1400151.

[52] N. W. Pech-May, A. Mendioroz, and A. Salazar. "Simultaneous Measurement of the In-Plane and in-Depth Thermal Diffusivity of Solids Using Pulsed Infrared Thermography with Focused Illumination." In: *NDT & E International* 77 (Jan. 2016), pp. 28–34. ISSN: 09638695. DOI: 10.1016/j.ndteint.2015.10.001.

[53] E. J. Zimney, G. H. B. Dommett, R. S. Ruoff, and D. A. Dikin. "Correction Factors for 4-Probe Electrical Measurements with Finite Size Electrodes and Material Anisotropy: A Finite Element Study." In: *Measurement Science and Technology* 18.7 (July 1, 2007), pp. 2067–2073. ISSN: 0957-0233, 1361-6501. DOI: 10.1088/0957-0233/18/7/037.

[54] P. Scholle and M. Sinapius. "Measurement of Two-Dimensional Electrical Potential Fields in CFRP Using Four-Probe Resistance Scans." In: *Journal of Physics Communications* 5.12 (Dec. 1, 2021), p. 125005. ISSN: 2399-6528. DOI: 10.1088/2399-6528/ac2e54.

[55] J. D. Acosta, M. Jalalvand, S. A. Malik, and A. Hamilton. "Understanding and Estimating the Electrical Resistance Between Surface Electrodes on a UD Carbon Fibre-Reinforced Composite Layer." In: *Journal of Composites Science* 9.11 (Nov. 8, 2025), p. 615. ISSN: 2504-477X. DOI: 10.3390/jcs9110615.

[56] S. Van Den Berg, M. Luckabauer, S. Wijskamp, and R. Akkerman. "Determination of the Anisotropic Electrical Conductivity of Carbon Fabric Reinforced Composites by the Six-Probe Method." In: *Journal of Thermoplastic Composite Materials* 36.11 (Nov. 2023), pp. 4257–4283. ISSN: 0892-7057, 1530-7980. DOI: 10.1177/08927057231154546.

[57] E. Frank, L. M. Steudle, D. Ingildeev, J. M. Spörl, and M. R. Buchmeiser. "Carbon Fibers: Precursor Systems, Processing, Structure, and Properties." In: *Angewandte Chemie International Edition* 53.21 (May 19, 2014), pp. 5262–5298. ISSN: 1433-7851. DOI: 10.1002/anie.201306129.

[58] B. A. Newcomb. "Processing, Structure, and Properties of Carbon Fibers." In: *Composites Part A: Applied Science and Manufacturing* 91 (Dec. 2016), pp. 262–282. ISSN: 1359835X. DOI: 10.1016/j.compositesa.2016.10.018.

[59] S.-J. Park. *Carbon Fibers*. Vol. 210. Springer Series in Materials Science. Singapore: Springer Singapore, 2018. ISBN: 978-981-13-0537-5. DOI: 10.1007/978-981-13-0538-2.

[60] I. Hatta, T. Yamane, S. Katayama, and M. Todoki. "The Measurements of Thermal Conductivity of Carbon Fibers." In: *Journal of Wide Bandgap Materials* 7.4 (Apr. 1, 2000), pp. 294–305. ISSN: 1524511X. DOI: 10.1106/QLXQ-CADP-HC2M-F14U.

[61] V. Safarova and J. Gregr. "Electrical Conductivity Measurement of Fibers and Yarns." In: *7th International Conference - TEXSCI 2010*. TEXSCI 2010. Liberec, Czech Republic, 2010.

[62] K. Shirasu, C. Nagai, and K. Naito. "Mechanical Anisotropy of PAN-based and Pitch-Based Carbon Fibers." In: *Mechanical Engineering Journal* 7.4 (2020), pp. 19-00599-19–00599. ISSN: 2187-9745. DOI: 10.1299/mej.19-00599.

[63] K. Naito, C. Nagai, and Yoshihisa Tanaka. "Transverse Compressive Properties of Carbon/Glass Hybrid Thermoplastic Composite Rods." In: *Journal of Physical Science and Application* 9.1 (Jan. 28, 2019). ISSN: 21595348. DOI: 10.17265/2159-5348/2019.01.003.

[64] R. Maurin, P. Davies, N. Baral, and C. Baley. "Transverse Properties of Carbon Fibres by Nano-Indentation and Micro-mechanics." In: *Applied Composite Materials* 15.2 (Mar. 2008), pp. 61–73. ISSN: 0929-189X. DOI: 10.1007/s10443-008-9057-3.

[65] T. Csanádi, D. Németh, C. Zhang, and J. Dusza. "Nanoindentation Derived Elastic Constants of Carbon Fibres and Their Nanostructural Based Predictions." In: *Carbon* 119 (Aug. 2017), pp. 314–325. ISSN: 00086223. DOI: 10.1016/j.carbon.2017.04.048.

[66] W. Voigt. "Ueber Die Beziehung Zwischen Den Beiden Elasticitätsconstanten Isotroper Körper." In: *Annalen der Physik* 274.12 (1889), pp. 573–587. ISSN: 1521-3889. DOI: 10.1002/andp.18892741206.

[67] A. Reuss. "Berechnung Der Fließgrenze von Mischkristallen Auf Grund Der Plastizitätsbedingung Für Einkristalle ." In: *ZAMM - Journal of Applied Mathematics and Mechanics / Zeitschrift für Angewandte Mathematik und Mechanik* 9.1 (1929), pp. 49–58. ISSN: 1521-4001. DOI: 10.1002/zamm.19290090104.

[68] M. A. Islam and K. Begum. "Prediction Models for the Elastic Modulus of Fiber-reinforced Polymer Composites: An Analysis." In: *Journal of Scientific Research* 3.2 (Apr. 28, 2011), pp. 225–238. ISSN: 2070-0245, 2070-0237. DOI: 10.3329/jsr.v3i2.6881.

[69] J. Aboudi, S. M. Arnold, and Brett. *Micromechanics of Composite Materials*. Elsevier, 2013. ISBN: 978-0-12-397035-0. DOI: 10.1016/C2011-0-05224-9.

[70] J. C. Halpin and J. L. Kardos. "The Halpin-Tsai Equations: A Review." In: *Polymer Engineering & Science* 16.5 (May 1976), pp. 344–352. ISSN: 0032-3888, 1548-2634. DOI: 10.1002/pen.760160512.

[71] A. G. Facca, M. T. Kortschot, and N. Yan. "Predicting the Elastic Modulus of Natural Fibre Reinforced Thermoplastics." In: *Composites Part A: Applied Science and Manufacturing* 37.10 (Oct. 2006), pp. 1660–1671. ISSN: 1359835X. DOI: 10.1016/j.compositesa.2005.10.006.

[72] T. Mori and K. Tanaka. "Average Stress in Matrix and Average Elastic Energy of Materials with Misfitting Inclusions." In: *Acta Metallurgica* 21.5 (May 1973), pp. 571–574. ISSN: 00016160. DOI: 10.1016/0001-6160(73)90064-3.

[73] Y. C. Kim, H.-K. Jang, G. Joo, and J. H. Kim. "A Comparative Study of Micromechanical Analysis Models for Determining the Effective Properties of Out-of-Autoclave Carbon Fiber–Epoxy Composites." In: *Polymers* 16.8 (Apr. 14, 2024), p. 1094. ISSN: 2073-4360. DOI: 10.3390/polym16081094.

[74] G. W. Milton. *The Theory of Composites*. 1. publ. Cambridge Monographs on Applied and Computational Mathematics 6. Cambridge: Cambridge University Press, 2002. 719 pp. ISBN: 978-0-521-78125-1.

[75] W. Nasri, Z. Driss, R. Djebali, K.-Y. Lee, H.-H. Park, A. Bezazi, and P. N. B. Reis. "Thermal Study of Carbon-Fiber-Reinforced Polymer Composites Using Multiscale Modeling." In: *Materials* 16.22 (Nov. 19, 2023), p. 7233. ISSN: 1996-1944. DOI: 10.3390/ma16227233.

[76] M. O. H. Schutzeichel, T. Kletschkowski, and H. P. Monner. "Microscale Thermal Modelling of Multifunctional Composite Materials Made from Polymer Electrolyte Coated Carbon Fibres Including Homogenization and Model Reduction Strategies." In: *Applied Mechanics* 2.4 (Oct. 1, 2021), pp. 739–765. ISSN: 2673-3161. DOI: 10.3390/applmech2040043.

[77] H. Yu, D. Heider, and S. Advani. “A 3D Microstructure Based Resistor Network Model for the Electrical Resistivity of Unidirectional Carbon Composites.” In: *Composite Structures* 134 (Dec. 2015), pp. 740–749. ISSN: 02638223. DOI: 10.1016/j.compstruct.2015.08.131.

[78] F. Lundström, K. Frogner, and M. Andersson. “A Resistor Network Model for Analysis of Current and Temperature Distribution in Carbon Fibre Reinforced Polymers during Induction Heating.” In: *Journal of Composite Materials* 56.20 (Aug. 2022), pp. 3159–3183. ISSN: 0021-9983, 1530-793X. DOI: 10.1177/00219983221108442.

[79] P. Scholle. *A Two-Dimensional Piezoresistivity Model for Anisotropic Materials and Its Application in Self-Sensing of Carbon Fiber Reinforced Plastics*. 1st ed. Mechanics and Adaptronics Series. Cham: Springer, 2023. 1 p. ISBN: 978-3-031-23766-9.

[80] *Introduction of jER™ Epoxy Resins. Product information / presentation*. Mitsubishi Chemical Corporation. Tokyo, Japan, July 3, 2025.

[81] *NTPT ThinPreg™ 402. Data Sheet*. Version 1.6. North Thin Ply Technology. Renens, Switzerland, May 11, 2017.

[82] International Organization for Standardization. *Plastics — Differential scanning calorimetry (DSC) — Part 1: General principles*. ISO 11357-1. Geneva, Switzerland, 2016.

[83] International Organization for Standardization. *Carbon-fibre-reinforced composites — Determination of the resin, fibre and void contents*. ISO 14127. Geneva, Switzerland, 2001.

[84] International Organization for Standardization. *Plastics — Methods for determining the density of non-cellular plastics — Part 1: Immersion method, liquid pycnometer method and titration method*. International Standard ISO 1183-1. Geneva, Switzerland, 2019.

[85] ASTM International. *Standard Test Method for Measuring the Damage Resistance of a Fiber-Reinforced Polymer Matrix Composite to a Drop-Weight Impact Event*. ASTM Standard D7136/D7136M. West Conshohocken, PA, USA, 2015.

[86] S. Fakirov and C. Fakirova. “Direct Determination of the Orientation of Short Glass Fibers in an Injection-molded Poly(Ethylene Terephthalate) System.” In: *Polymer Composites* 6.1 (Jan. 1985), pp. 41–46. ISSN: 0272-8397, 1548-0569. DOI: 10.1002/pc.750060108.

[87] G. Fischer and P. Eyerer. "Measuring Spatial Orientation of Short Fiber Reinforced Thermoplastics by Image Analysis." In: *Polymer Composites* 9.4 (Aug. 1988), pp. 297–304. ISSN: 0272-8397, 1548-0569. DOI: 10.1002/pc.750090409.

[88] C. Eberhardt and A. Clarke. "Fibre-Orientation Measurements in Short-Glass-Fibre Composites. Part I: Automated, High-Angular-Resolution Measurement by Confocal Microscopy." In: *Composites Science and Technology* 61.10 (Aug. 2001), pp. 1389–1400. ISSN: 02663538. DOI: 10.1016/S0266-3538(01)00038-0.

[89] G. Zak, C. B. Park, and B. Benhabib. "Estimation of Three-Dimensional Fibre-Orientation Distribution in Short-Fibre Composites by a Two-Section Method." In: *Journal of Composite Materials* 35.4 (Feb. 2001), pp. 316–339. ISSN: 0021-9983, 1530-793X. DOI: 10.1177/002199801772662190.

[90] N. D. Sharp, J. E. Goodsell, and A. J. Favaloro. "Measuring Fiber Orientation of Elliptical Fibers from Optical Microscopy." In: *Journal of Composites Science* 3.1 (Mar. 2, 2019), p. 23. ISSN: 2504-477X. DOI: 10.3390/jcs3010023.

[91] S. G. Advani and C. L. Tucker. "The Use of Tensors to Describe and Predict Fiber Orientation in Short Fiber Composites." In: *Journal of Rheology* 31.8 (Nov. 1987), pp. 751–784. ISSN: 0148-6055, 1520-8516. DOI: 10.1122/1.549945.

[92] M. Krause, J. M. Hausherr, B. Burgeth, C. Herrmann, and W. Krenkel. "Determination of the Fibre Orientation in Composites Using the Structure Tensor and Local X-ray Transform." In: *Journal of Materials Science* 45.4 (Feb. 2010), pp. 888–896. ISSN: 0022-2461, 1573-4803. DOI: 10.1007/s10853-009-4016-4.

[93] C. Creighton, M. Sutcliffe, and T. Clyne. "A Multiple Field Image Analysis Procedure for Characterisation of Fibre Alignment in Composites." In: *Composites Part A: Applied Science and Manufacturing* 32.2 (Feb. 2001), pp. 221–229. ISSN: 1359835X. DOI: 10.1016/S1359-835X(00)00115-9.

[94] K. Kratmann, M. Sutcliffe, L. Lilleheden, R. Pyrz, and O. Thomsen. "A Novel Image Analysis Procedure for Measuring Fibre Misalignment in Unidirectional Fibre Composites." In: *Composites Science and Technology* 69.2 (Feb. 2009), pp. 228–238. ISSN: 02663538. DOI: 10.1016/j.compscitech.2008.10.020.

[95] H. Shen, S. Nutt, and D. Hull. "Direct Observation and Measurement of Fiber Architecture in Short Fiber-Polymer Composite Foam through Micro-CT Imaging." In: *Composites Science and Technology* 64.13–14 (Oct. 2004), pp. 2113–2120. ISSN: 02663538. DOI: 10.1016/j.compscitech.2004.03.003.

[96] T. B. Nguyen Thi, M. Morioka, A. Yokoyama, S. Hamanaka, K. Yamashita, and C. Nonomura. "Measurement of Fiber Orientation Distribution in Injection-Molded Short-Glass-Fiber Composites Using X-ray Computed Tomography." In: *Journal of Materials Processing Technology* 219 (May 2015), pp. 1–9. ISSN: 09240136. DOI: 10.1016/j.jmatprotec.2014.11.048.

[97] M. J. Emerson, K. M. Jespersen, A. B. Dahl, K. Conradsen, and L. P. Mikkelsen. "Individual Fibre Segmentation from 3D X-ray Computed Tomography for Characterising the Fibre Orientation in Unidirectional Composite Materials." In: *Composites Part A: Applied Science and Manufacturing* 97 (June 2017), pp. 83–92. ISSN: 1359835X. DOI: 10.1016/j.compositesa.2016.12.028.

[98] A. Bernasconi, F. Cosmi, and P. Hine. "Analysis of Fibre Orientation Distribution in Short Fibre Reinforced Polymers: A Comparison between Optical and Tomographic Methods." In: *Composites Science and Technology* 72.16 (Nov. 2012), pp. 2002–2008. ISSN: 02663538. DOI: 10.1016/j.compscitech.2012.08.018.

[99] J. Kim and D. Lee. "Measurement of Fiber Orientation Angle in FRP by Intensity Method." In: *Journal of Materials Processing Technology* 201.1–3 (May 2008), pp. 755–760. ISSN: 09240136. DOI: 10.1016/j.jmatprotec.2007.11.149.

[100] A. Nagura, K. Okamoto, K. Itoh, Y. Imai, D. Shimamoto, and Y. Hotta. "The Ni-plated Carbon Fiber as a Tracer for Observation of the Fiber Orientation in the Carbon Fiber Reinforced Plastic with X-ray CT." In: *Composites Part B: Engineering* 76 (July 2015), pp. 38–43. ISSN: 13598368. DOI: 10.1016/j.compositesb.2015.02.009.

[101] R. A. Smith, L. J. Nelson, M. J. Mienczakowski, and R. E. Challis. "Automated Analysis and Advanced Defect Characterisation from Ultrasonic Scans of Composites." In: *Insight - Non-Destructive Testing and Condition Monitoring* 51.2 (Feb. 2009), pp. 82–87. ISSN: 1354-2575. DOI: 10.1784/insi.2009.51.2.82.

[102] R. A. Smith. *Use of 3D Ultrasound Data Sets to Map the Localised Properties of Fibre-Reinforced Composites*. July 21, 2010. URL: https://eprints.nottingham.ac.uk/31253/ (visited on 08/18/2025).

[103] X. Yang, E. Verboven, B.-f. Ju, and M. Kersemans. "Comparative Study of Ultrasonic Techniques for Reconstructing the Multilayer Structure of Composites." In: *NDT & E International* 121 (July 2021), p. 102460. ISSN: 09638695. DOI: 10.1016/j.ndteint.2021.102460.

[104] X. Yang, B.-f. Ju, and M. Kersemans. "Ultrasonic Tomographic Reconstruction of Local Fiber Orientation in Multi-Layer Composites Using Gabor Filter-Based Information Diagram Method." In: *NDT & E International* 124 (Dec. 2021), p. 102545. ISSN: 09638695. DOI: 10.1016/j.ndteint.2021.102545.

[105] X. Yang, B.-F. Ju, and M. Kersemans. "Assessment of the 3D Ply-by-Ply Fiber Structure in Impacted CFRP by Means of Planar Ultrasound Computed Tomography (pU-CT)." In: *Composite Structures* 279 (Jan. 2022), p. 114745. ISSN: 02638223. DOI: 10.1016/j.compstruct.2021.114745.

[106] L. Ambrozinski, J. Mrowka, M. O'Donnell, and I. Pelivanov. "Detection and Imaging of Local Ply Angle in Carbon Fiber Reinforced Plastics Using Laser Ultrasound and Tilt Filter Processing." In: *Composites Part A: Applied Science and Manufacturing* 126 (Nov. 2019), p. 105581. ISSN: 1359835X. DOI: 10.1016/j.compositesa.2019.105581.

[107] M. Liu, Z. Li, S. Wang, Z. Zhang, and C. M. Leung. "Quantitative Characterization of Out-of-Plane Fiber Wrinkling in Thick CFRP with Double-side Inverse-Variance Weight-Synthetic Ultrasonic Imaging." In: *Composites Part A: Applied Science and Manufacturing* 166 (Mar. 2023), p. 107376. ISSN: 1359835X. DOI: 10.1016/j.compositesa.2022.107376.

[108] T. Ma, Y. Li, Z. Zhou, and J. Meng. "Wrinkle Detection in Carbon Fiber-Reinforced Polymers Using Linear Phase FIR-Filtered Ultrasonic Array Data." In: *Aerospace* 10.2 (Feb. 15, 2023), p. 181. ISSN: 2226-4310. DOI: 10.3390/aerospace10020181.

[109] C. Tang, B. Liang, and W. Zhang. "Detect and Visualize Non-Uniform Yarn Orientations on Preformed CFRP Parts Using Automatic Scanning and Image Processing." In: *Journal of Manufacturing Processes* 102 (Sept. 2023), pp. 1043–1058. ISSN: 15266125. DOI: 10.1016/j.jmapro.2023.08.031.

[110] X. Li, E. A. Patterson, W.-C. Wang, and W. J. R. Christian. "Prediction of Residual Strains Due to In-Plane Fibre Waviness in Defective Carbon-Fibre Reinforced Polymers Using Ultrasound Data." In: *Journal of Nondestructive Evaluation* 42.1 (Mar. 2023), p. 2. ISSN: 0195-9298, 1573-4862. DOI: 10.1007/s10921-022-00910-0.

[111] G. Mook, R. Lange, and O. Koeser. "Non-Destructive Characterisation of Carbon-Fibre-Reinforced Plastics by Means of Eddy-Currents." In: *Composites Science and Technology* 61.6 (May 2001), pp. 865–873. ISSN: 02663538. DOI: 10.1016/S0266-3538(00)00164-0.

[112] H. Heuer, M. Schulze, and N. Meyendorf. "Non-Destructive Evaluation (NDE) of Composites: Eddy Current Techniques." In: *Non-Destructive Evaluation (NDE) of Polymer Matrix Composites*. Elsevier, 2013, pp. 33–55. ISBN: 978-0-85709-344-8. DOI: 10.1533/9780857093554.1.33.

[113] M. H. Schulze, H. Heuer, M. Küttner, and N. Meyendorf. "High-Resolution Eddy Current Sensor System for Quality Assessment of Carbon Fiber Materials." In: *Microsystem Technologies* 16.5 (May 2010), pp. 791–797. ISSN: 0946-7076, 1432-1858. DOI: 10.1007/s00542-010-1047-3.

[114] G. Bardl, A. Nocke, C. Cherif, M. Pooch, M. Schulze, H. Heuer, M. Schiller, R. Kupke, and M. Klein. "Automated Detection of Yarn Orientation in 3D-draped Carbon Fiber Fabrics and Preforms from Eddy Current Data." In: *Composites Part B: Engineering* 96 (July 2016), pp. 312–324. ISSN: 13598368. DOI: 10.1016/j.compositesb.2016.04.040.

[115] C. Schmidt, C. Schultz, P. Weber, and B. Denkena. "Evaluation of Eddy Current Testing for Quality Assurance and Process Monitoring of Automated Fiber Placement." In: *Composites Part B: Engineering* 56 (Jan. 2014), pp. 109–116. ISSN: 13598368. DOI: 10.1016/j.compositesb.2013.08.061.

[116] S. H. McGee and R. L. McCullough. "Characterization of Fiber Orientation in Short-Fiber Composites." In: *Journal of Applied Physics* 55.5 (Mar. 1, 1984), pp. 1394–1403. ISSN: 0021-8979, 1089-7550. DOI: 10.1063/1.333230.

[117] S. Zambal, W. Palfinger, M. Stöger, and C. Eitzinger. "Accurate Fibre Orientation Measurement for Carbon Fibre Surfaces." In: *Pattern Recognition* 48.11 (Nov. 1, 2015), pp. 3324–3332. ISSN: 0031-3203. DOI: 10.1016/j.patcog.2014.11.009.

[118] R. Fujita and H. Nagano. "Novel Fiber Orientation Evaluation Method for CFRP/CFRTP Based on Measurement of Anisotropic in-Plane Thermal Diffusivity Distribution." In: *Composites Science and Technology* 140 (Mar. 2017), pp. 116–122. ISSN: 02663538. DOI: 10.1016/j.compscitech.2016.12.006.

[119] S. Unnikrishnakurup, R. T. Kidangan, C. Krishnamurthy, K. Balasubramaniam, and A. Ngo. "Assessment of Fiber Orientation and Order in Carbon Fiber Reinforced Polymer Composites Using Induction Thermography and Radon Transform Analysis." In: *Composites Part B: Engineering* 296 (May 2025), p. 112224. ISSN: 13598368. DOI: 10.1016/j.compositesb.2025.112224.

[120] ASTM International. *ASTM E2580-24: Standard Practice for Ultrasonic Testing of Flat Panel Composites and Sandwich Core Materials Used in Aerospace Applications*. ASTM Standard. 2024.

[121] DIN. *DIN EN ISO 5577 Zerstörungsfreie Prüfung - Ultraschallprüfung - Terminologie*. Norm. Berlin, 2017. DOI: 10.31030/2559170.

[122] J. Krautkrämer and H. Krautkrämer. *Ultrasonic Testing of Materials*. Berlin, Heidelberg: Springer Berlin Heidelberg, 1990. ISBN: 978-3-662-10682-2. DOI: 10.1007/978-3-662-10680-8.

[123] J. Blitz and G. Simpson. *Ultrasonic Methods of Non-Destructive Testing*. 1. ed. Non-Destructive Evaluation Series. London: Chapman & Hall, 1996. 264 pp. ISBN: 978-0-412-60470-6.

[124] D. Ensminger and L. J. Bond. *Ultrasonics: Fundamentals, Technologies, and Applications*. 4th ed. Boca Raton: CRC Press, Dec. 14, 2023. ISBN: 978-0-429-28696-4. DOI: 10.1201/9780429286964.

[125] L. W. Schmerr. *Fundamentals of Ultrasonic Nondestructive Evaluation: A Modeling Approach*. Springer Series in Measurement Science and Technology. Cham: Springer International Publishing, 2016. ISBN: 978-3-319-30461-8. DOI: 10.1007/978-3-319-30463-2.

[126] L. E. Kinsler, ed. *Fundamentals of Acoustics*. 4th ed. New York: Wiley, 2000. 1 p. ISBN: 978-0-471-84789-2.

[127] B. A. Auld. *Acoustic Fields and Waves in Solids*. New York: Wiley, 1973. 423 pp. ISBN: 978-0-471-03700-2.

[128] K. Ono. "A Comprehensive Report on Ultrasonic Attenuation of Engineering Materials, Including Metals, Ceramics, Polymers, Fiber-Reinforced Composites, Wood, and Rocks." In: *Applied Sciences* 10.7 (Mar. 25, 2020), p. 2230. ISSN: 2076-3417. DOI: 10.3390/app10072230.

[129] H. Yu. "Scanning Acoustic Microscopy for Material Evaluation." In: *Applied Microscopy* 50.1 (Dec. 2020), p. 25. ISSN: 2287-4445. DOI: 10.1186/s42649-020-00045-4.

[130] R. A. Casarotto, J. C. Adamowski, F. Fallopa, and F. Bacanelli. "Coupling Agents in Therapeutic Ultrasound: Acoustic and Thermal Behavior." In: *Archives of Physical Medicine and Rehabilitation* 85.1 (Jan. 2004), pp. 162–165. ISSN: 00039993. DOI: 10.1016/S0003-9993(03)00293-4.

[131] J. P. Dumoulin and J. F. Belleval. "Flaw Classification in Composites Using Ultrasonic Echography." In: *Ultrasonic Methods in Evaluation of Inhomogeneous Materials*. Ed. by A. Alippi and W. G. Mayer. Dordrecht: Springer Netherlands, 1987, pp. 207–217. ISBN: 978-94-010-8099-6. DOI: 10.1007/978-94-009-3575-4_15.

[132] Hillger NDT GmbH. *Inspection Systems with Immersion Technique*. Accessed: 19 December 2025. Hillger NDT GmbH. 2024. URL: https://www.hillger-ndt.de/en/home/service-offer/immersion-technique/inspection-systems-with-immersion-technique (visited on 12/19/2025).

[133] D. Gabor. "Theory of Communication. Part 1: The Analysis of Information." In: *Journal of the Institution of Electrical Engineers - Part III: Radio and Communication Engineering* 93.26 (Nov. 1946), pp. 429–441. ISSN: 2054-0604. DOI: 10.1049/ji-3-2.1946.0074.

[134] P. Gammell. "Improved Ultrasonic Detection Using the Analytic Signal Magnitude." In: *Ultrasonics* 19.2 (Mar. 1981), pp. 73–76. ISSN: 0041624X. DOI: 10.1016/0041-624X(81)90111-6.

[135] J. F. Mansur Rodrigues Filho and P. Bélanger. "Probe Standoff Optimization Method for Phased Array Ultrasonic TFM Imaging of Curved Parts." In: *Sensors* 21.19 (Oct. 7, 2021), p. 6665. ISSN: 1424-8220. DOI: 10.3390/s21196665.

[136] V. Tunukovic, S. McKnight, R. Pyle, Z. Wang, E. Mohseni, S. Gareth Pierce, R. K. W. Vithanage, G. Dobie, C. N. MacLeod, S. Cochran, and T. O'Hare. "Unsupervised Machine Learning for Flaw Detection in Automated Ultrasonic Testing of Carbon Fibre Reinforced Plastic

Composites." In: *Ultrasonics* 140 (May 2024), p. 107313. ISSN: 0041624X. DOI: 10.1016/j.ultras.2024.107313.

[137] Z. Wu, H. Huang, R. Zhang, J. Liu, and J. Tang. "An Ultrasonic In-Line Inspection Data Processing Method Considering Invalid Data Caused by Sensor Failure." In: *Measurement Science and Technology* 35.1 (Jan. 1, 2024), p. 015601. ISSN: 0957-0233, 1361-6501. DOI: 10.1088/1361-6501/acfbee.

[138] A. M. Siddiolo and R. G. Maev. "A 2D - FFT Signal Processing Technique to Enhance the Contrast of Air-coupled Ultrasonic C-Scans." In: *eJNDT Vol.11 No.3*. 5th International Workshop, Advances in Signal Processing for NDE of Materials. Québec City, Canada, 2005.

[139] V. V. a. A. Yashchuk, E. H. Anderson, and S. K. Barber. "Calibration of the Modulation Transfer Function of Surface Profilometers with Binary Pseudo-Random Test Standards: Expanding the Application Range." In: *Proceedings of SPIE*. 2010.

[140] A. De Cheveigné and D. Arzounian. "Robust Detrending, Rereferencing, Outlier Detection, and Inpainting for Multichannel Data." In: *NeuroImage* 172 (May 2018), pp. 903–912. ISSN: 10538119. DOI: 10.1016/j.neuroimage.2018.01.035.

[141] H. Hwang and R. Haddad. "Adaptive Median Filters: New Algorithms and Results." In: *IEEE Transactions on Image Processing* 4.4 (Apr. 1995), pp. 499–502. ISSN: 10577149. DOI: 10.1109/83.370679.

[142] F. Giavazzi, P. Edera, P. J. Lu, and R. Cerbino. "Image Windowing Mitigates Edge Effects in Differential Dynamic Microscopy." In: *The European Physical Journal E* 40.11 (Nov. 2017), p. 97. ISSN: 1292-8941, 1292-895X. DOI: 10.1140/epje/i2017-11587-3.

[143] A. V. Oppenheim and R. W. Schafer. *Discrete-Time Signal Processing*. Third edition, Pearson New international edition. Always Learning. Harlow: Pearson, 2014. ISBN: 978-1-292-03815-5.

[144] J. Körbelin, P. Goralski, B. Kötter, F. Bittner, H.-J. Endres, and B. Fiedler. "Damage Tolerance and Notch Sensitivity of Bio-Inspired Thin-Ply Bouligand Structures." In: *Composites Part C: Open Access* 5 (July 2021), p. 100146. ISSN: 26666820. DOI: 10.1016/j.jcomc.2021.100146.

[145] A. N. Salazar. "On Thermal Diffusivity." In: *European Journal of Physics* 24.4 (July 1, 2003), pp. 351–358. ISSN: 0143-0807, 1361-6404. DOI: 10.1088/0143-0807/24/4/353.

[146] X. Zhang, S. Fujiwara, and M. Fujii. "Measurements of Thermal Conductivity and Electrical Conductivity of a Single Carbon Fiber." In: *International Journal of Thermophysics* 21.4 (2000), pp. 965–980. ISSN: 0195928X. DOI: 10.1023/A:1006674510648.

[147] C. Ye, H. Wu, S.-p. Zhu, Z. Fan, D. Huang, F. Han, J.-s. Liu, J.-x. Yang, and H.-b. Liu. "Microstructure of High Thermal Conductivity Mesophase Pitch-Based Carbon Fibers." In: *New Carbon Materials* 36.5 (Oct. 2021), pp. 980–985. ISSN: 18725805. DOI: 10.1016/S1872-5805(21)60050-1.

[148] A. Kumar, M. Ammar, A. Canizarès, J. Vicente, and B. Rousseau. "Determination of the Longitudinal Thermal Conductivity of Low-ordered Carbon Fibers by Using an Optothermal Raman Technique." In: *Journal of Raman Spectroscopy* 55.1 (Jan. 2024), pp. 86–98. ISSN: 0377-0486, 1097-4555. DOI: 10.1002/jrs.6616.

[149] R. Shokrani Havigh and H. Mahmoudi Chenari. "A Comprehensive Study on the Effect of Carbonization Temperature on the Physical and Chemical Properties of Carbon Fibers." In: *Scientific Reports* 12.1 (June 23, 2022), p. 10704. ISSN: 2045-2322. DOI: 10.1038/s41598-022-15085-x.

[150] J. Zhou, Q. Xi, J. He, X. Xu, T. Nakayama, Y. Wang, and J. Liu. "A Thermal Resistance Network Model for Heat Conduction of Amorphous Polymers." Version 1. In: *Phys. Rev. Materials 4* (2019). DOI: 10.48550/ARXIV.1909.07607.

[151] Z. Li, Y. Sun, F. Hu, D. Liu, X. Zhang, J. Ren, H. Guo, M. Shalash, M. He, H. Hou, S. M. El-Bahy, D. Pan, Z. M. El-Bahy, and Z. Guo. "An Overview of Polymer-Based Thermally Conductive Functional Materials." In: *Journal of Materials Science & Technology* 218 (May 2025), pp. 191–210. ISSN: 10050302. DOI: 10.1016/j.jmst.2024.07.053.

[152] J. Hennig and W. Knappe. "Anisotropy of Thermal Conductivity in Stretched Amorphous Linear Polymers and in Strained Elastomers." In: *Journal of Polymer Science Part C: Polymer Symposia* 6.1 (Jan. 1964), pp. 167–174. ISSN: 0449-2994, 1935-3065. DOI: 10.1002/polc.5070060119.

[153] V. M. Nazarychev and S. V. Lyulin. "The Effect of Mechanical Elongation on the Thermal Conductivity of Amorphous and Semicrystalline Thermoplastic Polyimides: Atomistic Simulations." In: *Polymers* 15.13 (July 1, 2023), p. 2926. ISSN: 2073-4360. DOI: 10.3390/polym15132926.

[154] Y. Jia, Z. Mao, W. Huang, and J. Zhang. "Effect of Temperature and Crystallinity on the Thermal Conductivity of Semi-Crystalline Polymers: A Case Study of Polyethylene." In: *Materials Chemistry and Physics* 287 (Aug. 2022), p. 126325. ISSN: 02540584. DOI: 10.1016/j.matchemphys.2022.126325.

[155] S. Xu, J. Liu, and X. Wang. "Thermal Conductivity Enhancement of Polymers via Structure Tailoring." In: *Journal of Enhanced Heat Transfer* 27.5 (2020), pp. 463–489. ISSN: 1065-5131. DOI: 10.1615/JEnhHeatTransf.2020034592.

[156] X. Pan, M. G. Debije, and A. P. H. J. Schenning. "High Thermal Conductivity in Anisotropic Aligned Polymeric Materials." In: *ACS Applied Polymer Materials* 3.2 (Feb. 12, 2021), pp. 578–587. ISSN: 2637-6105, 2637-6105. DOI: 10.1021/acsapm.0c01340.

[157] L. Rayleigh. "On the Influence of Obstacles Arranged in Rectangular Order upon the Properties of a Medium." In: *The London, Edinburgh, and Dublin Philosophical Magazine and Journal of Science* 34.211 (Dec. 1892), pp. 481–502. ISSN: 1941-5982, 1941-5990. DOI: 10.1080/14786449208620364.

[158] T. B. Lewis and L. E. Nielsen. "Viscosity of Dispersed and Aggregated Suspensions of Spheres." In: *Transactions of the Society of Rheology* 12.3 (Sept. 1, 1968), pp. 421–443. ISSN: 0038-0032. DOI: 10.1122/1.549114.

[159] Y. J. Chen, X. J. Ren, P. Zhang, T. Zhang, and A. B. Wu. "Measurement of Thermal Conductivity of CFRPs and Thermal Conductance of the Cold-to-Warm Joint at Low Temperatures." In: *IEEE Transactions on Applied Superconductivity* 22.3 (June 2012), pp. 7700704–7700704. ISSN: 1051-8223, 1558-2515. DOI: 10.1109/TASC.2011.2177231.

[160] H.-B. Shim, M.-K. Seo, and S.-J. Park. "Thermal Conductivity and Mechanical Properties of Various Cross-Section Types Carbon Fiber-Reinforced Composites." In: *Journal of Materials Science* 37.9 (2002), pp. 1881–1885. ISSN: 00222461. DOI: 10.1023/A:1014959603892.

[161] F. Touni. "Untersuchung Des Elektrischen Und Thermischen Anisotropieverhaltens von Faserverbundwerkstoffen." MA thesis. Hamburg University of Technology, Aug. 2023.

[162] International Organization for Standardization. *ISO 8302 - Thermal Insulation - Determination of Steady-State Thermal Resistance and Related Properties - Guarded Hot Plate Apparatus*. 1991.

[163] ASTM International. *ASTM C177-19 - Standard Test Method for Steady-State Heat Flux Measurements and Thermal Transmission Properties by Means of the Guarded-Hot-Plate Apparatus*. 2019. DOI: 10.1520/C0177-19.

[164] K. D. Maglić, A. Cezairliyan, and V. E. Peletsky, eds. *Compendium of Thermophysical Property Measurement Methods*. Boston, MA: Springer US, 1992. ISBN: 978-1-4613-6445-0. DOI: 10.1007/978-1-4615-3286-6.

[165] L. Vozár and W. Hohenauer. "Flash Method of Measuring the Thermal Diffusivity. A Review." In: *High Temperatures-High Pressures* 35/36.3 (2003), pp. 253–264. ISSN: 0018-1544, 1472-3441. DOI: 10.1068/htjr119.

[166] O. Breitenstein, W. Warta, and M. Langenkamp. *Lock-in Thermography: Basics and Use for Evaluating Electronic Devices and Materials*. Vol. 10. Springer Series in Advanced Microelectronics. Berlin, Heidelberg: Springer Berlin Heidelberg, 2010. ISBN: 978-3-642-02416-0. DOI: 10.1007/978-3-642-02417-7.

[167] W. Nunes Dos Santos, P. Mummery, and A. Wallwork. "Thermal Diffusivity of Polymers by the Laser Flash Technique." In: *Polymer Testing* 24.5 (Aug. 2005), pp. 628–634. ISSN: 01429418. DOI: 10.1016/j.polymertesting.2005.03.007.

[168] NETZSCH Analyzing & Testing. *NanoTR — Time-Domain Thermoreflectance Analyzer*. 2025. URL: https://analyzing-testing.netzsch.com/en/products/time-domain-thermoreflectance-analyzer-tdtr/nanotr (visited on 09/15/2025).

[169] L. Gaverina, M. Bensalem, A. Bedoya, J. González, A. Sommier, J. Battaglia, A. Salazar, A. Mendioroz, A. Oleaga, J. Batsale, and C. Pradere. "Constant Velocity Flying Spot for the Estimation of In-Plane Thermal Diffusivity on Anisotropic Materials." In: *International Journal of Thermal Sciences* 145 (Nov. 2019), p. 106000. ISSN: 12900729. DOI: 10.1016/j.ijthermalsci.2019.106000.

[170] NETZSCH Analyzing & Testing. *GHP 456 Titan — Guarded Hot Plate Apparatus*. 2025. URL: https://analyzing-testing.netzsch.com/en/products/thermal-conductivity/ghp-456-titan (visited on 09/15/2025).

[171] ASTM International. *ASTM C518-21 - Test Method for Steady-State Thermal Transmission Properties by Means of the Heat Flow Meter Apparatus*. 2021. DOI: 10.1520/C0518-21.

[172] NETZSCH Analyzing & Testing. *HFM 446 Lambda Eco-Line — Heat Flow Meter*. 2025. URL: https://analyzing-testing.netzsch.com/en/products/thermal-conductivity/hfm-446-lambda-eco-line-medium (visited on 09/15/2025).

[173] R. D. Cowan. "Pulse Method of Measuring Thermal Diffusivity at High Temperatures." In: *Journal of Applied Physics* 34.4 (Apr. 1, 1963), pp. 926–927. ISSN: 0021-8979, 1089-7550. DOI: 10.1063/1.1729564.

[174] NETZSCH Analyzing & Testing. *LFA 467 HyperFlash — Light Flash Apparatus for Thermal Diffusivity and Conductivity*. 2025. URL: https://analyzing-testing.netzsch.com/en/products/thermal-diffusivity-and-conductivity/lfa-467-hyper-flash-light-flash-apparatus (visited on 09/15/2025).

[175] L. Fabbri and P. Fenici. "Three-Dimensional Photothermal Radiometry for the Determination of the Thermal Diffusivity of Solids." In: *Review of Scientific Instruments* 66.6 (June 1, 1995), pp. 3593–3600. ISSN: 0034-6748, 1089-7623. DOI: 10.1063/1.1146443.

[176] A. Salazar, A. Sánchez-Lavega, A. Ocáriz, J. Guitonny, J. C. Pandey, D. Fournier, and A. C. Boccara. "Novel Results on Thermal Diffusivity Measurements on Anisotropic Materials Using Photothermal Methods." In: *Applied Physics Letters* 67.5 (July 1995), pp. 626–628. ISSN: 0003-6951. DOI: 10.1063/1.115410.

[177] A. Bedoya, E. Marín, J. J. Puldón, and C. García-Segundo. "On the Thermal Characterization of Insulating Solids Using Laser-Spot Thermography in a Front Detection Configuration." In: *International Journal of Thermophysics* 44.2 (Feb. 2023), p. 27. ISSN: 0195-928X, 1572-9567. DOI: 10.1007/s10765-022-03138-2.

[178] A. Bedoya, F. Rodríguez-Valdés, and E. Marín. "Laser-Spot Lock-in Thermography with a Non-Research-Grade Thermal Camera: From Thermal Diffusivity Measurements to Visualizing Free Convection." In: *Infrared Physics & Technology* 137 (Mar. 2024), p. 105161. ISSN: 13504495. DOI: 10.1016/j.infrared.2024.105161.

[179] A. Wolf, P. Pohl, and R. Brendel. "Thermophysical Analysis of Thin Films by Lock-in Thermography." In: *Journal of Applied Physics* 96.11 (Dec. 1, 2004), pp. 6306–6312. ISSN: 0021-8979, 1089-7550. DOI: 10.1063/1.1811390.

[180] K. Miyachi, Y. Muranaka, S. Nonaka, A. Ueno, and H. Nagano. "Measurement of Thermal Diffusivity and Evaluation of Fiber Condition of Discontinuous Fiber CFRP." In: *Infrared Physics & Technology* 115 (June 2021), p. 103743. ISSN: 13504495. DOI: 10.1016/j.infrared.2021.103743.

[181] A. Salazar, M. Colom, and A. Mendioroz. "Laser-Spot Step-Heating Thermography to Measure the Thermal Diffusivity of Solids." In: *International Journal of Thermal Sciences* 170 (Dec. 2021), p. 107124. ISSN: 12900729. DOI: 10.1016/j.ijthermalsci.2021.107124.

[182] A. Bedoya, J. Rojas-Trigos, J. Hernández-Wong, A. Calderón, and E. Marín. "Visualizing Heat-Convection Using Laser Spot Step Heating Thermography." In: *International Journal of Thermal Sciences* 200 (June 2024), p. 108974. ISSN: 12900729. DOI: 10.1016/j.ijthermalsci.2024.108974.

[183] P. W. Nolte, T. Malvisalo, F. Wagner, and S. Schweizer. "Thermal Diffusivity of Metals Determined by Lock-in Thermography." In: *Quantitative InfraRed Thermography Journal* 14.2 (July 3, 2017), pp. 218–225. ISSN: 1768-6733. DOI: 10.1080/17686733.2017.1329777.

[184] D. Yu Golovin, A. G. Divin, A. A. Samodurov, A. I. Tyurin, and Y. I. Golovin. "Temperature Diffusivity Measurement and Nondestructive Testing Requiring No Extensive Sample Preparation and Using Stepwise Point Heating and IR Thermography." In: *Failure Analysis*. Ed. by Z.-M. Huang and S. Hemeda. IntechOpen, Dec. 18, 2019. ISBN: 978-1-83968-253-7. DOI: 10.5772/intechopen.88302.

[185] H. Dong, B. Zheng, and F. Chen. "Infrared Sequence Transformation Technique for in Situ Measurement of Thermal Diffusivity and Monitoring of Thermal Diffusion." In: *Infrared Physics & Technology* 73 (Nov. 2015), pp. 130–140. ISSN: 13504495. DOI: 10.1016/j.infrared.2015.09.021.

[186] T. Gfroerer, R. Phillips, and P. Rossi. "Thermal Diffusivity Imaging." In: *American Journal of Physics* 83.11 (Nov. 2015), pp. 923–927. ISSN: 0002-9505, 1943-2909. DOI: 10.1119/1.4928277.

[187] C. Basheer, C. Krishnamurthy, and K. Balasubramaniam. "Hot-Rod Thermography for in-Plane Thermal Diffusivity Measurement." In: *Measurement* 103 (June 2017), pp. 235–240. ISSN: 02632241. DOI: 10.1016/j.measurement.2017.02.022.

[188] S. Genna and N. Ucciardello. "A Thermographic Technique for In-Plane Thermal Diffusivity Measurement of Electroplated Coatings." In: *Optics & Laser Technology* 113 (May 2019), pp. 338–344. ISSN: 00303992. DOI: 10.1016/j.optlastec.2019.01.004.

[189] V. Kalyanavalli, T. A. Ramadhas, and D. Sastikumar. "Determination of Thermal Diffusivity of Basalt Fiber Reinforced Epoxy Composite Using Infrared Thermography." In: *Measurement* 134 (Feb. 2019), pp. 673–678. ISSN: 02632241. DOI: 10.1016/j.measurement.2018.11.004.

[190] P. Bison, F. Cernuschi, and S. Capelli. "A Thermographic Technique for the Simultaneous Estimation of In-Plane and in-Depth Thermal Diffusivities of TBCs." In: *Surface and Coatings Technology* 205.10 (Feb. 2011), pp. 3128–3133. ISSN: 02578972. DOI: 10.1016/j.surfcoat.2010.11.013.

[191] T. Aujeszky, G. Korres, and M. Eid. "Measurement-Based Thermal Modeling Using Laser Thermography." In: *IEEE Transactions on Instrumentation and Measurement* 67.6 (June 2018), pp. 1359–1369. ISSN: 0018-9456, 1557-9662. DOI: 10.1109/TIM.2017.2785138.

[192] T. Pierre, É. Geslain, M. Courtois, A. Magueresse, and T. Colinart. "In-Plane Thermal Diffusivity Estimation by Radial Fin Method." In: *Infrared Physics & Technology* 120 (Jan. 2022), p. 103998. ISSN: 13504495. DOI: 10.1016/j.infrared.2021.103998.

[193] S. N. Pandya, B. J. Peterson, R. Sano, K. Mukai, E. A. Drapiko, A. G. Alekseyev, T. Akiyama, M. Itomi, and T. Watanabe. "Calibration of a Thin Metal Foil for Infrared Imaging Video Bolometer to Estimate the Spatial Variation of Thermal Diffusivity Using a Photo-Thermal Technique." In: *Review of Scientific Instruments* 85.5 (May 1, 2014), p. 054902. ISSN: 0034-6748, 1089-7623. DOI: 10.1063/1.4873713.

[194] NETZSCH Analyzing & Testing. *TCT 716 Lambda — Thermal Conductivity Tester*. 2025. URL: https://analyzing-testing.netzsch.com/en/products/thermal-conductivity/tct-716-lambda (visited on 09/15/2025).

[195] M. Liu, B. Wang, Z. Wu, J. Ma, M. Li, and D. Tang. "Influence of the Graphite Coating on the Intrinsic Thermal Diffusivity Measurement of Alumina Ceramics via Laser Flash Analysis." In: *Ceramics International* 51.25 (Oct. 2025), pp. 45336–45343. ISSN: 02728842. DOI: 10.1016/j.ceramint.2025.07.251.

[196] F. Sun, S. Mishra, P. H. McGuinness, Z. H. Filipiak, I. Marković, D. A. Sokolov, N. Kikugawa, J. W. Orenstein, S. A. Hartnoll, A. P. Mackenzie, and V. Sunko. "A Spatially Resolved Optical Method to Measure Thermal Diffusivity." In: *Review of Scientific Instruments* 94.4 (Apr. 2023), p. 043003. ISSN: 0034-6748, 1089-7623. DOI: 10.1063/5.0098800.

[197] J. B. J. Fourier. *Théorie Analytique de La Chaleur*. 1st ed. Cambridge University Press, 2009. ISBN: 978-1-108-00180-9. DOI: 10.1017/CBO9780511693229.

[198] R. B. Bird, W. E. Stewart, and E. N. Lightfoot. *Transport Phenomena*. Revised ed. New York: Wiley, 2007. ISBN: 978-0-470-11539-8.

[199] K. Cole, J. Beck, A. Haji-Sheikh, and B. Litkouhi. *Heat Conduction Using Greens Functions*. 0th ed. CRC Press, 2010. ISBN: 978-0-429-10918-8. DOI: 10.1201/9781439895214.

[200] A. Bedoya, A. Salazar, A. Mendioroz, and E. Marín. "Measuring the In-Plane Thermal Diffusivity of Anisotropic Solids by Lock-in Infrared Thermography: Laser-spot vs Laser-Line Heating." In: *Journal of Applied Physics* 135.13 (Apr. 2024), p. 135102. ISSN: 0021-8979, 1089-7550. DOI: 10.1063/5.0198882.

[201] G. v. Rossum and F. L. Drake. *The Python Language Reference*. Release 3.0.1 [Repr.] Python Documentation Manual / Guido van Rossum; Fred L. Drake [Ed.] Pt. 2. Hampton, NH: Python Software Foundation, 2010. 109 pp. ISBN: 978-1-4414-1269-0.

[202] J. D. Hunter. "Matplotlib: A 2D Graphics Environment." In: *Computing in Science & Engineering* 9.3 (2007), pp. 90–95. DOI: 10.1109/MCSE.2007.55.

[203] P. Virtanen, R. Gommers, T. E. Oliphant, M. Haberland, T. Reddy, D. Cournapeau, E. Burovski, P. Peterson, W. Weckesser, J. Bright, S. J. van der Walt, M. Brett, J. Wilson, K. J. Millman, N. Mayorov, A. R. J. Nelson, E. Jones, R. Kern, E. Larson, C. Carey, I. Polat, Y. Feng, E. W. Moore, J. VanderPlas, D. Laxalde, J. Perktold, R. Cimrman, I. Henriksen, E. A. Quintero, C. R. Harris, R. K. Archibald, A. H. Ribeiro, F. Pedregosa, and P. van Mulbregt. "SciPy 1.0: Fundamental Algorithms for Scientific

Computing in Python." In: *Nature Methods* 17 (2020), pp. 261–272. DOI: 10.1038/s41592-019-0686-2.

[204] M. Zimmermann and P. Fischer. *NiceGUI: A Simple Python Framework for Web-Based User Interfaces*. Version 2.0, retrieved from https://github.com/zauberzeug/nicegui. 2024. URL: https://nicegui.io.

[205] A. Salazar, A. Mendioroz, A. Bedoya, and E. Marín. "Comment on "A Spatially Resolved Optical Method to Measure Thermal Diffusivity" [Rev. Sci. Instrum. 94, 043003 (2023)]." In: *Review of Scientific Instruments* 95.4 (Apr. 2024), p. 047101. ISSN: 0034-6748, 1089-7623. DOI: 10.1063/5.0190267.

[206] M. Ashby. "Microstructural Design of Composite Materials." In: *Encyclopedia of Materials: Science and Technology*. Elsevier, 2001, pp. 1357–1361. ISBN: 978-0-08-043152-9. DOI: 10.1016/B0-08-043152-6/00253-9.

[207] W. Pabst and S. Hříbalová. "Describing the Effective Conductivity of Two-Phase and Multiphase Materials via Weighted Means of Bounds and General Power Means." In: *JOM* 71.11 (Nov. 2019), pp. 4005–4014. ISSN: 1047-4838, 1543-1851. DOI: 10.1007/s11837-019-03693-4.

[208] R. Simpkin. "Derivation of Lichtenecker's Logarithmic Mixture Formula From Maxwell's Equations." In: *IEEE Transactions on Microwave Theory and Techniques* 58.3 (Mar. 2010), pp. 545–550. ISSN: 0018-9480, 1557-9670. DOI: 10.1109/TMTT.2010.2040406.

[209] K. Lichtenecker. "Die Herleitung Des Logarithmischen Mischungsgesetzes Aus Allgemeinen Prinzipien Der Stationaren Stromung." In: *Physikalische Zeitschrift* 32 (1931), pp. 255–260.

[210] B. Liu, X. Feng, and S.-M. Zhang. "The Effective Young's Modulus of Composites beyond the Voigt Estimation Due to the Poisson Effect." In: *Composites Science and Technology* 69.13 (2009), pp. 2198–2204. ISSN: 02663538. DOI: 10.1016/j.compscitech.2009.06.004.

[211] H. Corporation. *Hexply M21 Datasheet*. Mar. 2007.

[212] NTPT. *CFRP ThinPreg TP402 Datasheet*. 2017.

[213] X. Huang, P. Jiang, and T. Tanaka. "A Review of Dielectric Polymer Composites with High Thermal Conductivity." In: *IEEE Electrical Insulation Magazine* 27.4 (July 2011), pp. 8–16. ISSN: 1558-4402. DOI: 10.1109/MEI.2011.5954064.

[214] F. H. Gojny, M. H. G. Wichmann, B. Fiedler, I. A. Kinloch, W. Bauhofer, A. H. Windle, and K. Schulte. "Evaluation and Identification of Electrical and Thermal Conduction Mechanisms in Carbon Nanotube/Epoxy Composites." In: *Polymer* 47.6 (Mar. 2006), pp. 2036–2045. ISSN: 0032-3861. DOI: 10.1016/j.polymer.2006.01.029.

[215] I. Toray Composite Materials America. *TORAYCA Technical Manual*. Apr. 2020.

[216] D. Jang, D. S. Lee, A. Lee, H.-I. Joh, and S. Lee. "Opto-Thermal Technique for Measuring Thermal Conductivity of Polyacrylonitrile Based Carbon Fibers." In: *Journal of Industrial and Engineering Chemistry* 78 (2019), pp. 137–142. ISSN: 1226086X. DOI: 10.1016/j.jiec.2019.06.025.

[217] Y. Buser, E. Krämer, R. Akkerman, and W. Grouve. "Reliable Longitudinal Electrical Conductivity Characterisation of Unidirectional CFRP Tapes." In: *Composites Part A: Applied Science and Manufacturing* 188 (Jan. 2025), p. 108550. ISSN: 1359835X. DOI: 10.1016/j.compositesa.2024.108550.

[218] M. F. Haider, P. K. Majumdar, S. Angeloni, and K. L. Reifsnider. "Nonlinear Anisotropic Electrical Response of Carbon Fiber-Reinforced Polymer Composites." In: *Journal of Composite Materials* 52.8 (Apr. 2018), pp. 1017–1032. ISSN: 0021-9983, 1530-793X. DOI: 10.1177/0021998317719999.

[219] T. Dhanya and C. S. Yerramalli. "Lightning Strike Effect on Carbon Fiber Reinforced Composites – Effect of Copper Mesh Protection." In: *Materials Today Communications* 16 (Sept. 2018), pp. 124–134. ISSN: 23524928. DOI: 10.1016/j.mtcomm.2018.05.009.

[220] Y. Zhu, Y. Ming, B. Wang, Y. Duan, H. Xiao, C. Zhang, J. Sun, and X. Tian. "Finite Element Analysis of Lightning Damage Factors Based on Carbon Fiber Reinforced Polymer." In: *Materials* 14.18 (Sept. 10, 2021), p. 5210. ISSN: 1996-1944. DOI: 10.3390/ma14185210.

[221] H. Lee, O. Galstyan, A. Babajanyan, B. Friedman, G. Berthiau, J. Kim, D. S. Han, and K. Lee. "Characterization of Anisotropic Electrical Conductivity of Carbon Fiber Composite Materials by a Microwave Probe Pumping Technique." In: *Journal of Composite Materials* 50.15 (June 2016), pp. 1999–2004. ISSN: 0021-9983, 1530-793X. DOI: 10.1177/0021998315599591.

[222] J. Guo, X. Gao, E. Toma, and U. Netzelmann. "Anisotropy in Carbon Fiber Reinforced Polymer (CFRP) and Its Effect on Induction Thermography." In: *NDT & E International* 91 (Oct. 2017), pp. 1–8. ISSN: 09638695. DOI: 10.1016/j.ndteint.2017.05.004.

[223] U. Netzelmann and J. Guo. "Induction Thermography on CFRP and the Role of Anisotropy." In: *Proceedings of the 2018 International Conference on Quantitative InfraRed Thermography*. 2018 Quantitative InfraRed Thermography. QIRT Council, 2018. DOI: 10.21611/qirt.2018.063.

[224] S.-Y. Wang, G.-H. Xie, H.-Y. Xia, S. Xu, Z.-H. Lin, and S.-Q. Li. "A Review on Resistance-Based Self-Sensing of Carbon Fiber-Reinforced Polymer Subjected to Loads." In: *Advanced Engineering Materials* 27.13 (July 2025), p. 2500244. ISSN: 1438-1656, 1527-2648. DOI: 10.1002/adem.202500244.

[225] Y. Tao, R. Zhang, X. Hu, Y. Ou, M. Ren, J. Sun, H. Zhang, and T. Peijs. "A Comprehensive Review on Fiber-Based Self-Sensing Polymer Composites for in Situ Structural Health Monitoring." In: *Advanced Composites and Hybrid Materials* 8.5 (Oct. 2025), p. 339. ISSN: 2522-0128, 2522-0136. DOI: 10.1007/s42114-025-01413-y.

[226] R. Franz and G. Wiedemann. "Ueber Die Wärme-Leitungsfähigkeit Der Metalle." In: *Annalen der Physik* 165.8 (Jan. 1853), pp. 497–531. ISSN: 0003-3804, 1521-3889. DOI: 10.1002/andp.18531650802.

[227] L. Lorenz. "Bestimmung Der Wärmegrade in Absolutem Maasse." In: *Annalen der Physik* 223.11 (Jan. 1872), pp. 429–452. ISSN: 0003-3804, 1521-3889. DOI: 10.1002/andp.18722231107.

[228] Y. Xue, Z. Li, G. Li, X. Xu, J. Ding, B. Gu, and B. Sun. "Modeling of Multi-Scale 3-D Conductive Network and Electrical Conductivity of Carbon Fiber Braided Composites." In: *Composites Part A: Applied Science and Manufacturing* 187 (Dec. 2024), p. 108479. ISSN: 1359835X. DOI: 10.1016/j.compositesa.2024.108479.

[229] X. Luo, M. Qu, and D. W. Schubert. "Electrical Conductivity and Fiber Orientation of Poly(Methyl Methacrylate)/Carbon Fiber Composite Sheets with Various Thickness." In: *Polymer Composites* 42.2 (Feb. 2021), pp. 548–558. ISSN: 0272-8397, 1548-0569. DOI: 10.1002/pc.25846.

[230] W. Bauhofer and J. Z. Kovacs. "A Review and Analysis of Electrical Percolation in Carbon Nanotube Polymer Composites." In: *Composites Science and Technology* 69.10 (Aug. 2009), pp. 1486–1498. ISSN: 02663538. DOI: 10.1016/j.compscitech.2008.06.018.

[231] J. B. Park, T. Okabe, and N. Takeda. "New Concept for Modeling the Electromechanical Behavior of Unidirectional Carbon-Fiber-Reinforced Plastic under Tensile Loading." In: *Smart Materials and Structures* 12.1 (Feb. 1, 2003), pp. 105–114. ISSN: 0964-1726. DOI: 10.1088/0964-1726/12/1/312.

[232] Z. Xia, T. Okabe, J. Park, W. Curtin, and N. Takeda. "Quantitative Damage Detection in CFRP Composites." In: *Composites Science and Technology* 63.10 (Aug. 2003), pp. 1411–1422. ISSN: 02663538. DOI: 10.1016/S0266-3538(03)00083-6.

[233] H. D. Roh, S. Y. Oh, and Y.-B. Park. "Self-Sensing Impact Damage in and Non-Destructive Evaluation of Carbon Fiber-Reinforced Polymers Using Electrical Resistance and the Corresponding Electrical Route Models." In: *Sensors and Actuators A: Physical* 332 (Dec. 2021), p. 112762. ISSN: 09244247. DOI: 10.1016/j.sna.2021.112762.

[234] *PeakTech 2170 LCR-/ESR Meter: Operating Manual (DE/EN)*. PeakTech GmbH. Nov. 2024.

[235] L. E. Bengtsson. "A Microcontroller-Based Lock-in Amplifier for Sub-Milliohm Resistance Measurements." In: *Review of Scientific Instruments* 83.7 (July 1, 2012), p. 075103. ISSN: 0034-6748, 1089-7623. DOI: 10.1063/1.4731683.

[236] A. C. Lazanas and M. I. Prodromidis. "Electrochemical Impedance Spectroscopy-A Tutorial." In: *ACS Measurement Science Au* 3.3 (June 21, 2023), pp. 162–193. ISSN: 2694-250X, 2694-250X. DOI: 10.1021/acsmeasuresciau.2c00070.

[237] C. Prodan and C. Bot. "Correcting the Polarization Effect in Very Low Frequency Dielectric Spectroscopy." In: *Journal of Physics D: Applied Physics* 42.17 (Sept. 7, 2009), p. 175505. ISSN: 0022-3727, 1361-6463. DOI: 10.1088/0022-3727/42/17/175505.

[238] J. Janesch. *Two-Wire vs. Four-Wire Resistance Measurements: Which Configuration Makes Sense for Your Application?* Keithley Instruments, Inc. (Tektronix portfolio). May 2013. URL: https://download.tek.com/document/2Wire_4Wire%20Resistance%20Article.pdf (visited on 12/28/2025).

[239] H.-h. Wu, S.-c. Li, J.-n. Zhang, and L. Tong. "Electrical Resistivity Response of Unidirectional Thin-Ply Carbon Fiber Reinforced Polymers." In: *Composite Structures* 228 (Nov. 2019), p. 111342. ISSN: 02638223. DOI: 10.1016/j.compstruct.2019.111342.

[240] A. Arteiro, C. Furtado, G. Catalanotti, P. Linde, and P. Camanho. "Thin-Ply Polymer Composite Materials: A Review." In: *Composites Part A: Applied Science and Manufacturing* 132 (May 2020), p. 105777. ISSN: 1359835X. DOI: 10.1016/j.compositesa.2020.105777.

[241] J. Schindelin, I. Arganda-Carreras, E. Frise, V. Kaynig, M. Longair, T. Pietzsch, S. Preibisch, C. Rueden, S. Saalfeld, B. Schmid, J.-Y. Tinevez, D. J. White, V. Hartenstein, K. Eliceiri, P. Tomancak, and A. Cardona. "Fiji: An Open-Source Platform for Biological-Image Analysis." In: *Nature Methods* 9.7 (July 2012), pp. 676–682. ISSN: 1548-7091, 1548-7105. DOI: 10.1038/nmeth.2019.

[242] N. Otsu. "A Threshold Selection Method from Gray-Level Histograms." In: *IEEE Transactions on Systems, Man, and Cybernetics* 9.1 (Jan. 1979), pp. 62–66. ISSN: 0018-9472, 2168-2909. DOI: 10.1109/TSMC.1979.4310076.

[243] L. Vincent and P. Soille. "Watersheds in Digital Spaces: An Efficient Algorithm Based on Immersion Simulations." In: *IEEE Transactions on Pattern Analysis and Machine Intelligence* 13.6 (June 1991), pp. 583–598. ISSN: 01628828. DOI: 10.1109/34.87344.

[244] K. R. Rao, D. N. Kim, and J. J. Hwang. "Two-Dimensional Discrete Fourier Transform." In: K. Rao, D. Kim, and J.-J. Hwang. *Fast Fourier Transform - Algorithms and Applications*. Dordrecht: Springer Netherlands, 2010, pp. 127–184. ISBN: 978-1-4020-6628-3. DOI: 10.1007/978-1-4020-6629-0_5.

[245] J. W. Cooley and J. W. Tukey. "An Algorithm for the Machine Calculation of Complex Fourier Series." In: *Mathematics of Computation* 19.90 (1965), pp. 297–301. ISSN: 0025-5718, 1088-6842. DOI: 10.1090/S0025-5718-1965-0178586-1.

[246] R. C. Gonzalez and R. E. Woods. *Digital Image Processing*. Fourth edition, global edition. New York: Pearson, 2017. 1 p. ISBN: 978-0-13-335672-4.

[247] F. Harris. "On the Use of Windows for Harmonic Analysis with the Discrete Fourier Transform." In: *Proceedings of the IEEE* 66.1 (1978), pp. 51–83. ISSN: 0018-9219. DOI: 10.1109/PROC.1978.10837.

[248] Teledyne FLIR LLC. *Spinnaker Software Development Kit (SDK)*. Version 3.2, available at `https://www.flir.com/products/spinnaker-sdk/`. Teledyne FLIR Integrated Imaging Solutions. 2023.

[249] The HDF Group. *Hierarchical Data Format, Version 5 (HDF5)*. Version 1.14, `https://www.hdfgroup.org/solutions/hdf5/`. The HDF Group. 2023.

[250] G. Poulin, S. Corlay, R. Menegaux, et al. *H5Web: Web-based HDF5 Viewer and Visualization Library*. Developed by the European Synchrotron Radiation Facility (ESRF) and QuantStack. 2024. URL: `https://github.com/silx-kit/h5web`.

[251] C. R. Harris, K. J. Millman, S. J. van der Walt, R. Gommers, P. Virtanen, D. Cournapeau, E. Wieser, J. Taylor, S. Berg, N. J. Smith, R. Kern, M. Picus, S. Hoyer, M. H. van Kerkwijk, M. Brett, A. Haldane, J. F. del Río, M. Wiebe, P. Peterson, P. Gérard-Marchant, K. Sheppard, T. Reddy, W. Weckesser, H. Abbasi, C. Gohlke, and T. E. Oliphant. "Array programming with NumPy." In: *Nature* 585 (2020), pp. 357–362. DOI: `10.1038/s41586-020-2649-2`.

[252] W. McKinney. "pandas: a foundational Python library for data analysis and statistics." In: *Python for Data Analysis* (2012). See also `https://pandas.pydata.org/`.

[253] B. Grüning, A. Inc., and QuantStack. *Mamba and Conda: Open-Source Package Management for Scientific Computing*. Mamba is a fast, drop-in replacement for Conda written in C++. 2023. URL: `https://github.com/mamba-org/mamba`.

A Appendix: Fiber Orientation Detection

A.1 Software Repository: CompoSE

- Developers: Julian Karsten, Louis Braun

CompoSE is a software tool for **Compo**site **S**onar **E**valuation, developed to standardize the ultrasonic data processing workflow from raw file import to depth-resolved analysis and reporting for fiber-reinforced polymer composites. Conceptually, CompoSE sits between a reusable framework and a project-specific analysis implementation: core modules provide a consistent data model, configuration handling, logging, parsing, processing, and figure generation, while the main entry point assembles these building blocks into the concrete processing pipelines used throughout this thesis; detailed description in Section 4.3. In the current implementation, raw Hillgus (.hgv) files are imported by a dedicated parser that extracts acquisition metadata (e.g., scan increments, sampling rate, sound-speed settings, and data offsets) and reconstructs the measurement into a three-dimensional tensor $\mathcal{U}(x_i, y_j, t_k)$ for subsequent depth-resolved evaluation. Pre-processing utilities support spatial and depth ROI definition, amplitude scaling, Hilbert-based envelope computation, automated front- and back-wall localization, specimen cropping, and robust handling of corrupted regions through controlled inpainting and exclusion rules. Building on these steps, the fiber-orientation module implements slice-wise texture analysis in the Fourier domain (2D-FFT, polar re-sampling, radial-band selection, and peak-based angular evaluation), thereby producing the depth-resolved orientation outputs reported in the results section (Section 4.4).

From a user-experience perspective, CompoSE is designed for pragmatic laboratory operation: it can be executed as a script-driven workflow while still offering lightweight interactive input where expert supervision is beneficial. When launched without explicit arguments, the software prompts the user to select an input dataset via a minimal file-selection dialog and automatically loads an associated JSON configuration if present; otherwise, a default configuration is

instantiated. During parsing and pre-processing, interactive Matplotlib [202] widgets are used to support manual selection of key parameters such as depth ranges and amplitude thresholds in a transparent and reproducible manner. All processing decisions are persisted by exporting the active configuration to the output directory together with a structured set of diagnostic plots (A-/B-/C-scan views, interface maps, FFT and polar spectra, and angular spectra), while a unified logging layer records parameter choices and runtime information for traceability. This combination of modular components, reproducible configuration snapshots, and minimal GUI interaction enables both rapid exploratory evaluation and consistent batch-style processing of larger measurement campaigns.

A.2 Methodology Flowchart

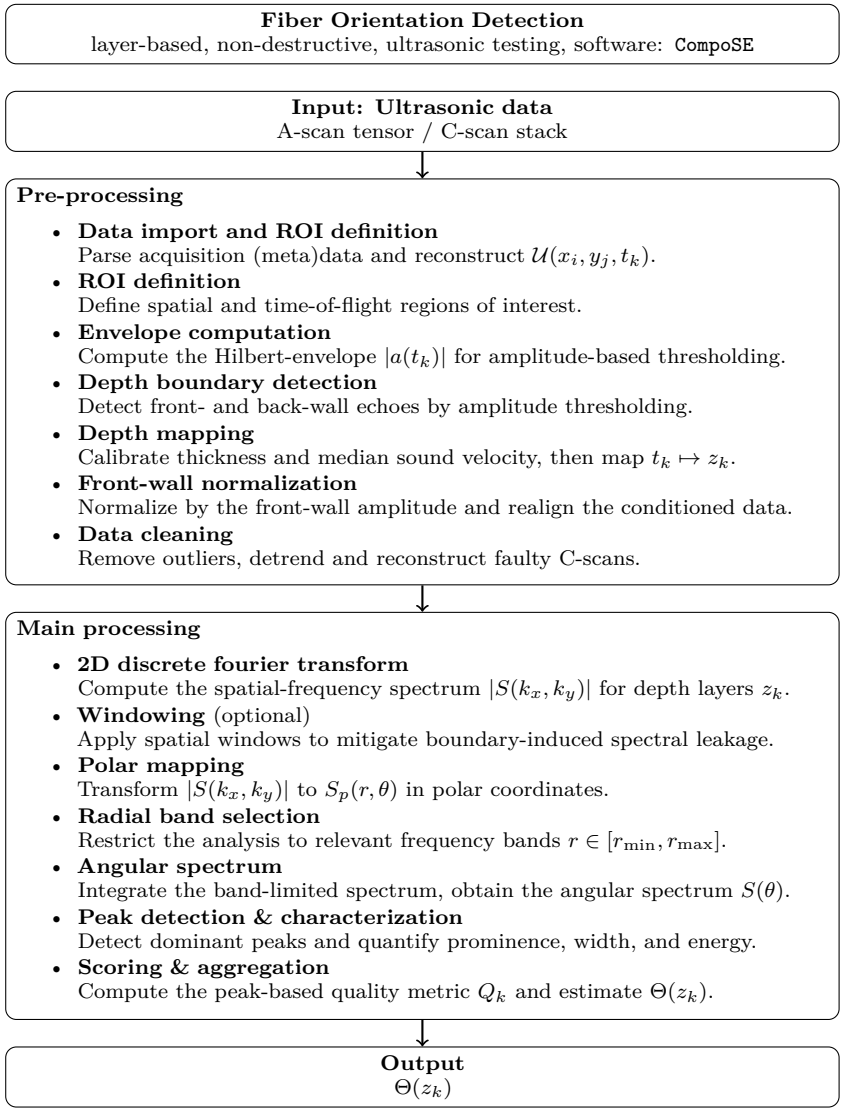


Figure A.1: Layer-based ultrasonic fiber orientation detection: from ultrasonic data input to the depth-resolved orientation estimate $\Theta(z_k)$.

A.3 2D Discrete Fourier Transform

The objective of the two-dimensional discrete Fourier transform (2D-FFT) is to map a two-dimensional spatial signal into the frequency domain, thereby decomposing it into its constituent spatial-frequency components. For a discrete input array $x(n_1, n_2)$ of size $N_1 \times N_2$, the 2D-FFT is defined as [244]

$$X^{\mathrm{F}}(k_1, k_2) = \sum_{n_1=0}^{N_1-1} \sum_{n_2=0}^{N_2-1} x(n_1, n_2)\, W_{N_1}^{n_1 k_1} W_{N_2}^{n_2 k_2}, \tag{A.1}$$

where $x(n_1, n_2)$ denotes the discrete spatial signal sampled at indices n_1 and n_2, $X^{\mathrm{F}}(k_1, k_2)$ is the corresponding complex-valued Fourier coefficient at frequency indices k_1 and k_2, and N_1 and N_2 are the numbers of samples along the two spatial directions (i.e., the image dimensions). The indices $n_1 \in \{0, \ldots, N_1 - 1\}$ and $n_2 \in \{0, \ldots, N_2 - 1\}$ enumerate spatial sample positions, while $k_1 \in \{0, \ldots, N_1 - 1\}$ and $k_2 \in \{0, \ldots, N_2 - 1\}$ enumerate discrete spatial-frequencies. The factors W_{N_1} and W_{N_2} are the complex roots of unity that generate the orthogonal Fourier basis functions along each dimension, i.e.,

$$W_{N_1} = \exp\!\left(-\mathrm{i}\,\frac{2\pi}{N_1}\right), \qquad W_{N_2} = \exp\!\left(-\mathrm{i}\,\frac{2\pi}{N_2}\right). \tag{A.2}$$

In practice, FFT algorithms are used to efficiently compute Equation (A.1) [245]. While the formal definition is compact, it can be unintuitive at first glance. In the present work, 2D-FFT is primarily used as an analysis tool through SciPy [203] (Python) implementations, and its practical meaning is most easily conveyed by inspecting what it does to simple controlled input patterns.

A key qualitative fact is that oriented quasi-periodic structures in the spatial domain produce distinct spectral peaks at specific locations in the frequency domain: a single oriented sinusoid (or stripe pattern) yields two symmetric peaks at $\pm\mathbf{k}$ in the Fourier spectrum. The radial distance $|\mathbf{k}|$ from the origin increases with spatial frequency (i.e., the spacing of the features decreases), while the azimuthal direction of $\mathbf{k}$ encodes the dominant wave-vector orientation. Consequently, changes in spacing primarily shift spectral magnitude radially, while changes in orientation rotate the spectral pattern azimuthally [246].

To build intuition, Figures A.2 and A.3 contrasts four synthetic input images with their corresponding 2D-FFT magnitude representations. Each spatial image

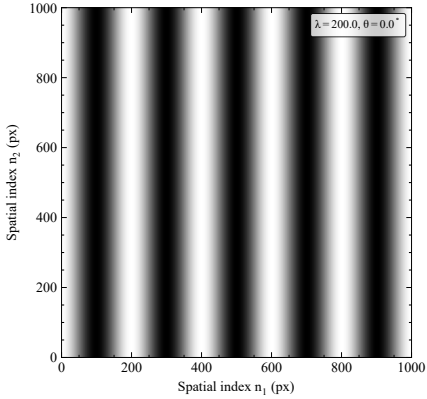
is a single (or two superpositioned) oriented sinusoidal pattern. The Fourier plots show the centered spectrum. In these examples, three effects are highlighted:

(i) Spacing / frequency effect: decreasing the spatial period increases the spatial frequency, moving the peak pair further away from the origin; see Figures A.2c and A.2d.

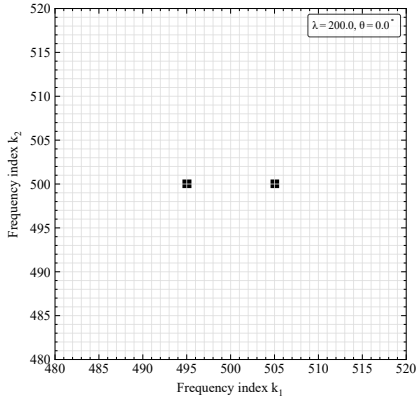
(ii) Directional / azimuth effect: rotating the spatial pattern rotates the peak pair accordingly, thereby encoding the dominant direction in the spectrum; see Figures A.3a and A.3b.

(iii) Superposition effect: adding multiple oriented components yields multiple peak pairs, each associated with one contributing direction and spatial frequency; see Figures A.3c and A.3d.

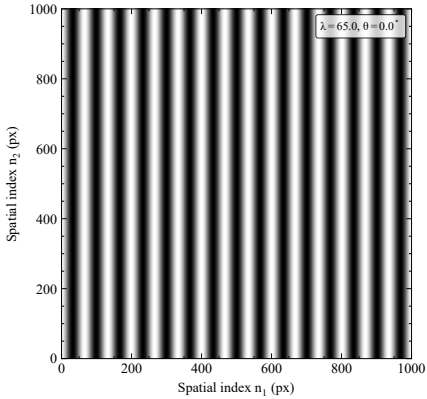
In ultrasonic testing, C-scan images often exhibit oriented texture-like signatures. When such directional patterns are present, the 2D-FFT yields a compact frequency-domain view in which preferred orientations appear as symmetric peak pairs or elongated lobes. Orientation can then be inferred by locating the dominant azimuthal directions of these spectral features. For CFRP, this provides a physically consistent route to quantify in-plane tow/fiber direction from C-scan texture: characteristic spacing shifts the peak radius (spatial frequency), whereas changes in ply angle or lay-up direction primarily rotate the peak azimuth, which supports automated orientation mapping and comparative interpretation across laminate regions.



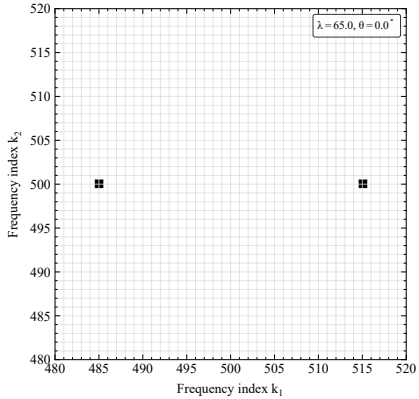
(a) Reference sinusoidal pattern.



(b) Reference 2D-FFT magnitude.

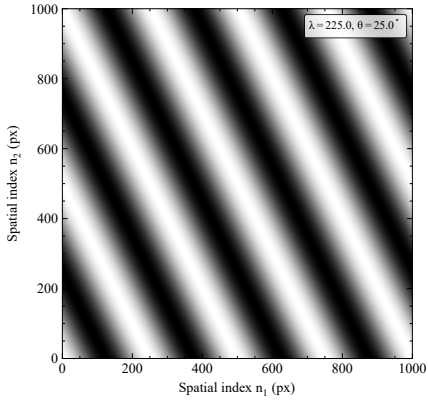


(c) Higher spatial frequency (smaller spacing).

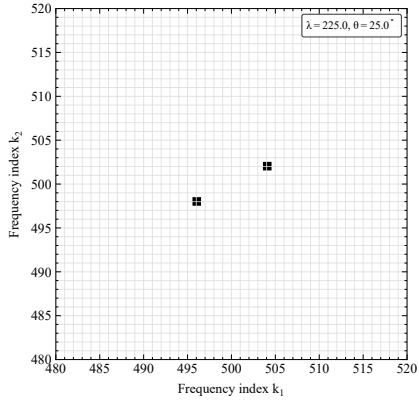


(d) Peaks shift radially outward with frequency.

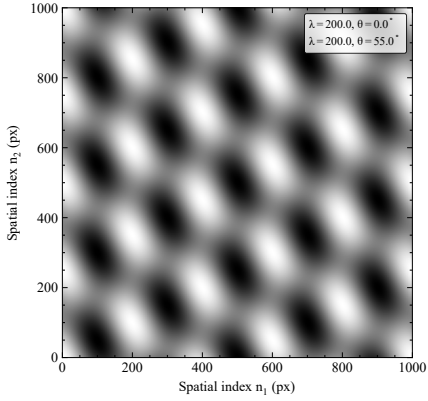
Figure A.2: 2D-FFT demonstration: spacing and frequency. Left: spatial-domain input patterns. Right: centered 2D-FFT magnitude representations.



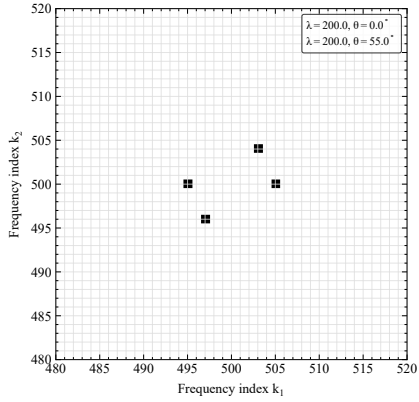
(a) Rotated sinusoidal pattern (direction change).



(b) Peak pair rotates azimuthally with direction.



(c) Superposition of two sinusoidal patterns.

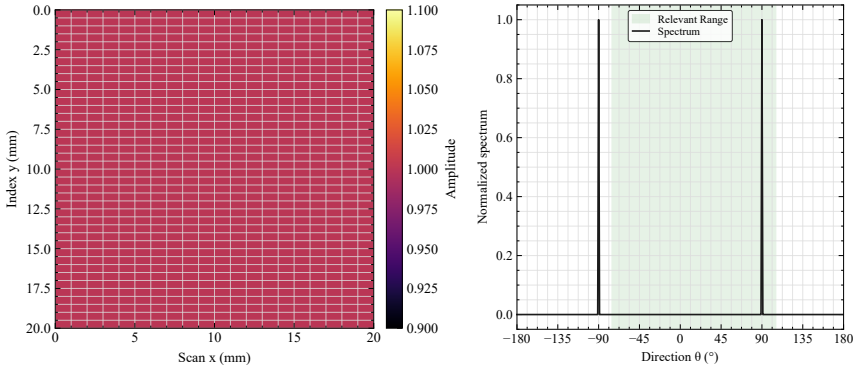


(d) Multiple peak pairs correspond to contributing components.

Figure A.3: 2D-FFT demonstration: direction, azimuth and superposition. Left: spatial-domain input patterns. Right: centered 2D-FFT magnitude representations.

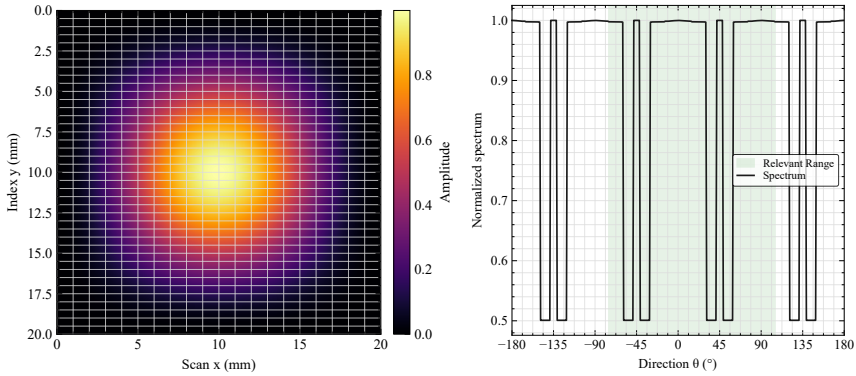
A.4 2D Windowing Functions

This appendix provides a comparative visualization of commonly used two-dimensional windowing functions and their influence on the resulting 2D-FFT spectra. As a reference case, a homogeneous C-scan consisting of constant intensity values equal to one is considered (Figure A.4a). The corresponding two-dimensional Fourier transform of this unwindowed signal is shown in Figure A.4b. For some windowing functions under consideration (Hann, Tukey, Blackman, and Gaussian) [143, 247], the applied spatial window is illustrated in the left subfigure (a), while the resulting two-dimensional Fourier magnitude spectrum is shown in the corresponding right subfigure (b). This representation highlights how different windowing functions suppress boundary-induced spectral leakage at the expense of introducing characteristic artifacts in the frequency domain. The comparison serves to illustrate the trade-offs inherent to windowing in 2D FFT-based orientation analysis. [244]



(a) Reference C-scan. **(b)** 2D FFT spectrum, no windowing.

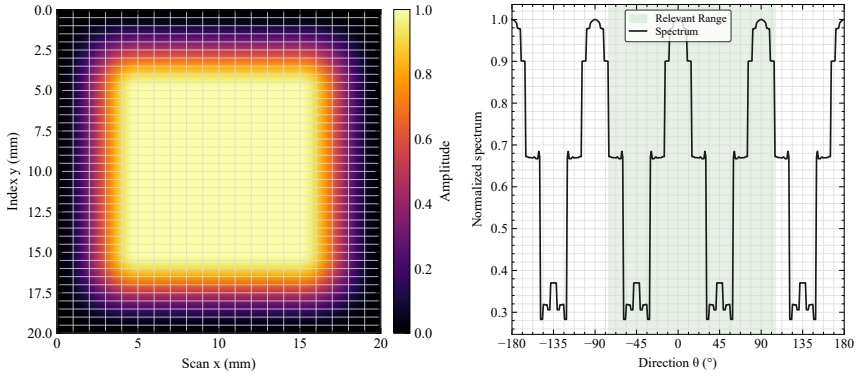
Figure A.4: Two-dimensional Fourier spectrum of a homogeneous reference C-scan with unit amplitude without windowing.



(a) Reference C-Scan after Hann window function application.

(b) 2D FFT spectrum after windowing.

Figure A.5: Effect of the Hann window on the two-dimensional Fourier spectrum of a homogeneous C-scan with unit amplitude.



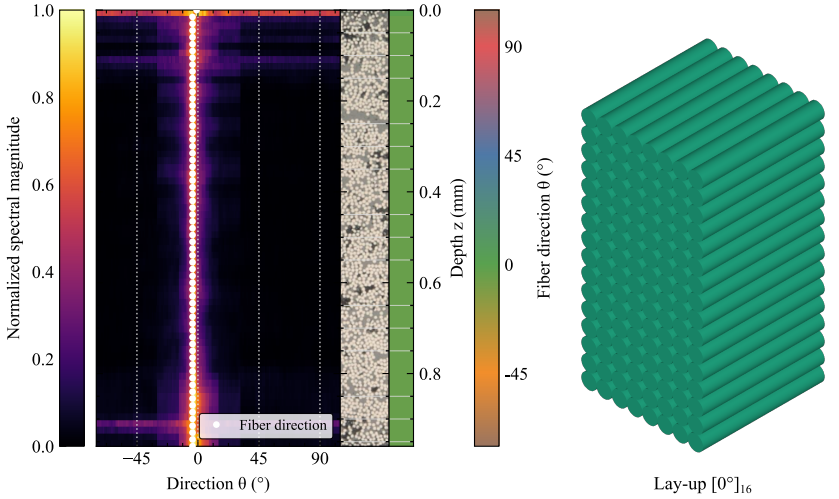
(a) Reference C-Scan after Tukey window function application.

(b) 2D FFT spectrum after windowing.

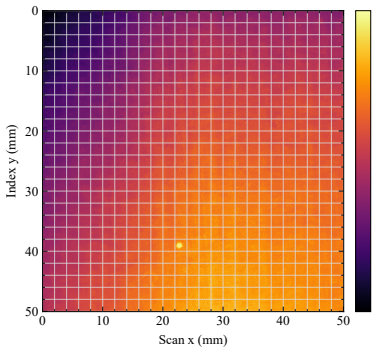
Figure A.6: Effect of the Tukey window on the two-dimensional Fourier spectrum of a homogeneous C-scan with unit amplitude.

A.5 Supporting Results

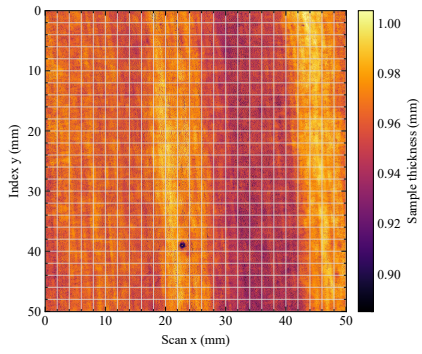
A.5.1 Unidirectional Laminates



(a) Trough thickness fiber-orientation analysis, micrograph and weighted score Q_k (left); schematic of the lay-up, with the 0° plies highlighted in green (right).

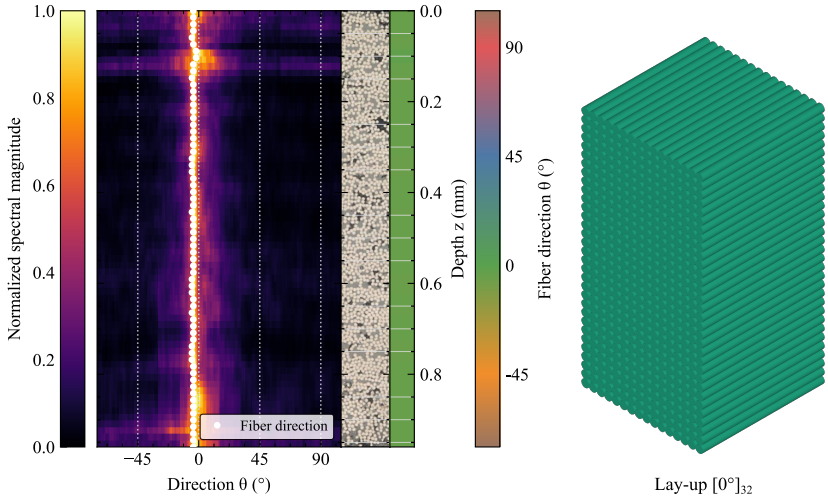


(b) Top surface (front-wall).

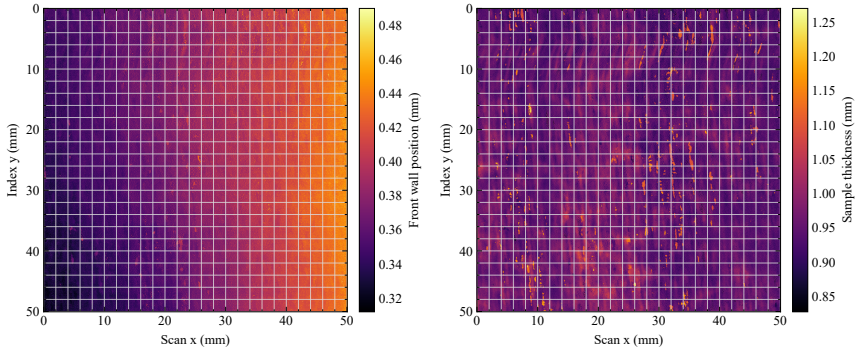


(c) Thickness (front-to-back-wall).

Figure A.7: Trough-thickness fiber-orientation analysis of a 60 gsm unidirectional CFRP laminate (UD-60).



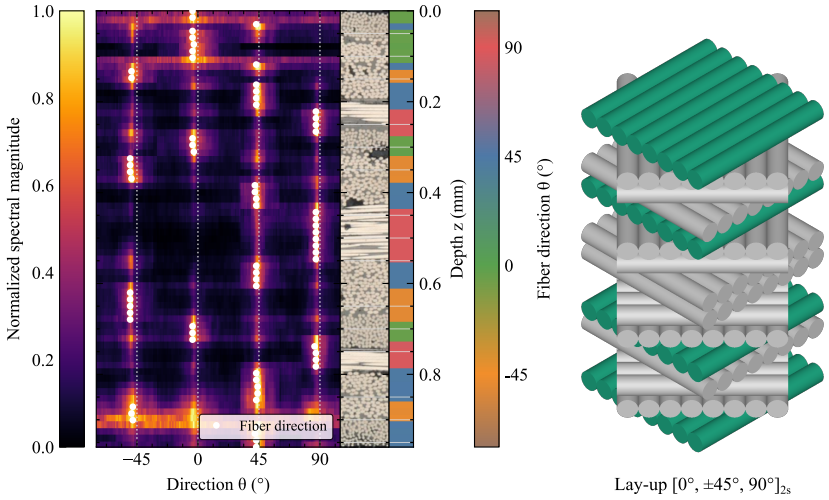
(a) Trough thickness fiber-orientation analysis, micrograph and weighted score Q_k (left); schematic of the lay-up, with the 0° plies highlighted in green (right).



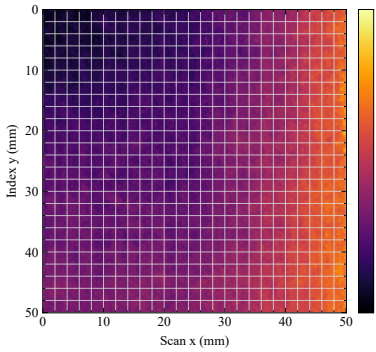
(b) Top surface (front-wall). **(c)** Thickness (front-to-back-wall).

Figure A.8: Trough-thickness fiber-orientation analysis of a 30 gsm unidirectional CFRP laminate (UD-30).

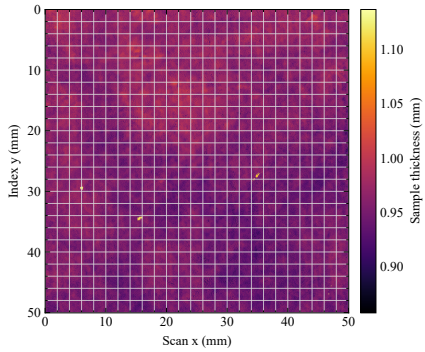
A.5.2 Quasi-Isotropic Laminates



(a) Trough thickness fiber-orientation analysis, micrograph and weighted score Q_k (left); schematic of the lay-up, with the 0° plies highlighted in green (right).

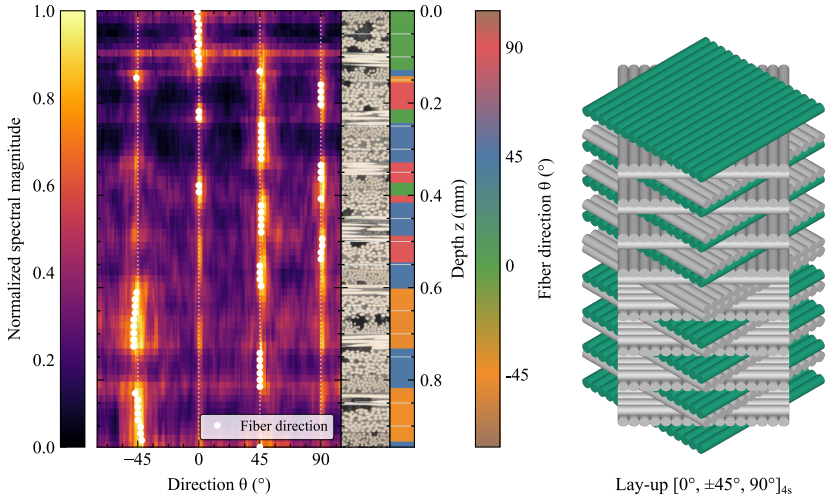


(b) Top surface (front-wall).

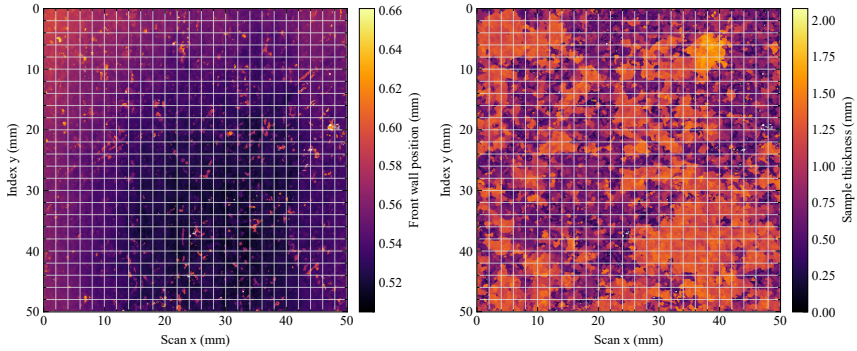


(c) Thickness (front-to-back-wall).

Figure A.9: Trough-thickness fiber-orientation analysis of a 60 gsm quasi-isotropic CFRP laminate (QI-60).



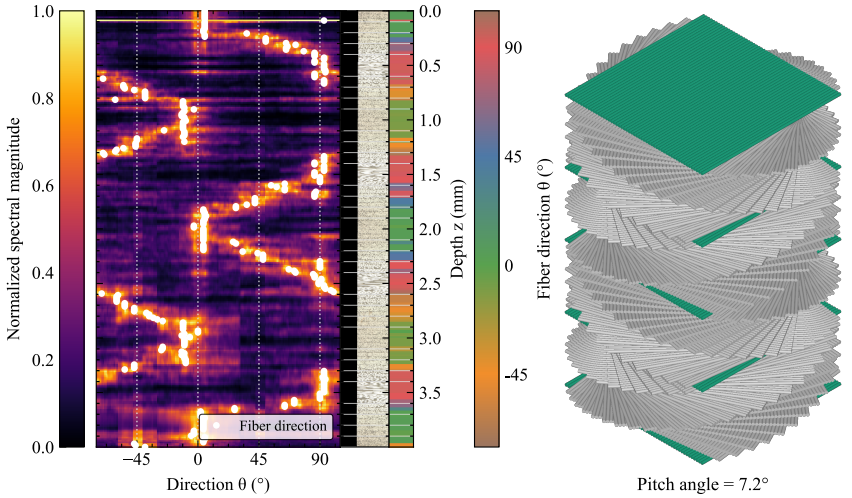
(a) Trough thickness fiber-orientation analysis, micrograph and weighted score Q_k (left); schematic of the lay-up, with the 0° plies highlighted in green (right).



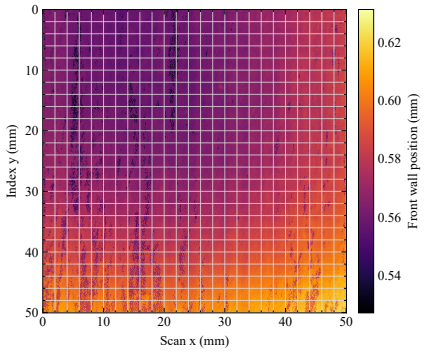
(b) Top surface (front-wall). **(c)** Thickness (front-to-back-wall).

Figure A.10: Trough-thickness fiber-orientation analysis of a 30 gsm quasi-isotropic CFRP laminate (QI-30).

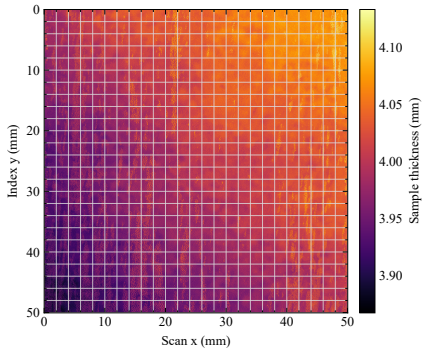
A.5.3 Bouligand Laminates



(a) Trough thickness fiber-orientation analysis, micrograph and weighted score Q_k (left); schematic of the lay-up, with the 0° plies highlighted in green (right).

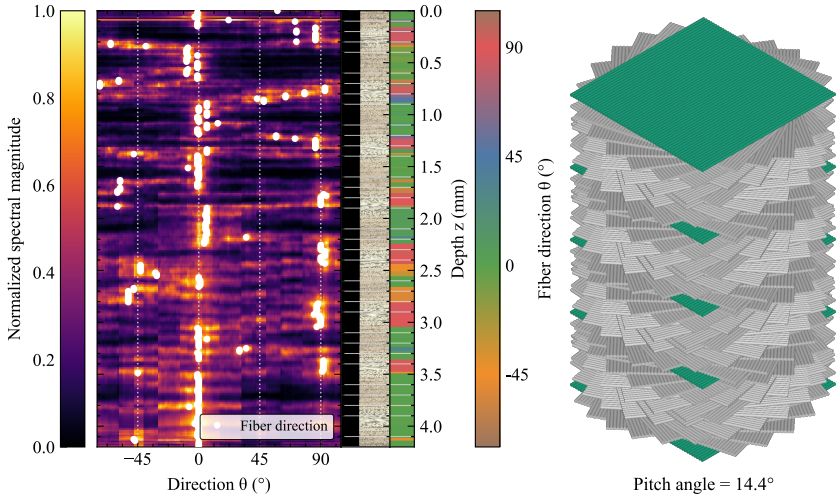


(b) Top surface (front-wall).

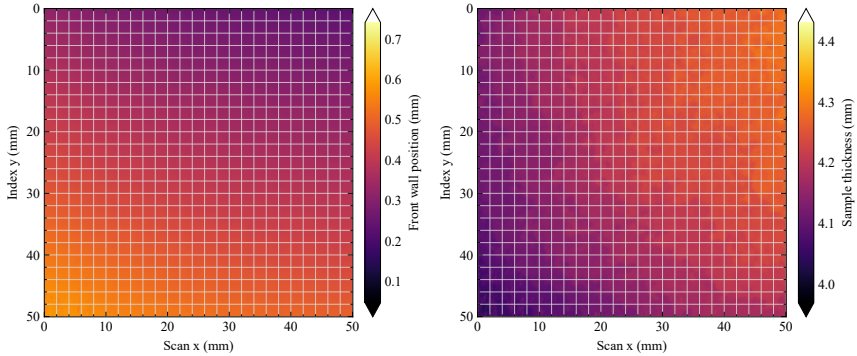


(c) Thickness (front-to-back-wall).

Figure A.11: Trough-thickness fiber-orientation analysis of a 40 gsm, 7.2° Bouligand CFRP laminate (BL-7.2°).



(a) Trough thickness fiber-orientation analysis, micrograph and weighted score Q_k (left); schematic of the lay-up, with the 0° plies highlighted in green (right).



(b) Top surface (front-wall). **(c)** Thickness (front-to-back-wall).

Figure A.12: Trough-thickness fiber-orientation analysis of a 40 gsm, 14.4° Bouligand CFRP laminate (BL-14.4°).

B Appendix: Anisotropic Thermal Properties

B.1 Software Repository: TCAM

- Developers: Julian Karsten, Lisa Fahs

The software framework TCAM (**T**hermal **C**onductivity of **A**nisotropic **M**aterials), constitutes a modular and extensible tool-chain for the contactless characterization of thermal transport properties in anisotropic materials using infrared thermography. The repository provides a unified environment that integrates experimental control, data acquisition, signal evaluation, and visual representation of thermal diffusion processes. Its design follows the principle of scientific reproducibility, ensuring that all measurement configurations, device states, and evaluation parameters are stored together with the corresponding experimental data.

The structure of the TCAM repository reflects the sequential workflow of a typical thermophysical experiment. The main application serves as a measurement interface, implemented as a graphical user interface using the NiceGUI [204] framework; see Figure B.1. Within this environment, the operator can control multiple hardware components in real time, including a FLIR infrared camera via the Spinnaker SDK [248], a Korad programmable power supply for temperature control via a Peletier element, an Arduino-based temperature sensor unit, and a Cobolt laser spot heating source. All components are encapsulated by dedicated worker classes that manage the communication threads and maintain synchronized data flow between hardware and graphical front-end. During measurement, binary thermal image data is streamed continuously from the infrared camera and stored together with the corresponding metadata in a HDF5-based [249] data structure. This approach ensures both high acquisition throughput and complete traceability of the experimental configuration.

Subsequent data processing is performed within the second main module, which provides an interactive graphical environment for the evaluation of recorded

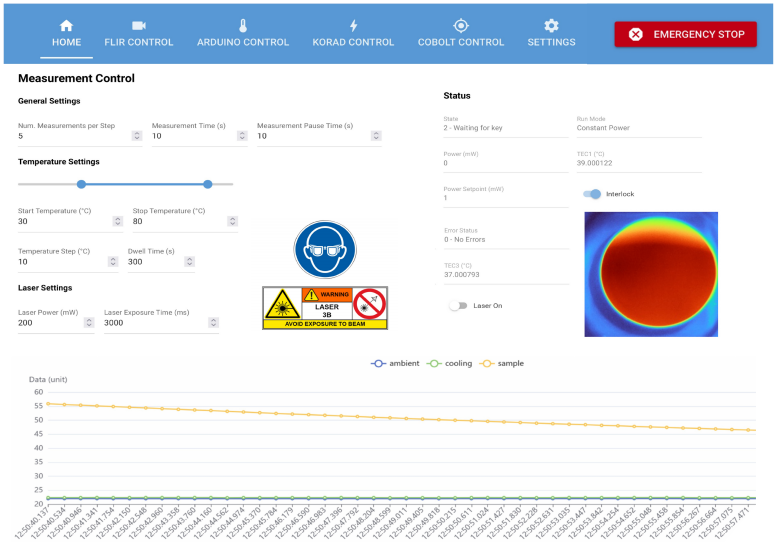


Figure B.1: TCAM GUI for hardware control and data acquisition; collage representing general functions.

data sets; see Figure B.2. The evaluation pipeline converts the temporally resolved infrared images into polar and radial coordinate systems, allowing the investigation of heat propagation as a function of angular direction. By applying one-dimensional Gaussian fits to the temperature profiles over time, the software automatically extracts parameters such as amplitude, variance, and quality of fit. From the temporal evolution of the squared Gaussian spread factor, the thermal diffusivity is derived by linear regression, which can subsequently be converted to the anisotropic thermal conductivity λ using the density and specific heat capacity of the investigated material. The results, including fitted parameters, processed images, and derived quantities, are stored in a structured HDF5 file that serves as the central data container for subsequent visualization.

An important addition to the software ecosystem is the integration of H5Web [250], a browser-based visualization tool for HDF5 data [249]. H5Web provides an interactive interface that allows users to explore multidimensional datasets, heatmaps, and hierarchical metadata structures directly within a web browser without the need for separate post-processing scripts. By linking the HDF5 result files generated by TCAM to an H5Web instance, it becomes possible to

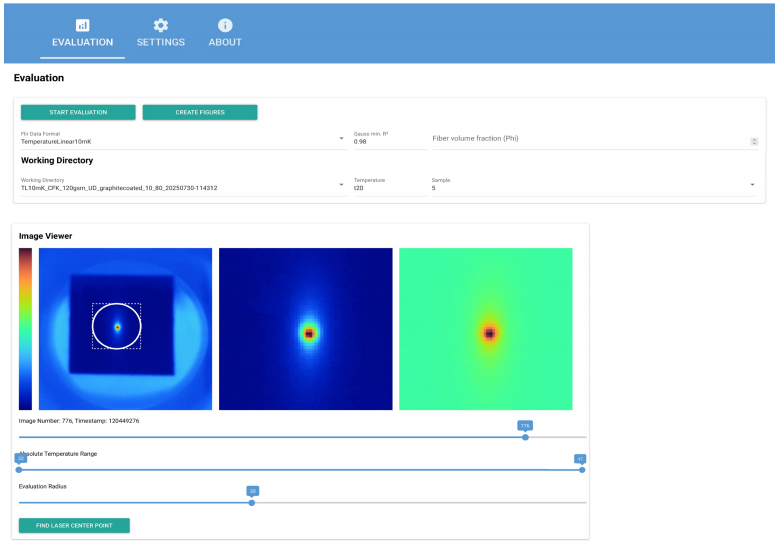


Figure B.2: TCAM GUI for initial data visualization and evaluation; collage representing general functions.

interactively inspect heat maps, temperature profiles, and fit results, while simultaneously viewing the corresponding experimental metadata; see Figure B.3.

The third major component is dedicated to dynamic visualization of the experimental and evaluated data. It enables the generation of high-quality 2D and 3D animations of the temperature evolution, supporting both fixed- and adaptive-temperature scaling modes. This module is optimized for the creation of presentation-ready media and facilitates an intuitive comparison of thermal diffusion behavior under varying experimental conditions. The visualizations operate directly on the HDF5 evaluation files, thus maintaining complete consistency with the underlying measurement data.

From a software engineering perspective, the repository follows an object-oriented design pattern, which promotes reusability, modularity, and maintainability of code. Each subsystem—camera control, power management, signal evaluation, and visualization—is implemented as an independent class hierarchy with clearly defined interfaces. The graphical user interface and the computational back-end are separated logically but operate concurrently through asynchronous communication. Numerical processing is based on well-established scientific

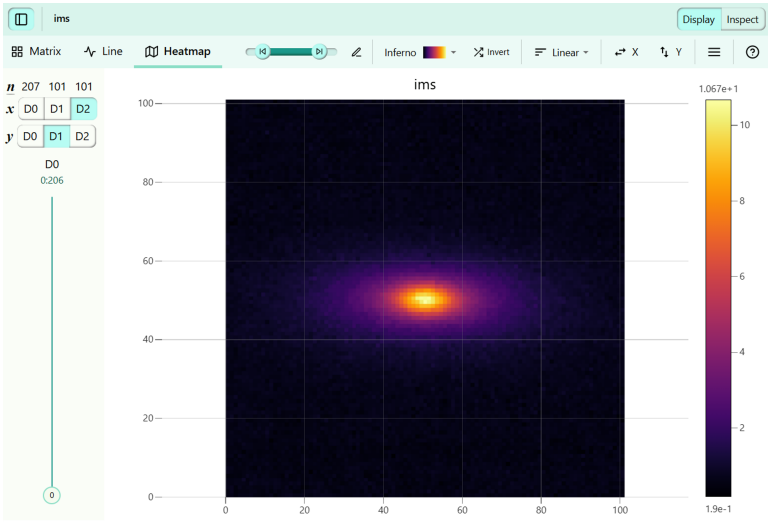


Figure B.3: TCAM HDF5 data structure and H5Web visualization tool.

Python libraries such as NumPy [251], SciPy [203], Pandas [252], and Matplotlib [202], while device interaction is performed through serial communication and vendor-provided SDKs. All configuration parameters are stored in the YAML format, allowing human readability, fully reproducible experiment execution, and batch-based data processing.

The TCAM repository is distributed together with a reproducible Python environment, defined through Mamba/Conda [253] configuration files and optional installation scripts that include the specific dependencies required for FLIR camera control and visualization. Each experimental session generates comprehensive logs containing timestamps, hardware states, and parameter values, ensuring the transparency and verifiability of the measurement process.

B.2 Methodology Flowchart

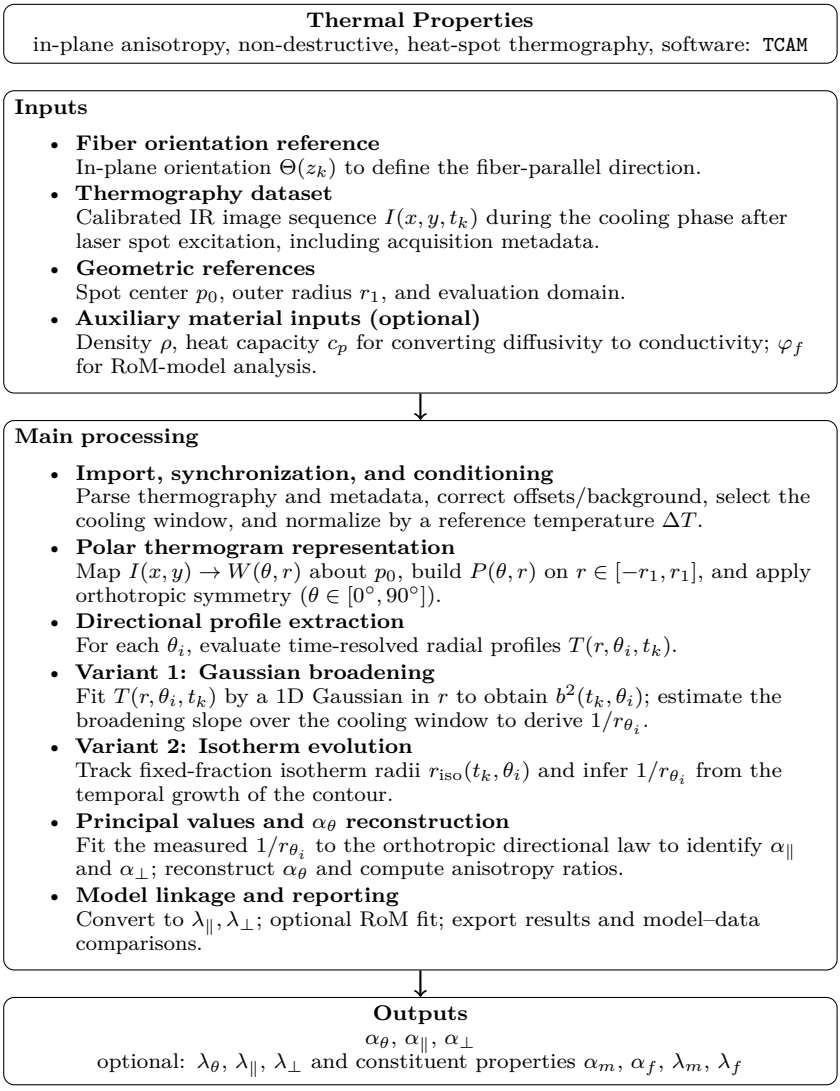


Figure B.4: Thermal anisotropy evaluation workflow implemented in software framework `TCAM`.

B.3 Polar Isotherm Evolution

Isotherms of the anisotropic Green's function in (5.46) are defined implicitly by

$$T(r, \theta, t) = f\, T(0, 0, t), \qquad f \in (0, 1), \tag{B.1}$$

corresponding to the same fixed fraction f used for Cartesian isotherms, as shown in Section 5.1.6. The polar representation of the anisotropic Green's function, Equation (5.19) is reduced to

$$\frac{r^2}{4t}\, r_\theta = c, \qquad c = -\ln f. \tag{B.2}$$

Thus, each isotherm at time t forms a polar curve $r_{\mathrm{isoT}}(t, \theta)$ that satisfies

$$r^2_{\mathrm{isoT}}(t, \theta) = \frac{4c\, t}{r_\theta}. \tag{B.3}$$

Equation (B.3) is the polar analogue of the Cartesian ellipse relation in Equation (5.19). Tracking the temporal evolution of a polar isotherm provides a direct method for extracting the directional inverse resistivity to diffusion $1/r_\theta$. For a fixed contour level $f \in (0, 1)$, define the isothermal radius as the solution of

$$r_{\mathrm{isoT}}(t, \theta) = r(t; \theta, f). \tag{B.4}$$

Experimentally, $r_{\mathrm{isoT}}(t, \theta)$ is obtained by identifying, for each time frame and angle θ, the radial position at which the temperature equals $f\, T(0, 0, t)$, with $T(0, 0, t)$ denoting the instantaneous temperature at the center of the heating spot. An example of the resulting spatio–temporal map and extracted isothermal radii is shown in Figure B.5.

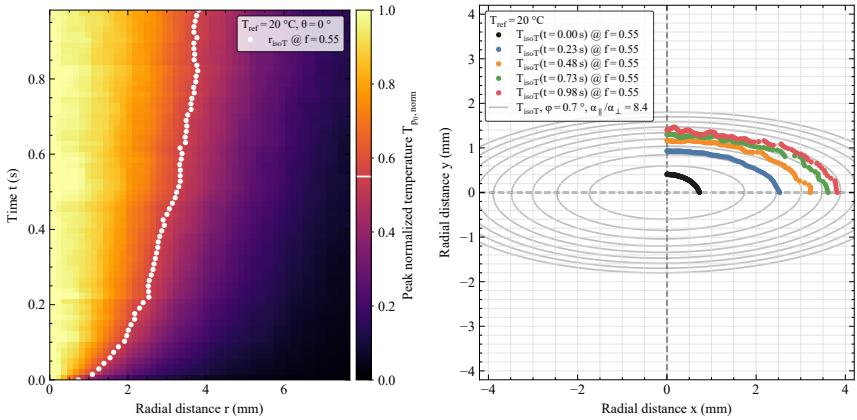
Squaring the measured radii and fitting their temporal evolution yields the affine relation

$$r^2_{\mathrm{isoT}}(t, \theta) = \frac{4c}{r_\theta}\, t + r_0^2(\theta), \tag{B.5}$$

where $r_0^2(\theta)$ accounts for finite initial spot size, instrument response, or point-spread effects.

Differentiating Equation (B.5) and solving for the reciprocal resistivity projection yields

$$\frac{1}{r_\theta} = \frac{1}{4c}\, \frac{d}{dt} r^2_{\mathrm{isoT}}(t, \theta). \tag{B.6}$$



(a) Isothermal radius $r_{\mathrm{isoT}}(t)$ at $f = 0.55$ in fiber direction.

(b) Isothermal representation in Cartesian space at $f = 0.55$.

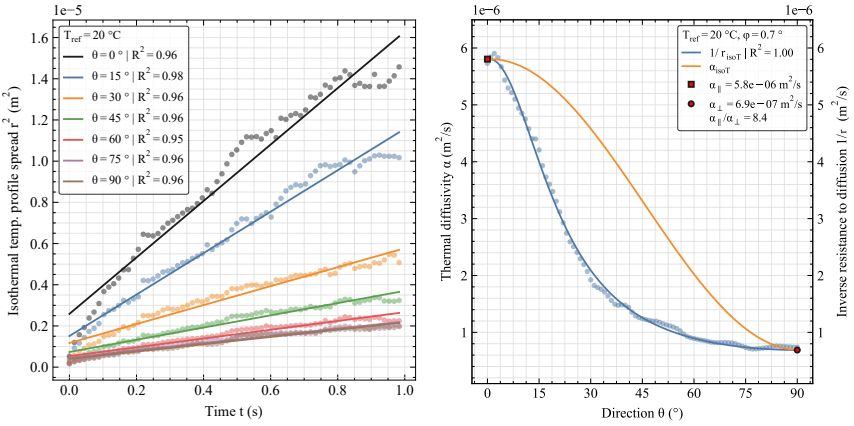
Figure B.5: Evolution of isotherms during the cooling process of a 120 gsm unidirectional CFRP laminate (UD-120).

A representative set of $r^2_{\mathrm{isoT}}(t, \theta)$ curves and their corresponding inverse resistivities and extracted diffusivities is shown in Figure B.6. Because the scaling constant $c = -\ln f$ is independent of θ, the angular dependence of $1/r_\theta$ is preserved. Thus, fitting $r^2_{\mathrm{isoT}}(t, \theta)$ over an appropriate time interval provides the full directional inverse resistivity to diffusion, from which the principal in-plane diffusivities α_x, α_y as well as the general directional diffusivities α_θ follow Equations (5.25) and (5.27).

As for all in-plane orthotropic properties, the directional response is π-periodic and symmetric with respect to the material axes. Therefore, measurements on the interval $\theta \in [0°, 90°]$ are sufficient to reconstruct the complete anisotropic diffusivity tensor.

In practice, only a narrow range of isotherm fractions f is experimentally usable. Low fractions ($f \ll 0.3$) suffer from poor signal-to-noise ratio, while high fractions ($f \gtrsim 0.7$) are distorted by the laser spot shape, detector saturation, and nonlinearities near the peak. Each chosen f introduces a different scaling constant $c = -\ln f$, making the extracted slopes sensitive to noise, local gradients, and segmentation errors in contour detection.

Because of these limitations, Gaussian fitting, based on the full radial temperature profile, is generally more robust. It uses all pixel information simultaneously,



(a) Directional diffusive broadening $r^2_{\mathrm{isoT}}(t, \theta)$.

(b) Inverse resistivity and extracted diffusivities.

Figure B.6: Directional diffusive broadening, inverse thermal resistivity, and diffusivity obtained from the isothermal-widening model. UD-CFRP: 120 gsm T700SC, ThinPreg 402.

avoids selecting a specific isotherm level and suppresses spatial noise through global regression.

C Appendix: Anisotropic Electrical Properties

C.1 Software Repository: PolAR

- Developers: Julian Karsten

PolAR is a Python-based analysis tool for **P**olygon-based **A**nalytical **R**esistivity. The software implements the analytical evaluation workflow used in this thesis to infer orthotropic in-plane resistivities of UD CFRP from angular resistance measurements on regular n-sided polygon specimens with face electrodes. PolAR combines a reusable modeling core with an application-oriented execution layer: a structured data model captures geometry, electrode configuration, material metadata, measurement vectors $R(\theta_i)$, and estimator settings; automatic validation and geometry derivations provide consistent parameter handling (e.g., face length, apothem, and model-specific transition angles). The analytical model is implemented in a piecewise formulation that separates the longitudinal-dominant regime at $\theta = 0^\circ$ from the transverse/mixed regime for $\theta \geq \alpha$, enabling a physically interpretable parameter identification. In the current implementation, $\rho_\parallel$ is obtained directly from the measured R_{0°, while $\rho_\perp$ and an optional additive resistance offset are identified from the Case 2 data via configurable aggregation strategies (least-squares, relative least-squares, mean, or median), with optional regularization for numerically stable offset fitting. The resulting parameter set is then used to predict $R(\theta)$ over the admissible angular range, and fit quality metrics (RMSE and R^2) are computed to quantify model agreement.

From a user-experience perspective, PolAR is designed as a configuration-driven, reproducible workflow rather than an interactive GUI application. Measurement datasets are provided through JSON input files that contain specimen definitions and measured angle–resistance pairs; the tool supports both single-run execution and batch processing of multiple input files, which is particularly useful for systematic thickness or geometry studies. For each run, PolAR writes a self-contained output JSON that includes the full setup and the fitted results, ensuring traceability of all model assumptions and numerical choices. In addition, the

tool generates a combined overlay plot comparing measured resistances with the analytical predictions and indicating the transition angle, thereby providing an immediate visual quality check and a publication-ready figure output. Consistent plotting style can be enforced through an optional centralized figure configuration module.

C.2 Methodology Flowchart

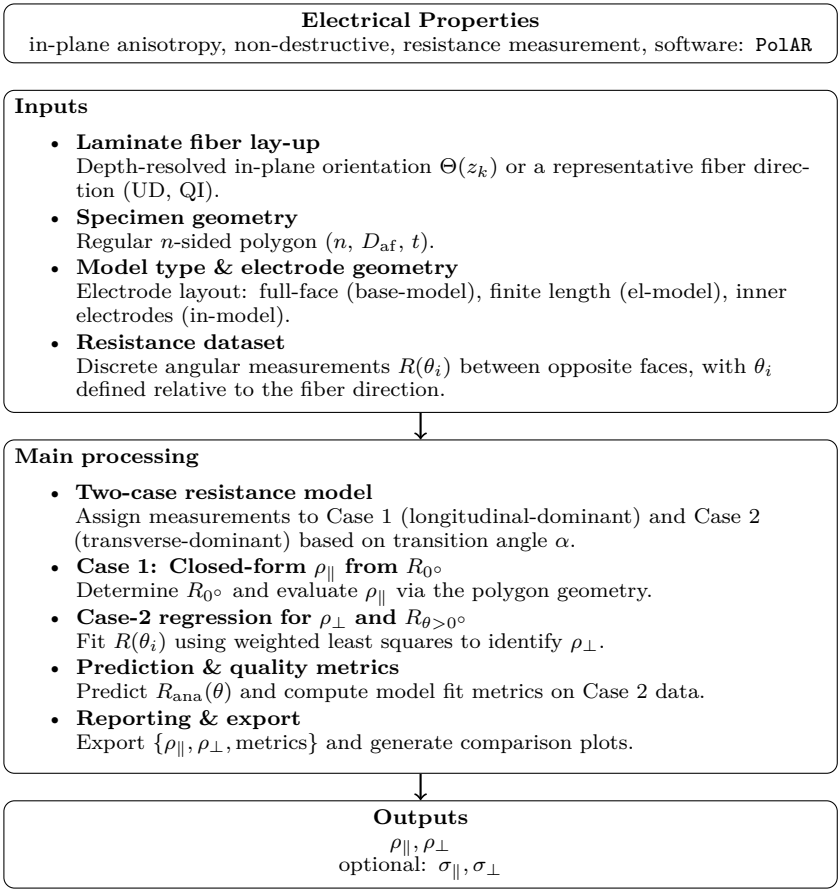


Figure C.1: Electrical anisotropy evaluation workflow implemented in the software framework `PolAR`.

C.3 Base Model - Parameter Variation

Material Thickness To assess the sensitivity of the base model with respect to geometric and specimen parameters, a parametric variation is considered in which the material resistivities $\rho_{\parallel}$ and $\rho_{\perp}$ are held constant, while the specimen thickness t is varied. Since the base-model expressions are Ohmic and scale inversely with the conducting cross section, thickness variations lead to predictable resistance scaling. For compactness, a thickness scaling factor is introduced as

$$\eta_t \;:=\; \frac{t}{t_{\mathrm{ref}}}, \qquad t_{\mathrm{ref}} > 0, \tag{C.1}$$

where t_{ref} denotes a chosen reference thickness. The corresponding resistance ratios are evaluated relative to the base-model reference at t_{ref}.

Because $R_1^{(\mathrm{base})}(\theta_i) \propto 1/t$ for fixed $\rho_{\parallel}$ and fixed geometric terms $D_{e,1}^{(\mathrm{base})}(\theta_i)$ and $W_{\mathrm{e},1}^{(\mathrm{base})}(\theta_i)$, the thickness-scaled ratio becomes

$$\frac{R_1^{(\mathrm{base})}(\theta_i;\, t)}{R_1^{(\mathrm{base})}(\theta_i;\, t_{\mathrm{ref}})} \;=\; \frac{t_{\mathrm{ref}}}{t} \;=\; \frac{1}{\eta_t}, \qquad \theta_i \le \alpha. \tag{C.2}$$

Analogously, the transverse contribution scales with $1/t$ for fixed $\rho_{\perp}$. If the longitudinal term is assumed to follow the same thickness scaling (i.e., it represents an Ohmic contribution with identical $1/t$ dependence), then the total Case 2 resistance obeys the same ratio:

$$\frac{R_2^{(\mathrm{base})}(\theta_i;\, t)}{R_2^{(\mathrm{base})}(\theta_i;\, t_{\mathrm{ref}})} \;=\; \frac{t_{\mathrm{ref}}}{t} \;=\; \frac{1}{\eta_t}, \qquad \theta_i \ge \alpha, \tag{C.3}$$

i.e., for unchanged $\rho_{\parallel}$ and $\rho_{\perp}$, halving the specimen thickness doubles the predicted resistance at all admissible orientations.

Polygon Side Number A second parametric variation concerns the polygon side number n, while $\rho_{\parallel}$ and $\rho_{\perp}$ are again held constant. For opposite-face measurements, n must be even, and for an ideal sampling of the full orthotropic interval $0^\circ \le \theta \le 90^\circ$ including both bounds, n is typically chosen as a multiple of four. Increasing n reduces the face offset angle $\beta = 2\pi/n$ and therefore refines the available angular resolution. In addition, changing n modifies the geometric scaling through the n-dependence of the face length s and/or the across-flats dimension D_{af}. Two limiting design scenarios are relevant: either (i) the across-flats

dimension is held constant and the face length follows $s^{(D)}(n) = D_{\mathrm{af}} \tan(\pi/n)$, or (ii) the face length is held constant and the across-flats dimension follows $D_{\mathrm{af}}^{(s)}(n) = s \cot(\pi/n)$. These scalings affect Case 1 and Case 2 in fundamentally different ways: in Case 1 the face length enters primarily as an effective electrode width (and thus cross-sectional area $s\,t$), whereas in Case 2 the relevant separation is governed by the arc-length l_{arc} along the polygon perimeter, which scales linearly with s.

Index-consistent scaling. The relations derived below are *index-consistent*, i.e. they compare measurements taken at the same electrode-step index i across different n. With $\theta_i = i\beta = i\,2\pi/n$, the discrete angle set $\{\theta_i\}$ changes with n, but each θ_i corresponds to the same number of face-to-face steps and thus to the same nominal path topology. Under this interpretation, the n-dependence of the Case 2 geometric factor reduces to $\tan(\pi/n)$ (for constant D_{af}) or $\cot(\pi/n)$ (for constant s), which motivates the following compact dimensionless n-scaling factors relative to a reference polygon $n_{\mathrm{ref}} \in \mathbb{N}$:

$$\eta_n^{(D)} := \frac{\tan\left(\frac{\pi}{n}\right)}{\tan\left(\frac{\pi}{n_{\mathrm{ref}}}\right)}, \qquad \eta_n^{(s)} := \frac{\cot\left(\frac{\pi}{n}\right)}{\cot\left(\frac{\pi}{n_{\mathrm{ref}}}\right)}, \qquad n_{\mathrm{ref}} \in \mathbb{N}. \tag{C.4}$$

The corresponding resistance ratios are evaluated relative to the base-model reference at n_{ref}.

At $\theta_i = 0^\circ$, the base-model reference satisfies $R_{0^\circ}^{(\mathrm{base})} \propto D_{\mathrm{af}}/(s\,t)$. Hence, under constant D_{af} the variation is driven by the effective face width $s^{(D)}(n)$ and yields

$$\frac{R_{0^\circ}^{(\mathrm{base})}(n;\, D_{\mathrm{af}})}{R_{0^\circ}^{(\mathrm{base})}(n_{\mathrm{ref}};\, D_{\mathrm{af}})} = \frac{1}{\eta_n^{(D)}}, \tag{C.5}$$

whereas under constant s it is driven by the n-dependent separation $D_{\mathrm{af}}^{(s)}(n)$ and yields

$$\frac{R_{0^\circ}^{(\mathrm{base})}(n;\, s)}{R_{0^\circ}^{(\mathrm{base})}(n_{\mathrm{ref}};\, s)} = \eta_n^{(s)}. \tag{C.6}$$

For Case 2, the transverse contribution follows $R_{2\perp}^{(\mathrm{base})} \propto l_{\mathrm{arc}}/D_{\mathrm{af}}$. Since $l_{\mathrm{arc}} \propto s$, the constant-$D_{\mathrm{af}}$ scenario inherits the scaling with $s^{(D)}(n)$, leading to

$$\frac{R_2^{(\mathrm{base})}(\theta_i;\, n, D_{\mathrm{af}}) - R_{2\parallel}^{(\mathrm{base})}(\theta_i)}{R_2^{(\mathrm{base})}(\theta_i;\, n_{\mathrm{ref}}, D_{\mathrm{af}}) - R_{2\parallel}^{(\mathrm{base})}(\theta_i)} = \eta_n^{(D)}, \qquad \theta_i \geq \alpha, \tag{C.7}$$

whereas under constant s the arc-length factor is fixed and the scaling is governed by the inverse change of $D_{\mathrm{af}}^{(s)}(n)$, yielding

$$\frac{R_2^{(\mathrm{base})}(\theta_i;\, n, s) - R_{2\parallel}^{(\mathrm{base})}(\theta_i)}{R_2^{(\mathrm{base})}(\theta_i;\, n_{\mathrm{ref}}, s) - R_{2\parallel}^{(\mathrm{base})}(\theta_i)} \;=\; \frac{1}{\eta_n^{(s)}}, \qquad \theta_i \geq \alpha. \tag{C.8}$$

As a practical example, increasing the number of sides from $n_{\mathrm{ref}} = 12$ to $n = 24$ yields $\eta_n^{(D)} = \tan(\pi/24)/\tan(\pi/12) \approx 0.5$ and $\eta_n^{(s)} = \cot(\pi/24)/\cot(\pi/12) \approx 2.0$. Accordingly, under constant D_{af} the transverse Case 2 contribution is reduced to ≈ 0.5 while the 0° reference resistance increases by the reciprocal factor ≈ 2.0, whereas under constant s the 0° reference resistance increases by ≈ 2.0 while the transverse Case 2 contribution decreases by the reciprocal factor ≈ 0.5. In practice, the observed scaling of the total resistance may deviate from these idealized trends if a non-negligible longitudinal contribution $R_{2\parallel}^{(\mathrm{base})}(\theta_i)$ is present, because such an additive term is not governed by $l_{\mathrm{arc}}/D_{\mathrm{af}}$ and therefore does not necessarily follow the same n-dependence as the transverse component.

Transverse and Through-Thickness Resistivity Although the present framework targets in-plane resistivities, the parameter $\rho_\perp$ must be interpreted as an effective transverse resistivity. In a UD CFRP laminate, the laminate thickness is orders of magnitude larger than the fiber diameter, and the electrodes span the full thickness. As a result, transverse charge transport in Case 2 is not purely in-plane, but generally involves mixed-mode pathways that include both in-plane transverse segments and through-thickness excursions, governed by the availability and probability of fiber–fiber contacts and junctions across the thickness. Consequently, $\rho_\perp$ can change due to manufacturing-related effects such as fiber waviness, resin-rich regions, coatings or sizing, and variations in fiber areal weight that alter the density of inter-fiber contacts in the thickness direction.

To assess the sensitivity of the base model with respect to such effective transverse transport changes, a parametric variation is considered in which all geometric parameters (including n, D_{af}, s, and t) and $\rho_\parallel$ are held constant, while $\rho_\perp$ is varied. For compactness, a transverse resistivity scaling factor is introduced as

$$\eta_{\rho_\perp} \;:=\; \frac{\rho_\perp}{\rho_{\perp,\mathrm{ref}}}, \qquad \rho_{\perp,\mathrm{ref}} > 0, \tag{C.9}$$

where $\rho_{\perp,\mathrm{ref}}$ denotes a chosen reference value. Since the Case 2 transverse contribution is Ohmic and scales linearly with $\rho_\perp$ for fixed geometry, the relative change of the isolated transverse term is

$$\frac{R_2^{(\mathrm{base})}(\theta_i;\,\rho_\perp) - R_{2\parallel}^{(\mathrm{base})}(\theta_i)}{R_2^{(\mathrm{base})}(\theta_i;\,\rho_{\perp,\mathrm{ref}}) - R_{2\parallel}^{(\mathrm{base})}(\theta_i)} \;=\; \frac{\rho_\perp}{\rho_{\perp,\mathrm{ref}}} \;=\; \eta_{\rho_\perp}, \qquad \theta_i \geq \alpha, \tag{C.10}$$

i.e., for unchanged geometry and $\rho_\parallel$, doubling the effective transverse resistivity $\rho_\perp$ doubles the predicted Case 2 resistance contribution associated with transverse (mixed-mode) transport, whereas any additional longitudinal contribution $R_{2\parallel}^{(\mathrm{base})}(\theta_i)$ may reduce the apparent scaling of the total measured resistance if it remains comparatively small or insensitive to $\rho_\perp$.

C.4 Model Comparison

Assuming that $\rho_\parallel$ and $\rho_\perp$ are intrinsic material constants, i.e., identical for all cases and electrode variants, the different model variants modify primarily the geometric factors in $R_1(\theta_i)$ and $R_2(\theta_i)$. To express these effects concisely, dimensionless resistance ratios are introduced using the capital gamma notation,

$$\Gamma_k^{(a/b)}(\theta_i) \;:=\; \frac{R_k^{(a)}(\theta_i)}{R_k^{(b)}(\theta_i)}, \qquad k \in \{1,2\}, \tag{C.11}$$

where (a/b) denotes the compared model variants (e.g., (el/base) or (in/el)). For improved readability of the Case 2 expressions, the following compact notations are further employed:

$$K \;:=\; \frac{\rho_\perp}{t}\,\tan\!\left(\frac{\pi}{n}\right), \qquad x_i \;:=\; \frac{n}{\pi}\,\theta_i. \tag{C.12}$$

Base model vs. Small Electrodes Model For Case 1, the electrode-center distance is unchanged, and the difference enters through the electrode footprint-limited effective width. The relative change is

$$\frac{R_1^{(\mathrm{el})}(\theta_i)}{R_1^{(\mathrm{base})}(\theta_i)} \;=\; \frac{1}{\eta_{\mathrm{el}}}, \qquad \theta_i \leq \tilde{\alpha}. \tag{C.13}$$

For Case 2, only the arc-length separation changes from $s\left(\frac{n}{\pi}\theta_i - 1\right)$ in the base model to $s\left(\frac{n}{\pi}\theta_i - \eta_{\mathrm{el}}\right)$ for small electrodes. The exact ratio reads

$$\frac{R_2^{(\mathrm{el})}(\theta_i)}{R_2^{(\mathrm{base})}(\theta_i)} = \frac{K\,(x_i - \eta_{\mathrm{el}}) + R_{2\parallel}^{(\mathrm{el})}(\theta_i)}{K\,(x_i - 1) + R_{2\parallel}^{(\mathrm{base})}(\theta_i)}, \qquad \theta_i \geq \tilde{\alpha}. \tag{C.14}$$

If, as a simplifying assumption, the longitudinal term is taken to be identical for both variants, $R_{2\parallel}^{(\mathrm{el})}(\theta_i) = R_{2\parallel}^{(\mathrm{base})}(\theta_i) =: R_{2\parallel}(\theta_i)$, then Equation (C.14) reduces to

$$\frac{R_2^{(\mathrm{el})}(\theta_i)}{R_2^{(\mathrm{base})}(\theta_i)} = \frac{x_i - \eta_{\mathrm{el}} + \delta(\theta_i)}{x_i - 1 + \delta(\theta_i)}, \qquad \delta(\theta_i) := \frac{R_{2\parallel}(\theta_i)}{K}, \qquad \theta_i \geq \tilde{\alpha}. \tag{C.15}$$

In the additional limiting case that the longitudinal contribution in Case 2 is negligible compared to the transverse term, i.e. $\delta(\theta_i) \approx 0$, one obtains the purely geometric approximation

$$\frac{R_2^{(\mathrm{el})}(\theta_i)}{R_2^{(\mathrm{base})}(\theta_i)} \approx \frac{x_i - \eta_{\mathrm{el}}}{x_i - 1} = 1 + \frac{1 - \eta_{\mathrm{el}}}{x_i - 1}, \qquad x_i = \frac{n}{\pi}\theta_i, \qquad \theta_i \geq \tilde{\alpha}. \tag{C.16}$$

Small Electrodes Model vs. Inner Electrodes Model In Case 1, the dominant conduction path is the direct fiber-parallel connection between the two active electrodes; the inner electrodes do not lie on this path. Hence, within the present model,

$$\frac{R_1^{(\mathrm{in})}(\theta_i)}{R_1^{(\mathrm{el})}(\theta_i)} = 1, \qquad \theta_i \leq \tilde{\alpha}. \tag{C.17}$$

In Case 2, using the compact notation from Equation (C.12), the small-electrode and inner-electrode variants are

$$\begin{aligned} R_2^{(\mathrm{el})}(\theta_i) &= K\,(x_i - \eta_{\mathrm{el}}) + R_{2\parallel}^{(\mathrm{el})}(\theta_i), \\ R_2^{(\mathrm{in})}(\theta_i) &= K\,x_i\,(1 - \eta_{\mathrm{el}}) + R_{2\parallel}^{(\mathrm{in})}(\theta_i), \qquad \theta_i \geq \tilde{\alpha}. \end{aligned} \tag{C.18}$$

The exact ratio therefore reads

$$\frac{R_2^{(\mathrm{in})}(\theta_i)}{R_2^{(\mathrm{el})}(\theta_i)} = \frac{K\,x_i\,(1 - \eta_{\mathrm{el}}) + R_{2\parallel}^{(\mathrm{in})}(\theta_i)}{K\,(x_i - \eta_{\mathrm{el}}) + R_{2\parallel}^{(\mathrm{el})}(\theta_i)}, \qquad \theta_i \geq \tilde{\alpha}. \tag{C.19}$$

If, as a simplifying assumption, the longitudinal term is taken to be identical for both variants, $R_{2\parallel}^{(\mathrm{in})}(\theta_i) = R_{2\parallel}^{(\mathrm{el})}(\theta_i) =: R_{2\parallel}(\theta_i)$, then Equation (C.19) reduces to

$$\frac{R_2^{(\mathrm{in})}(\theta_i)}{R_2^{(\mathrm{el})}(\theta_i)} \;=\; \frac{x_i\,(1-\eta_{\mathrm{el}}) + \delta(\theta_i)}{x_i - \eta_{\mathrm{el}} + \delta(\theta_i)}, \qquad \delta(\theta_i) := \frac{R_{2\parallel}(\theta_i)}{K}, \qquad \theta_i \geq \tilde{\alpha}. \tag{C.20}$$

In the additional limiting case that the longitudinal contribution in Case 2 is negligible, $\delta(\theta_i) \approx 0$, one obtains the purely geometric approximation

$$\frac{R_2^{(\mathrm{in})}(\theta_i)}{R_2^{(\mathrm{el})}(\theta_i)} \;\approx\; \frac{x_i\,(1-\eta_{\mathrm{el}})}{x_i - \eta_{\mathrm{el}}}, \qquad \theta_i \geq \tilde{\alpha}. \tag{C.21}$$

Base model vs. Inner Electrodes. For a compact comparison, the base-to-inner ratio is obtained by chaining the two intermediate ratios,

$$\frac{R_k^{(\mathrm{in})}(\theta_i)}{R_k^{(\mathrm{base})}(\theta_i)} \;=\; \frac{R_k^{(\mathrm{in})}(\theta_i)}{R_k^{(\mathrm{el})}(\theta_i)} \cdot \frac{R_k^{(\mathrm{el})}(\theta_i)}{R_k^{(\mathrm{base})}(\theta_i)}, \qquad k \in \{1, 2\}. \tag{C.22}$$

For Case 1, the inner electrodes do not lie on the dominant longitudinal conduction path, the first factor equals unity, such that

$$\frac{R_1^{(\mathrm{in})}(0^\circ)}{R_1^{(\mathrm{base})}(0^\circ)} \;=\; \frac{1}{\eta_{\mathrm{el}}}. \tag{C.23}$$

For Case 2, using Equation (C.12), and assuming identical longitudinal contributions for all variants, $R_{2\parallel}^{(\mathrm{base})}(\theta_i) = R_{2\parallel}^{(\mathrm{el})}(\theta_i) = R_{2\parallel}^{(\mathrm{in})}(\theta_i) =: R_{2\parallel}(\theta_i)$, this simplifies to

$$\frac{R_2^{(\mathrm{in})}(\theta_i)}{R_2^{(\mathrm{base})}(\theta_i)} \;=\; \frac{x_i\,(1-\eta_{\mathrm{el}}) + \delta(\theta_i)}{x_i - 1 + \delta(\theta_i)}, \qquad \delta(\theta_i) := \frac{R_{2\parallel}(\theta_i)}{K}, \qquad \theta_i \geq \tilde{\alpha}. \tag{C.24}$$

In the additional limiting case where the longitudinal contribution is negligible, $\delta(\theta_i) \approx 0$, one obtains

$$\frac{R_2^{(\mathrm{in})}(\theta_i)}{R_2^{(\mathrm{base})}(\theta_i)} \;\approx\; \frac{x_i\,(1-\eta_{\mathrm{el}})}{x_i - 1}, \qquad \theta_i \geq \tilde{\alpha}. \tag{C.25}$$

Supervised Student Theses

[1] L. Braun. “Ultraschalluntersuchungen an Verbundwerkstoffen – CompoSE: Allgemeine Merkmalserkennung.” BA thesis. Hamburg University of Technology, Aug. 2025.

[2] L. Fahs. “Charakterisierung der Temperaturleitfähigkeit in der Ebene von anisotropen kohlenstofffaserverstärkten Verbundwerkstoffen mittels Laser-Infrarot-Thermografie.” Project Thesis. Hamburg University of Technology, Sept. 2025.

[3] J. Tschentscher. “Detektion und Analyse von Mikrorissen in Faser-Kunststoff-Verbundwerkstoffen anhand von Mikroschliffbildern mithilfe von Machine Learning.” MA thesis. Hamburg University of Technology, Mar. 2025.

[4] S. Wienhold. “Untersuchungen von wasserlöslichem PVAL-Stickgrund und Phenoxygarn im Tailored Fiber Placement Prozess.” BA thesis. Hamburg University of Technology, Sept. 2025.

[5] N. Andresen. “Neugestaltung des Kofferraums eines EPAC-Leichtkraftfahrzeugs von Hopper Mobility zur Erschließung von Leichtbaupotenzialen.” BA thesis. Hamburg University of Technology, Oct. 2024.

[6] L. Fahs. “Untersuchung der anisotropen elektrischen und thermischen Leitfähigkeit von Thin-Ply Faserverbundwerkstoffen.” BA thesis. Hamburg University of Technology, May 2024.

[7] L. Möller. “Untersuchung des Leichtbaupotentials von Faserverbundwerkstoffen bei der Konstruktion des Daches eines EPAC-Leichtkraftfahrzeugs von Hopper Mobility.” MA thesis. Hamburg University of Technology, Apr. 2024.

[8] J. Sorejevic. “Entwicklung eines Reparaturkonzepts für GFK-Bauteile am Beispiel des Hopper Leichtkraftfahrzeugs.” MA thesis. Hamburg University of Technology, Dec. 2024.

[9] F. Touni. “Analyse und Simulation des progressiven Schadenswachstums in Thin-Ply Laminaten.” Project Thesis. Hamburg University of Technology, Nov. 2023.

[10] F. Touni. “Untersuchung des elektrischen und thermischen Anisotropieverhaltens von Faserverbundwerkstoffen.” MA thesis. Hamburg University of Technology, Aug. 2023.

[11] O. Yücel. “Rotatorischer FFF-3D-Druck: Prozessadaption zur additiven Fertigung von Darmstents.” Project Thesis. Hamburg University of Technology, Aug. 2023.

[12] T. Albrecht. “Fertigungsprozess- und Vernetzungsoptimierung von Hot Melt (HM)3D-Druckfilament.” BA thesis. Hamburg University of Technology, Dec. 2022.

[13] M. Bormann. “Entwicklung einer CFK-Rotorkomponente für einen Axialflussmotor.” BA thesis. Hamburg University of Technology, Mar. 2022.

[14] L. Christensen. “Duromer- und Glasfaserverbund-Flexibilisierung mithilfe Partiell Reagierter Substrukturen (PRS).” MA thesis. Hamburg University of Technology, Aug. 2022.

[15] J. C. Otto. “Experimentelle Untersuchung und Bewertung einer Dosierpumpe für Fused-Layer-Modeling-3D-Druck-Systeme.” BA thesis. Hamburg University of Technology, May 2022.

[16] L. Christensen. “Multifunktionale Kunststoffe durch In-Situ-Strukturierung der Polymermorphologie: Härtervariation.” Project Thesis. Hamburg University of Technology, Apr. 2021.

[17] K. Fischer. “Entwicklung und Validierung eines Messsystems für die elektrische Impedanz- und Widerstandstomographie.” Project Thesis. Hamburg University of Technology, Feb. 2021.

[18] K. Fischer. “Weiterentwicklung eines Messsystems für die elektrische Widerstandstomographie für kohlenstofffaserverstärkten Kunststoff.” MA thesis. Hamburg University of Technology, Oct. 2021.

[19] D. A. Nguyen. “pyEIT in der Anwendung: Schadendetektion und -Lokalisierung in CFK mittels elektrischer Widerstandstomografie.” BA thesis. Hamburg University of Technology, Feb. 2021.

[20] J. Sorejevic. “Parameteroptimierung für FFF-3D-Druck-Prozesse handelsüblicher Thermoplaste.” BA thesis. Hamburg University of Technology, May 2021.

[21] A. Strunz. “Multifunktionale Kunststoffe durch In-Situ-Strukturierung der Polymermorphologie: Harzvariation.” Project Thesis. Hamburg University of Technology, Apr. 2021.

[22] J. Jacobs. “Mechanische und thermische Validierung des DirectPreg-Prozesses.” BA thesis. Hamburg University of Technology, Oct. 2020.

[23] M. C. Killi. “Einflussparameteranalyse der Laminatqualität von in Out-of-Autoclave-Prozessen verarbeiteten und direktimprägnierten Textilien.” MA thesis. Hamburg University of Technology, Sept. 2020.

[24] M. Neubacher. “Pultrusion von faserverstärkten Kunststoffprofilen für Anwendungen in der Luftfahrt – Materialevaluation & Prozessoptimierung.” BA thesis. Hamburg University of Technology, Dec. 2020.

[25] S. Selz. “Untersuchung des Versagensverhaltens von Thin-Ply CFK-Hybrid Laminaten unter zyklischer Temperaturbelastung.” Project Thesis. Hamburg University of Technology, Aug. 2020.

[26] R. L.-S. Sum. “Prozesskontrolle und Einfluss der Linienpressung beim Imprägnierprozess.” Project Thesis. Hamburg University of Technology, July 2020.

[27] F. Touni. “Analyse des Imprägnierverhaltens von Glasfasertextilen im Imprägnierwalzwerkprozess.” BA thesis. Hamburg University of Technology, Dec. 2020.

[28] O. Yücel. “Einfluss partikulärer Füllstoffe auf das Brandverhalten und die mechanischen Eigenschaften von Epoxidharzen.” BA thesis. Hamburg University of Technology, June 2020.

[29] G. Öcalan. “Untersuchung des Einflusses verschiedener Vorbehandlung von Edelstahlfolien auf die Anhaftung zwischen Edelstahl und CFK.” Project Thesis. Hamburg University of Technology, May 2019.

[30] J. Tobaben. “Prozessentwicklung und Parameterstudie für die Out-of-Autoklav Fertigung direktimprägnierter Textilien.” BA thesis. Hamburg University of Technology, Nov. 2019.

The student theses by Braun [1], Fahs [6, 2], and Touni [10] provided key inputs for this dissertation.

Research Projects

[1] J. M. Karsten, J. Drummer, B. Fiedler, T. Müller-Hansen, M. Halama, and P. Herrmann. *Hopper – Entwicklung einer neuen Fahrzeugklasse zwischen Auto und Fahrrad für die moderne urbane Personenbeförderung*. Schlussbericht 51167777. IFB Hamburg, Oct. 2025.

[2] J. M. Karsten, M. Segelken, and B. Fiedler. *DCFP - Direct Continuous Fiber Placement*. Schlussbericht C4T527. Technische Universität Hamburg, Dec. 2023.

[3] J. M. Karsten, K. P. von Berg, H. Wittich, B. Fiedler, S. Detjen, B. Riecken, S. Kaysser, C. Keun, and A. Kehne. *HM3D - Reaktiver multifunktionaler Duromerwerkstoff mit thermoplastischen Eigenschaften für filamentbasierte 3D-Druckprozesse*. Schlussbericht 03XP0292C. Bundesministerium für Bildung und Forschung, Jan. 2023.

[4] J. M. Karsten, B. Kötter, B. Fiedler, C. Keun, B. Riecken, S. Kaysser, A. Brouschkin, U. Köpke, J. Buck, M. Fette, and J.-P. Wulfsberg. *COMP-1633 - Flame Retardant FRP Systems for Aircraft Interior Applications*. Schlussbericht 03INT504BB. Bundesministerium für Bildung und Forschung, June 2021.

[5] J. M. Karsten, K. Kröning, and B. Fiedler. *Multifunktionale Kunststoffe durch In-Situ-Strukturierung der Polymermorphologie*. Schlussbericht C4T224. Technische Universität Hamburg, Feb. 2021.

Scientific Publications

[1] K. M. Eckert, J. Bonsen, A. Hajnal, J. Gmeiner, J. Hasse, M. Adrian, J. M. Karsten, P. A. Kißling, A. Penn, B. Fiedler, G. A. Luinstra, and I. Smirnova. "Enhancing Swelling Kinetics of pNIPAM Lyogels: The Role of Crosslinking, Copolymerization, and Solvent." In: *Fluid Phase Equilibria* 597 (Oct. 2025), p. 114462. ISSN: 03783812. DOI: 10.1016/j.fluid.2025.114462.

[2] J. M. Karsten, F. Touni, and B. Fiedler. "An Efficient Testing Method to Determine the Anisotropic Thermal Conductivity of Long-Fiber Reinforced Composites." In: *Proceedings of the 21st European Conference on Composite Materials*. 21st European Conference on Composite Materials (ECCM21). Vol. Volume 4 - Experimental techniques. Nantes, France: The European Society for Composite Materials (ESCM) and the Ecole Centrale de Nantes, 2024, pp. 70–77. ISBN: 978-2-912985-01-9.

[3] H. Wittich, L. Christensen, J. M. Karsten, and B. Fiedler. "Thermoset and Glass Fiber Composite Flexibilization Using Partially Reacted Substructures (PRS)." In: *Proceedings of the 21st European Conference on Composite Materials*. 21st European Conference on Composite Materials (ECCM21). Vol. Volume 3 - Material and Structural Behavior – Simulation & Testing. Nantes, France: The European Society for Composite Materials (ESCM) and the Ecole Centrale de Nantes, 2024, pp. 952–959. ISBN: 978-2-912985-01-9.

[4] A. Lühring, B. Fiedler, C. Keun, J. Hoppe, J. M. Karsten, M. Hoppe, P. Bitomsky, S. Kaysser, S. Detjen, T. Schueppstuhl, T. Konieczny, Z. Kállai, and B. Riecken. "Minimizing Mechanical Anisotropy in Fused Filament Fabrication Through Innovative Thermoset Materials and Additive Manufacturing Processes." In: *SAMPE 2023*. SAMPE 2023. NA SAMPE, 2023. ISBN: 978-1-934551-43-1. DOI: 10.33599/nasampe/s.23.0326.

[5] J. Langot, T. Pelzmann, P. Chávez-Gómez, C. Boanta, J. M. Karsten, B. Fiedler, M. Lévesque, and E. Robert. "Multi-Physics Modeling of the Ignition of Polymer Matrix Composites Exposed to Fire." In: *Fire Safety Journal* 122 (June 2021), p. 103312. ISSN: 03797112. DOI: 10.1016/j.firesaf.2021.103312.

[6] B. Kötter, J. M. Karsten, J. Körbelin, and B. Fiedler. "CFRP Thin-Ply Fibre Metal Laminates: Influences of Ply Thickness and Metal Layers on Open Hole Tension and Compression Properties." In: *Materials* 13.4 (Feb. 18, 2020), p. 910. ISSN: 1996-1944. DOI: 10.3390/ma13040910.

[7] M. Schuett, J. M. Karsten, L. Schott, H. Wittich, K. Schulte, and B. Fiedler. "Experimental and Analytical Study of an CF-PEEK Fastener All Composites Single-Lap Shear Joint under Static and Fatigue Loading." In: *CEAS Aeronautical Journal* 10.2 (June 2019), pp. 565–587. ISSN: 1869-5582, 1869-5590. DOI: 10.1007/s13272-018-0334-z.

[8] T. Augustin, J. M. Karsten, and B. Fiedler. "Detection and Localization of Impact Damages in Carbon Nanotube–Modified Epoxy Adhesive Films with Printed Circuits." In: *Structural Health Monitoring* 17.5 (Sept. 2018), pp. 1166–1177. ISSN: 1475-9217, 1741-3168. DOI: 10.1177/1475921717738140.

[9] T. Augustin, J. M. Karsten, B. Kötter, and B. Fiedler. "Health Monitoring of Scarfed CFRP Joints under Cyclic Loading via Electrical Resistance Measurements Using Carbon Nanotube Modified Adhesive Films." In: *Composites Part A: Applied Science and Manufacturing* 105 (Feb. 2018), pp. 150–155. ISSN: 1359835X. DOI: 10.1016/j.compositesa.2017.11.015.

[10] T. Augustin, J. M. Karsten, and B. Fiedler. "Impact Damage Detection and Localization of Adhesively Bonded Fiber Reinforced Structures Using Silver Nanoparticle Based Printed Circuits." In: *Structural Health Monitoring 2017*. Structural Health Monitoring 2017. DEStech Publications, Inc., Sept. 28, 2017. ISBN: 978-1-60595-330-4. DOI: 10.12783/shm2017/14020.

[11] N. Kosmann, J. M. Karsten, M. Schuett, K. Schulte, and B. Fiedler. "Determining the Effect of Voids in GFRP on the Damage Behaviour under Compression Loading Using Acoustic Emission." In: *Composites Part B: Engineering* 70 (Mar. 2015), pp. 184–188. ISSN: 13598368. DOI: 10.1016/j.compositesb.2014.11.010.